Kelemen, P.B., Kikawa, E., Miller, D.J., et al., 2004
Proceedings of the Ocean Drilling Program, Initial Reports Volume 209

7. SITE 1272[1]

Shipboard Scientific Party[2]

OPERATIONS SUMMARY

Transit to Site 1272

Site 1272 is the northernmost of our drilling locations on the transect of sites south of the 15°20′N Fracture Zone on the northwestern flank of the inside corner high. The site was targeted based on reviews of videotapes from *Faranaut* Dives 5 and 2, near the top of the ridge where most of the dive samples were serpentinized peridotite. Site 1272 is ~3.7 nmi north of Site 1271.

Hole 1272A

Having protected our supply of drill collars during earlier operations, we elected to increase the length of our bottom-hole assembly (BHA) at this site in order to achieve deeper penetration without placing the top of the BHA below the seafloor. Fourteen 8.25-in drill collars (nominally a total of 131 m long) were lowered at the end of the drill string while we positioned the vessel over the Global Positioning System coordinates of our camera survey starting position (Fig. F1). We surveyed along a shallow-dipping, sediment-covered slope and selected a drilling target located in flat terrain between the depths of *Faranaut* Dive 2 samples FR02-11 and FR02-12 (both serpentinized peridotite) (see Fig. F2). A push-in test with the drill string indicated the sediment cover was only ~1 m thick. Hole 1272A was spudded at 2045 hr on 7 June 2003. Core 1R advanced to 12.9 meters below seafloor (mbsf) (Table T1). Coring continued through Core 27R to a depth of 131.0 mbsf with no difficulty but slow penetration (average = 2.2 m/hr). Since the core we were recovering was clay rich and we encountered several intervals of drilling-induced disturbance, we elected to use core liners inside the core barrels to see if recovery might improve. Core liners were used on Cores

F1. Subsea camera survey track and hole location, p. 39.

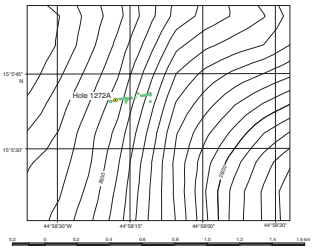

F2. Bathymetric section for Site 1272, p. 40.

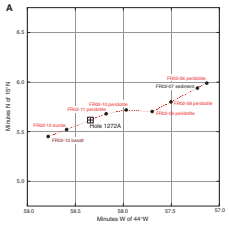

T1. Coring summary, Site 1272, p. 121.

[1]Examples of how to reference the whole or part of this volume.
[2]Shipboard Scientific Party addresses.

21R and 23R through 27R, and recovery improved to values as high as 79% (average = ~55%, compared to ~30% recovery in similar lithology cored without liners).

The Lamont-Doherty Earth Observatory (LDEO) Drill String Accelerometer tool was deployed with Cores 12R and 14R. After coring to 131 mbsf with little change in the character of the recovered core or in drilling conditions, we decided to terminate coring and begin wireline logging.

Two logging tool strings were deployed in the hole. Both the triple combination (triple combo) and Formation MicroScanner (FMS)-sonic tool strings reached within 6–7 m of the bottom of the hole. With logging completed, the pipe was pulled clear of the seafloor at 0245 hr on 12 May. By 0730 hr, the ship was secured for transit, ending operations at Site 1272.

IGNEOUS AND MANTLE PETROLOGY

Drilling in Hole 1272A provided 27 cores from a penetration depth of 131.5 m (recovery = 31.5%). The upper part is composed almost entirely of fine- to medium-grained mafic rocks with a subordinate amount of peridotite. The section below 56 mbsf is nearly the inverse, almost exclusively peridotite with only a small amount of mafic material. Thus, we divide the core into two lithologic units, Unit I diabase and Unit II harzburgite.

Lithology and Stratigraphy

Unit I

Interval: Sections 209-1272A-1R-1 through 12R-1
Depth: 0–56 mbsf
Lithology: diabase

Unit I includes the first 11 cores of the hole and contains 75% diabase and 25% peridotite (Fig. F3). It is unclear if the rocks that compose Unit I (1) are part of a talus pile, (2) represent a coherent package of rocks, or (3) are a talus pile that has been intruded by dikes. Fine-grained cobbles with weathering rinds that appear to be concentric in Section 209-1272A-7R-1 suggest these are fragments that were weathered on or near the seafloor. Medium-grained gabbroic rocks make up much of Sections 209-1272A-3R-1 and 4R-1 and appear to be sampled from a coherent section. The paleomagnetic and structural data are ambiguous as to the nature of Unit I. For simplicity, we assume that this section is coherent and so name all the fine-grained mafic rocks accordingly.

The top of Unit I contains peridotite, almost entirely dunite, that has been subjected to extensive alteration, completely masking its original texture (both serpentinization and near-surface oxidation). A small amount of harzburgite is present in the lower portion of Unit I in Sections 209-1272A-8R-1, 9R-1, and 10R-1 (Fig. F3). The mafic rocks in Unit I have significant variations in their grain size, from completely aphanitic to fine grained and even medium grained. Unit I is composed mainly of diabase but includes some microgabbros and gabbros. These are distinguished based on grain size and texture. Diabases have grain sizes that range from aphanitic to fine grained, microgabbros are fine grained, and gabbros are medium grained or coarser. The textural dis-

F3. Downhole lithologic and modal variations, p. 42.

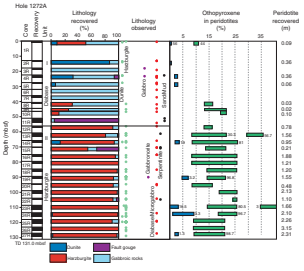

tinction between diabases and microgabbros is based on the modal homogeneity of the sample. Diabases are defined as having a felty texture with randomly distributed plagioclase laths throughout and are modally homogeneous. Microgabbros can have felty textured plagioclase or be more massive, but those with a felty texture have distinctive modal segregations of plagioclase laths into a framework in the sample (Fig. F4). Using these criteria, the bulk of the gabbroic rocks in Unit I are classified as diabase. They are very fine grained, and in thin section some can be seen to contain devitrified glass. The only microgabbro in Unit I is found in Section 209-1272A-1R-1 (Pieces 6–8). There are two intervals of gabbroic rocks in Unit I in intervals 209-1272A-3R-1, 0–110 cm, and 4R-1, 68–140 cm.

Unit II

Interval: Sections 209-1272A-12R-1 through 27R-1
Depth: 56–131 mbsf
Lithology: harzburgite

Unit II consists of a thick (75.0 m drilled; 27.7 m recovered) sequence of serpentinized harzburgite. A limited number of small pieces of fine-grained mafic rocks (3.5%, representing 0.97 m recovered) were recovered at the top of several drilled sections and are interpreted as talus introduced during drilling. No peridotite/gabbro contacts are present. Five dunite horizons (3.4%) are also present (Fig. F3). The dunite is defined by areas that are orthopyroxene-free (or contain <5% orthopyroxene) within harzburgite. These areas are bands or ovoid patches in cross section (Figs. F5, F6) and might correspond to lens-shaped (interfingered?) material, a few centimeters wide. The harzburgite is texturally quite homogeneous at the scale of the hole, having coarse-grained protogranular textures. High-temperature banding defined by orthopyroxene-rich layers is present in some places (Fig. F7A). Plastic deformation and recrystallization below the solidus is absent except for some slight deformation in a few places, and the textures are truly protogranular (see "Crystal-Plastic Fabrics and Deformation Intensity," p. 14, in "Harzburgite Section (56–131 mbsf)" in "Structural Geology"). The two dominant mineral phases are olivine and orthopyroxene, forming 96%–98% of the rocks. Spinel is almost exclusively associated with orthopyroxene, forming aggregates as large as 5 mm. Its abundance varies with that of orthopyroxene and is in the 1%–2% range. Clinopyroxene can be observed where the rocks are less serpentinized. It forms tiny grains associated with orthopyroxene crystals, never exceeding 2% in modal proportion.

In >83% of the harzburgites, modal orthopyroxene contents vary between 15% (28% of samples) and 25% (20% of the samples), with 35% of the samples having ~20% orthopyroxene. The ratio of olivine to orthopyroxene generally varies at the decimeter scale, but finer-scale variations also occur in some intervals (Fig. F7B). Locally, the amount of orthopyroxene increases to as much as 30%–40% (Fig. F7C) or is as low as 10% (Fig. F8). Orthopyroxene-rich harzburgite forms a mere 2.5% of the Unit II, whereas harzburgite with <15% orthopyroxene constitutes ~15% of Unit II. Although the harzburgite is generally uniform in composition, several discrete sequences can be discerned in Unit II.

Between 60.7 and 63.4 mbsf (Sections 209-1272A-13R-1 and 13R-2), a sequence of orthopyroxene-rich harzburgite (30%–35% orthopyroxene) sandwiches a meter of harzburgite (10%–20% orthopyroxene). Most of Cores 209-1272A-14R and 15R (starting at the top of Section

F4. Textures in fine-grained mafic rocks, p. 43.

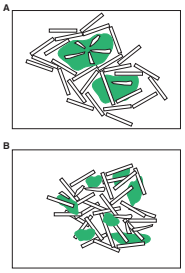

F5. Dunite areas within harzburgite, p. 44.

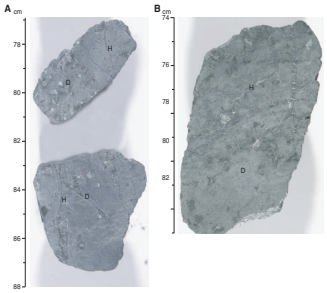

F6. Alternating bands of dunite and harzburgite, p. 45.

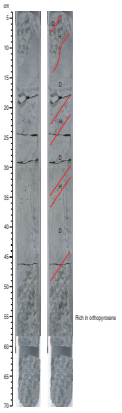

F7. Foliation and orthopyroxene in harzburgite, p. 46.

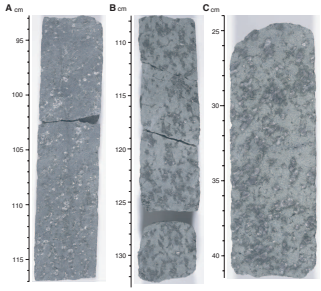

14R-1 [65.7 mbsf] down to the bottom of Section 15R-1 [70.6 mbsf]) consist of a meter-thick sequence of harzburgite with 10%–15% orthopyroxene interlayered with harzburgite containing 25% orthopyroxene. The orthopyroxene-poor sequence contains the uppermost dunite horizon.

Below 75.1 mbsf (in Section 209-1272A-16R-1), orthopyroxene content ranges from 10% to 30% on a centimeter to meter scale. Nevertheless, the averaged contents of orthopyroxene mode allow us to determine a sequence starting in Core 209-1272A-16R (75.1 mbsf) and finishing at the bottom of Section 24R-1 (114.9 mbsf). In this sequence, corresponding to ~13 m of recovered peridotite, nearly 80% of harzburgites contain 20%–25% orthopyroxene. Intervals of harzburgites containing <15% orthopyroxene with thicknesses varying from 5 to 15 cm form four horizons (Fig. F3). Two of these horizons are dunite. Core 209-1272A-23R contains the longest piece of dunite. In this interval, dunite alternates with harzburgite (Fig. F5). There are 1- to 3-cm-wide orthopyroxene-rich bands of harzburgite within the dunite. The harzburgite below the dunite contains as much as 40% orthopyroxene (Fig. F5). Orthopyroxene-rich harzburgite (30%) also constitutes the bottom of the Section 209-1272A-23R-2, but is only 13 cm thick, with a recovery gap beneath it.

A last sequence (Section 209-1272A-24R-2 [114.9–119.9 mbsf to the bottom of the hole]) is composed of 8.54 m of recovered peridotites in which harzburgite containing 15%–20% orthopyroxene forms ~85% of the rocks. Harzburgite containing >20% orthopyroxene is not present, whereas peridotites with <15%–10% orthopyroxene constitute 14% of the rocks. There are two dunite horizons in this sequence. One is 3 cm thick in Section 209-1272A-24R-2, and the other is 7 cm thick in Section 27R-1 (Fig. F3).

Lithologic Characterization

Mafic Rocks

Based on their grain size, texture, and composition, all of the gabbroic rocks in Unit I are interpreted as having liquid compositions—none have a significant cumulate component. The diabases and microgabbros are relatively uniform in appearance in hand sample and thin section. Clear evidence of quench crystallization in some diabases is preserved in the form of skeletal olivine and plagioclase and spherulites composed of devitrified glass and needles of plagioclase and clinopyroxene (Fig. F9). The most distinctive rocks in Unit I are the quartz-olivine gabbros found in intervals 209-1272A-3R-1, 0–110 cm, and 4R-1, 68–137 cm. They are visually distinctive in hand sample, having a strong modal segregation with patches of mafic minerals surrounded by a network of felsic minerals (Fig. F10). They also contain ~15% pore space into which plagioclase, quartz, amphibole, and other igneous minerals have grown. The mineralogy of these rocks is complicated and includes (in decreasing abundance): plagioclase, olivine, clinopyroxene, quartz, oxides, amphibole, biotite, and apatite. The mafic-rich areas contain poikilitic crystals of olivine and subophitic clinopyroxene with a minor amount of orthopyroxene. The olivine crystals are often intergrown with single plagioclase crystals and cut by others (Fig. F11). The felsic areas are composed predominantly of plagioclase with a lesser amount of quartz and accessory oxides, amphibole, orthopyroxene, biotite, and apatite. Most of the quartz is associated with the pore space,

F8. Orthopyroxene-poor harzburgite and orthopyroxene-bearing dunite, p. 47.

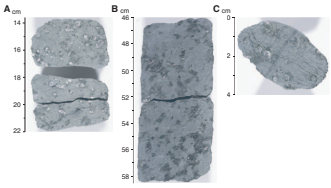

F9. Quench textures in fine-grained mafic rocks, p. 48.

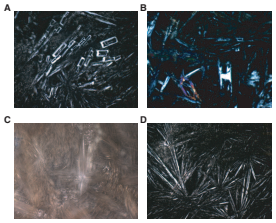

F10. Felsic and mafic domains in the quartz-olivine gabbros, p. 49.

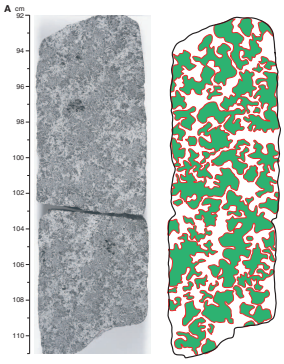

F11. Olivine grain intergrown with a plagioclase grain, p. 51.

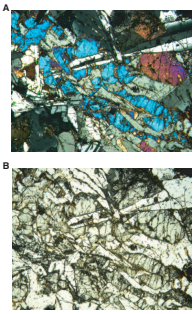

in places as subhedral or even euhedral crystals (Fig. F12). The quartz does not display undulatory extinction, a feature common to igneous quartz induced by strain generated by volume changes on cooling. Small acicular apatite crystals are included in both plagioclase and quartz, with the highest abundance of these needles in felsic minerals near pores (Fig. F13). The shapes of the pores are defined by the negative crystal faces of plagioclase, quartz, oxides, and less commonly by pyroxene or amphibole.

Most of the mafic rocks in Unit II are aphanitic, and some even have glass rinds. They occur near the top of the cored intervals, and we interpret them as having fallen into the hole during recovery processes. However, in Section 209-1272A-19R-1 there is an interval of coarse-grained oxide gabbronorite (Fig. F14). The orthopyroxene in this rock has coarse exsolution lamellae of clinopyroxene, suggesting that it cooled slowly. The rock has been deformed at submagmatic temperatures, as indicated by the development of pyroxene and plagioclase neoblasts around the subhedral to euhedral igneous crystals. The oxide is interstitial and there is no evidence that the deformation is localized into the more oxide-rich portions of the rock.

Harzburgite

The harzburgite in Hole 1272A has a coarse-grained protogranular texture defined by varying proportions of olivine, orthopyroxene, and minor clinopyroxene and spinel. In hand sample, orthopyroxene appears as anhedral grains that partially enclose large (1–2.5 cm wide) olivine-only domains (Fig. F15A). Some orthopyroxene grains are thinner and somewhat elongated along olivine grain boundaries and larger and more equant at the junctions of several olivine grains (Fig. F15). With increasing orthopyroxene/olivine ratios, the orthopyroxene forms clusters of a few crystals that occupy areas as large as the olivine-only domains (Fig. F15B).

In thin section, several features characterize the harzburgite textures:

1. Olivine–orthopyroxene relationships: Olivine/orthopyroxene grain boundaries are smoothly curved (Fig. F16A) with orthopyroxene enclosing olivine (Fig. F16B, F16C) or interstitial (Fig. F16D, F16E). The almost complete serpentinization of olivine makes it difficult to determine olivine grain size. It seems, however, that olivine grain size ranges from 2 to 10 mm. The smaller grains are not neoblasts but are polygonal to subhedral grains that are partially enclosed within orthopyroxene margins (Fig. F16B, F16C).
2. Orthopyroxene crystals in clusters have smoothly curved to near-polygonal grain boundaries (Fig. F17A, F17B). Clinopyroxene may fill orthopyroxene-bounded triple junctions (Fig. F17A) or rim orthopyroxene grains (Fig. F17B–F17D). Orthopyroxene grains in these clusters are generally more equant and include less olivine.
3. Spinel is abundant (1.5%–2%) and characteristically intergrown with the rims of orthopyroxene grains. This spinel has a vermicular shape, and the spinel–orthopyroxene association looks like a symplectic intergrowth (Fig. F18A, F18B). Spinel–orthopyroxene intergrowths are common in abyssal peridotite. In Site 1268 harzburgite, these intergrowths typically occur at orthopyroxene grain boundaries where the orthopyroxene has recrystallized

F12. Euhedral, doubly terminated quartz crystal, p. 52.

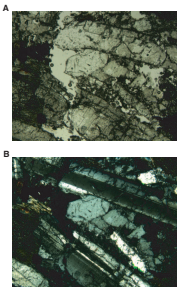

F13. Apatite needles in quartz and plagioclase, p. 53.

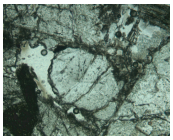

F14. Oxide gabbronorite, p. 54.

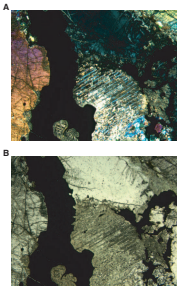

F15. Relationship between olivine and orthopyroxene, p. 55.

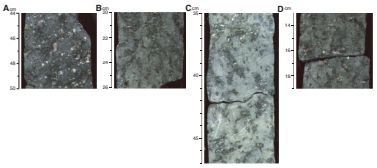

F16. Olivine–orthopyroxene relationships, p. 56.

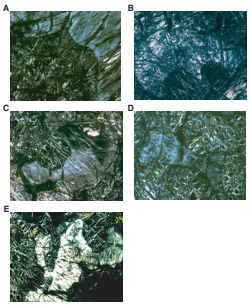

into subgrains. In this context, the spinel is indeed interstitial to the silicate subgrains and its occurrence may be interpreted as the result of recrystallization of earlier orthopyroxene richer in aluminum and chromium (higher-temperature orthopyroxene). However, the Site 1272 harzburgite underwent little or no plastic deformation, so the orthopyroxene margins might not be recrystallized (Fig. F18A, F18B). In these rocks it can be seen that the vermicular spinel extends into adjacent olivine (Fig. F18). In other places, the symplectic intergrowths pseudomorph a polygonal to oval mineral, possibly olivine, that has been replaced by spinel and unidentified alteration phase (Fig. F18F). Similar intergrowths occur at olivine grain boundaries in dunites from Hole 1271B and are interpreted as the result of olivine–melt reaction.

Dunite

Dunite is present in both Units I and II. The dunite from Unit I is completely altered except for spinel, which has the same reddish color as spinel in dunite from Site 1271. Spinel occurs as small euhedral to subhedral grains disseminated throughout the serpentinized matrix. A thin section from Unit II that includes a dunite/harzburgite contact in Section 209-1272A-23R-1 (Fig. F6) reveals several striking features. Spinel is absent from the dunite but is abundant in the harzburgite, associated with the orthopyroxene. This spinel forms large (#1 mm) euhedral to blocky anhedral grains within and near orthopyroxene (Fig. F19A, F19B). Two centimeters from the contact with the dunite, some of the spinel is still blocky but some of it is vermicular along orthopyroxene grain boundaries (Fig. F19C). The different spinel shapes suggest that the vermicular, symplectite-like spinel typical of Site 1272 harzburgite texturally reequilibrated into euhedral grains at the dunite contact (Fig. F19D). Similar gradual changes in the spinel texture are described in ophiolites from peridotite adjacent to dunites (Matsumoto and Arai, 2001).

Discussion

Whether Unit I is a coherent outcrop, a mass of talus, or something in between, it is clear that the break between Unit I and Unit II is very sharp, and the presence of a crushed interval between them suggests they are juxtaposed by a fault (see "Structural Geology," p. 11). All the mafic rocks in Unit I crystallized rapidly at relatively low pressures. The fine-grained rocks have quench textures, and some contain intersertal glass. Even the medium-grained quartz-olivine gabbro has the characteristics of a quenched rock. The pore spaces are interpreted to be miarolitic cavities formed by the trapping of exsolved volatile elements from the rapidly crystallizing liquid. The presence of olivine and quartz in the same rock but segregated into discrete mafic and felsic portions indicates that the crystallizing liquid did not remain in equilibrium with the solid assemblage.

The harzburgite of Unit II has a protogranular texture and little clinopyroxene, suggesting it is residual mantle from which extensive melt extraction has taken place. However, the amount of dunite in Hole 1272A is less than that in other peridotite-bearing holes sampled during Leg 209. These observations appear to be at odds since dunite is considered to be a reaction product between melt and harzburgite (e.g., Boud-

F17. Clinopyroxene–orthopyroxene relationships, p. 57.

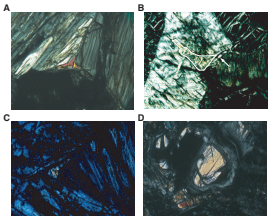

F18. Symplectic spinel intergrowths at orthopyroxene margins, p. 58.

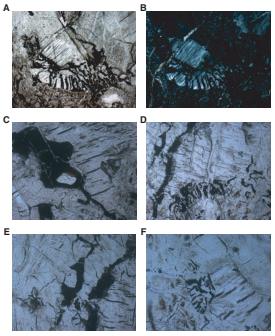

F19. Orthopyroxene/spinel textural relationships, p. 59.

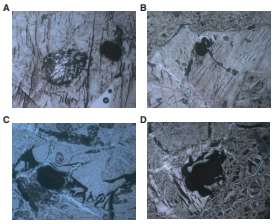

ier and Nicolas, 1972; Dick, 1977; Quick, 1981; Kelemen, 1990), so one might expect more dunite to be associated with more extensive melt extraction. One explanation for this apparent discrepancy is that the centimeter- to meter-scale variation of modal orthopyroxene in the harzburgite may have been produced by dissolution of orthopyroxene by interaction with basaltic liquid migrating by porous flow. However, the orthopyroxene grain size does not decrease as the orthopyroxene proportion decreases as is expected if orthopyroxene-poor harzburgite and dunite were formed by varying degrees of dissolution. Alternatively, it could be that the liquid was efficiently focused into a few narrow channels now represented by dunites, or the lack of dunite in this section might indicate that this portion of the mantle was strongly depleted prior to the current melting event.

The common occurrence of symplectic intergrowths between spinel and orthopyroxene in harzburgites may be indicative of some sort of reaction in the shallow upper mantle. Because the orthopyroxene-spinel-(olivine?) intergrowths occur preferentially along olivine/orthopyroxene boundaries, it can also be interpreted as the product of rapid crystallization of melt at the end of the partial melting. This would be analogous to the way clinopyroxene–spinel–olivine intergrowths form in residual clinopyroxene-bearing peridotites (Seyler et al., 2001, 2003).

METAMORPHIC PETROLOGY

A 131.0-m-long section of very highly to completely altered harzburgite and dunite and intercalated fresh to highly altered mafic units (basalt, diabase, and gabbro) was drilled in Hole 1272A (average recovery = 28.6%). In comparison to Sites 1268, 1270, and 1271, alteration of ultramafic rocks in Hole 1272A is relatively uniform. In the uppermost 100 m, harzburgite and dunite are completely altered to serpentine and magnetite, with minor brucite in some intervals. Variable amounts of the mineral iowaite are present in most samples of serpentinized harzburgite and dunite below Core 209-1272A-12R (56 mbsf). Some sections of core are characterized by unusually soft clayey serpentinites and serpentine mud. Mafic rocks in Hole 1272A are variably altered. Oxidative low-temperature alteration is usually slight and mainly affects olivine phenocrysts and microphenocrysts. Lower greenschist facies alteration is indicated by the presence of green amphibole, chlorite/smectite, talc, and minor albite and quartz (up to 70% total alteration). A quartz-biotite-amphibole gabbroic/dioritic intrusive unit in Sections 209-1272A-1R-1 and 3R-1 also shows greenschist facies alteration and a minor low-temperature oxidative alteration overprint. Low-temperature oxidative alteration of ultramafic rocks, manifest in red to brown clay and Fe oxyhydroxide and aragonite veining, is more abundant at Site 1272 than at Sites 1268, 1270, and 1271.

Hydrothermal Alteration

Alteration of Ultramafic Rocks

During serpentinization, harzburgite and dunite are very highly to completely altered to dark green to green serpentinite consisting of serpentine and magnetite. Locally, brucite and/or iowaite are common (Fig. F20; Table T2). The microtextures of serpentinized harzburgites and dunites range from pseudomorphic mesh-rim textures to transi-

F20. Photograph and XRD from Section 23R-1, p. 60.

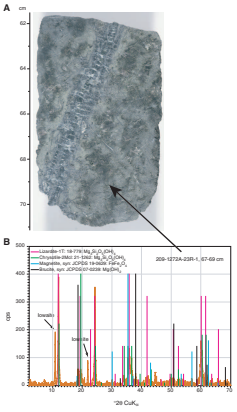

T2. XRD results, p. 122.

tional ribbon textures (Fig. F21) to rare nonpseudomorphic interlocking textures. Microscopic, apparently fibrous serpentine veins are common and include length-slow γ-serpentine (chrysotile) as well as length-fast α-serpentine veins (lizardite). The latter type of microveins was not observed in cores from any of the previous sites. The uppermost 100 m is completely altered, except for relics of spinel. In the lowermost 31 m of Hole 1272A, serpentinization of olivine and orthopyroxene is incomplete and >1%–3% of these phases are preserved. The first occurrence of relict orthopyroxene in Unit II was observed in hand specimen in Section 209-1272A-22R-1 at a depth of 103.9 mbsf. The first occurrence of orthopyroxene relics (1%) in thin section is from Sample 209-1272A-21R-1 (Piece 4, 50–53 cm) (99.4 mbsf), and the first sample with a trace of fresh olivine is Sample 23R-1 (Piece 2, 7–11 cm; 108.6 mbsf). The proportions of relict primary phases can be as high as 8% total (e.g., 3% olivine and 5% orthopyroxene in Sample 209-1272A-25R-1 [Piece 15, 123–126 cm]). Sample 209-1272A-27R-2 (Piece 10, 97–99 cm) has 5% relict olivine. The overall decrease in alteration intensity in the lowermost part of Hole 1272A is displayed in Figure F22. Consistent with this observed decrease in alteration intensity are increases in density and sonic velocity in the bottom part of the hole (see **"Porosity, Density, and Seismic Velocity,"** p. 27, in "Physical Properties"). In the uppermost 30 m, oxidative alteration of serpentinized harzburgite and dunite to reddish brown clay, carbonate, and Fe oxyhydroxide is abundant (Fig. F23), particularly in proximity to carbonate-clay–cemented fault breccias (e.g., Sections 209-1272A-1R-1 and 4R-1). A fault gouge deeper in the core (Section 209-1272A-25R-2) lacks oxidative alteration. Some intervals within the oxidatively altered harzburgite and dunite of Unit I have noticeable amounts of relict olivine and orthopyroxene (e.g., 5% orthopyroxene and 3% olivine in Sample 209-1272A-1R-1, 7–11 cm).

There are two aspects of the alteration of ultramafic rocks in Hole 1272A that are unusual. The first peculiarity is that fine-grained magnetite-serpentine stringers, typically associated with replacement of olivine, are basically absent in samples from Hole 1272A. Instead, coarse magnetite is developed in the cores rather than the mesh rims of the serpentine mesh texture (Fig. F24).

The second notable difference between serpentinites of Site 1272 and those from other sites is the abundance of soft clayey serpentinized harzburgites and serpentine mud (hereafter called clay alteration). Clay alteration is most obvious in Sections 209-1272A-12R-1, 16R-1, 18R-1, and 24R-1, where large parts of the core were extremely soft and plastic when retrieved from the core barrel. After being exposed to air for more than a day, the core from these intervals developed shrinkage fractures and an overall crumbly appearance. In their most extreme form, these rocks have the appearance of mud (e.g., Sections 209-1272A-C-11R-1, 11R-2, 18R-2, and 19R-2). Compositionally, clay-altered serpentinite is not markedly different from the solid serpentinite in adjacent sections of the core, except for their unusually high H_2O contents (>20 wt%) (see **"Geochemistry,"** p. 20).

However, characteristic peaks at 8.1 and 4.07 Å in X-ray diffractograms show that these samples contain the mineral iowaite (Fig. F20). Iowaite is a rare magnesium-iron hydroxychlorite, which was discovered in Precambrian serpentinite (Kohls and Rodda, 1967). It has been recognized in Ocean Drilling Program (ODP) drill core of serpentinite mud volcanoes in the Izu-Bonin forearc (Heling and Schwarz, 1992) and from altered serpentinite at the Iberian margin (Gibson et al., 1996). The structure of iowaite is similar to brucite; however, it contains

F21. α-serpentine wrapped around bastite, p. 61.

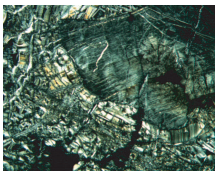

F22. Alteration intensity plot, p. 62.

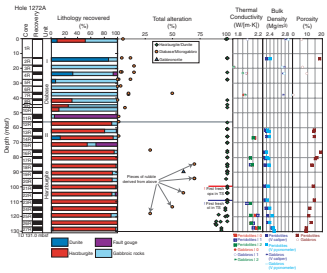

F23. Photograph and XRD of aragonite-veined dunite, p. 63.

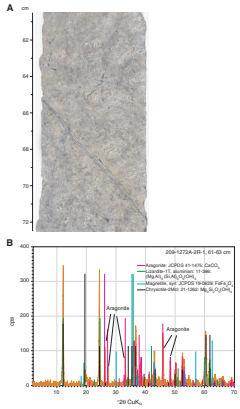

F24. Coarse magnetite in a serpentine mesh-rim texture, p. 64.

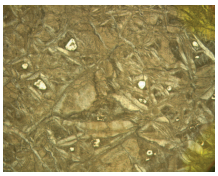

significant ferric iron and chlorine. Based on analyses by Allmann and Donnay (1969) the structural formula is

$$[Mg(OH)_2]_4FeOCl \cdot nH_2O \ (n = 1–4).$$

Results of differential thermoanalyses show that the water in iowaite is gradually driven off as the temperature rises to 280°C and that the structure begins to collapse at 315°C (Kohls and Rodda, 1967). This is consistent with our results showing that the two major peaks of iowaite disappear from the diffractogram after the powder has been heated to 370°C (Fig. **F25**). All X-ray diffraction (XRD) analyses of samples from Section 209-1272A-12R-1 and downhole show these peaks with variable intensities, indicating that iowaite is present in the soft, visibly clay-altered serpentinites as well as in the hard serpentine (Fig. **F20**). In thin section, we noted brown patches with a poor polish that show wavy extinction of aggregates and straight extinction of individual fibers.

It has been inferred that iowaite may be formed from iron-bearing brucite under oxidizing conditions (Heling and Schwarz, 1992). This process involves the oxidation of Fe^{2+} in brucite to Fe^{3+}, generating a charge imbalance, which is rectified by incorporating Cl^- between brucite layers. In a model suggested for iowaite formation in serpentinite muds at the Izu-Bonin arc, this reaction takes place immediately below the seafloor as a result of infiltration of ambient seawater (Heling and Schwarz, 1992). However, occurrences of iowaite in serpentinites at 710–810 mbsf at the Iberian margin (ODP Site 897) have been related to circulating low-temperature Cl-rich brines (Gibson et al., 1996). Here, iowaite is restricted to a zone with elevated Cl^- concentrations in bulk-rock analyses (up to 1 wt%) and it is inferred that alteration is this area was probably independent of the earlier serpentinization and later surficial oxidative alteration.

The observation of common iowaite distinguishes Hole 1272A from all other sites drilled during Leg 209. A distinctive stage of alteration, postdating serpentinization, may have occurred in this area and may have been associated with fluid flow along the major fault zones observed in this hole (see **"Structural Geology,"** p. 11).

In this regard it is interesting to note that all serpentinized harzburgites have similar molar (Mg + Fe)/Si ratios (1.74 ± 0.05; Table **T4**), consistent with that of a harzburgite precursor with 25% orthopyroxene. A dunite sample (Sample 209-1272A-23R-1 [Piece 2, 12–14 cm]) has a molar (Mg + Fe)/Si ratio = 1.95, which is close to that of olivine. These data suggest that enrichment of the rocks in silica (or removal of Mg or Fe) is insignificant, at least in relation to the large changes in (Mg + Fe)/Si observed in rocks from Hole 1268A that underwent additional hydrothermal alteration after serpentinization, including replacement of serpentine by talc.

F25. XRD after freeze drying, glycolization, and heating, p. 65.

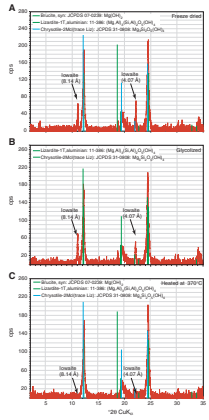

Alteration of Mafic Rocks

Small rounded pieces of fresh to slightly altered basalt are interspersed throughout the first six cores from Hole 1272A and at the top of cores from greater depths, where they probably represent rubble that fell down the hole. These basalts show only minor replacement of olivine microphenocrysts by clay and oxyhydroxide and local red staining of plagioclase. Section 209-1272A-7R-1 represents a coherent volcanic unit composed of gray to greenish brown variably altered spherulitic basalt and microgabbro. In hand specimen, the gray spherulitic basalt

does not show visible alteration. However, thin sections of Samples 209-1272A-7R-1, 87–89 cm, and 7R-1, 113–115 cm, have 5%–9% alteration of glass to very fine grained brown to gray clay. A thin section of Sample 209-1272A-7R-1 (Piece 15, 94–96 cm) reveals 60% alteration of plagioclase, pyroxene, and mesostasis to green amphibole and chlorite/smectite.

Different varieties of fine- to medium-grained mafic rocks, including diabase, gabbro, and diorite, were cored in Hole 1272A. The first occurrence of mafic rocks is in Section 209-1272A-1R-1, where a dike of moderately altered (20%), fine-grained diabase/microgabbro crosscuts dunite. Plagioclase in the diabase is slightly altered to chlorite and minor talc, whereas pyroxene is moderately altered, dominantly to green amphibole and chlorite, and olivine is completely altered to talc and magnetite (Fig. F26). Locally, the diabase underwent oxidative alteration, indicated by brown discoloration of the rock. A second intrusive body was cored in Sections 209-1272A-3R-1 and 4R-1 (Fig. F27). This medium-grained myarolitic rock is probably dioritic, indicated by the abundance of quartz, biotite, apatite, amphibole, and its chemical composition (see "Igneous and Mantle Petrology," p. 2, and "Geochemistry," p. 20). Quartz in this rock is clearly primary, although traces of secondary quartz are also present, replacing plagioclase along with chlorite/smectite. Plagioclase alteration to chlorite/smectite is locally intense (Fig. F28). Orthopyroxene and clinopyroxene are also partly replaced by green amphibole, chlorite/smectite, and minor talc. The total alteration is between 15% and 20%. Fluid inclusions in primary quartz are abundant. Multiphase liquid-vapor-solid inclusions (Fig. F29) have as many as three solid phases, including one or two optically isotropic minerals (halite and sylvite?), a birefringent mineral, and a vapor bubble and could have formed as a result of supercritical phase separation of seawater-derived fluids or trapping of magmatic fluids.

A third type of gabbroic intrusion is highly altered (60%) oxide gabbro in Section 209-1272A-19R-1. A thin section of Sample 209-1272A-19R-1, 33–35 cm, indicates that the plagioclase and pyroxene are replaced predominantly by fibrous to acicular green amphibole, subordinate chlorite, and a trace of talc.

Vein Description

The total volume of veins accounts for 0.7% of the core in Hole 1272A, which is substantially less than that observed at Sites 1268, 1270, and 1271. In fact, several sections of completely altered dunite or harzburgite are devoid of any veining. Furthermore, slightly to moderately altered basalt, diabase, and microgabbro in Hole 1272A were affected by veining (Fig. F30). The vein mineralogy is dominated by serpentine (84.8%) and carbonate (13%) with minor magnetite (1.9%) and clay (0.3%) (Fig. F31). Several generations of veins can be distinguished that show consistent crosscutting relationships and systematic changes in abundance with depth. Carbonate veins (chiefly aragonite) are only present in the uppermost 30 m, whereas serpentine veins are abundant below 60 mbsf (Fig. F30; Table T3).

The first vein generation is represented by locally banded, composite, black serpentine-magnetite veins (e.g., Section 209-1272A-13R-1). In proximity of the fault gouge in Section 209-1272A-25R-2, the abundance of serpentine-magnetite veins increases somewhat. This vein type is crosscut by magnetite-free green picrolite veins.

F26. Talc, chlorite-smectite, and magnetite in gabbro, p. 66.

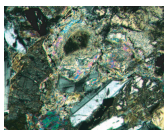

F27. Oxidation halo and melt pocket, p. 67.

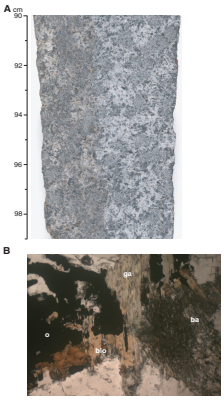

F28. Replacement of plagioclase by chlorite/smectite, p. 68.

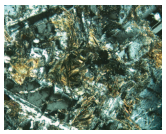

F29. Solid-liquid-vapor fluid inclusion in quartz, p. 69.

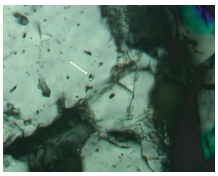

F30. Vein mineral abundances, p. 70.

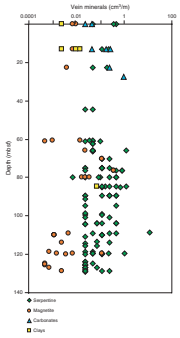

Sigmoidal, fibrous chrysotile veins usually form wispy en echelon arrays and crosscut both the black to green serpentine-magnetite veins and the green picrolite veins. An exceptional 15-cm-long and 3-mm-wide serpentine-magnetite vein in interval 209-1272A-24R-1, 85–110 cm, probably formed synchronously with sigmoidal chrysotile veins. This can be deduced from the complex crosscutting relations: some of the sigmoidal chrysotile veins can be traced across the large serpentine-magnetite vein, whereas other chrysotile veins appear to be cut and offset by the large vein. The abundance of wispy chrysotile veins decreases with depth, and virtually no veins of this generation occur below Section 209-1272A-25R-1. Locally, these chrysotile veins contain some clay, which imparts a dusty appearance to the vein (e.g., interval 209-1272A-24R-1, 17–19 cm). Throughout most of Hole 1272A these veins are paragranular. However, in Section 209-1272A-22R-1 (Pieces 3, 7, 11, and 16) transgranular chrysotile veins crosscut orthopyroxene grains and in Section 15R-1 the veins are oriented at a high angle to the main foliation of the host rock.

Gray, vuggy aragonite veins are restricted to the upper 30 m of Hole 1272A and crosscut the three different types of serpentine veins described above. Locally (e.g., Sections 209-1272A-2R-1 and 5R-1), the carbonate veins contain a dark claylike material, possibly celadonite (Sample 2R-1, 66–68 cm). These veins are similar to the carbonate veins at Site 1271, and they are interpreted as the result of late low-temperature oxidative alteration.

F31. Vein mineral proportions, p. 71.

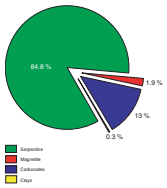

T3. Vein mineralogy, p. 123.

STRUCTURAL GEOLOGY

Core from Hole 1272A provides information about the extent of crystal-plastic deformation and melt interaction, as well as the nature, extent, and geometry of brittle to brittle-ductile structures in serpentinized harzburgite encountered from 56 to 131 mbsf. The upper 56 m of the hole may represent talus including blocks as large as 5 m in maximum dimension composed of various lithologies including basalt, diabase, diorite, gabbro, harzburgite, dunite, and sedimentary breccias (see **"Site 1272,"** p. 39, in "Site Summaries" in the "Leg 209 Summary" chapter for more details).

The tectonic setting of Hole 1272A is within the inside corner, proximal to the ridge transform intersection. Hole 1272A provides a chance to more fully understand tectonic processes and fault geometries in such a region, possibly influenced by ridge and transform tectonics. FMS images and other downhole logging information, which assisted in the interpretation or definition of major brittle structures and their geometry, are presented in this context (also see **"Downhole Measurements,"** p. 32).

Structure and Stratigraphy within the Upper 56 m of the Cored Interval

Sections 209-1272A-1R-1, 2R-1, 4R-1, 5R-1, 8R-1, 9R-1, and 10R-1 contain mixtures of pieces of ultramafic rock and basalts, diabase, gabbro, and/or diorite. Sections 209-1272A-3R-1, 6R-1, and 7R-1 lack ultramafic rock but do contain diabasic to basaltic rocks. In addition, Sections 209-1272A-4R-1 and 5R-1 contain carbonate-cemented breccias mixed with igneous rocks and mantle peridotites. The mafic samples contained in Cores 209-1272A-1R to 10R are characterized by rust-

colored weathering stains on the surface and within joints and cracks (Fig. F32). Many of the ultramafic rocks show a weathered bright orange color typical of seafloor weathering rinds but atypical of plutonic and ultramafic rocks drilled below seafloor to basement penetration depths of 10–20 m. Many of the igneous rocks in the upper section are undeformed and require no structural analysis. Local piece-by-piece structure of the ultramafic rocks is difficult to assess in the upper cored section because of their small piece size, unoriented nature, and weathered and altered characteristics. Attempts to obtain crystal-plastic foliation directions from a few oriented pieces in the upper 56 m resulted in aberrant data points when compared with the main cluster in the harzburgite basement (see **"Crystal-Plastic Fabrics and Deformation Intensity,"** p. 14, in "Harzburgite Section [56–131 mbsf]"). The polymictic nature of the assemblage in each section of core, the fact that mantle and plutonic rocks are mixed with basaltic and sedimentary rocks, the anomalous structures, and the weathering style suggest that there may not be coherent basement in the upper 56 m of the cored interval.

Recovery of lithified breccias also suggests that a talus or rubble zone was encountered in the upper 56 m. A coarse-grained, cohesive, nonfoliated breccia was encountered in Section 209-1272A-5R-1 (Pieces 7, 9, and 10) (Fig. F33). Angular to subangular clasts of serpentinite and minor basalt are supported by a fine-grained orange carbonate-rich matrix. Some of the clasts are angular lithic fragments that have undergone fracturing, rotation, and frictional sliding with respect to a larger parent clast. These protocataclasite fragments are included in a finer-grained matrix of similar ultramafic composition. The clasts were deformed during a semibrittle process and were lithified prior to the formation of the sedimentary breccia. The enclosing carbonate matrix is relatively undeformed. The breccias may have formed in or near a fault zone based on the presence of protocataclasite and the abundance of ultramafic clasts. The matrix of the breccia is cut by a few late brittle carbonate veins, and each clast is surrounded by a coating of carbonate vein infill, caused by matrix shrinkage during tectonic activity, dewatering, and final lithification.

The paleomagnetic data are equivocal, as discussed in **"Paleomagnetism,"** p. 28, and in **"Site 1272,"** p. 39, in "Site Summaries" in the "Leg 209 Summary" chapter (Fig. F34). Below 56 mbsf, the paleomagnetic results indicate stable magnetic inclinations and declinations. Above 56 mbsf the paleomagnetic results show large variations downhole, with as much as a 90° variation in inclination orientation within a single section. Ten meters of quartz-olivine gabbro gives internally consistent results (see **"Paleomagnetism,"** p. 28, for details) that are parallel to the remanent magnetization in the harzburgites between 56 and 131 mbsf. In the context of the hypothesis that a tectonic breccia was cored in the upper 56 m of Hole 1272A, the similarity between the magnetic inclinations recorded in Cores 209-1272A-3R to 4R and the harzburgites below 56 mbsf either must be a coincidence or be explained by the quartz-olivine gabbro being intrusive dikes in the talus pile.

Hole 1272A was logged with FMS imaging starting at 46 mbsf (see **"Downhole Measurements,"** p. 32). The vertical resolution of the FMS images is ~5 mm, allowing conductive and nonconductive features such as fractures and faults, magmatic and alteration veins, clasts within matrix, and oxide-rich layers to be recognized.

Above 56 mbsf, which we interpret as the top of basement, FMS images show typical "clast-in-matrix" geometries along the borehole wall.

F32. Weathered clasts from the rubble zone, p. 72.

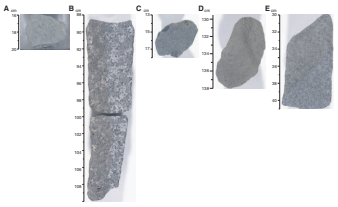

F33. Protocataclasite harzburgite in carbonate-cemented breccia, p. 73.

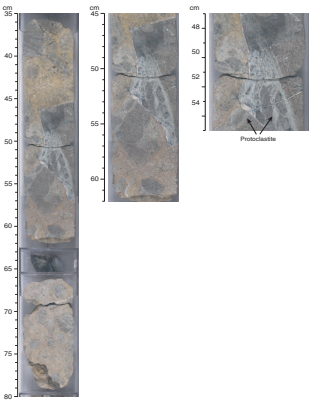

F34. Archive-half magnetic measurements, p. 74.

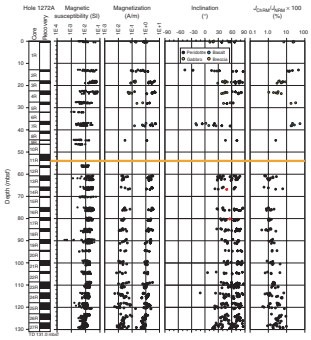

The clasts appear as bright spots (high resistivity) on the image with the matrix material showing darker colors (more conductive and probably water saturated). Figure F35 illustrates an example of this image pattern and shows the recovery over Section 209-1272A-11R-1, which consisted of only 36 cm of rock over the 5-m cored interval. The low recovery in this section included a polymict assemblage of basalt, diabase, and harzburgite with some clasts showing the effects of weathering and none as wide as a cut cylindrical core.

F35. FMS image above the harzburgitic basement, p. 75.

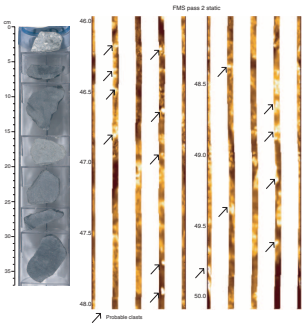

Harzburgite Section (56–131 mbsf)

Below Core 209-1272A-10R, recovery was limited in two sections (11R-1 and 11R-2) to pebble-sized or smaller clasts and matrix composed almost exclusively of green serpentinized peridotite, pieces of cross-fibered serpentinite from veins, and fine silt-sized particles of serpentine. These two sections are interpreted to represent drill cuttings of peridotite. The first semicoherent section of ultramafic rocks was encountered just below 56 mbsf in Section 209-1272A-12R-1. The ultramafic materials in this section, however, are unusual. Section 209-1272A-12R-1 (Piece 1) recovered a basalt followed by nine subsequent pieces of highly altered harzburgite. The harzburgite, although appearing intact, had the consistency of mud (Fig. F36). When dried, this mud consolidated somewhat but became brittle and commonly friable. In addition, these unusually altered harzburgites contain iowaite, a brucitelike, Cl-bearing mineral with a layered structure, in what may be the first reported occurrence from the Mid-Atlantic Ridge (see "Metamorphic Petrology," p. 7). Serpentine minerals may form muds that are unusually weak (e.g., Phipps and Ballotti, 1992).

F36. Altered harzburgites from the top of basement, p. 76.

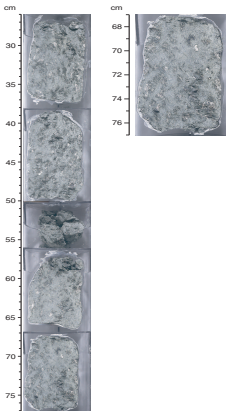

Below this depth, the recovery typically consisted of protogranular harzburgite and was distinctly different from the polymict assemblages above. Small pieces of basalt and gabbro were sampled at the top or base of the succeeding cored sections, but these are interpreted as fragments of fallen material from the upper part of the hole. Section 209-1272A-15R-1, which had low recovery of small pieces, did recover two allochthonous weathered basalt and diabases (Pieces 4 and 5) in the middle of the core, but all other pieces are likely to have been derived from the harzburgite section.

The cored interval of harzburgite extends from Sections 209-1272A-12R-1 to 27R-1 (~56–131 mbsf). Samples were generally completely altered to secondary phases in the upper part of the section based on thin section examination and visual inspection of the core (see "Metamorphic Petrology," p. 7). Textural classification could not be completed for the highly altered and weathered Section 209-1272A-12R-1 because pieces showed extreme plastic behavior at low temperatures and deformed on handling. Below this section, however, visual and thin section inspection allowed estimation of textures and fabrics in the samples. Also, below Section 209-1272A-21R-1 some fresh primary minerals were preserved. This is reflected in an increase in bulk density of the intervals at the base of the cored interval (see "Porosity, Density, and Seismic Velocity," p. 27, in "Physical Properties").

Lithologic Variation and Contacts Measured

Primary lithologic variation in the section was minor, apart from subtle variations in pyroxene modal abundance, four samples of oxide gabbro in Section 209-1272A-19R-1 (Pieces 6–9), and a single dunite

band with an upper and lower boundary of harzburgite in Section 23R-1 (Piece 2) (Fig. F37). The dunite band is bounded sharply at 11 cm by an upper harzburgite contact and at 50 cm by a lower harzburgite contact. The layer is inclined at 50° in the cut face of the core and is ~25 cm thick. The orientation of the upper and lower contacts of the dunite with adjacent harzburgite were measured, with poles plotted in Figure F38. The paleomagnetic-corrected orientations of the dunite/harzburgite compositional boundaries are close to the main cluster of crystal-plastic foliation planes, which are defined by the preferred dimensional orientation of spinel and pyroxene in the adjacent harzburgite (see below). This may be consistent with transposition of compositional layering into the foliation plane during mantle deformation.

Crystal-Plastic Fabrics and Deformation Intensity

Crystal-plastic deformation in the harzburgite section of Hole 1272A is limited. The section consists largely of protogranular harzburgite with very little recrystallization (Fig. F39). Measurements of crystal-plastic deformation intensity of a few samples from the upper 56 m of Hole 1272A are plotted, but this may not be an intact section.

Within the harzburgite, the mesoscopic and microscopic crystal shape fabrics are poorly developed (Fig. F40). A total of 15 small intervals in the core displayed a weak but measurable crystal-plastic foliation. In many cases, the shape fabric could only be identified with confidence on the cut face of the core. If the cut face was not oriented in the dip azimuth direction of the foliation plane, likely for the weakest foliations, an accurate measurement was difficult to make. Shallow foliations also tend to be the weakest foliations. In Figure F38 we show all of the data collected, but we are most confident in the steepest dips measured in the cut face of the core, which do seem to cluster. Shallower dips measured in the cut face plot farther from the main cluster and may represent an apparent dip. Some of the scatter in the plot of poles to foliations in Figure F38 may be attributed to these measurement difficulties. Nonetheless, there is a concentration of poles plunging 40° along an azimuth of 255° in the reference frame that we used to reorient the data. Note that the paleomagnetic correction applied to each piece provides an internally consistent reference frame for the core.

Harzburgite textures in Hole 1272A are almost exclusively protogranular with only a few kink bands, strained grains, and occasional coarse neoblasts found in bastites. The distribution of crystal-plastic fabrics and low intensities (Fig. F41) suggests that the Hole 1272A section is one of the least deformed of those drilled during Leg 209, with no mylonitic or strongly porphyroclastic peridotites recovered. Most sections appear undeformed, preserving equidimensional orthopyroxene grains on the cut core face. In thin sections of samples from Hole 1272A, orthopyroxene is coarse, typically 3–7 mm, with grains as large as 13 mm. Olivine grains vary from 3–8 to 15 mm in diameter. Subgrains and kink bands are present in orthopyroxene, but much of the olivine is either strain free or contains slight wandering extinction and rare kink banding. There is no significant recrystallization of olivine, so Hole 1272A harzburgites lack the bimodal grain sizes typical of porphyroclastic textures.

Spinel grain shapes were generally preserved even in altered rocks at the top of the hole. Spinel shapes in harzburgite from 18 thin sections from Cores 209-1272A-13R to 27R are vermicular, indicating that these

F37. Dunite band in harzburgite, p. 77.

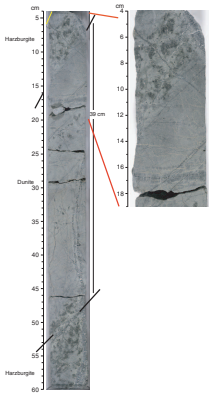

F38. Projection of poles to crystal-plastic foliation, p. 78.

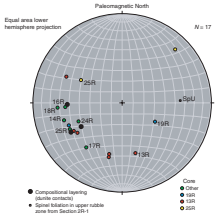

F39. Downhole crystal-plastic deformation intensity, p. 79.

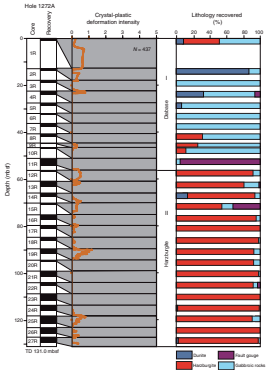

F40. Lack of mesoscopic crystal-plastic foliation in protogranular harzburgites, p. 80.

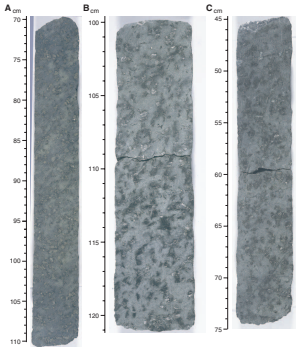

rocks have not experienced significant strain since the formation of the spinel. The exceptions are Sample 209-1272A-17R-1, 56–58 cm, where vermicular spinels have a common elongation direction but no pyroxene foliation is observable, and Sample 23R-1, 7–11 cm, where at the harzburgite/dunite contact the spinel shapes grade from slightly vermicular to anhedral-rounded in thin section. The spinel grains in this thin section are slightly elongate and show a clear foliation parallel to the pyroxene foliation in the adjacent harzburgite. At greater depth in the same piece, the spinel shapes still range from anhedral-euhedral to vermicular, but no pyroxene or spinel foliation is observable (e.g., Sample 209-1272A-23R-1, 62–64 cm).

Shown in Figure F42 are four examples of the protogranular textures in the Hole 1272A harzburgites. These closely resemble those at other sites, with the exception that the Hole 1272A harzburgites generally have coarser pyroxene and olivine grain size, >1 cm in places. Some of the orthopyroxene bastites have a marked interstitial habit (Fig. F42A), as is characteristic of the peridotites drilled at Sites 1268, 1270, and 1271. Deeply embayed orthopyroxene grains with smooth curved grain boundaries are more common than interstitial grains (Fig. F42B, F42C) as are more equant and granular forms (Fig. F42D).

Four small fragments of clinopyroxene-rich oxide gabbro or gabbronorite (Section 209-1272A-19R-1 [Pieces 6–9]) were recovered. All appear little deformed in hand sample. Two samples yielded thin sections. One appears undeformed, whereas the other underwent a weak to moderate crystal-plastic deformation (grade = ~1), with locally extensive recrystallization of primary clinopyroxene (Fig. F42E, F42F). Plagioclase, although abundant, was replaced by large patches of chlorite. Clinopyroxene neoblasts with unstrained exsolution lamellae are enclosed by iron-titanium oxides. This indicates that recrystallization of clinopyroxene neoblasts took place at high temperature prior to exsolution. Oxides may have accommodated later deformation, shielding the clinopyroxenes from additional strain.

Brittle to Brittle-Ductile Features

Cross-Fiber Anastomosing Serpentine Foliation

Foliation in serpentinized harzburgite, defined by anastomosing sets of serpentine and magnetite veins, is present in varying degrees through much of the Site 1272 core. Within harzburgite, serpentine foliation and veins tend to form anastomosing waves similar to those observed in Holes 1268A and 1270B (e.g., intervals 209-1270B-10R-1, 93–127 cm, and 13R-1, 69–74 cm). The amplitude of anastomosing waves in the foliation appears to be partially controlled by the size of pyroxene porphyroclasts and the degree to which veins are deflected around porphyroclasts. Foliation has strong, high-amplitude anastomosing waves where it is deflected around large pyroxene grains and is near planar where there is a small degree of deflection or small pyroxene grains. Where serpentine foliation is present in harzburgite with >30% fresh olivine, the foliation is defined by very fine serpentine and magnetite veins that are concentrated into olivine-rich bands. These veins are very similar in character to ribbon texture serpentinite as defined by O'Hanley (1996). Serpentine fibers are most commonly aligned perpendicular to vein walls, indicating formation of the foliation by dilatant fracturing rather than shear deformation.

F41. Crystal-plastic deformation intensity, p. 81.

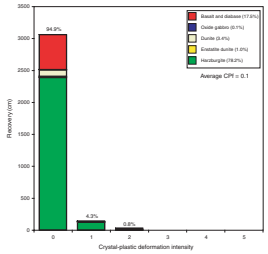

F42. High-temperature textures in peridotites, p. 82.

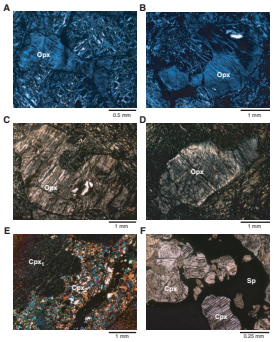

Alteration Veins

The diabase and quartz-olivine gabbros in the upper 56 m of Hole 1272A contain very few alteration veins. Conversely, the highly weathered oxidized peridotites in the uppermost 30 m of the hole from Sections 209-1272A-1R-1, 2R-2, 4R-1, and 5R-1 contain pervasive networks of black serpentine magnetite veins cut by less common green serpentine veins and by later carbonate veins. The planar carbonate veins contain aragonite and oxides and are up to 0.5 cm wide and $12 cm long. There are two crosscutting generations of carbonate veins, and they fill extensional fractures.

The peridotites from below Section 209-1272A-12R-1 (60.43 mbsf) contain four generations of serpentine veins and no carbonate veins. The first generation is composed of narrow (<1 mm wide), planar, black to dark green magnetite-serpentine veins that extend at least across the diameter of the core (Fig. **F43A, F43B, F43D**). These veins show complex crosscutting relationships. The second generation of veins consists of larger (as wide as 3–4 mm and as long as >30 cm) branching white- and green-banded serpentine veins (Fig. **F43B, F43D**). These veins are less common (<1 vein per section) and have steeper dips than the first generation of veins. The wallrock surrounding these veins commonly has dark 1- to 3-mm-wide alteration halos, and the veins themselves are always cut by small (<1 cm long) orthogonal tension cracks filled by white chrysotile (Fig. **F43B, F43D**). The tension cracks suggest that these serpentine veins were affected by volume expansion of the surrounding peridotite and, hence, that they formed before the last phase of pervasive serpentinization. These veins may originally have been magmatic veins that have been completely altered and serpentinized.

The third generation is represented by late talc-serpentine veins, examples of which can be seen in Sections 209-1272A-26R-1 and 27R-2. These veinlets are small (0.3 mm wide and 2–3 cm long) and relatively rare. The last generation of veins consists of small (<1 cm long) sigmoidal, en echelon chrysotile veinlets. These veinlets are ubiquitous throughout the core and commonly define a foliation (Fig. **F43C**) that generally dips ~45°, more rarely 80°–90° in the cut face of the core. These veinlets are similar to those that fill the tension cracks in the second generation of serpentine veins and probably formed at the same time during the last serpentinization event. A more detailed discussion of the mineralogy of the alteration veins can be found in **"Vein Description,"** p. 10, in "Metamorphic Petrology."

The intensity and orientation of veins were measured using the intensity scale outlined in **"Structural Geology,"** p. 9, in the "Explanatory Notes" chapter. The intensity of these veins is a measure of their average frequency in a 10-cm piece of core. The total intensity of alteration veining with depth for Hole 1272A is shown in Figure **F44.** Alteration vein intensity is generally low (≤2.5) and significantly lower than that seen in the peridotites at Sites 1268, 1270, and Site 1271. The moderately high alteration vein intensities in the upper 56 m of Hole 1272A reflect the presence of the highly altered oxidized peridotites. Below 56 mbsf (Section 209-1272A-12R-1), the background vein intensity is 0.5–1 and is approximately constant with increasing depth. There are four local peaks in the intensity of veining corresponding to the location of faults and fault gouges in Cores 209-1272A-13R (62.5 mbsf), 19R (86 mbsf), and 26R (123 mbsf), and the highly veined, 25-cm-thick dunite sand in Section 23R-1 (108 mbsf).

F43. Alteration veins cutting harzburgites and dunites, p. 83.

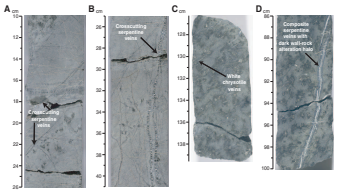

F44. Downhole alteration vein and cataclastic intensity, p. 84.

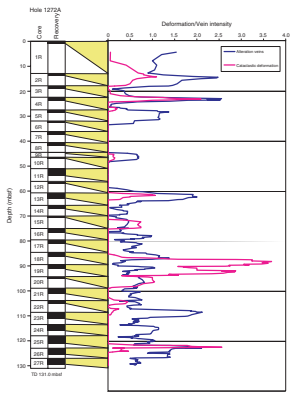

A total of 102 vein orientations were measured in the core. Dips vary from 15° to 90° (average dip = 52°) (Fig. F45). Figure F46 shows lower hemisphere plots showing the poles to the late metamorphic veins (black to dark green magnetite serpentine and white- and green-banded serpentine veins) below 56 mbsf, restored with the declination of the stable remnant magnetization pointing north. The reorientation of the veins using paleomagnetic data is discussed in "Structures in Peridotite and Gabbroic Intrusions," p. 8, in "Mantle Upwelling, Melt Transport, and Igneous Crustal Accretion" in the "Leg 209 Summary" chapter. The orientation data are clustered, and the data suggest that a population of the veins dip to the east at ~50° in the reference frame that we used to orient the data.

Serpentine Schist

Several small pieces of strongly foliated, white schistose serpentinite were recovered from the lower one-third of Hole 1272A (Samples 209-1272A-23R-1 [Piece 1, 0–3 cm], 21R-1 [Piece 6, 67–68 cm], 20R-1 [Piece 10, 59–60 cm], and 15R-1 [Pieces 10 and 11, 49–55 cm]). These samples are composed of fibrous white serpentine that fills 0.2- to 2-cm-wide veins that cut altered serpentinite. The serpentine fibers in these veins are aligned either syntaxially, indicating dilational opening; oblique to vein walls, indicating oblique shear opening; or as schistose mats parallel to vein walls. The veins that are filled by schistose serpentine contain elongate clasts of altered serpentinite with up to 10:1 length:width ratio and/or bound phacoidal shear polyhedra of altered serpentinite. A narrow (0.2 cm wide) fault zone down the centerline of a vein filled by syntaxial fibers in Sample 209-1272B-23R-1 (Piece 1, 0–3 cm) appears to have accommodated shear offset. The presence of extensive schistose and fault offset textures indicates that these samples represent a significant degree of shear strain accommodation. Although only a limited number of small pieces of white schistose serpentine were recovered from Hole 1272A, these pieces could be small portions of major fault systems that are not well represented in the recovered core. Borehole imaging by FMS logging of the Hole 1272A, presented in "Core-Log Correlations, FMS Imaging, and Orientation of Fault Zones," p. 18, below, aided in interpreting the significance of these small pieces. The results suggest that poor recovery correlates with highly fractured zones.

Fault Gouge

Several intervals of brittle, partially cohesive fault gouge (Fig. F47) were recovered from Hole 1272A (intervals 209-1272A-18R-1 [Piece 16, 122–123 cm, and Piece 18, 133–148 cm], 18R-2 [Pieces 1 and 2, 0–18 cm], 19R-1 [Piece 2, 4–6 cm, Piece 5, 20–21 cm, and Piece 23, 137–150 cm], 19R-2 [Pieces 1 and 2, 0–18 cm], and 25R-2 [Pieces 11 and 12, 107–125 cm]). These gouge samples are generally similar in character, with variations in the percentage of lithic clasts and overall clast size. They are semicohesive fault breccias consisting of serpentine and/or clay-rich matrices with matrix-supported subrounded to angular serpentinite clasts, ranging 0.03–5 cm in size in most samples, and altered pyroxene crystals. Intervals bounding most gouge zones are cut by a higher percentage of shear fractures than in bulk of the core recovered from Hole 1272A. These intensely fractured zones are revealed in a downhole plot of shear fracture intensity (Fig. F44). These gouges formed in late-occurring faults. Crosscutting relations are not present to determine the relative timing between the fault gouges and serpentine schists, but it is

F45. Downhole dips of serpentine, talc-serpentine, and chrysotile veins, p. 85.

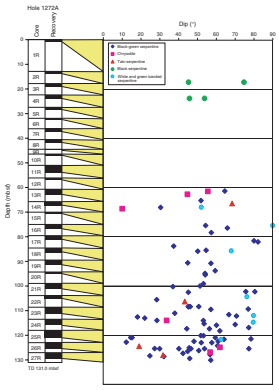

F46. Projection of poles to serpentine veins, p. 86.

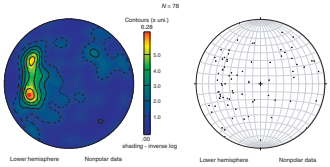

F47. Semiplastic fault gouges, p. 87.

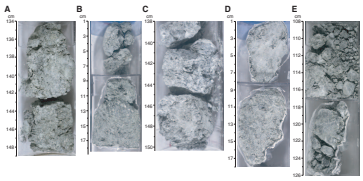

likely that fault gouges postdate the serpentine schists. Like the altered peridotite in Section 209-1272A-12R-1, the gouges were soft, plastic, and semiconsolidated (Fig. F47) when first recovered and stiffened later as they dried. If the in situ state of hydration is similar to that when the gouges initially arrived on board, the gouges may have had a weak rheology. Alternatively, drilling activity may have enhanced their water content and plasticity.

Core-Log Correlations, FMS Imaging, and Orientation of Fault Zones

The FMS images previously discussed are oriented so that both strike and dip can be calculated utilizing sine curve fits for planar features. Because FMS images allow orientation of the structural features observed in the cores, it is possible to relate core and/or borehole features to the tectonic environment (see "Downhole Measurements," p. 32, for further details). Our preliminary attempt to interpret correlations between core descriptions and FMS logs focused on fault gouges and serpentine schist where there was evidence of brittle to brittle-ductile deformation. We attempted to identify these features at similar depths in the borehole image and in the core and then to orient these structural features. In a few cases, after working with correlations of core and borehole observations and developing reliable working criteria, we extended the interpretation to regions in the borehole where similar features were observed but where there was a lack of core recovery or direct evidence of a fault zone. Unlike paleomagnetic data, in which the orientation of core in a geographical reference frame is dependent on the tectonic rotation model, FMS images with core pieces or sections provide a model-independent orientation for structural features. The FMS images can ultimately help to provide constraints on the paleomagnetic rotation model to be used.

We correlated gouges recovered in Sections 209-1272A-19R-1 and 19R-2 with the FMS log. Figure F48 shows the FMS image and segments of the two core sections containing gouges and conductive oxide gabbros. Like fractures, gouges are expected to be saturated with water at these shallow levels in the crust and thus highly conductive relative to the surrounding wallrock. The curated top of Section 209-1272A-19R-1 is located at a depth of 89.3 mbsf, but taking into account the partial recovery, the depth to the top of Section 19R-2 should be between 90.8 (unexpanded depth) and ~93 mbsf (expanded depth). The FMS image shows a conductive interval between 89 and 91.4 mbsf. After preliminary processing, the depth of particular features in the FMS image is accurate to ~1 m. Thus, the FMS image shows a strongly conductive zone, which may correspond to the level of the first significant gouge zone in the core, together with evidence for small resistive clasts between 89.6 and 90.5 mbsf. The curated top depth of the thicker gouge zone in the section is at 89.47 mbsf. A sine curve fit to the interval in the FMS image interpreted to represent the top of the thick gouge zone has a dip of 58° to the northeast striking N60°W. Thus, the fault is a high-angle fault dipping downslope in a direction oblique to the rift valley and the fracture zone. Its orientation is consistent with fault geometries at ridge/transform intersection inside corners, where the rift valley walls tend to curve away from the rift valley and toward the active transform.

A second gouge zone is present at the base of Section 209-1272A-19R-1 and the top of Section 19R-2 (Fig. F48). It may be correlated with a conductive zone with resistive clasts visible in the FMS image. It should be noted that the fault gouges sampled in the core were matrix-supported breccias with clasts, consistent with appearance of the con-

F48. FMS images of fault gouges and oxide gabbros, p. 88.

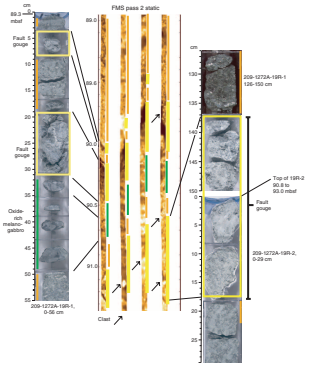

ductive zones in the FMS image. Lastly, conductive oxide gabbros might be the cause of the highly conductive zone in the FMS image between the two fault gouges.

A small sample of serpentine schist in Section 209-1272A-20R-1 (Piece 8) at 94.89 mbsf was correlated with the borehole FMS image (Fig. F49). A 1.7-m conductive zone with resistive clasts is recorded on the FMS image between 94.3 and ~96 mbsf. The top of the zone has a strike of N18°W and a dip of 49° toward the northeast. Thus, we interpret this feature as another fault dipping toward the rift valley and the fracture zone.

In Figure F50, a zone of conductive fault breccia was identified in the FMS image, based on the appearance of abundant resistive clasts within a conductive matrix. The zone begins at ~100.6 mbsf and appears to be ~1 m thick. The orientation of the top of the zone strikes N3.9°E and dips 26.8° to the southeast. The strike of this structure is close to the strike of the Mid-Atlantic rift valley in this region.

Analysis of the FMS images yielded 10 preliminary picks of fault gouge zone orientations that give a mean strike of N24°W. The orientations of these fault zones are plotted in Figure F79. Strikes of the 10 gouge zones vary from north–south, perpendicular to the spreading direction, to more northwesterly, with a mean strike of N24°W. Thus, most are oblique to the rift axis. However, gouge zones may locally have irregular boundaries and may not always be planar. In addition, the attitude of the bottom of a gouge zone does not always match the top, as is observed in subaerial gouge zones. However, it is clear that faults dip both toward and away from the rift valley. The considerable number of gouge zones imaged in the borehole indicates that there are dense networks of faults that intersect each other in the subsurface. We have only presented some gouge zones and there are many more fault zones imaged in the FMS log that are not included in Figure F79. We selected those that provided the best orientation data. In addition, there are many other planar fractures, which will require a significant post-cruise effort to delineate and orient in order to provide a more complete set of data on fault geometries at a ridge/transform intersection.

Orientation of Brittle Shear Fractures and Serpentine Foliations

Poles to shear fractures and poles to serpentine foliations rotated into a common frame of reference using the paleomagnetic data are presented in Figure F51. Fractures are generally shallow dipping, typically shallower than fault zones imaged by FMS. Most dip northeast in the reference frame that was used to reorient the data. A comparison of the brittle shear fracture intensity plot and the depth of gouge zones in the core or gouge imaged by FMS (Fig. F52) indicates a possible correspondence between the position of the gouge zones and the intensity of shear fractures. This indicates that fractures are probably related to faults corresponding to the gouge zones, perhaps antithetic or pinnate to the major fault zones. Serpentine foliations tend to have similar orientations but exhibit more of a dilational component than the shear fractures.

Discussion

The earliest deformation of the serpentinized harzburgites in Hole 1272A was a mild crystal-plastic deformation, with most harzburgites

F49. FMS image corresponding to a serpentine schist, p. 89.

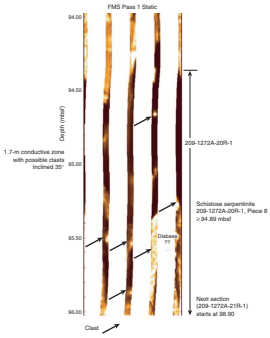

F50. FMS image of clasts in a possible fault gouge, p. 90.

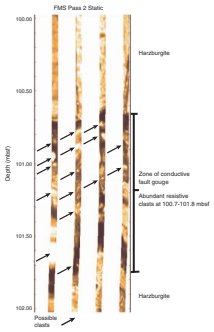

F51. Projection of poles to shear fractures and serpentine foliations, p. 91.

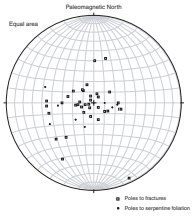

F52. Fracture and vein intensity vs. fault gouges, p. 92.

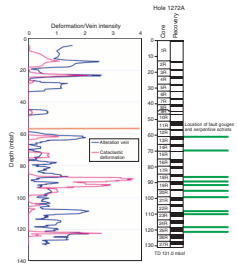

retaining coarse protogranular textures that likely formed under low deviatoric stresses at high temperatures. We observed no porphyroclastic or mylonitic textures in the harzburgites. Microscopic evidence for dynamic recrystallization was found only in one small oxide gabbro interval, suggesting that high-stress, moderate-temperature crystal-plastic deformation may have been localized in scarce mafic plutonic intervals in Hole 1272A. Qualitative strain estimates usually provided by elongation of pyroxene grains in the harzburgite were rarely possible because of the lack of deformation, resulting in the lowest crystal-plastic deformation intensity estimated for any peridotite cored during Leg 209.

An anastomosing serpentine foliation forms the dominant low-temperature fabric in the serpentinized peridotites. Serpentine fibers are generally orthogonal to the margins of the anastomosing vein sets, but fibers subparallel and oblique to vein walls indicate some shear component in their development. However, these and subsequent vein sets record dominantly dilational deformation. Vein intensity may correlate with the location of brittle fault zones. Some serpentine schists are present, and we believe that they are also associated with fault zones. High densities of brittle shear fractures are present near serpentine schists and gouge zones observed in the core or inferred from FMS imaging.

Gouge and fault zones represent the latest brittle deformation event recorded in the harzburgites. They are present in recovered core and inferred from FMS imaging. They intersect the borehole every 10 m or less and are as thick as 1.5 m. The gouges had the plasticity of typical pelagic mud when they were first recovered and may have a weak rheology in the subsurface. The frequency of these gouge zones in the borehole was unexpected but may help to explain areas of poor recovery in the harzburgites. More importantly, the low strength of the gouge zones may have important implications for serpentinite-hosted fault zones, as serpentine muds are five orders of magnitude weaker than massive serpentinites, with ultimate strengths three to four orders of magnitude lower than salt (Phipps and Ballotti, 1992). This property may permit aseismic slip on major fault zones within serpentinized peridotite and allow mass wasting within the high-relief rift mountains. The densities of serpentine muds are also significantly lower than the densities of massive serpentinites, suggesting that muds may rise diapirically, given their relative buoyancy and low-temperature plasticity.

A last tectonic event may be revealed by polymict lithologies above the harzburgite basement, which include lithified breccias with peridotite clasts that originated along brittle fault zones undergoing cataclasis. The clasts included protocataclasites of harzburgite.

GEOCHEMISTRY

We performed chemical analyses on ten harzburgites, two dunites, two basalts, a diabase, and two gabbronorites from Site 1272 selected by the shipboard scientific party, using inductively coupled plasma–atomic emission spectrometry (ICP-AES) for determining major and trace element concentrations and gas chromatography for H_2O and CO_2. These samples are representative of the rocks recovered from Hole 1272A (see **"Lithology and Stratigraphy,"** p. 2, and **"Lithologic Characterization,** p. 4, in "Igneous and Mantle Petrology" and **"Metamorphic Petrology,"** p. 7, for characterization of the lithologic units). The mafic samples, one harzburgite and one dunite, were sampled from Unit I.

The remaining peridotites were sampled from Unit II. The results for the major and trace elements, for both ultramafic and mafic rocks, are reported on a volatile-free basis in Table T4.

T4. Major and trace elements, p. 124.

Peridotites

Site 1272 peridotites are characterized by high volatile contents and loss on ignition (LOI) values (Fig. F53). Some of these peridotites display the highest LOI values measured during Leg 209. These high LOI values and H_2O concentrations are consistent with the visual core descriptions and XRD results (see "Metamorphic Petrology," p. 7) that show that Site 1272 harzburgites and dunites are completely altered to serpentine with minor brucite in some intervals. It should be noted that some sections of core were characterized by unusually soft, clayey serpentinites and serpentine mud (Sample 209-1272A-12R-1, 73–76 cm). Two samples from Unit I, a harzburgite (Sample 209-1272A-1R-1, 7–11 cm) and a dunite (Sample 2R-1, 61–63 cm) have the highest LOI (17.9 and 18.9 wt%, respectively) and H_2O contents (14.9 and 14.0 wt%) among the Site 1272 peridotites. These samples also have the highest CO_2 contents measured during Leg 209 (7.3 and 9.3 wt%, respectively). These high CO_2 contents are consistent with the visual core descriptions and XRD results (see "Metamorphic Petrology," p. 7), indicating that aragonite veins are present as part of a low-temperature alteration assemblage in the Unit I peridotites. This is in addition to the higher-temperature serpentinization that is also observed in these peridotites. The high CO_2 contents are correlated with high CaO (Fig. F54), suggesting metasomatic addition of $CaCO_3$ (also see Figs. F45, p. 124, and F46, p. 125, with accompanying text in the "Leg 209 Summary" chapter).

F53. LOI, SiO_2, and Fe_2O_3 vs. MgO, p. 93.

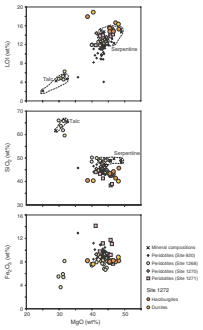

F54. CaO vs. CO, p. 94.

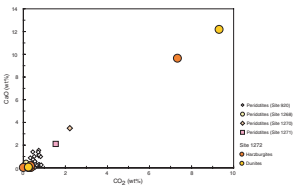

Site 1272 peridotite bulk rock compositions plot in a restricted range of values compared to Site 1271 peridotites (Fig. F53). Site 1272 Unit II peridotites, on average, display higher SiO_2 (42.5–43.2 wt%) and MgO (42.5–46.5 wt%) than the two Site 1272 Unit I peridotites, which are characterized by SiO_2 (~40.3 wt%) and MgO (38.7–40.5 wt%). These variations in MgO and SiO_2 content in the peridotite are not correlated with a difference in Fe_2O_3 concentration between Units I and II. The low Mg content in the Unit I peridotites might reflect a small amount of Mg loss that may occur during low-temperature alteration (e.g., Snow and Dick, 1995). It should be noted that despite the possible Mg loss, Site 1272 peridotites are characterized by high Mg# (100 × molar Mg/[Mg + Fe]) (90.3%–92.2%); the lowest values (90.3% and 91.3%) were found for the two samples from Unit I.

Site 1272 peridotites display lower Al_2O_3 contents than Leg 153 peridotites but are similar to Site 1268, 1270, and 1271 peridotites. In peridotites, most of the bulk rock Al_2O_3 content is concentrated in pyroxenes, and variations in Al_2O_3 content reflect the degree of fertility of peridotites. Site 1272 harzburgites have higher Al_2O_3 contents (0.57–0.78 wt%), whereas the Site 1272 dunites have lower Al_2O_3 contents (0.12 wt%). These low values suggest that prior to alteration Site 1272 peridotites were more refractory than Leg 153 peridotites. Except for the two Unit I peridotites, Site 1272 peridotites display low CaO contents (<0.03–0.19 wt%). CaO in peridotites is concentrated in clinopyroxene. The low and scattered CaO contents observed in Site 1272 peridotites suggests either preferential Ca loss during serpentinization and weathering and/or the presence of only minor amounts of clinopyroxene in these rocks. In contrast, the two samples from Site 1272 Unit I, a

harzburgite (Sample 209-1272A-1R-1, 7–11 cm) and a dunite (Sample 2R-1, 61–63 cm), have high CaO values (9.65–12.2 wt%). These samples also have the highest CO_2 and Sr (1790–2150 ppm) contents measured in Leg 209 peridotites. These values are consistent with the visual core descriptions and XRD results (see **"Metamorphic Petrology,"** p. 7), indicating that aragonite veins are present as part of the low-temperature alteration assemblage in Unit I peridotites.

The bulk rock composition of Sample 209-1272A-12R-1, 73–76 cm, a serpentinite mud, is similar to that of Site 1272 harzburgites, except for slight Na_2O enrichment (0.18 wt%). This higher Na_2O content suggests possible interaction with seawater or incorporation of gabbroic material during cataclastic deformation.

The trace element concentrations measured in Site 1272 peridotites fall in the range of the other peridotites analyzed during Leg 209. Cr and Ni behave as compatible elements, preferentially partitioning into the solid during partial melting. Site 1272 harzburgite Ni contents plot in the same range as those of Site 1268, 1270, and 1271 peridotites (2400–2900 ppm). Site 1272 dunites display slightly higher Ni concentrations (3000–3300 ppm), similar to the most Ni-enriched Site 1268 peridotites. The high Ni concentrations coupled with low Al_2O_3 contents (<1 wt%) in the Site 1272 peridotites suggests that olivine controls the Ni concentration. Cr content in Site 1272 peridotites (720–4885 ppm) is positively correlated with Al_2O_3 and plots in the same field as Site 1268 and 1270 peridotites except for the two Unit I peridotite samples (Fig. **F55**). Because nearly all of the Cr must be concentrated in spinel in these rocks, the correlation of Cr with Al_2O_3 suggests that spinel contributes a significant proportion to the bulk rock Al budget for the highly refractory, pyroxene-poor Site 1272 peridotites. The two Unit I peridotites display the highest Cr values (3400–4890 ppm) among Leg 209 peridotites. The lowest Cr is in the sample with the most depleted Al_2O_3 (Sample 209-1272A-2R-1, 61–63 cm; a dunite). Yet there are no variations in Al_2O_3 bulk rock content between Unit I and II dunites or between Unit I and II harzburgites. This difference in Cr content between Unit I and II peridotites may correspond to a variation in the spinel Cr/Al ratio.

Site 1272 peridotites are depleted in TiO_2 (<0.01–0.02 wt%), Zr (1.2–4.8 ppm), and Sr (<2 ppm except for the two Unit I aragonite-rich samples) and, to a lesser extent, in Sc (5–9 ppm) and V (12–50 ppm) compared to Leg 153 peridotites (Fig. **F56**). These moderately to highly incompatible elements preferentially partition into the liquid during partial melting. Their concentration range suggests that Site 1272 peridotites underwent higher degrees of partial melting than Leg 153 peridotites. Variations in TiO_2, Sr, and Zr in Site 1272 peridotites are within analytical error, but V and Sc are positively correlated with Al_2O_3. The dunites have lower concentrations of V (12 ppm) and Sc (4–5 ppm) compared to the harzburgites (20–50 and 6–9 ppm, respectively). V and Sc partition preferentially into clinopyroxene, and their correlation with Al_2O_3 content, a proxy for pyroxene content, suggests the presence of some minor amounts of clinopyroxene in these rocks before alteration. Alternatively, it should be noted that V and Sc may also be concentrated in spinel and magnetite. Therefore, as for Al_2O_3, spinel may also contribute to a significant amount to the bulk rock V and Sc budget for the highly refractory, pyroxene-poor Site 1272 peridotites.

F55. Ni vs. Mg# and Cr vs. Al_2O_3, p. 95.

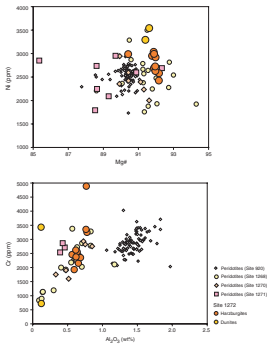

F56. TiO_2, Zr, V, and Sc vs. Al_2O_3, p. 96.

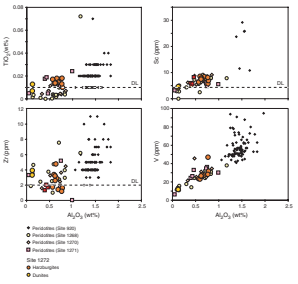

Mafic Rocks

The recovered mafic rocks, described as gabbronorite, diabase, and basalt, may be a single lithologic unit (termed diabase; Unit I) based on visual core and thin section descriptions (see "Igneous and Mantle Petrology," p. 2). We selected two gabbronorites, a diabase, and two basalts from this unit. Whereas these mafic rocks represent a range of magmas that may have cooled at different rates, each displays textural characteristics in thin section that suggest they cooled relatively quickly. This is especially true of Sample 209-1272A-7R-1, 109–113 cm, which comprises a matrix of devitrified glass containing plagioclase laths and needles with swallow-tail texture and a minor amount of olivine microphenocrysts, some of which display "hopperlike" texture (see "Igneous and Mantle Petrology," p. 2). Quench clinopyroxene and plagioclase are also present in the groundmass of this sample (see "Metamorphic Petrology," p. 7; Table T2).

The Site 1272 mafic rocks appear to form a coherent suite based on their major and trace element composition: MgO (6.1–8.8 wt%), Fe_2O_3 (9.5–10.3 wt%), TiO_2 (1.2–1.8 wt%), K_2O (0.15–0.64 wt%), Na_2O (2.6–3.2 wt%), Al_2O_3 (15.0–15.7 wt%), and CaO (10.9–11.6 wt%) (Fig. F57). The two gabbronorites and the diabase collectively span the observed compositional range, whereas the two basalts analyzed are similar to each other and to the diabase: MgO (7.4 wt%), total alkalis ($Na_2O + K_2O$ = 2.8–3.6 wt%), and SiO_2 (50.3–52.6 wt%). All analyzed samples have tholeiitic basalt compositions.

TiO_2 and K_2O are anticorrelated with MgO in these rocks. TiO_2 varies by a factor of ~1.5, whereas K_2O varies by a factor of 4. In contrast, Fe_2O_3, Al_2O_3, and CaO are relatively constant, as is the CaO/Al_2O_3 ratio. Total iron, calculated as FeO, is ~9 wt% at 8 wt% MgO and the corresponding value for Na_2O is ~2.6 wt% (Fig. F57). The Site 1272 mafic rocks generally show overlap with the compositions of basalts from the South Kane Fracture Zone (MARK) area (22°30′–22°50′N) (Meurer et al., 2001), although the Site 1272 rocks appear to be somewhat lower in TiO_2 and Na_2O (Fig. F57) (also see Fig. F39, p. 118, and accompanying text in the "Leg 209 Summary" chapter).

There is a negative correlation of H_2O with K_2O in the mafic rocks analyzed from Site 1272 (Fig. F58). This is somewhat unusual because mid-ocean-ridge basalts usually show a positive correlation between potassium and water content (Michael, 1995). The high H_2O contents of these rocks are probably a result of hydrothermal alteration. The negative trend seen in Figure F58 suggests the possibility of some K loss during alteration, which may suggest elevated temperatures (>150°C) of water-rock interaction, consistent with the presence of chlorite in some samples. Nonetheless, in comparison to the South MARK basalts, the Site 1272 mafic rocks are not obviously deficient in K (Fig. F57).

Site 1272 mafic rocks are depleted in Ni (<165–187 ppm), although they display slightly higher Ni content than the South MARK basalts (Meurer et al., 2001) with similar MgO content. Cr (41–338 ppm) shows a wide range of concentrations. Cr content is correlated with MgO in the Site 1270 mafic rocks and overlaps with the range of basalt data from the South MARK area (Meurer et al., 2001) (Fig. F59). Once again, Sample 209-1272A-4R-1, 82–85 cm, with the lowest MgO and Ni, is well outside the South MARK basalt range and is highly depleted in Cr (<41 ppm).

F57. TiO_2, K_2O, Al_2O_3, CaO, Na_2O, and FeO vs. MgO, p. 97.

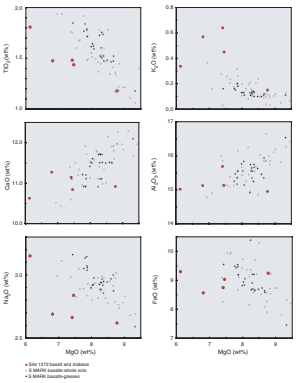

F58. H_2O vs. K_2O for mafic rocks, p. 98.

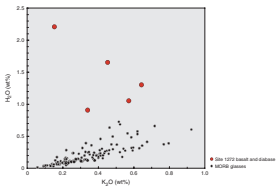

F59. Cr vs. MgO for mafic rocks, p. 99.

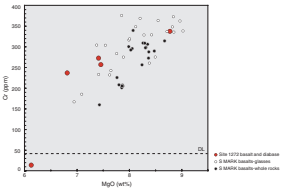

Incompatible trace element variations in the Site 1272 mafic rocks appear to be largely related to changes in MgO (Fig. F60), as observed previously for basalts from the South MARK area (Meurer et al., 2001). Sr and Zr in the Site 1272 mafic rocks each show a factor of 1.7 variation, similar to what is observed for Ti (1.5). In contrast, Ba varies by a factor of 7 (15–115 ppm) and is not simply related to MgO and Y content varies by only 20% (24–29 ppm).

F60. Zr vs. MgO and Sr vs. Zr for mafic rocks, p. 100.

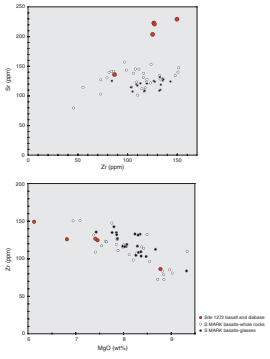

Discussion

Peridotites

Geochemical data on Site 1272 peridotites suggest that prior to alteration these rocks had chemical compositions similar to those of Site 1268 and 1270 peridotites and were more refractory than Leg 153 peridotites.

LOI values and volatile contents are particularly high in Site 1272 peridotites. All these rocks have been modified by alteration, predominantly to serpentine, leading to the addition of significant amounts of volatile constituents. In spite of their high volatile content, the major and trace element compositions show little evidence of compositional variation resulting from alteration, except for the two samples from Unit I and one harzburgite from Unit II, which was altered to a serpentinite mud. The two samples from Unit I show evidence of weathering and addition of carbonate (aragonite), which led to a strong enrichment in CaO, Sr, and CO_2 compared to other peridotites analyzed from Site 1272. The serpentinite mud, a former harzburgite, is slightly Na enriched compared to other Site 1272 harzburgites.

With the exception of the above-mentioned chemical changes attributed to alteration in some samples, the composition of Site 1272 harzburgites is remarkably homogeneous. Only a slight variation in Cr content between Unit and Unit II peridotites with similar Al_2O_3 content suggests a significant difference in composition between the two units, maybe associated with variations in the spinel Cr/Al ratio. Differences in Mg# between Unit I peridotites (90.3%–91.3%) and Unit II peridotites (91.6%–92.2%) could reflect differences in original composition or, possibly, Mg loss during seafloor weathering of the two Unit I samples.

Mafic Rocks

It is most reasonable to view the chemical results for the mafic rocks as defining three groups rather than a continuum: (1) one gabbronorite with high MgO (Sample 209-1272A-1R-1, 42–45 cm), (2) the diabase from Core 3R and the two basalt samples from Core 7R with intermediate MgO, and (3) a second gabbronorite with low MgO (Sample 4R-1, 82–85 cm). Although they consist of abundant plagioclase and variable amounts of pyroxene with lesser amounts of olivine (see **"Site 1272 Visual Core Descriptions"**), their compositions do not show appreciable effects of accumulation of either of these phases (Fig. F57). For example, plagioclase accumulation would lead to elevated Al_2O_3 at lower MgO, whereas olivine accumulation would lead to high MgO at low CaO. Instead, the mafic rocks approximate trends expected for fractional crystallization of olivine and plagioclase from an ocean-ridge basaltic magma.

The Site 1272 mafic rocks are chemically similar to basalts from elsewhere along the Mid-Atlantic Ridge. The major element variation indicates that crystal fractionation played an important role in producing their chemical composition. However, certain features indicate that these mafic rocks are not simply related by crystal fractionation from a common parental magma. Most significantly, incompatible elements show variable enrichment trends with decreasing MgO. The most incompatible elements, such as Ba and K, display a large range in concentration (enrichment factors = 7 and 4, respectively), whereas moderately incompatible elements such as Ti and Zr show a smaller variation (enrichment factors = 1.5–1.7). In our samples, Ba and K may have been affected by alteration and weathering. However, Meurer et al. (2001) found that basalt glasses from South MARK displayed similar variation, with overenrichment in the highly incompatible elements but underenrichment in moderately incompatible elements, relative to what could be produced by crystal fractionation. If Ba and K concentrations in the Site 1272 mafic rocks reflect original magmatic compositions, their variable enrichment might be due to a varying mantle source composition or to variation in the extent of mixing with small volumes of highly fractionated magma. The extremely low Cr and Ni contents of Sample 209-1272A-4R-1, 82–85 cm, suggest that if mixing with evolved magma plays a role, the end-member could be similar in composition to this gabbronorite.

The dispersion in chemical composition of Fe and Al with decreasing MgO is also not readily explained by crystal fractionation at a single depth. Crystallization of olivine and plagioclase at a fixed pressure would drive samples to higher FeO and lower Al_2O_3 with decreasing MgO. This is not observed in the Site 1272 mafic rocks that were analyzed. Their dispersion in major element oxides such as FeO and Al_2O_3 suggests that some of the chemical variability arises from polybaric crystal fractionation. This is also consistent with the detailed modeling of the South MARK basalts (Meurer et al., 2001), where it was demonstrated that crystallization over a range of pressures (ranging to 8 kbar, or 25 km depth below the seafloor) adequately accounts for the major element variability observed in lavas from that region. Similar conditions of magmatic differentiation may be present in the Site 1272 region.

PHYSICAL PROPERTIES

The physical properties of the peridotites and gabbros cored in Hole 1272A were characterized through a series of measurements on whole-core sections, split-core pieces, and discrete samples as described in "Physical Properties," p. 18, in the "Explanatory Notes" chapter. We measured natural gamma ray (NGR) activity and magnetic susceptibility on the multisensor track (MST) system and thermal conductivity, compressional wave velocity, density, and porosity. The rock names reported in data tables correspond to the primary lithologies determined by the igneous core description group. The data are summarized, as a function of depth, in Figure F61.

F61. Physical properties, p. 101.

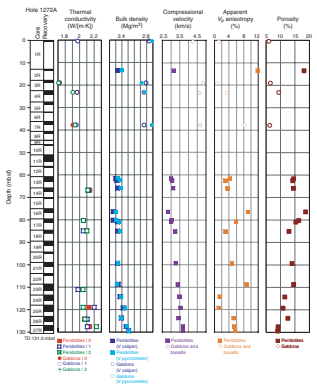

Natural Gamma Radiation

All cores recovered during Leg 209 were measured for 30 s using the NGR logger on the MST at intervals of 10 cm. Results are output in

counts per second and are shown in Figure F62. The cores from Hole 1272A mostly display natural radioactivity in the same range as the background radiation in the core laboratory on board the *JOIDES Resolution*. One peak >10 cps was recorded in the breccia recovered in Section 209-1272A-5R-1.

Magnetic Susceptibility

Magnetic susceptibility values were acquired on the MST at 2.5-cm intervals for all recovered cores. Core from Hole 1272A has high magnetic susceptibility (Fig. F62), which is related to the presence of magnetite in the recovered rocks. The magnetic susceptibilities of the peridotites at Site 1272 are comparable to those at Sites 1270 and 1271 (see Fig. F105, p. 159, in the "Site 1270" chapter, and Fig. F65, p. 109, in the "Site 1271" chapter). They are also comparable to the magnetic susceptibilities of the peridotites from Hess Deep (Gillis, Mével, Allan, et al., 1993) and from the MARK area (Cannat, Karson, Miller, et al., 1995) (see Fig. F88, p. 145, in the "Site 1268" chapter).

Thermal Conductivity

Thermal conductivity measurements were made at irregularly spaced intervals along the Hole 1272A gabbro, diabase, and peridotite cores. The data are summarized in Table T5. The thermal conductivities of the peridotite samples range 1.98–2.23 W/(m·K) (mean = 2.09 W/[m·K]); the thermal conductivity of the gabbros and diabases range 1.71–1.97 W/(m·K) (mean = 1.88 W/[m·K]). These values are lower than the thermal conductivities of peridotite and gabbroic rocks from ODP Holes 735B, 894G, and 923A at Atlantis Bank (Robinson, Von Herzen, et al., 1989; Dick, Natland, Miller, et al., 1999), Hess Deep (Gillis, Mével, Allan, et al., 1993), and MARK (Cannat, Karson, Miller, et al., 1995). They are also lower than the values measured at Sites 1269, 1270, and 1271 (Fig. F63). The low thermal conductivities of the peridotites are probably related to their high degree of serpentinization, as is also shown by their relatively low velocities and densities (see below).

As described in "Thermal Conductivity," p. 19, in "Physical Properties" in the "Explanatory Notes" chapter, measurements were taken in three directions on the cut face of the archive sample half, whenever possible. The purpose of these measurements was to determine the degree of apparent anisotropy. The apparent thermal conductivity anisotropy of peridotites, gabbros, and diabases measured in cores from Site 1272 ranges 0.1%–7.1% (Fig. F61; Table T5). Apparent thermal conductivity anisotropies measured from the beginning of Leg 209 (including Sites 1268, 1270, 1271, and 1272) are compiled in Figure F64. The apparent thermal conductivity anisotropy ranges 0.1%–12.6% (mean = 4.23%) in gabbros, diabases, troctolites, and peridotites.

Many of the core pieces in which we measured thermal conductivity were also sampled for measurements of porosity, density, velocity, and magnetic susceptibility. In Figure F65, mean values of thermal conductivity are plotted against bulk density for all Leg 209 sites through Site 1272, together with reference single crystal and monomineralic rock data (Clark, 1966; Clauser and Huenges, 1995). As expected from their high degree of alteration, the conductivities of the Leg 209 peridotites and troctolites are close to those of serpentine and talc. Gabbro and diabase values are similar to values reported for anorthite and anorthosite.

F62. MST magnetic susceptibility and NGR, p. 102.

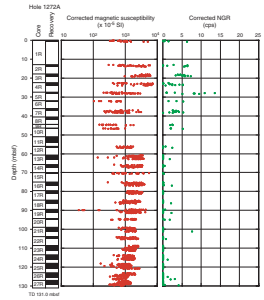

T5. Thermal conductivity, p. 125.

F63. Thermal conductivity, p. 103.

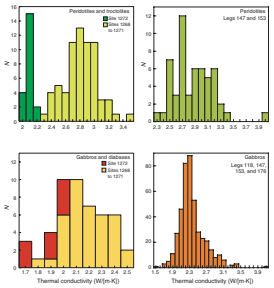

F64. Apparent thermal conductivity anisotropy, p. 104.

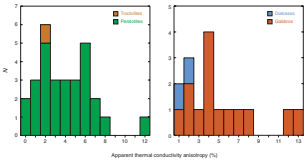

F65. Mean thermal conductivity vs. bulk density, p. 105.

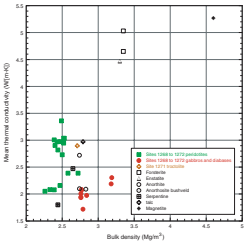

Porosity, Density, and Seismic Velocity

Bulk density, grain density, and porosity were measured on small sample chips (~3–6 cm^3) from Hole 1272A. *P*-wave velocity and wet bulk density were measured in cube samples, as described in **"*P*-Wave Velocity,"** p. 20, and **"Porosity and Density,"** p. 20, in "Physical Properties" in the "Explanatory Notes" chapter. These data are summarized in Table **T6.**

In Figure **F66,** the density and velocity data are compared with data from Legs 147 and 153, as well as Sites 1268, 1270, and 1271 (see **"Porosity, Density, and Seismic Velocity,"** p. 38, in "Physical Properties" in the "Site 1268" chapter, **"Porosity, Density, and Seismic Velocity,"** p. 41, in "Physical Properties" in the "Site 1270" chapter, and **"Porosity, Density, and Seismic Velocity,"** p. 33, in "Physical Properties" in the "Site 1271" chapter). Apparent compressional wave velocity anisotropy in the serpentinized peridotite samples from Site 1272 (1.1%–11.8%) is comparable to the anisotropy in samples from Sites 1268, 1270, and 1271. Similarly, the apparent compressional wave velocity anisotropy in the gabbro and diabase samples from Site 1272 (0.7%–8.2%), is comparable to the anisotropy in samples from Sites 1268, 1270, and 1271.

Velocities and densities in the peridotite samples from Site 1272 are lower than the densities and velocities of the ultramafic samples from Sites 1268, 1270, and 1271 and much lower than the velocities and densities of samples from Legs 147 (Gillis, Mével, Allan, et al., 1993) and 153 (Cannat, Karson, Miller, et al., 1995) (Figs. **F61, F66**). *P*-wave velocity and density, as well as thermal conductivity (Fig. **F61**), tend to increase downhole in the lower two recovered cores, pointing to progressively decreasing alteration at the bottom of the hole. The *P*-wave velocities and densities of the gabbro and diabase samples are comparable to the properties of gabbros from Leg 153 and to those of gabbros from the previous Leg 209 sites, except for the oxide-rich gabbros of Hole 1270B.

Densities and velocities in discrete samples from Site 1272 are compared to the downhole density and sonic velocity logs in Figure **F72** (see **"Downhole Measurements,"** p. 32). There is excellent agreement between the velocities in laboratory samples and the sonic log and good agreement between the densities determined from chip samples and the density log, whereas the densities estimated from the wet masses and dimensions of the cube samples are systematically lower than the wireline logging densities. Seismic velocities are particularly sensitive to thin (low porosity) cracks in the medium, whereas equant voids affect the density of the medium. Hence, the agreement between the laboratory data and the downhole logs indicates that the properties of the formation are not greatly affected by pervasive large-scale cracks or voids and that the samples may be taken as representative of the cored interval.

The discrepancy between the densities of the cube samples and the downhole logs led us to review the laboratory procedure. There are two potential sources of systematic error in these measurements. One is that some of the cube samples have small chips, particularly on their corners, that will cause the calculated volumes to be larger than the real volumes of the sample—but chips should affect only the densities of samples that are chipped, not the entire data set. The other possible source of error is systematic error in the measured dimensions of the cubes. We used the Hamilton Frame velocimeter (PWS3) caliper to mea-

T6. Porosity, density, and velocity, p. 126.

F66. *P*-wave velocity vs. wet bulk density, p. 106.

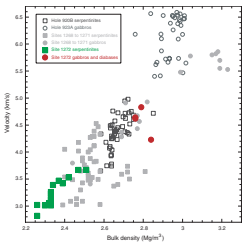

sure the dimensions of the cubes, which, though not strictly cubic, are all quite regular, right-rectangular parallelepipeds.

We tested several calipers, including PWS3, by measuring a machinist's standard (with steps of 0.5, 0.4, 0.3, 0.2, and 0.1 in) and a set of polycarbonate standards (with lengths of 20, 30, 40, and 50 mm). The results are summarized in Table T7. Of the several devices, calipers 1 and 2 show no statistically significant error, caliper 3 shows a slight systematic error, and PWS3 exhibits a comparatively large systematic error. Measurements made on the polycarbonate standards, which are used to calibrate the PWS3 caliper, suggest that the true lengths of the cylinders differ from their reported lengths.

T7. Caliper test data, p. 127.

Having determined that caliper 1 is not a source of systematic error, we remeasured all cubes from holes at Sites 1268, 1270, 1271, and 1272 to make better estimates of their densities, which we compare to the previous measurements made using PWS3 in Table T8. We find that the previous measurements are too low by ~1.6% on average. The tables and figures of these chapters as well as those of the "Physical Properties" sections in previous site chapters (Sites 1268, 1270, and 1271) were updated to take these revised density estimates into account.

T8. Caliper vs. PWS3 velocities, p. 128.

PALEOMAGNETISM

Magnetic results from Hole 1272A reveal two intervals with distinctive remanence characteristics, corresponding to the two lithologic units identified for this site (see "Lithology and Stratigraphy," p. 2 in "Igneous and Mantle Petrology"). Unit I (Cores 209-1272A-1R to 11R) includes dunite, harzburgite, gabbro, basalt, and sedimentary breccia. This unit is characterized by highly variable inclinations and demagnetization behaviors. It is difficult to establish whether the core from this unit is in situ, and thus the geological significance of the remanence from Unit I is uncertain. In contrast, the relatively uniform altered peridotites of lithologic Unit II (Cores 209-1272A-12R to 27R) show correspondingly little variation in magnetic properties. Unit II has uniformly positive inclinations (mean = ~45°) that are consistent with a normal polarity magnetization.

Continuous Measurements

Pass-through remanence measurements from lithologic Unit I were sparse as a result of the low core recovery and the short average length (generally <10 cm) of the core pieces. From Core 209-1272A-13R to the bottom of the hole (lithologic Unit II) the number of pieces >10 cm in length increases and magnetic measurements are more continuous (Fig. F67). All archive halves were subjected to stepwise alternating-field (AF) demagnetization, typically in 5-mT increments to 30 mT followed by 10-mT steps to a maximum peak field of 50 mT. When few pieces of sufficient length were present in a section, these pieces were measured individually to avoid edge effects from adjacent pieces with different orientations (see "Paleomagnetism," p. 33, in the "Site 1271" chapter).

F67. Archive-half magnetic measurements, p. 107.

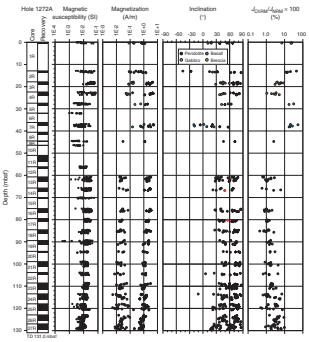

The natural remanent magnetization (NRM) intensities from Site 1272 cores range ~0.2–5 A/m. Altered harzburgites and dunites from lithologic Unit I generally have intensities <1 A/m, whereas the gabbros, microgabbros, and basalts from this unit typically have NRM intensities >1 A/m. The altered peridotites of lithologic Unit II show a trend of decreasing NRM intensity with depth, paralleling a downhole

decrease in magnetic susceptibility (Fig. F67). This trend is suggestive of lower degrees of serpentinization near the bottom of the hole, an inference that is supported by the increasing abundance of fresh olivine in the lowermost portion of Unit II (see "Igneous and Mantle Petrology," p. 2, and "Metamorphic Petrology," p. 7).

The initial inclinations for the archive halves are generally between 60° and 90°, reflecting the influence of a steep, presumably drilling-related overprint. This low-stability overprint is generally removed by AF demagnetization at 10–20 mT (Fig. F68B, F68D–F68F). Demagnetization of core pieces from lithologic Unit I reveals a range of stable inclinations from –45° to +60° (Fig. F61). The origin of this variability is discussed below in conjunction with the discrete sample results. After removal of the drilling remanence, a stable remanence direction with moderate positive inclinations (generally 30°–60°) is isolated for many samples from lithologic Unit II. However, in some cases the distinction between the drilling overprint and a final stable characteristic remanence (ChRM) direction is less obvious (Fig. F69D). Moreover, for the altered peridotites of Unit II, the stable remanence represents <10% of the NRM (average = 2.5%). Based on in part on comparison with results from discrete samples (see below), we suggest that the archive-half data from Unit II provides a reasonable approximation of the stable ChRM.

F68. Demagnetization, Unit I, p. 108.

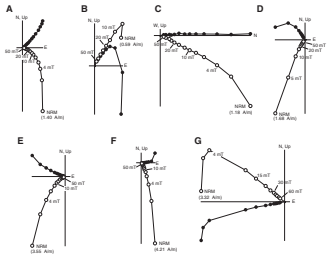

F69. Demagnetization, Unit II, p. 109.

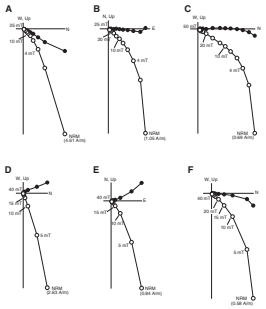

T9. Discrete sample data, p. 129.

Discrete Samples

The various lithologies of Unit I exhibit a range of behaviors during demagnetization (Fig. F68). A low-stability drilling overprint, generally removed by demagnetization at 10 mT, is evident in most lithologies. For most diabase/microgabbro samples (Fig. F68A, F68E) and the olivine gabbro from Core 209-1272A-4R (Fig. F68F), this low-stability overprint constitutes a large fraction of the remanence (the ChRM represents <10% of the NRM) (Table T9). In contrast, less drilling overprint is discernible in the weathered dunite from Core 209-1272A-2R (Fig. F68C) and the diabase/microgabbro from Core 7R (Fig. F68G). The final stable remanence direction for discrete samples from Unit I is highly variable (five samples have inclinations ranging from –38° to +52°).

The altered peridotites of Unit II exhibit much more uniform behavior during demagnetization (Fig. F69). All samples show a low-stability drilling overprint that is removed by demagnetization at ~10 mT. Although the final stable direction typically represents 1%–5% of the NRM, the ChRM direction is well isolated after demagnetization at 10–15 mT. A single sample from Core 209-1272A-27R has a ChRM representing 25% of the remanence (Table T9). Samples from Unit II also have low median destructive fields (MDF; the peak AF necessary to reduce the vector difference sum to 50% of its initial value) of ~2 mT. These low MDF values reflect the significant low-stability drilling overprint that is most likely carried by coarse-grained magnetite with low coercivities.

Remanence Directions

The geological significance of the ChRM directions isolated from samples in lithologic Unit I is uncertain. For example, five small (~9 cm) pieces of diabase/microgabbro from Core 209-1272A-7R were analyzed in pass-through mode and yielded very stable remanence but incoherent inclinations ranging –25°–20° (Fig. F67). A discrete sample from this same core (Fig. F68G) shows only a small drilling overprint

and a well-defined stable inclination of –39°. Moreover, both the archive-half and discrete sample data from Core 209-1272A-7R indicate high magnetic stability. The scattered remanence directions for samples with such high stability suggest that the core pieces are no longer in the orientations in which the ChRM was acquired. Other similarly aberrant directions are evident in the pass-through remanence data from other lithologies (e.g., dunite at Section 209-1272A-2R-1, 20 cm) (Fig. **F68B**).

Other intervals in Unit I have apparently coherent stable remanence directions that are generally compatible with the expected inclination at the site as well as with directions obtained from Unit II (see below). For example, some of the altered harzburgites and dunites of Cores 209-1272A-1R and 2R have ChRM directions with positive inclinations similar to the expected time-averaged inclination at the site (Fig. **F68C**). The gabbros from Cores 209-1272A-3R and 4R and breccias from Core 5R also have coherent, though significantly steeper, inclinations. The breccias (composed of angular clasts of peridotite) yielded coherent demagnetization results, with stable magnetization, positive and shallow inclinations, and no significant drilling overprint.

There are at least two possible explanations for the scattered remanence directions in portions of Unit I. First, many of these samples may represent rocks that have fallen from the walls of the borehole. This is a feasible scenario for core pieces that are smaller than the nominal diameter of the borehole (10–12 cm) as, for example, for the pieces from Core 209-1272A-7R that all have lengths <9.5 cm. If this explanation is valid for all pieces in Core 209-1272A-7R, then core pieces from higher levels might represent in situ samples. Alternatively, the directional heterogeneity in Unit I may represent sampling of a talus pile. In this case, individual core pieces (particularly for pieces longer than the width of the core liner and with parallel edges) may accurately reflect the vertical orientation of blocks within the talus pile. Because the origin of the inclination variation within Unit I remains uncertain, paleomagnetic data from this unit will not be considered further here.

Samples from lithologic Unit II, in contrast, have consistent positive inclinations that are broadly consistent with the expected normal polarity dipole inclination (28°) at the site (Fig. **F70**). Fourteen discrete samples from this unit yield an average inclination of 45.2° (+5.4°/–6.7° 95% confidence limits; κ = 42.4) using the inclination only technique of McFadden and Reid (1982). The distribution of inclinations obtained from archive-half measurements (Table **T10**) is slightly broader than that from the discrete samples. Nonetheless, the archive-half data yield a mean inclination (42.7° +1.4°/–3.5°; κ = 25.6; N = 139) that is nearly identical to the discrete sample mean inclination. The declination distributions from both discrete samples and archive halves are also similar, with a concentration of values in the northeast quadrant. This clustering of declination values presumably reflects the imposition of a relative orientation prior to splitting the cores.

The mean inclination for Site 1272 is statistically distinct (at the 95% confidence level) from the expected dipole inclination at the site. As suggested for previous sites, this inclination discrepancy suggests that the site has been tectonically rotated since acquisition of the remanence. Although counterclockwise rotations about a ridge-parallel (020°), horizontal rotation axis may initially steepen a normal polarity remanence, such a rotation would steepen the remanence by a maximum of ~8° and thus could not account for the observed inclination of 45°. Because Site 1272 was drilled on an inside corner bathymetric high (~10 km from the fracture zone) the rotation axes are poorly con-

F70. Inclinations and declinations, p. 110.

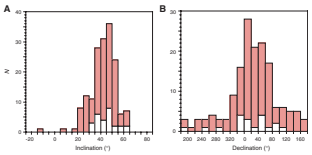

T10. Piece orientations, p. 130.

strained and other rotation axis orientations are possible. A more complete discussion of tectonic scenarios that could explain the remanence data can be found in "Structural Geology," p. 11.

Anisotropy of Magnetic Susceptibility

Anisotropy of magnetic susceptibility (AMS) was determined for all discrete samples from Site 1272 (Table T11). Given the uncertainty in whether samples from Unit I are in situ, only the magnetic fabric data from Unit II will be considered. The peridotite samples from this unit show variable degrees of anisotropy (P = maximum/minimum eigenvalues [1.04–1.37]). Most samples have oblate magnetic fabrics, although the three eigenvalues are distinct in all cases.

T11. AMS data, p. 133.

The remanent declinations from these same samples can be used to provide a first-order reorientation of the magnetic fabrics into a geographic reference frame. A simple vertical axis rotation has been applied to each sample to restore the magnetic declination to 360° under the assumption that the ChRM in each sample reflects a normal polarity magnetization that approximates the time-averaged dipole declination at the site. No attempt has been made to account for the declination offset that would result from tilts about horizontal rotation axes.

After this reorientation, the poles to magnetic foliation (the minimum eigenvectors) are mostly clustered in the southwest quadrant. The corresponding maximum eigenvectors are subhorizontal, with a mean trend/plunge of 151°/12° (Fig. F71). The reoriented magnetic foliations are approximately parallel to the dominant northeast-dipping planes, which have been interpreted as fractures, evident in the downhole resistivity images from the site (see "Downhole Measurements," p. 32). The susceptibility anisotropy is measured on discrete samples (free of fractures), and thus the reason for the close correspondence with the fractures imaged during logging is not immediately clear. One possibility is that the AMS data reflect the distribution of magnetite in serpentinite veins and these veins, in turn, may constitute (or be parallel to) planes of weakness for fracture formation.

F71. Projections of eigenvectors, Unit II, p. 111.

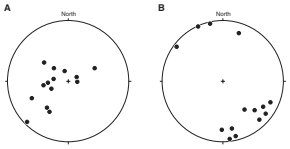

MICROBIOLOGY

Solid Samples

Samples 209-1272A-13R-1 (Piece 17, 121–127 cm) and (Piece 20, 142–150 cm)

At Site 1272 two samples were collected to characterize the microbial community inhabiting this environment. The rock samples are completely serpentinized harzburgites.

The samples were prepared as described in "Igneous Rocks," p. 24, in "Microbiology" in the "Explanatory Notes" chapter. The type and extent of contamination caused by drill fluids was evaluated as described in "Contamination Tests," p. 26, in "Microbiology" in the "Explanatory Notes" chapter. Pieces 17 and 20 were rinsed in nanopure water, and 1 mL of the collected water (34 mL) was filtered and examined under a fluorescence microscope. Microsphere concentration was >940 microspheres/mL of wash. A 0.4-g interior piece of the sample was examined under a fluorescence microscope to detect microsphere penetra-

tion. The results showed that the microspheres did not penetrate to the interior of the sample. Perfluorocarbon tracer was not used at this site.

Seawater and Water Samples and Atmospheric Data

One liter of surface water was collected and prepared for deoxyribonucleic acid (DNA) analysis and direct counts as described in **"Seawater and Water Samples,"** p. 26, in "Microbiology" in the "Explanatory Notes" chapter.

Table **T12** is a summary of atmospheric and surface water data for the period 5–13 June 2003. For surface water direct count data, 1 mL of water was stained as described in **"Surface Seawater,"** p. 26, in "Seawater and Water Samples" in "Microbiology" in the "Explanatory Notes" chapter. One milliliter of funnel rinse water was used as a control. Salinity, temperature, and pH values for all surface water values varied; salinity ranged 36.0–37.0 psu, temperature 25.5°–26.1°C, and pH 7.96–7.98. Surface water samples were collected between 1225 and 1345 hr. No surface water sample was collected on 12 June due to relocation of the ship. Air samples were collected for culture-based studies between 0640 and 0704 hr. Air sample volumes ranged 313.2–8856.0 L per sample. Microbial growth (colony forming units) was for the total volume at 48 and >96 hr of incubation (Table **T12**). Air temperatures, humidity, wind speed, and wind direction ranged 25.3°–26.4°C, 68.8%–82.8%, 4.5–6.7 m/s, and 67°–110°, respectively. Samples for shore-based analysis of bacterial community DNA and bacteria and viral direct counts were collected daily and stored according to protocol.

T12. Microbiology data, p. 134.

DOWNHOLE MEASUREMENTS

Operations

On 11 June, wireline logging operations in Hole 1272A began with the deployment of a tool string consisting of the Hostile Environment Gamma Ray Sonde (HNGS), the Hostile Environment Litho-Density Sonde (HLDS), and the Dual Induction Phasor Resistivity Tool (DIT-E). The Accelerator Porosity Sonde (APS) was left out of the standard triple combination (triple combo) configuration because of problems with initialization prior to the beginning of the wireline logging operations. After the first tool string deployment, a tool string composed of the Dipole Sonic Imager (DSI), the Scintillation Gamma Ray Tool (SGT), and FMS was used. Main and repeat passes of the entire logged interval were obtained during both tool string deployments. Wireline logging operations took a total of 10 hr, 50 min from beginning to end.

The water depth was estimated from pipe measurements at 2571 meters below rig floor (mbrf). Drilling operations reached a total depth of 131 mbsf, and the mechanical bit release was used to leaving the rotary core barrel bit at the bottom of the hole. A 20-bbl sepiolite mud sweep was done while finishing the coring operations. After releasing the bit, hole displacement operations consisted of 40 bbl (1264 strokes) of sepiolite mud. The bottom of the BHA was placed at a depth of 41 mbsf.

Borehole Condition and Data Quality

The wireline logging data were sent to the Borehole Research Group at LDEO via satellite transmission for processing, and the results were returned to the ship within 4 days. All data presented in this chapter have been processed and depth shifted as described in the following section.

All passes reached 125.5 mbsf, or 5.5 m above the maximum penetration. The wireline heave compensator was used to counter ship heave, which was a maximum of 1.7 m at the start of the logging operations and decreased to 1.45 m by the end. The BHA depths are as they appear on the logs after a differential depth shift (see depth shift discussion below) and a depth shift to the seafloor. After processing, there is a discrepancy with the original depths given by the drillers on board. Typical reasons for depth discrepancies are ship heave, use of the wireline heave compensator, and drill string and/or wireline stretch. The location of the BHA on the main passes of both tool string deployments is 38 mbsf.

Depth matching was done by choosing one log as reference (base log) and the features in the equivalent logs from the other runs were manually matched to the reference. The depth adjustments that were required to bring the match log in line with the base log were then applied to all the other logs from the same tool string. The original logs were depth matched to the first pass of the HNGS-HLDS-DIT-E tool string (the reference run) and were then shifted to the seafloor using –2571 m. The HNGS-HLDS-DIT-E pass 2 was matched to the reference run using the spherically focused resistivity (SFLU); the DSI-SGT-FMS pass 1 was matched to the reference run using caliper and gamma-ray logs; and the DSI-SGT-FMS pass 2 was matched to the DSI-SGT-FMS pass 1 using the caliper logs. The seafloor depth was not determined directly because there is no clear step in gamma radiation values, which are very low in this hole. The seafloor depth estimate of the drillers was used.

Bulk density data were recorded at a sampling interval of 2.54 cm. The enhanced bulk density curve is the result of Schlumberger enhanced processing technique performed on the MAXIS system on board the *JOIDES Resolution*. While in normal processing, short-spacing data is smoothed to match the long-spacing values; in enhanced processing this process is reversed. SGT gamma ray measurements were recorded at 15.24- and 5.08-cm sampling intervals.

The HNGS and SGT data were corrected for hole size and the HLDS values were corrected for standoff and hole diameter during the data recording. During the first pass, the DSI tool was run in *P*- and *S*-, high-frequency upper dipole, and crossed dipole modes; on the second pass, *P*- and *S*-, low-frequency lower dipole, and crossed dipole modes were used. Overall, the compressional wave data are good based on the coherency of the signal; the shear wave data from the second pass are better than those from the first pass.

Hole diameter was recorded with the hydraulic caliper on the HLDS (LCAL) and on the FMS (C1 and C2) tools. The borehole was in good condition, typically 10–13 in wide except for occasional thin washouts, the largest of which is at 95 mbsf (Fig. F72). Additional information about the logs can be found in "Downhole Measurements," p. 29, in the "Explanatory Notes" chapter.

F72. Geophysical logs, p. 112.

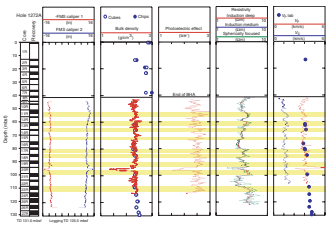

Electrical Resistivity Measurements

Electrical resistivity values measured in Hole 1272A are low throughout the entire logged interval. Electrical resistivity values from both passes show deep measurements (IDPH) that range 2.1–4.7 Ωm, intermediate (IMPH) measurements of 0.9–8.3 Ωm; and shallow (SFLU) measurements that range 1.6–7.2 Ωm (Fig. F72). The SFLU curve shows the widest range of variability, most likely due to changes in fracture intensity and alteration. Several zones with higher resistivity values correlate well with similar changes in density, photoelectric effect (PEF), and velocity (Fig. F72).

Density and Photoelectric Effect Measurements

High-resolution density measurements show values ranging 1.3–2.7 g/cm³. The average density for the entire logged interval is 2.3 g/cm³, consistent with the overall high degree of serpentinization observed in the peridotites. Densities are especially low in the interval 94–96 mbsf, where a fault zone or large fracture was encountered. In keeping with the HLDS measurements, which show a washout at 95 mbsf, the density values indicate a large standoff (i.e., distance between the tool sensors and the borehole wall). Overall, logging densities correlate well with laboratory measurements (Fig. F72), although densities in rock cubes tend to be lower than the logging densities and laboratory density measurements made on rock chips (see **"Porosity, Density, and Seismic Velocity,"** p. 27, in "Physical Properties"). The PEF values range 1.5–3.0 barn/e⁻ (mean PEF for the logged interval = 2.45 barn/e⁻). The relatively low PEF values are also consistent with the high degree of serpentinization (see Table T13, p. 75, in the "Explanatory Notes" chapter), whereas the larger values may reflect the presence of magnetite, as seen in the core magnetic susceptibility logs (see **"Magnetic Susceptibility,"** p. 26, in "Physical Properties").

Sonic Measurements

Compressional wave velocities from both passes range 2.1–5.2 km/s (mean = 3.0 km/s). In general, these compressional wave velocities are lower than expected values for lower oceanic crust and upper mantle and may reflect the high degree of serpentinization and/or the fractured nature of the rocks recovered from this hole. Compressional wave velocities correlate well with laboratory measurements made at ambient pressure (Fig. F72). Shear wave velocities are generally low, ranging 0.5–3.1 km/s (mean = 1.2 km/s). Postcruise processing and detailed analysis of the shipboard slowness time coherence processing and cross-dipole measurements will determine any potential velocity anisotropy or shear wave splitting associated with structural features imaged with the FMS.

Inclinometry and Magnetic Measurements

The General Purpose Inclinometry Tool (GPIT) run in conjunction with the FMS, contains a triaxial fluxgate magnetometer (see **"Downhole Measurements,"** p. 29, in the "Explanatory Notes" chapter) that can provide information on the intensity and direction of magnetization in the formation (Fig. F73). In the simple case of a uniformly magnetized, horizontally layered medium, the vertical anomaly measured in the borehole will have the opposite sign from the vertical compo-

F73. GPIT orientation and magnetic field logs, p. 113.

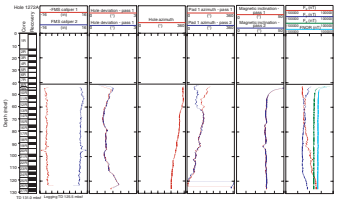

nent of the formation magnetization (e.g., Ito et al., 1995; Gallet and Courtillot, 1989). Moreover, for a normal polarity magnetization formed in the Northern Hemisphere, the horizontal anomaly will be 180° out of phase with respect to the vertical anomaly. The relative amplitudes of the horizontal and vertical anomalies are dictated by the inclination of the formation magnetization.

Magnetic data for peridotite samples (lithologic Unit II) from Hole 1272A reveal a normal polarity remanence with an average inclination of ~45° (see **"Paleomagnetism,"** p. 28). Initial inspection of the magnetic anomaly data from Hole 1272A reveal that both horizontal and vertical anomalies are positive, apparently at odds with the pattern expected from the paleomagnetic data from samples at this site. Two factors contribute to this discrepancy. First, the strong magnetization of the drill pipe generates a positive vertical anomaly for a significant distance below the end of the pipe. Second, the calibration of the fluxgate sensors is apparently inaccurate, leading to an offset, particularly in the vertical anomaly. The offset in the vertical fluxgate sensor is poorly constrained by the data from Hole 1272A, but an estimate of the possible calibration error can be obtained from FMS logging results from Leg 197 (Tarduno, Duncan, Scholl, et al., 2002). Here, the vertical component of the ambient field measured >100 m from the drill pipe in weakly magnetized sediments is 1000–2000 nT larger than the true value.

To partially compensate for these effects, we removed an estimate of the anomaly associated with the drill pipe (Fig. **F74A**) from the vertical anomaly measured in the borehole. An offset of 1000 nT inferred from Leg 197 data was assumed for the vertical fluxgate (the base level of the modeled drill pipe signal), although the Leg 197 results suggest that this value could be larger. The resulting magnetic anomaly pattern more closely corresponds to the expected pattern (Fig. **F74B**). Below ~60 mbsf, the vertical and horizontal anomalies show similar amplitude patterns that are 180° out of phase. Notably, the anomalies at ~90 mbsf are consistent with the presence of a highly magnetized (normal polarity) zone, presumably reflecting ~1 m thickness for the oxide-rich gabbroic rocks recovered in this interval. Additional calibration postcruise studies on the GPIT will be required onshore to validate these initial results.

Formation MicroScanner Measurements

FMS images show many zones that are characterized by high fracture density and deformation. Fault gouge samples recovered from Section 209-1272A-19R-1 correlate with an interval with high resistivity contrast interpreted to represent a highly fractured interval between 89.5 and 93 mbsf (Fig. **F75**). Oxide gabbro samples from this core could be responsible for the dark resistive bands found in interval 90.2–90.9 mbsf (Fig. **F75**). The interval 94.2–95.9 mbsf also corresponds to a zone where fault gouge samples were recovered in Section 209-1272A-19R-2 (Fig. **F76**). The interval with resistivity contrast most indicative of intense faulting is 100.5–101.9 mbsf (Fig. **F77**). This interval is characterized by thick, sharp-bounded conductive zones and defining the top and bottom contacts, a series of resistive clasts (white round features) that suggest brecciation, and some faint high-angle features that suggest either additional fracturing or veining episodes. A total of 2.1 m was recovered from a 5-m cored interval that corresponds to Core 209-1272A-21R, including a soapstone (interval 21R-1, 67–70 cm).

Preliminary structural analyses of fracture patterns show 78 features striking roughly northwest–southeast and dipping mostly northeast

F74. GPIT estimation of magnetic anomalies, p. 114.

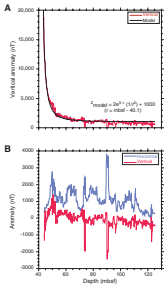

F75. FMS images of a potential faulted zone, p. 115.

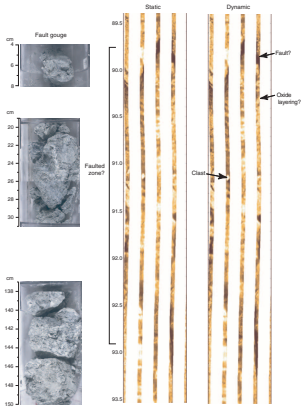

F76. Apparent fault and steep fractures in FMS images, p. 116.

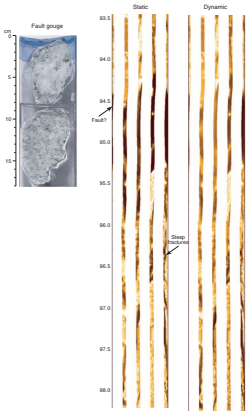

(Fig. F78). Dip magnitudes range between 10° and close to 90°, with most the dips ranging 40°–60°. Highly fractured and brecciated intervals interpreted from FMS images and correlated with fault gouge recovered in core strike in a general northwest–southeast direction and dip northeast–southwest (Fig. F79). The general northwest–southeast strike of most of the identified features indicates that faults and fractures are oblique to both the fracture zone and the Mid-Atlantic rift valley. These orientations are consistent with orientations of serpentine veins and fractures measured on the core face and rotated into a geographical reference frame using paleomagnetic data (see **"Structures in Peridotite and Gabbroic Intrusions,"** p. 8, in "Mantle Upwelling, Melt Transport, and Igneous Crustal Accretion" in the "Leg 209 Summary" chapter).

Natural Radioactivity Measurements

Formation natural radioactivity was measured during each run with two different tools. The SGT measured total gamma counts, whereas the HNGS provided spectral measurements. The different gamma ray tools show the same general patterns throughout the logged interval. The high-resolution total counts curve from the SGT and spectral data from the HNGS are shown in Figure F80 for simplicity. The SGT curve has low values (0.0–6.4 gAPI). The spectral gamma ray measurements also show very low values that in many instances are below the tool detection limits for Th (0.7 ppm), U (0.35 ppm), and K (0.18 wt%). The spectral data show a general inverse relationship between thorium and uranium as well as a general increase in potassium with depth.

F77. Apparent fault zone in FMS images, p. 117.

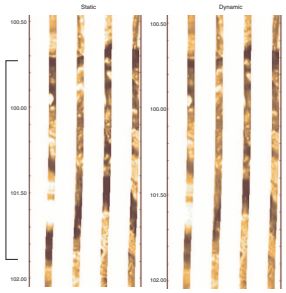

F78. Strike and dip azimuth and magnitude from FMS images, p. 118.

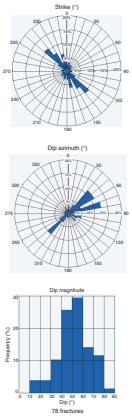

F79. Fault gouge attitudes from core-log measurements, p. 119.

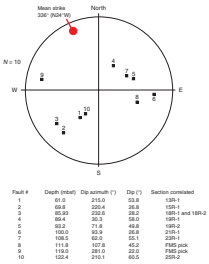

F80. Resistivity and gamma ray correlation, p. 120.

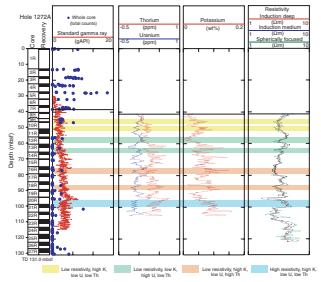

REFERENCES

Allman, R., and Donnay, J.D.H., 1969. About the structure of iowaite. *Am. Mineral.,* 54:296–299.

Boudier, F., and Nicolas, A., 1972. Fusion partielle gabbroique dans la Iherzolite de Lanzo. *Bull. Suisse Mineral. Petrogr.,* 52:39–56.

Cannat, M., Karson, J.A., Miller, D.J., et al., 1995. *Proc. ODP, Init. Repts.,* 153: College Station, TX (Ocean Drilling Program).

Casey, J.F., 1997. Comparison of major- and trace-element geochemistry of abyssal peridotites and mafic plutonic rocks with basalts from the MARK region of the Mid-Atlantic Ridge. *In* Karson, J.A., Cannat, M., Miller, D.J., and Elthon, D. (Eds.), *Proc. ODP, Sci. Results,* 153: College Station, TX (Ocean Drilling Program), 181–241.

Clark, S.P., 1966. Thermal conductivity. *In* Clark, S.P. (Ed.), *Handbook of Physical Constants*. Mem.—Geol. Soc. Am., 97:461–482.

Clauser, C., and Huenges, E., 1995. Thermal conductivity of rocks and minerals. *In* Ahrens, T.J. (Ed.), *A Handbook of Physical Constants: Rock Physics and Phase Relations* (Vol. 3), Am. Geophys. Union, Ref. Shelf Ser., 3:105–126.

Deer, W.A., Howie, R.A., and Zussman, J., 1992. *An Introduction to the Rock-Forming Minerals* (2nd ed.): Harlow, United Kingdom (Longman Scientific Technical).

Dick, H.J.B., 1977. Evidence of partial melting in the Josephine peridotite. *In* Dick, H.J.B. (Ed.), *Magma Genesis*. Bull.—Oreg. Dep. Geol. Miner. Ind., 96:59–62.

Dick, H.J.B., Natland, J.H., Miller, D.J., et al., 1999. *Proc. ODP, Init. Repts.,* 176 [CD-ROM]. Available from: Ocean Drilling Program, Texas A&M University, College Station, TX 77845-9547, U.S.A.

Dilek, Y., Coulton, A., and Hurst, S.D., 1997. Serpentinization and hydrothermal veining in peridotites at Site 920 in the MARK area. *In* Karson, J.A., Cannat, M., Miller, D.J., and Elthon, D. (Eds.), *Proc. ODP, Sci. Results,* 153: College Station, TX (Ocean Drilling Program), 35–59.

Fujiwara, T., Lin, J., Matsumoto, T., Kelemen, P.B., Tucholke, B.E., and Casey, J., 2003. Crustal evolution of the Mid-Atlantic Ridge near the Fifteen-Twenty Fracture Zone in the last 5 Ma. *Geochem., Geophys., Geosyst.,* 4:10.1029/2002GC000364.

Gallet, Y., and Courtillot, V., 1989. Modeling magnetostratigraphy in a borehole. *Geophysics,* 54:973–983.

Gibson, I.L., Beslier, M.-O., Cornen, G., Milliken, K.L., and Seifert, K.E., 1996. Major- and trace-element seawater alteration profiles in serpentinite formed during the development of the Iberia Margin, Site 897. *In* Whitmarsh, R.B., Sawyer, D.S., Klaus, A., and Masson, D.G. (Eds.), *Proc. ODP, Sci. Results,* 149: College Station, TX (Ocean Drilling Program), 519–527.

Gillis, K., Mével, C., Allan, J., et al., 1993. *Proc. ODP, Init. Repts.,* 147: College Station, TX (Ocean Drilling Program).

Heling, D., and Schwarz, A., 1992. Iowaite in serpentinite muds at Sites 778, 779, 780, and 784: a possible cause for the low chlorinity of pore waters. *In* Fryer, P., Pearce, J.A., Stokking, L.B., et al., *Proc. ODP, Sci. Results,* 125: College Station, TX (Ocean Drilling Program), 313–323.

Ito, H., Nogi, Y., and Larson, R.L., 1995. Magnetic reversal stratigraphy of Jurassic oceanic crust from Hole 801C. *In* Haggerty, J.A., Premoli Silva, I., Rack, F., and McNutt, M.K. (Eds.), *Proc. ODP, Sci. Results,* 144: College Station, TX (Ocean Drilling Program), 641–647.

Iturrino, G.J., Miller, D.J., and Christensen, N.I., 1996. Velocity behavior of lower crustal and upper mantle rocks from a fast-spreading ridge at Hess Deep. *In* Mével, C., Gillis, K.M., Allan, J.F., and Meyer, P.S. (Eds.), *Proc. ODP, Sci. Results,* 147: College Station, TX (Ocean Drilling Program), 417–440.

Kelemen, P.B., 1990. Reaction between ultramafic rock and fractionating basaltic magma, I. Phase relations, the origin of calc-alkaline magma series, and the formation of discordant dunite. *J. Petrol.,* 31:51–98.

Kohls, D.W., and Rodda, J.L., 1967. Iowaite, a new hydrous magnesium hydroxide-ferric oxychloride from the Precambrian of Iowa. *Am. Mineral.,* 52:1261–1271.

Matsumoto, I., and Arai, S., 2001. Morphological and chemical variation of chromian spinel in dunite-harzburgite complexes from the Snagun zone (SW Japan): implications for mantle/melt reaction and chromitite formation processes. *Mineral. Petrol.,* 73:305–323.

McFadden, P.L., and Reid, A.B., 1982. Analysis of paleomagnetic inclination data. *Geophys. J. R. Astron. Soc.,* 69:307–319.

Meurer, W.P., Sturm, M.A., Klein, E.M., and Karson, J.A., 2001. Basalt compositions from the Mid-Atlantic Ridge at the SMARK area (22°30′N to 22°50′N): implications for parental liquid variability at isotopically homogeneous spreading centers. *Earth Planet. Sci. Lett.,* 186:451-469.

Michael, P., 1995. Regionally distinctive source of depleted MORB: evidence for trace elements and H_2O. *Earth Planet. Sci. Lett.,* 131:301–320.

Miller, D.J., and Christensen, N.I., 1997. Seismic velocities of lower crustal and upper mantle rocks from the slow-spreading Mid-Atlantic Ridge, south of the Kane Fracture Transform Zone (MARK). *In* Karson, J.A., Cannat, M., Miller, D.J., and Elthon, D. (Eds.), *Proc. ODP, Sci. Results,* 153: College Station, TX (Ocean Drilling Program), 437–454.

O'Hanley, D.S., 1996. Serpentinites: records of tectonic and petrological history. *Oxford Monogr. Geol. Geophys.,* Vol. 34.

Phipps, S.P., and Ballotti, D., 1992. Rheology of serpentinite muds in the Mariana-Izu-Bonin forearc. *In* Fryer, P., Pearce, J.A., Stokking, L.B., et al., *Proc. ODP, Sci. Results,* 125: College Station, TX (Ocean Drilling Program), 363–372.

Quick, J.E., 1981. The origin and significance of large, tabular dunite bodies in the Trinity peridotite, northern California. *Contrib. Mineral. Petrol.,* 78:413–422.

Robinson, P.T., Von Herzen, R., et al., 1989. *Proc. ODP, Init. Repts.,* 118: College Station, TX (Ocean Drilling Program).

Seyler, M., Cannat, M., and Mével, C., 2003. Evidence for major element heterogeneity in the mantle source of abyssal peridotites from the Southwest Indian Ridge (52° to 68°E). *Geochem., Geophys., Geosys.,* 4:10.1029/2002GC000305.

Seyler, M., Toplis, M.J., Lorand, J.-P., Luguet, A., and Cannat, M., 2001. Clinopyroxene microtextures reveal incompletely extracted melts in abyssal peridotites. *Geology,* 29:155–158.

Snow, J.E., and Dick, H.J.B., 1995. Pervasive magnesium loss by marine weathering of peridotite. *Geochim. Cosmochim. Acta,* 59:4219–4235.

Tarduno, J.A., Duncan, R.A., Scholl, D.W., et al., 2002. *Proc. ODP, Init. Repts.,* 197 [CD-ROM]. Available from: Ocean Drilling Program, Texas A&M University, College Station TX 77845-9547, USA.

Figure F1. Bathymetric map indicating subsea camera survey track and hole location. Bathymetric data courtesy of T. Fujiwara and T. Matsumoto of JAMSTEC (Fujiwara et al., 2003).

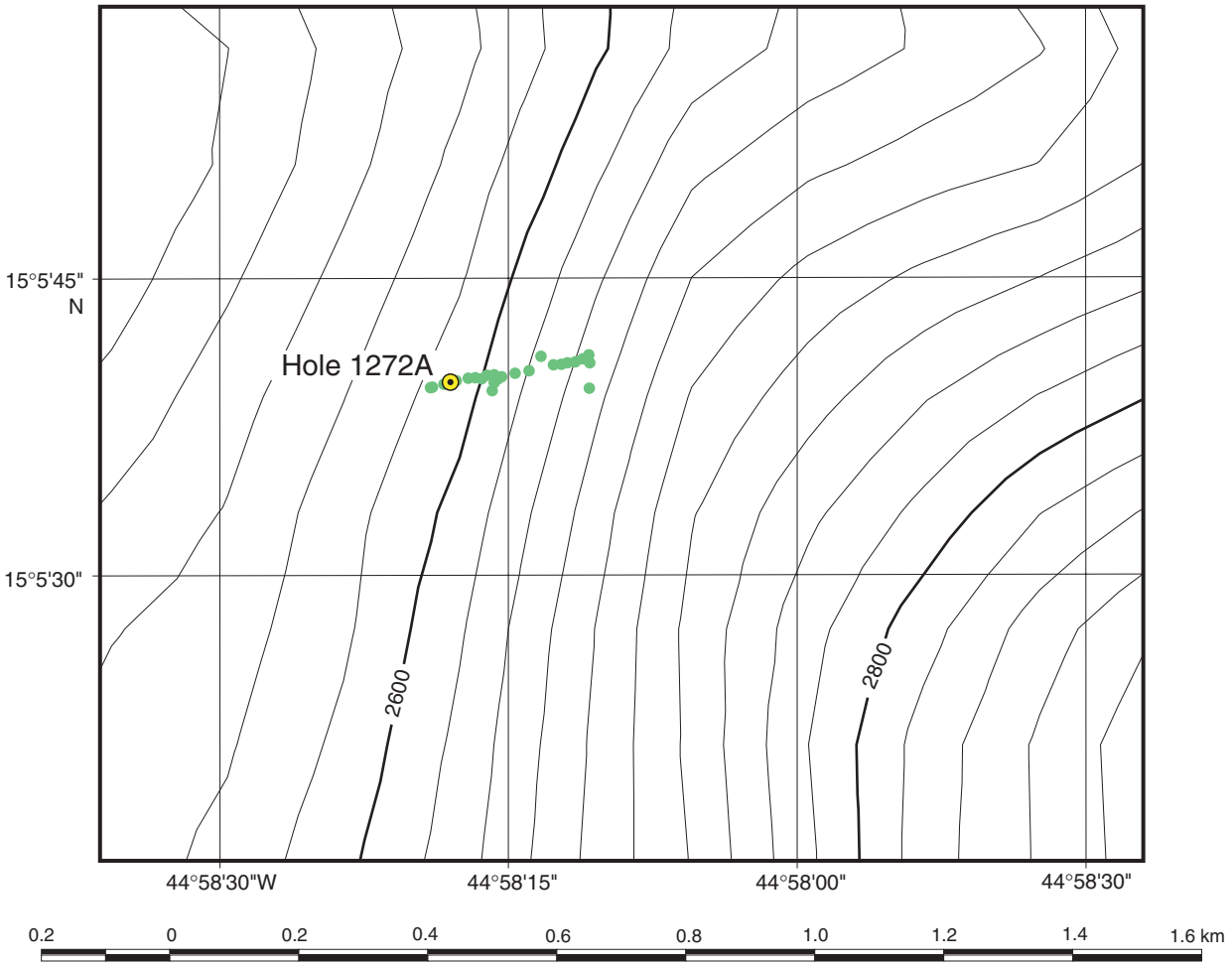

Figure F2. A. Location map with track of *Faranaut* Dive 2 (red line), locations and lithologies of samples from that dive, and the approximate position of Hole 1272A. (Continued on next page.)

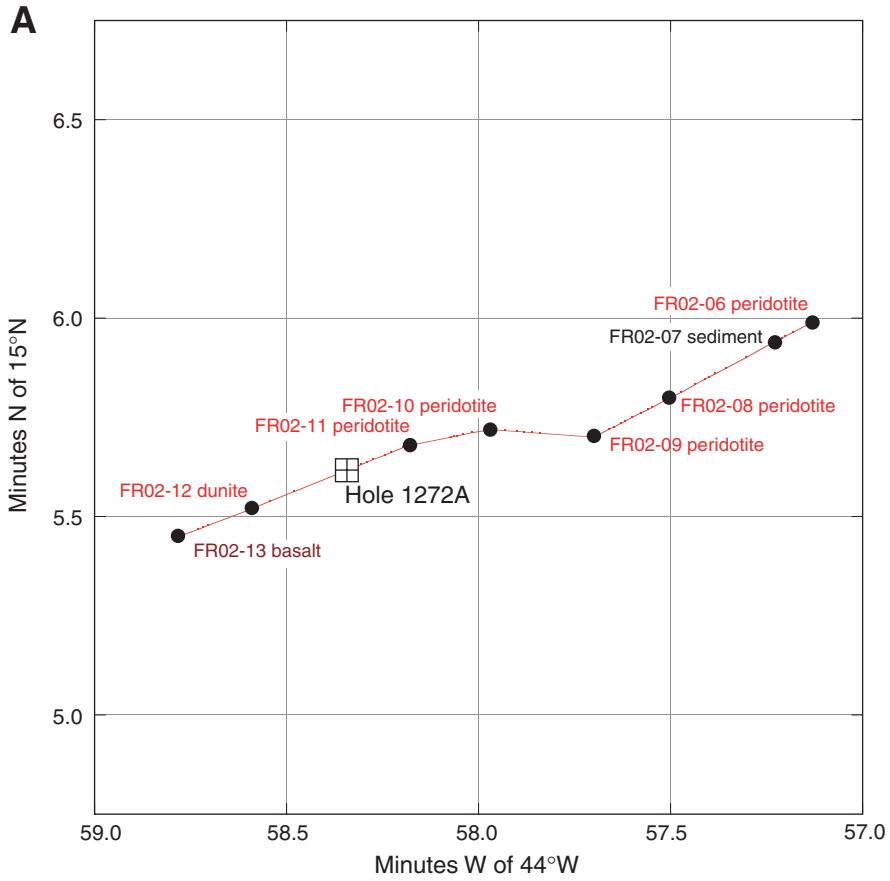

Figure F2 (continued). B. Bathymetric section based on *Faranaut* Dive 2, projected along 248° with no vertical exaggeration. Locations and lithologies of samples collected during the dive and the approximate position of Hole 1272A are indicated.

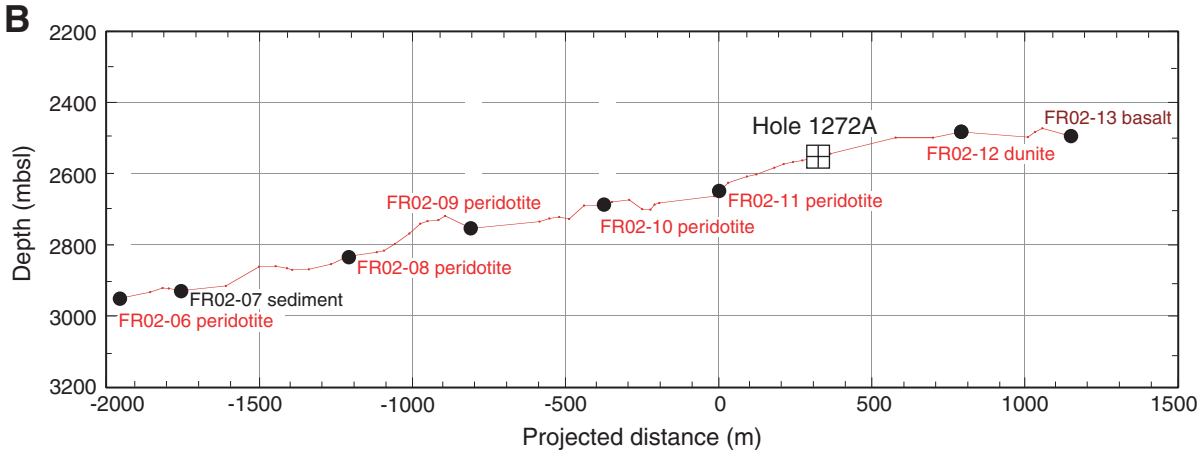

Figure F3. Hole 1272A lithology and stratigraphy and modal orthopyroxene in peridotites. The bars in the modal orthopyroxene column depict the range in orthopyroxene contents in that interval, with broken bars and percentages indicating discontinuous variations in modal proportions. In Unit II, fine-grained mafic rocks (represented as "diabase and microgabbros" in the figure) were recovered only at the top of drilled sections and are interpreted as rubble introduced during drilling. Also noted are the total recoveries of peridotite in each section. TD = total depth.

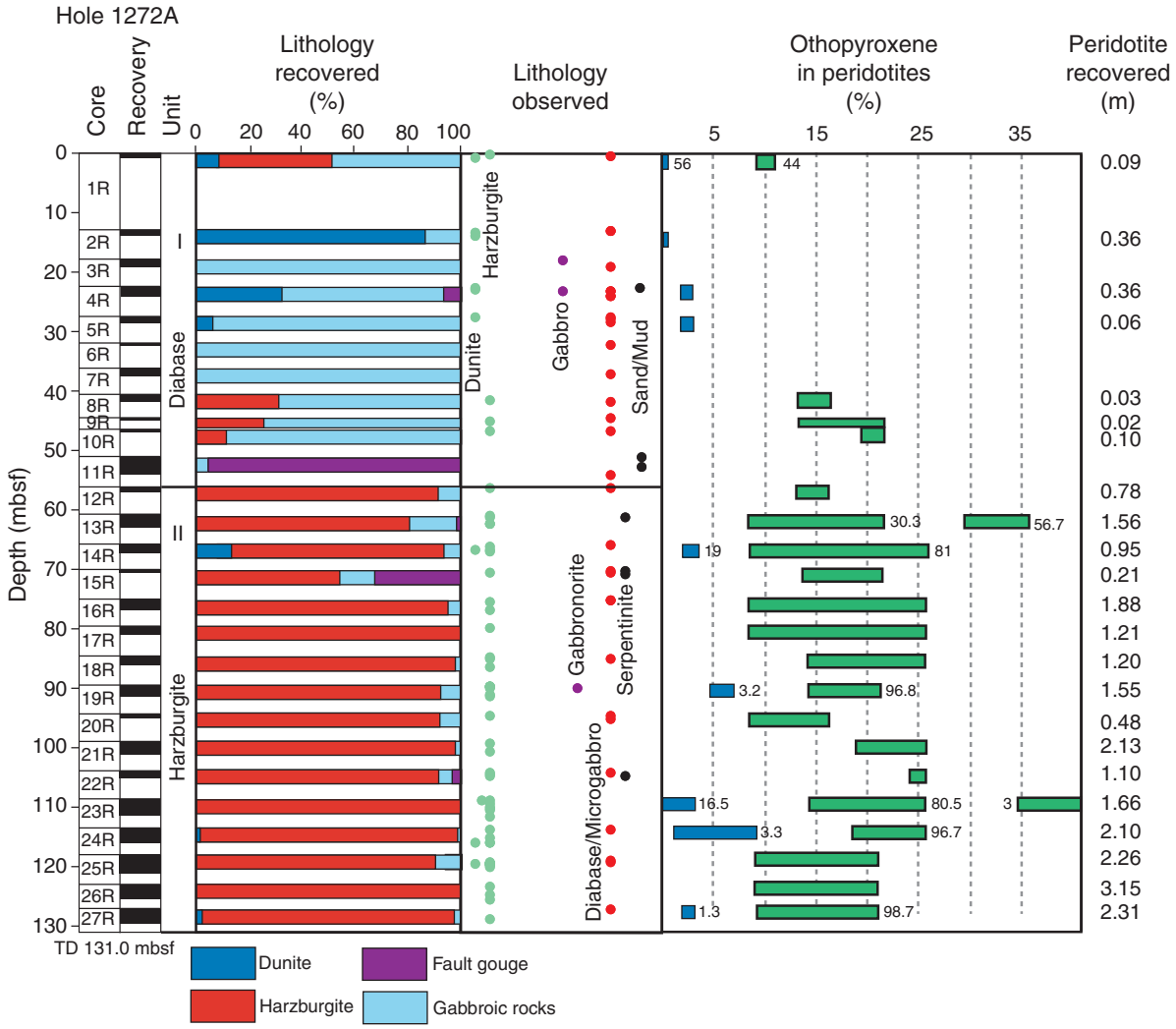

Figure F4. Representation of textures developed in fine-grained mafic rocks. **A.** In this sample the white plagioclase crystals define a through-going network in which the mafic minerals occur intergrown with plagioclase. **B.** In this sample the plagioclase is uniformly distributed in a felty or jack-straw pattern. The texture in A is developed under more slowly cooled conditions and so is distinguished as a microgabbro, whereas the texture in B is indicative of rapid cooling to form a diabase.

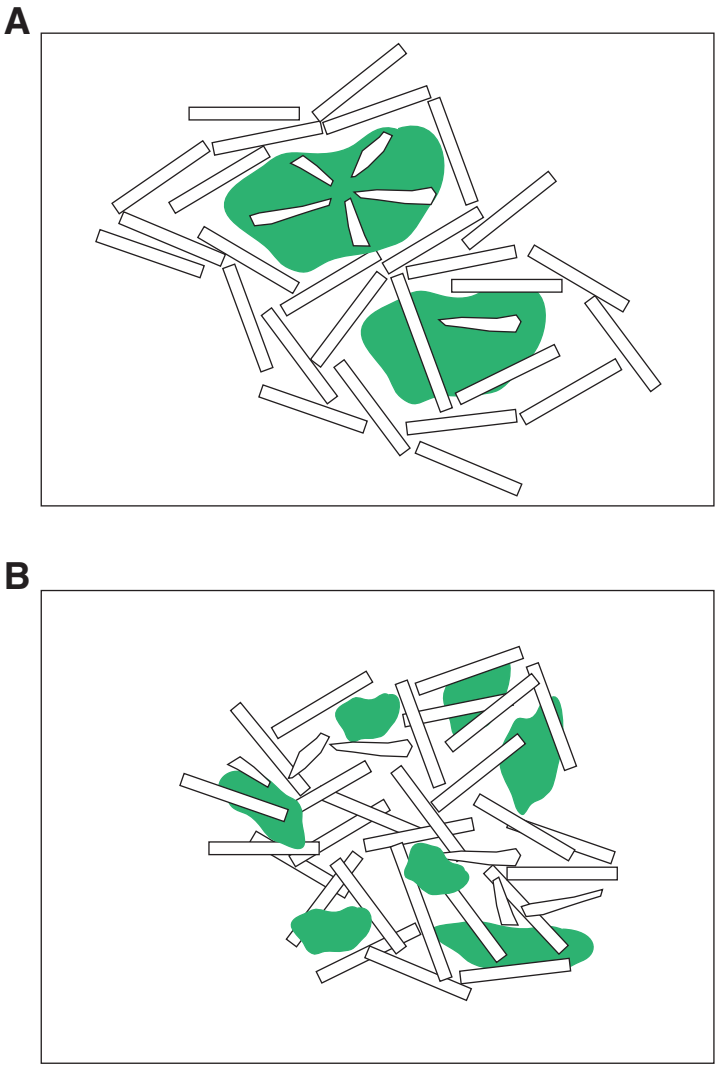

Figure F5. Close-up photographs of dunite (D) areas within harzburgite (H). **A.** Interval 209-1272A-14R-1, 77–87 cm. **B.** Interval 209-1272A-24R-2, 74–84 cm.

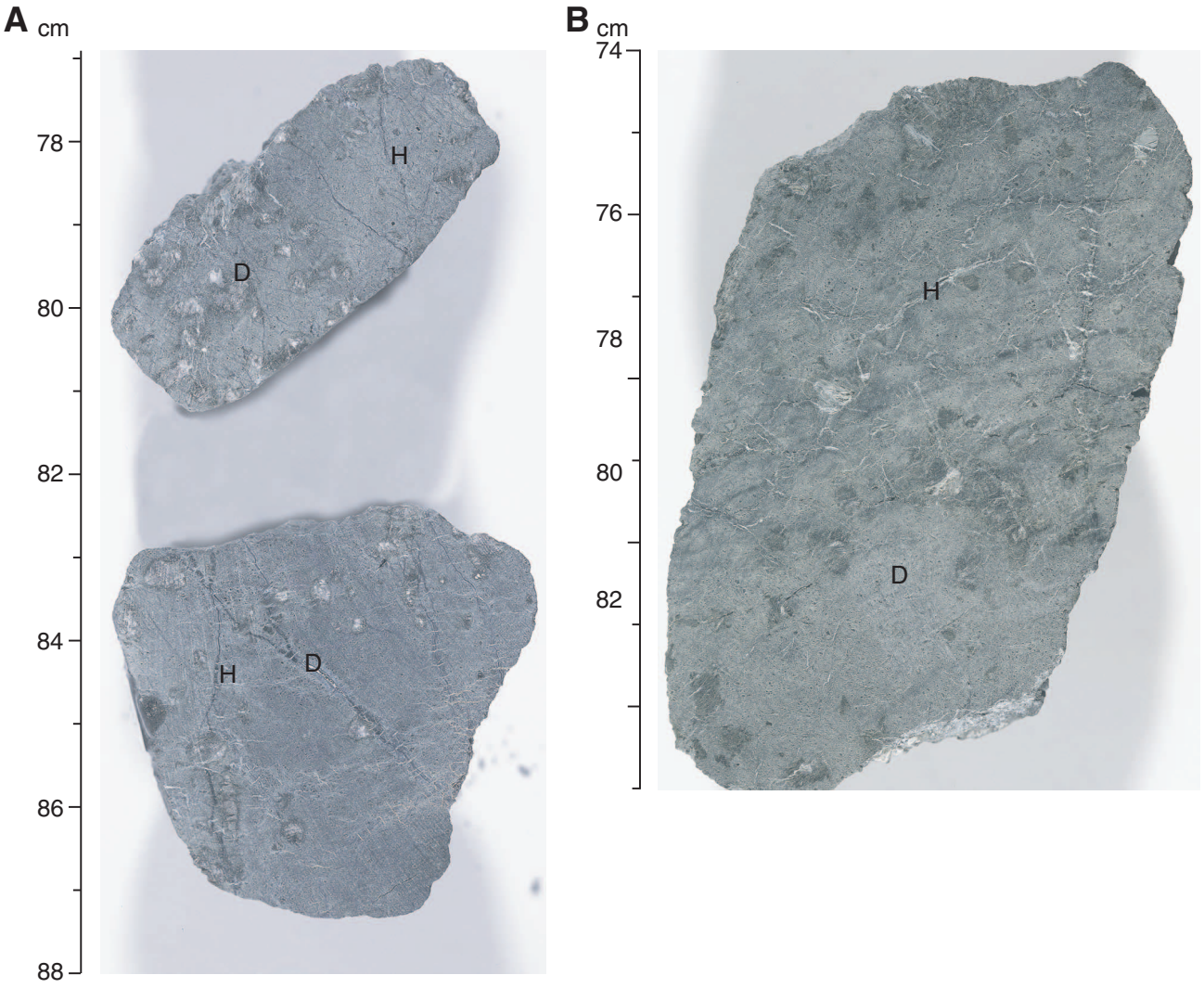

Figure F6. Close-up photograph of alternating bands of dunite (D) and harzburgite (H). Harzburgite at the bottom is enriched in orthopyroxene (opx) (interval 209-1272A-23R-1 [Pieces 2 and 3, 4–71 cm]).

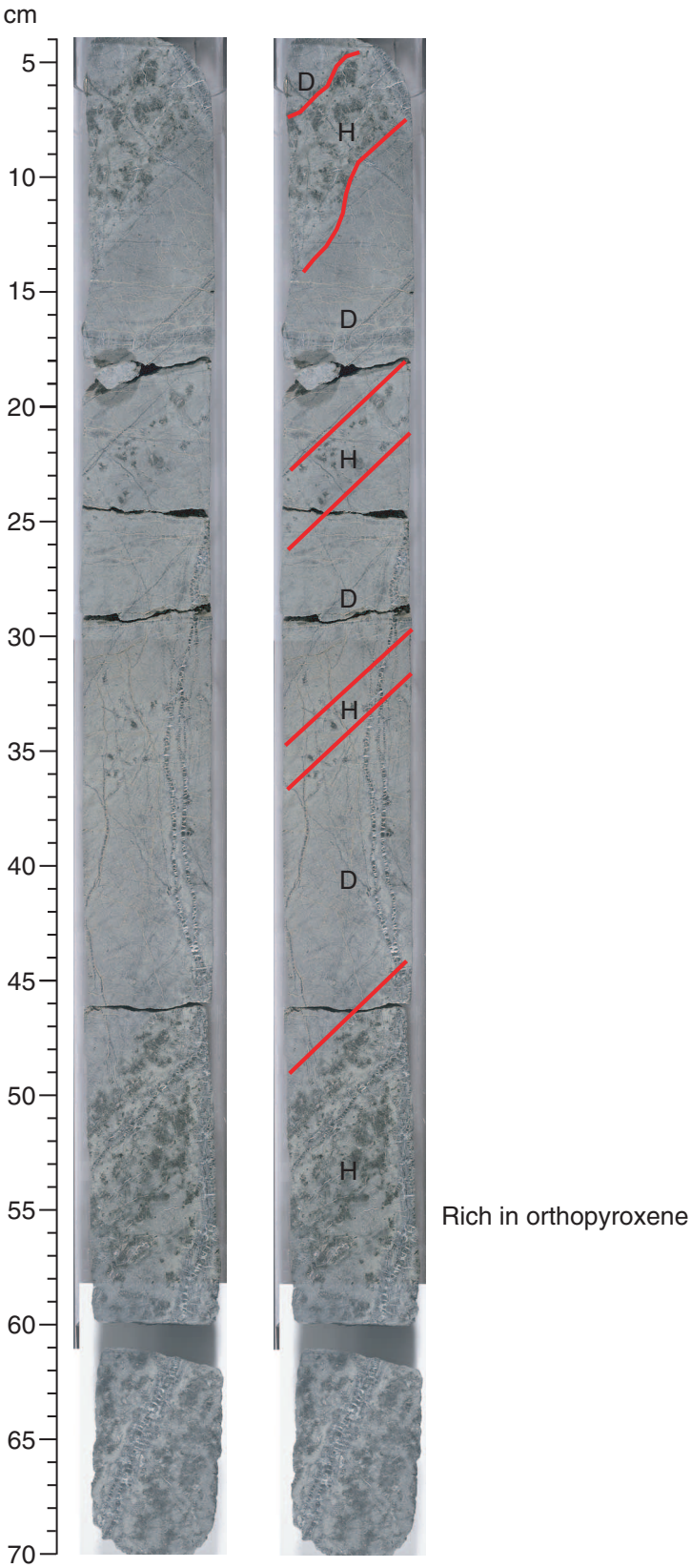

Figure F7. Close-up photographs. **A.** High-temperature foliation (interval 209-1272A-13R-1, 93–117 cm). **B.** Small-scale variations of the orthopyroxene contents (interval 209-1272A-21R-1, 108–133 cm). **C.** Example of orthopyroxene-rich harzburgite (interval 209-1272A-13R-2, 24–41 cm).

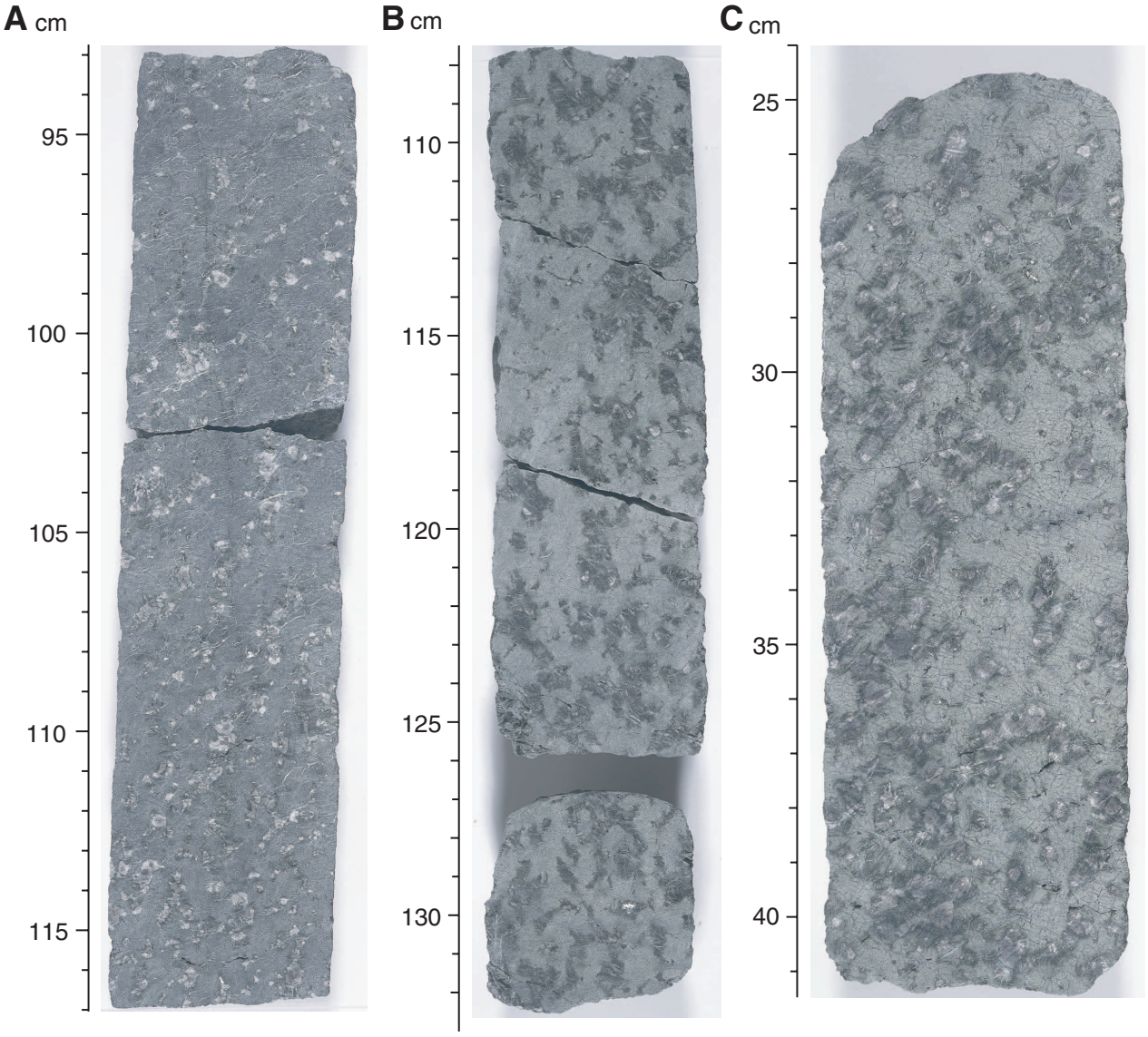

Figure F8. Close-up photographs of orthopyroxene in harzburgite. **A.** Orthopyroxene-poor harzburgite (interval 209-1272A-16R-1, 14–22 cm). **B.** Orthophyroxene-poor harzburgite (interval 209-1272A-21R-1, 46–58 cm). **C.** Orthopyroxene-bearing dunite showing coarse grains of orthopyroxene (interval 209-1272A-19R-1, 0–4 cm).

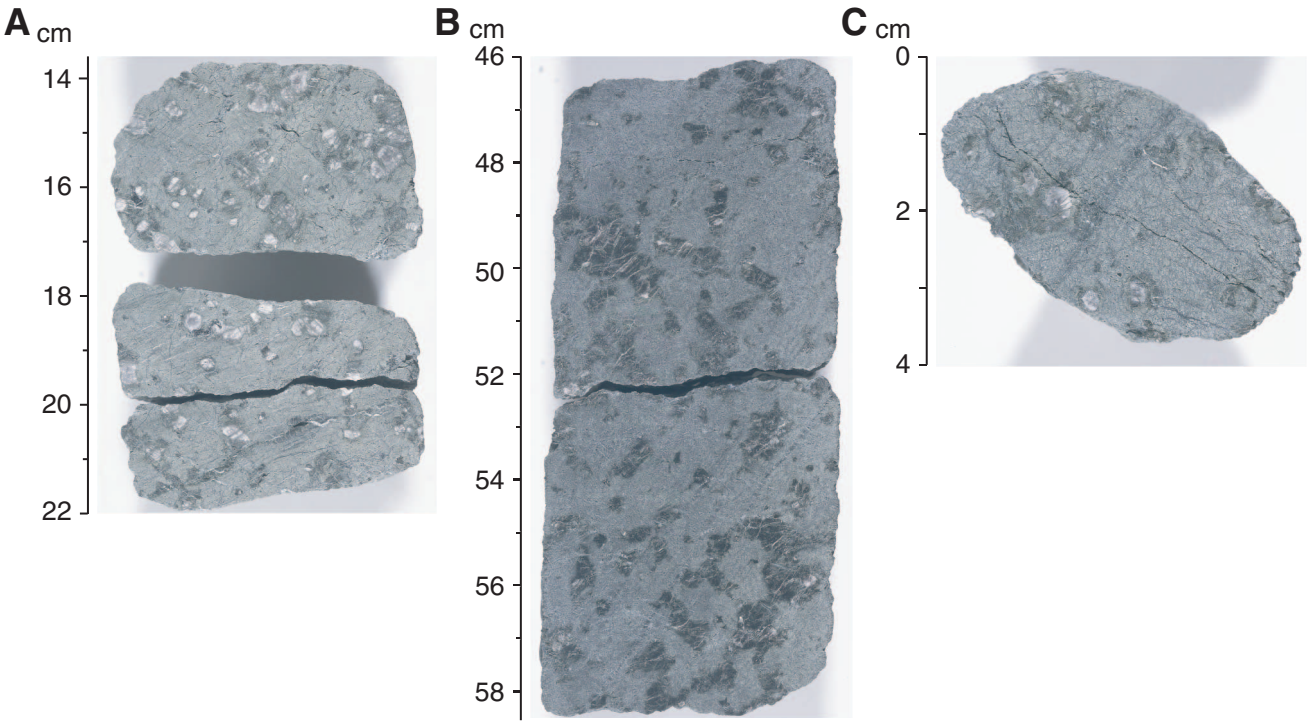

Figure F9. Photomicrographs showing examples of quench textures in fine-grained mafic rocks from Unit I. **A.** Skeletal plagioclase microlites with "hopperlike" crystal habit in spherulitic diabase (Sample **209-1272A-7R-1, 113–115 cm**) (cross-polarized light [XPL]: condenser lens; field of view [FOV] = 0.7 mm; image 1272A_028). **B.** Hollow olivine microlite and plagioclase microlites with swallow tails indicate quench crystallization in the groundmass of spherulitic diabase (Sample **209-1272A-7R-1, 87–89 cm**) (XPL: condenser lens; FOV = 0.7 mm; image 1272A_024). **C.** Very fine hairlike crystals are interwoven in the groundmass of spherulitic diabase (Sample **209-1272A-7R-1, 87–89 cm**) (plane-polarized light: condenser lens; FOV = 0.7 mm; image 1272A_023). **D.** Interpenetrating blades of plagioclase crystals forming a spinnifex-like texture (Sample **209-1272A-7R-1, 113–115 cm**) (XPL: condenser lens; FOV = 1.4 mm; image 1272A_030).

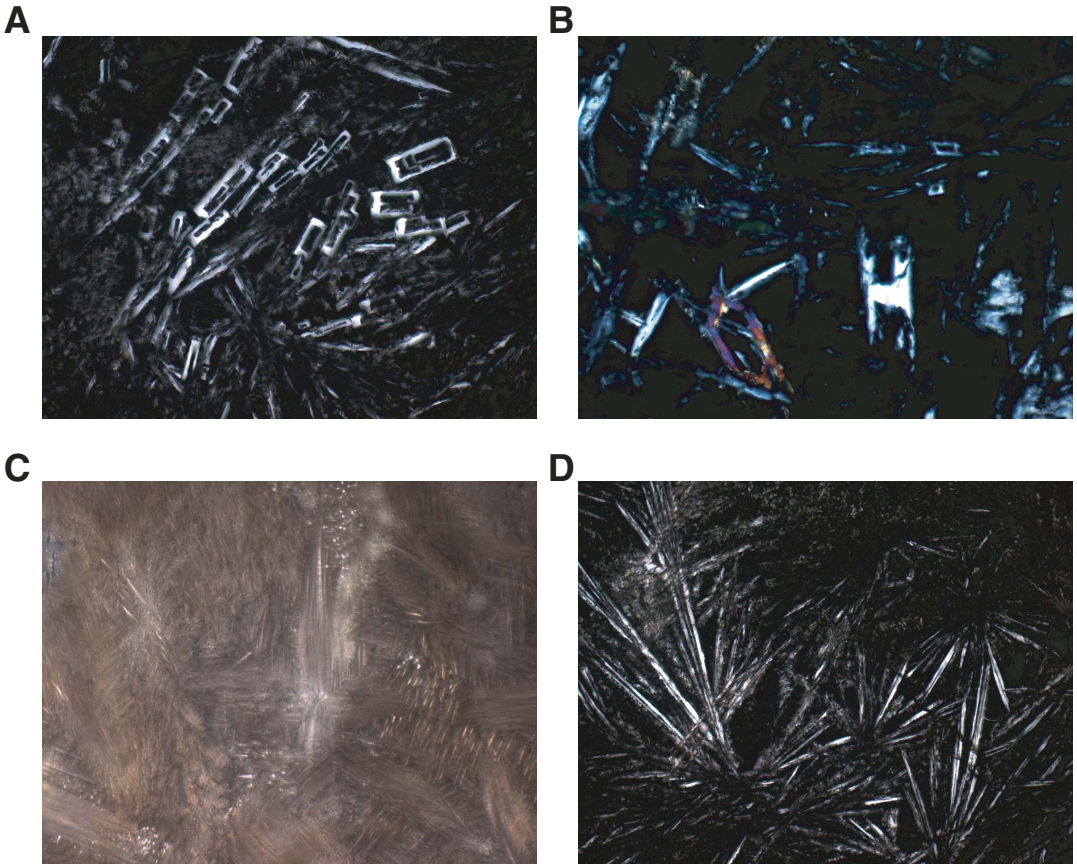

Figure F10. Digital and false color images of the distribution of felsic and mafic domains in the quartz-olivine gabbros compared to the rock images. **A.** A larger portion of the rock that provides a sense of the mafic-rich domains is isolated with a matrix of felsic material (interval 209-1272A-4R-1, 92–111 cm). (Continued on next page.)

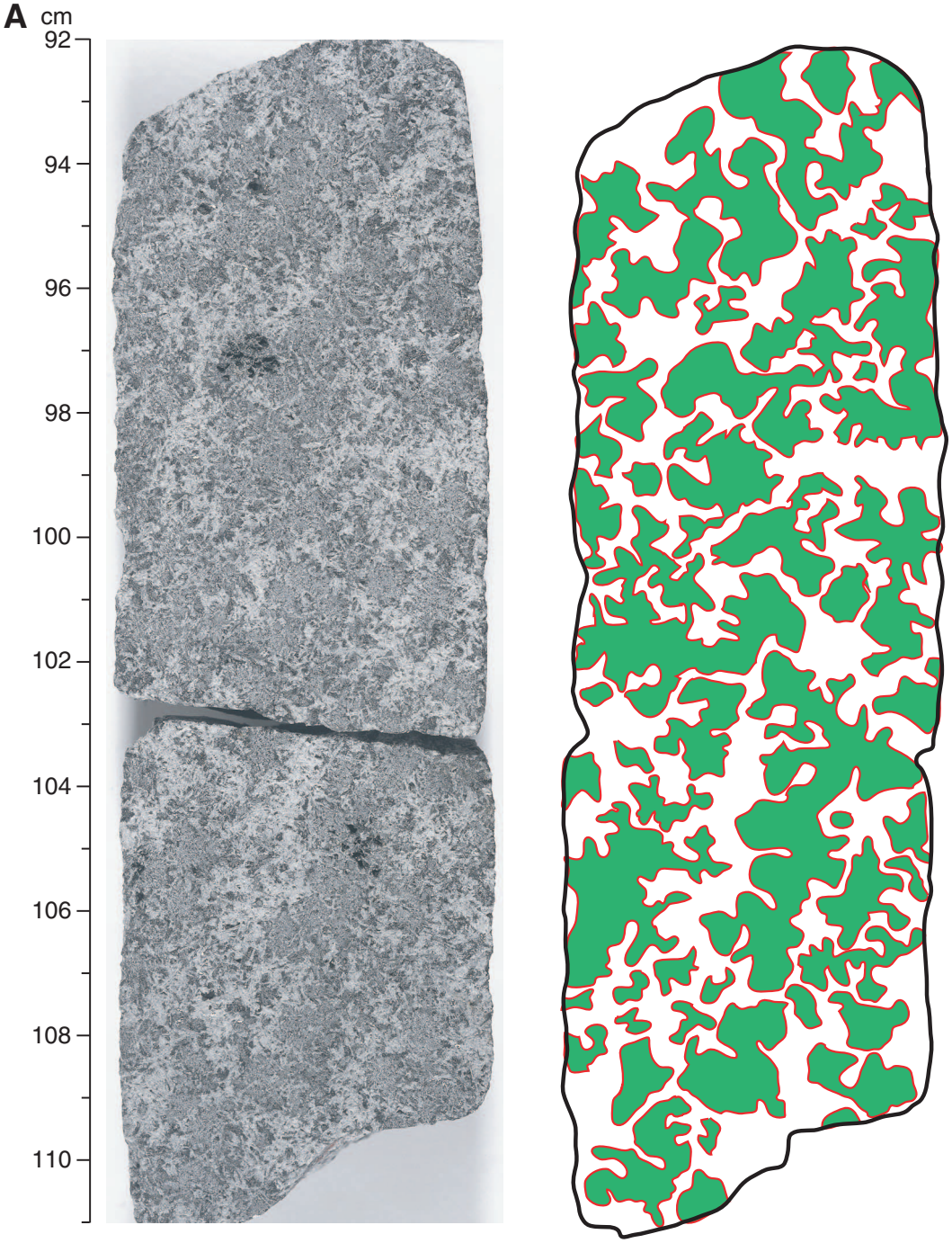

Figure F10 (continued). B. A more detailed view, in which it can be seen that the oxide minerals (darkest in the photo) are preferentially concentrated either within or at the margins of the felsic domains (interval 209-1272A-4R-1, 111–124 cm).

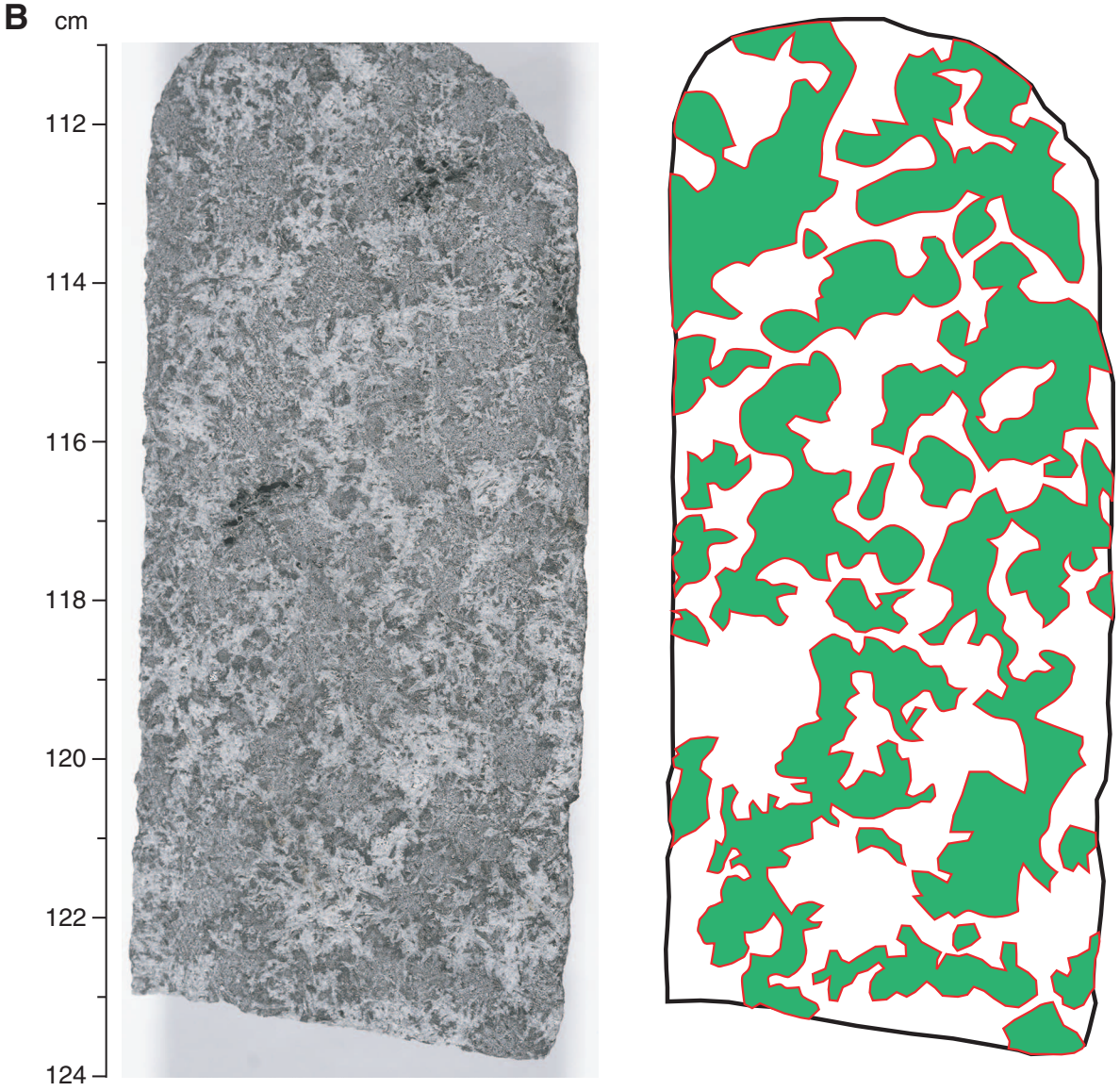

Figure F11. Photomicrographs showing images of an olivine grain (blue) intergrown with a plagioclase grain. The plagioclase crystal is a consistent shade of gray and spans the entire length of the olivine crystal in the field of view (FOV). The olivine is also cut by other large plagioclase crystals. Note the lack of accessory minerals such as quartz, oxides, and apatite (Sample **209-1272A-3R-1, 96–98 cm**). **A.** Cross-polarized light: blue filter; FOV = 2.75 mm; image 1272A_006. **B.** Plane-polarized light: blue filter; FOV = 2.75 mm; image 1272A _007).

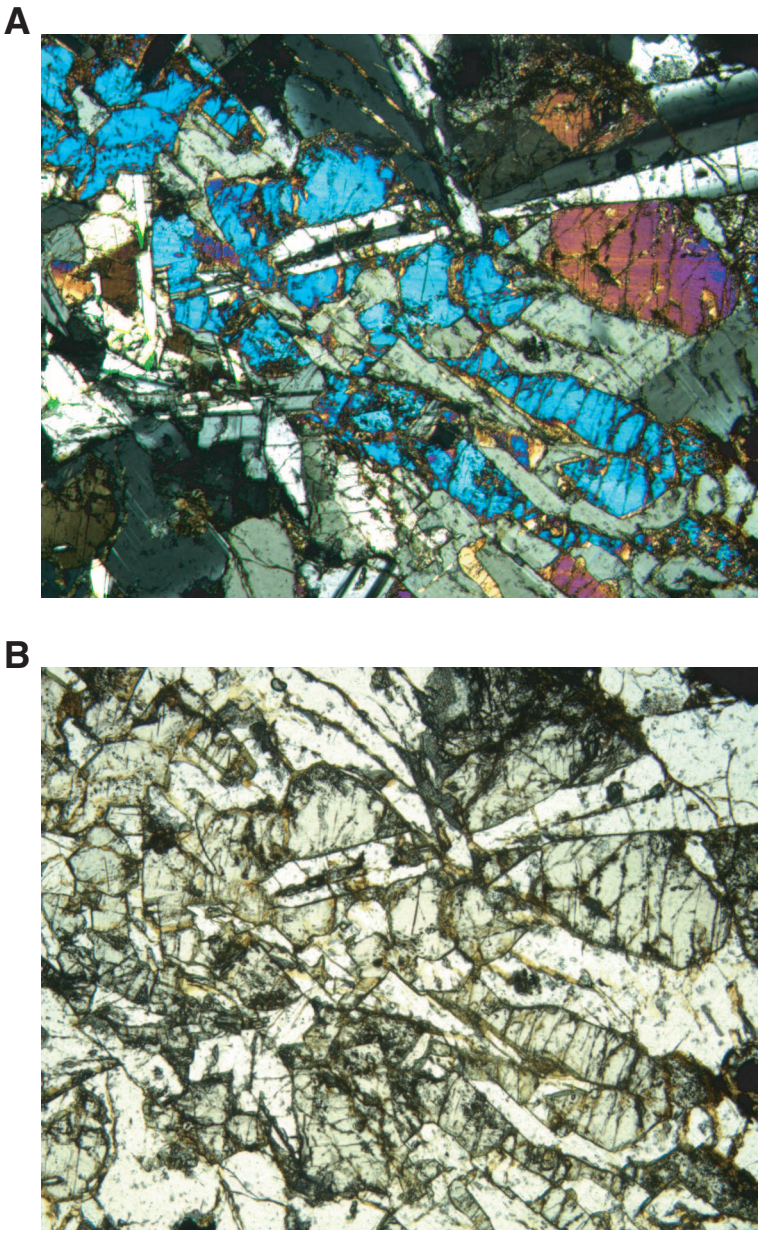

Figure F12. Photomicrographs showing a euhedral, doubly terminated quartz crystal growing into pore space. Also adjoining the pore space are abundant crystals of plagioclase with lesser proportions of oxides and amphibole (on the left side of the pore) (Sample **209-1272A-4R-1, 87–90 cm**). **A.** Plane-polarized light: blue filter/blue + dark gray filter; field of view = 2.75 mm; image 1272A_001. **B.** Cross-polarized light: blue filter; field of view = 2.75 mm; image 1272A_002.

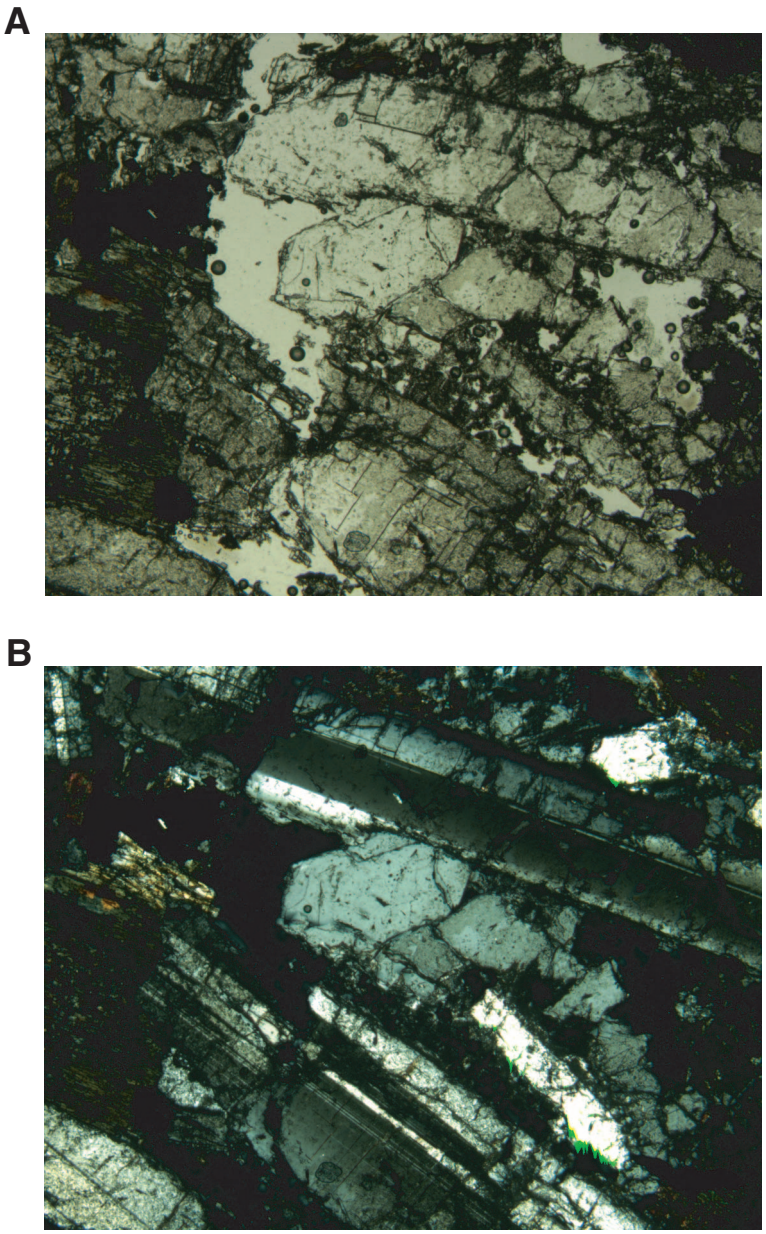

Figure F13. Photomicrograph showing apatite needles in quartz and plagioclase adjacent to a pore space (Sample **209-1272A-4R-1, 87–90 cm**) (plane-polarized light: blue + dark gray filter; field of view = 1.4 mm; image 1272A_003).

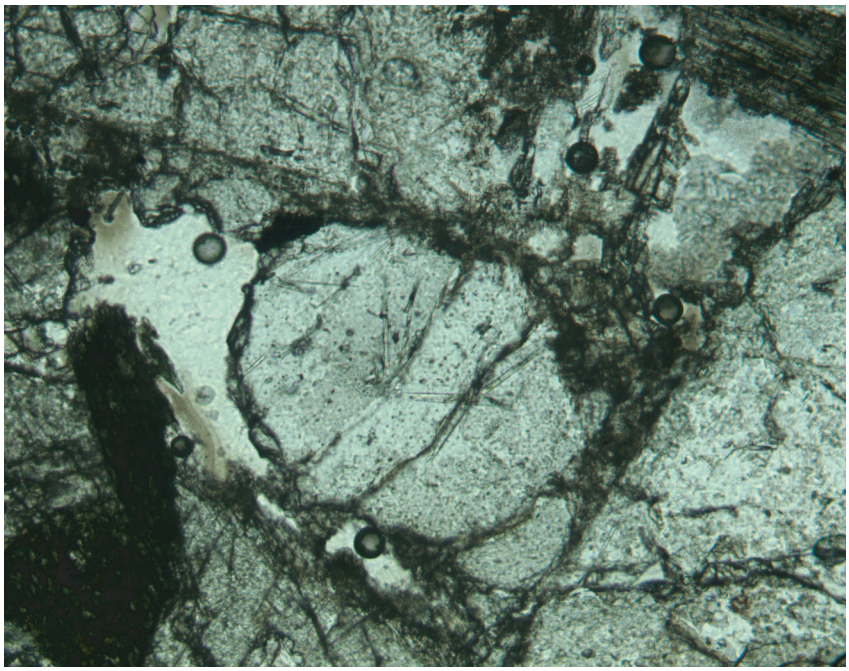

Figure F14. Photomicrograph in cross-polarized and plane-polarized light of an oxide gabbronorite. Shown are large crystals of clinopyroxene (brightly colored on the left), interstitial oxide, orthopyroxene with blue exsolution lamellae of clinopyroxene, and plagioclase (colorless in plane-polarized light). Note the development of neoblasts at the margins of the pyroxene and plagioclase grains (Sample **209-1272A-19R-1, 33–35 cm**) (field of view = 5.5 mm). **A.** Cross-polarized light: blue filter; image 1272A_004. **B.** Plane-polarized light: blue filter; field of view = 1.4 mm; image 1272A_005.

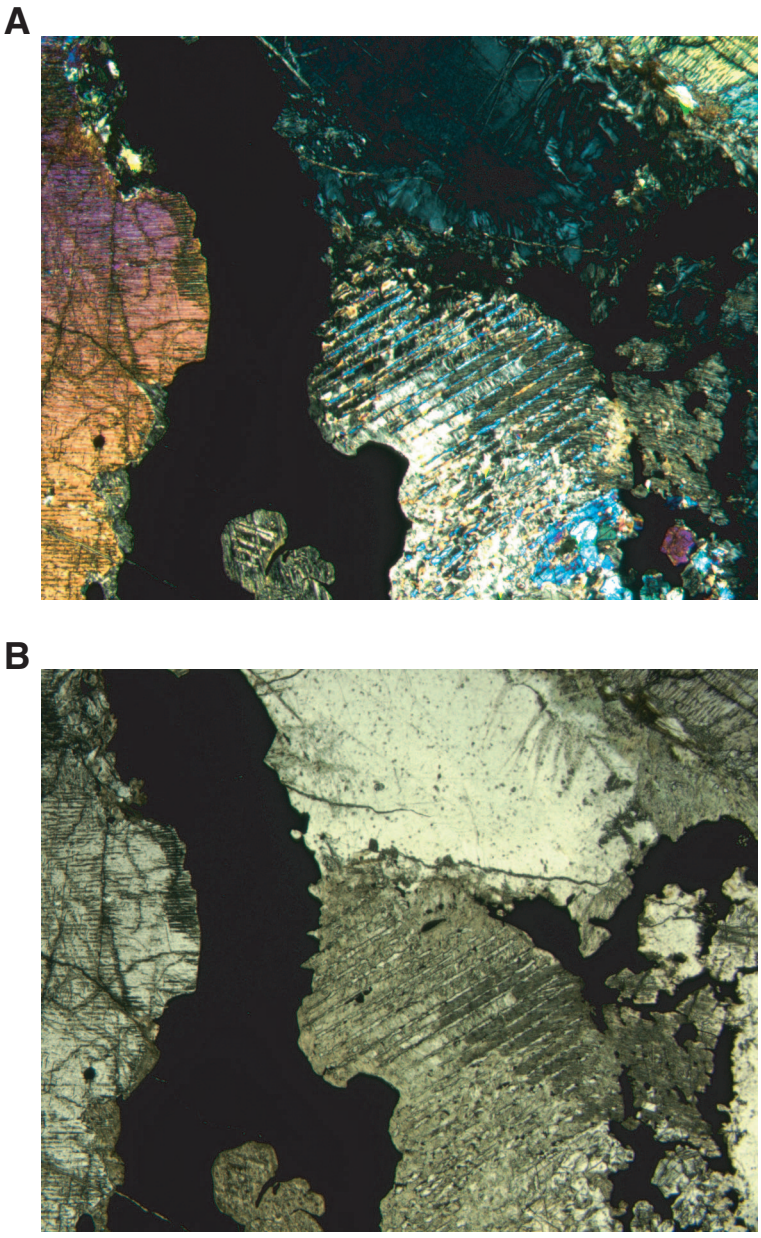

Figure F15. Close-up photographs of examples of textures showing the relationships between olivine and orthopyroxene in hand samples. **A.** Polygonal olivine domains, 6–13 mm, are surrounded by interstitial orthopyroxenes (interval 209-1272A-14R-1, 44–50 cm). **B.** Orthopyroxene crystals are interstitial between olivine domains in the lower half. In the upper half, they form two clusters that occupy area as large as olivine domains (interval 209-1272A-21R-2, 20–26 cm). **C.** An elongated orthopyroxene grain is present at 38–40 cm (interval 209-1272A-24R-2, 35–47 cm). **D.** Small orthopyroxene clusters and elongated interstitial orthopyroxene enclose olivine domains (interval 209-1272A-21R-2, 13–19 cm).

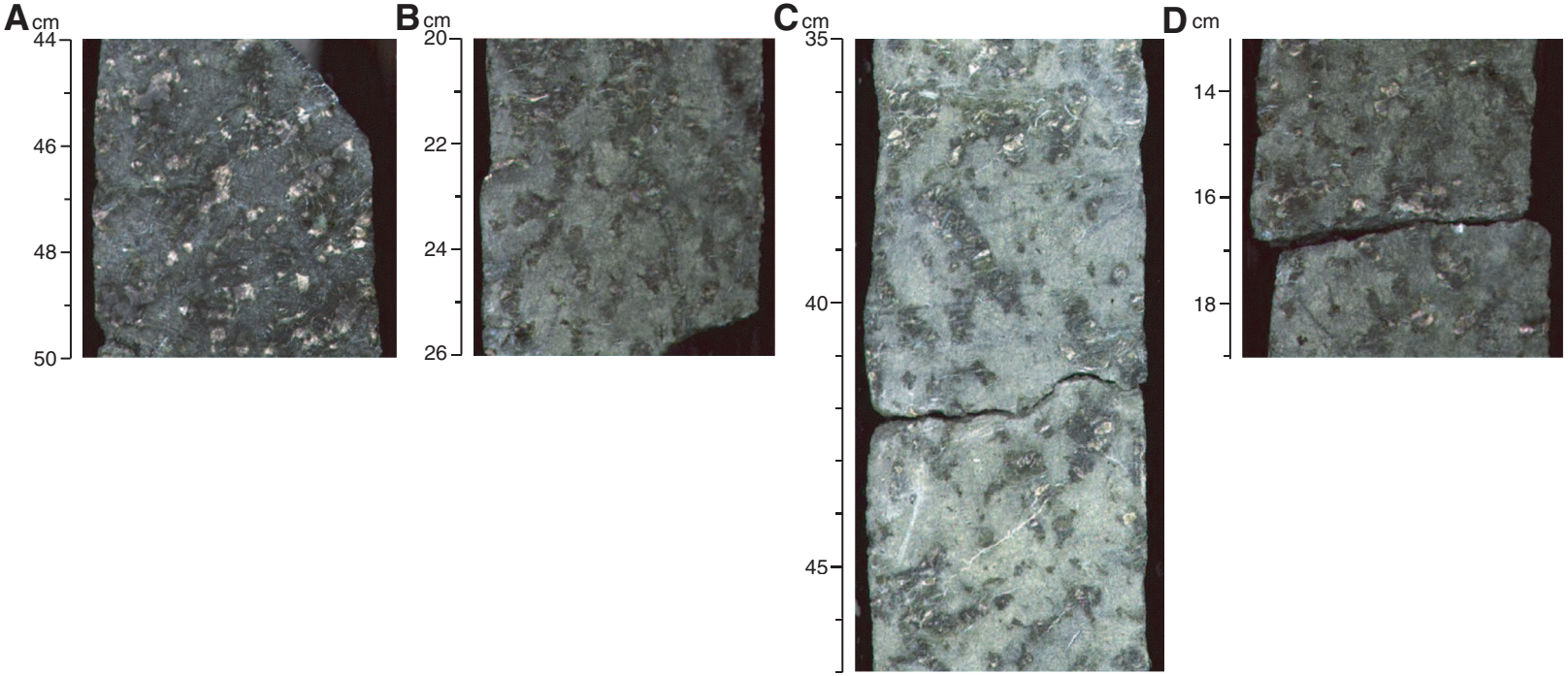

Figure F16. Photomicrographs showing olivine and orthopyroxene relationships. **A.** Smoothly curved olivine/orthopyroxene grain boundary (Sample **209-1272A-27R-1, 50–52 cm**) (cross-polarized light [XPL]; field of view [FOV] = 2.75 mm; image 1272A_034). **B.** Curved orthopyroxene partially enclosing olivine grains at its left border (Sample **209-1272A-13R-2, 33–36 cm**) (XPL; FOV = 2.75 mm; image 1272A_033). **C.** Anhedral, equant orthopyroxene enclosing an olivine grain (Sample **209-1272A-25R-1, 123–126 cm**) (XPL; FOV = 5.5 mm; image 1272A_035). **D.** Orthopyroxene interstitial between four olivine grains (Sample **209-1272A-13R-2, 33–36 cm**) (XPL; FOV = 2.75 mm; image 1272A_031). E. Orthopyroxene partially interstitial due to deep olivine embayments (Sample **209-1272A-18R-1, 46–48 cm**) (XPL: blue filter; FOV = 2.75 mm; image 1272A_016).

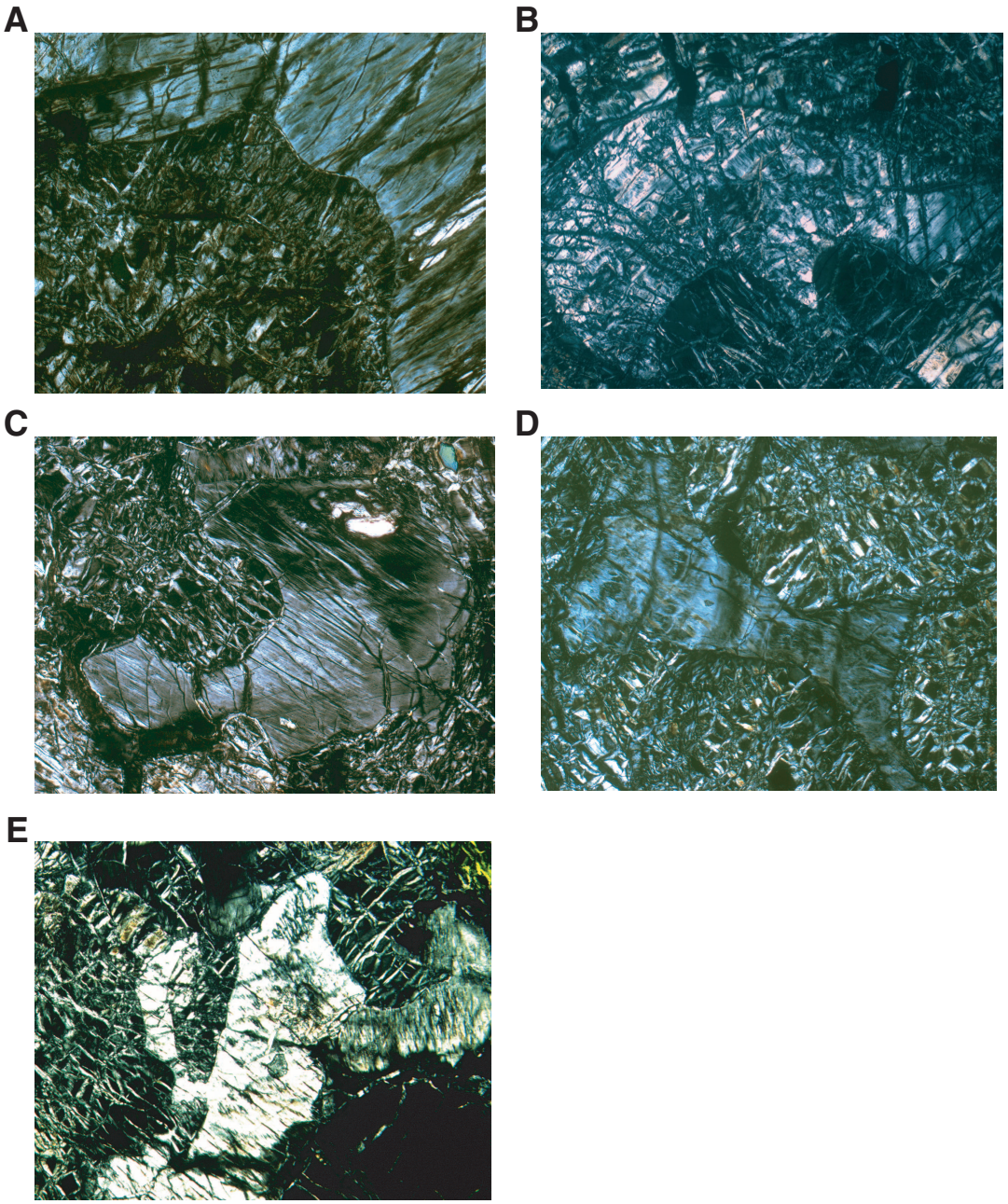

Figure F17. Photomicrographs showing clinopyroxene and orthopyroxene relationships. **A.** Clinopyroxene-filled triple junction between orthopyroxene crystals (Sample **209-1272A-27R-1, 123–126 cm**) (cross-polarized light [XPL]: blue filter; field of view [FOV] = 1.4 mm; image 1272A_020). **B.** Smoothly curved contact between two orthopyroxenes with intergranular clinopyroxene (pointed by an arrow); a clinopyroxene lamellae (outlined in white) grew in the left orthopyroxene (Sample **209-1272A-18R-1, 46–48 cm**) (XPL: blue filter; FOV = 0.7 mm; image 1272A_017). **C, D.** Sample **209-1272A-17R-1, 127–129 cm;** (C) clinopyroxene at an orthopyroxene grain boundary (XPL; FOV = 0.7 mm; image 1272A_018); (D) clinopyroxene at an orthopyroxene grain boundary (XPL: blue filter; FOV = 1.4 mm; image 1272A_019).

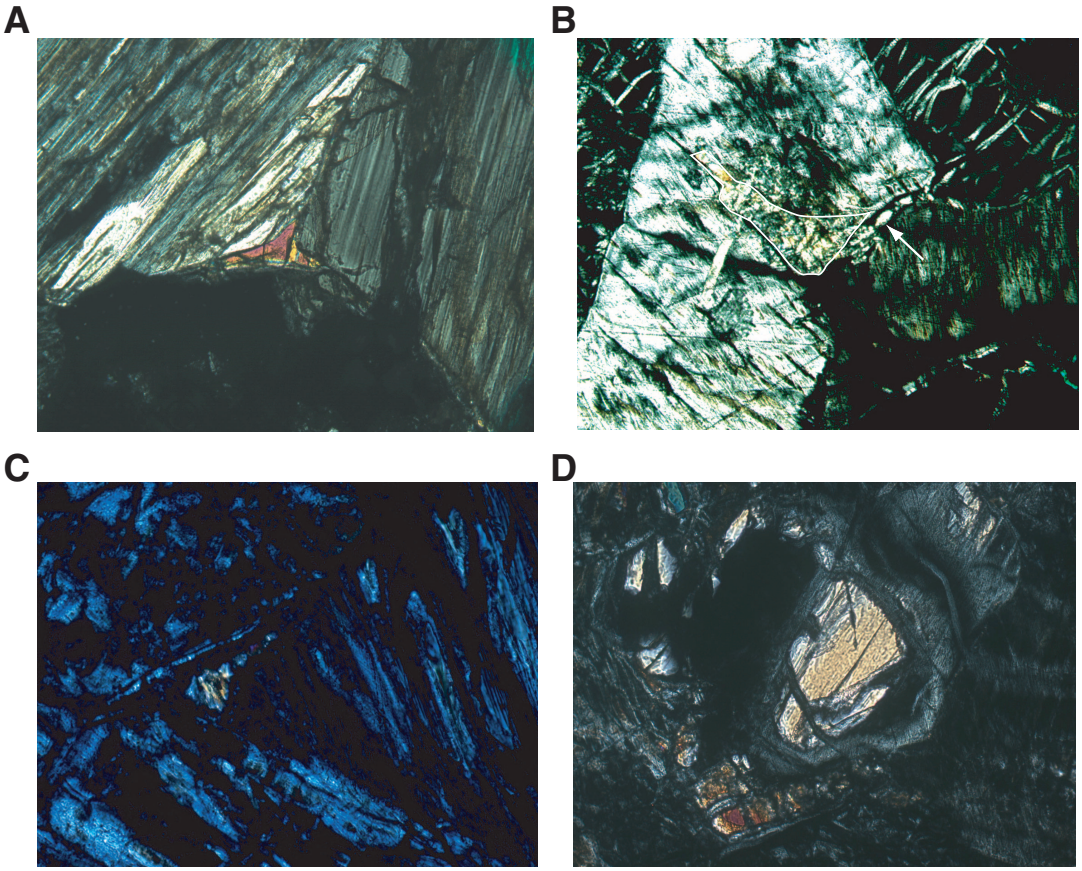

Figure F18. Photomicrographs showing symplectic intergrowths involving spinel at orthopyroxene margins. **A, B.** Sample 209-1272A-27R-1, 136–138 cm. (A) Plane-polarized light (PPL): blue filter; field of view (FOV) = 2.75 mm; image 1272A_021. (B) Cross-polarized light (XPL): blue filter; FOV = 2.75 mm; image 1272A_022. **C–E.** Olivine enclosed in spinel. (C) Sample 209-1272A-13R-2, 33–36 cm (PPL; FOV = 1.4 mm; image 1272A_032). (D) Sample 209-1272A-17R-1, 127–129 cm (PPL; FOV = 1.4 mm; image 1272A_037). (E) close-up of image D showing two grains almost totally enclosed in spinel that resemble serpentinized olivine (PPL; FOV =2.75 mm; image 1272A_038). **F.** Polygon-shaped intergrowth (close-up of image A) (Sample 209-1272A-17R-1, 127–129 cm) (PPL; FOV = 1.4 mm; image 1272A_036).

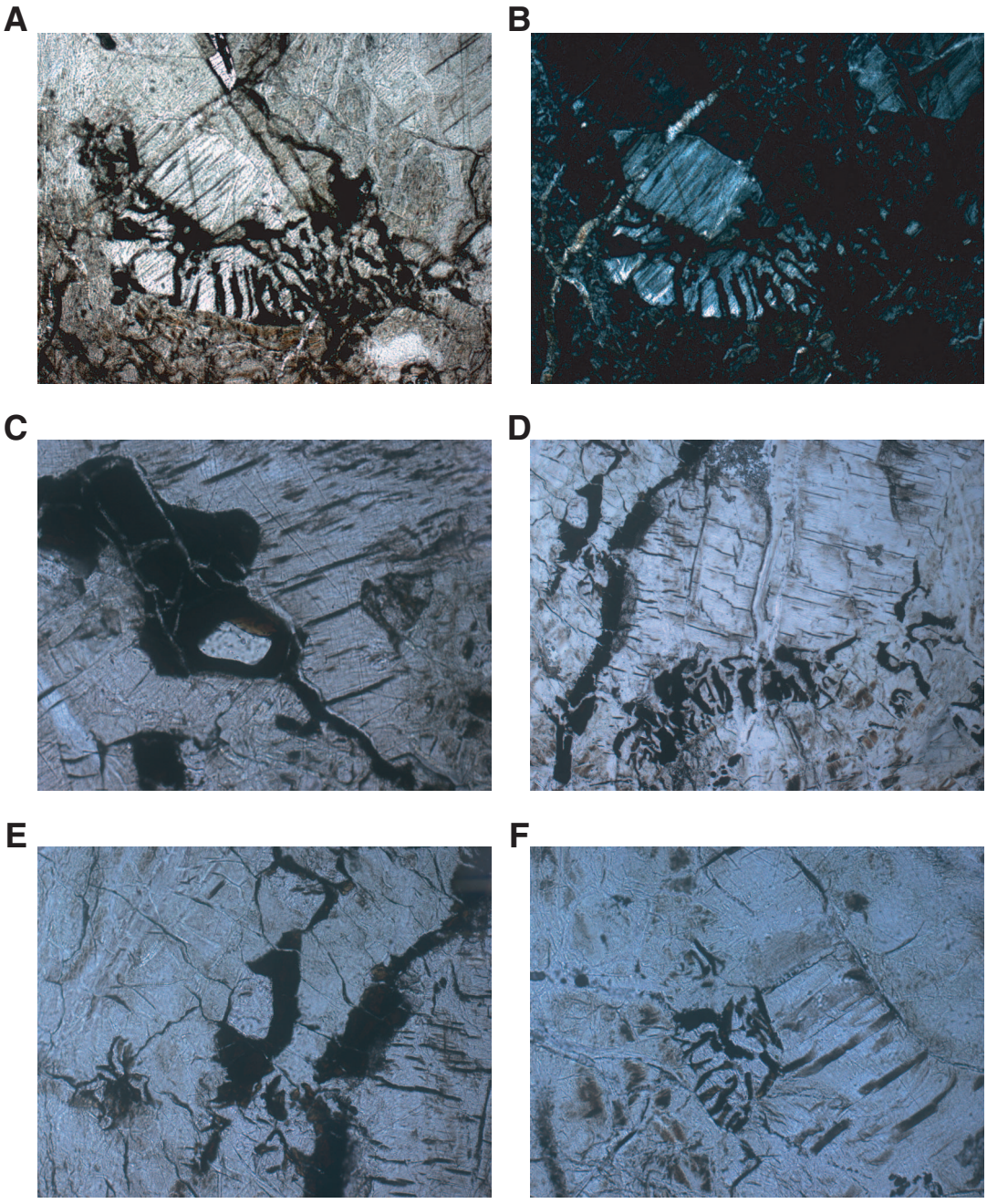

Figure F19. Photomicrographs showing orthopyroxene/spinel relationships (Sample 209-1272A-23R-1, 7–11 cm). **A, B.** Plane-polarized light (PPL); field of view (FOV) = 2.75 mm; (A) harzburgite at the contact with dunite (image 1272A_039); (B) euhedral spinel in orthopyroxene (image 1272A_040). **C.** Orthopyroxene with spinel intergrowth at the border; the latter partially recrystallized into blocky spinel (PPL; FOV = 1.4 mm; image 1272A_042). **D.** Partially recrystallized spinel associated with orthopyroxene (PPL; FOV = 2.75 mm; image 1272A_041).

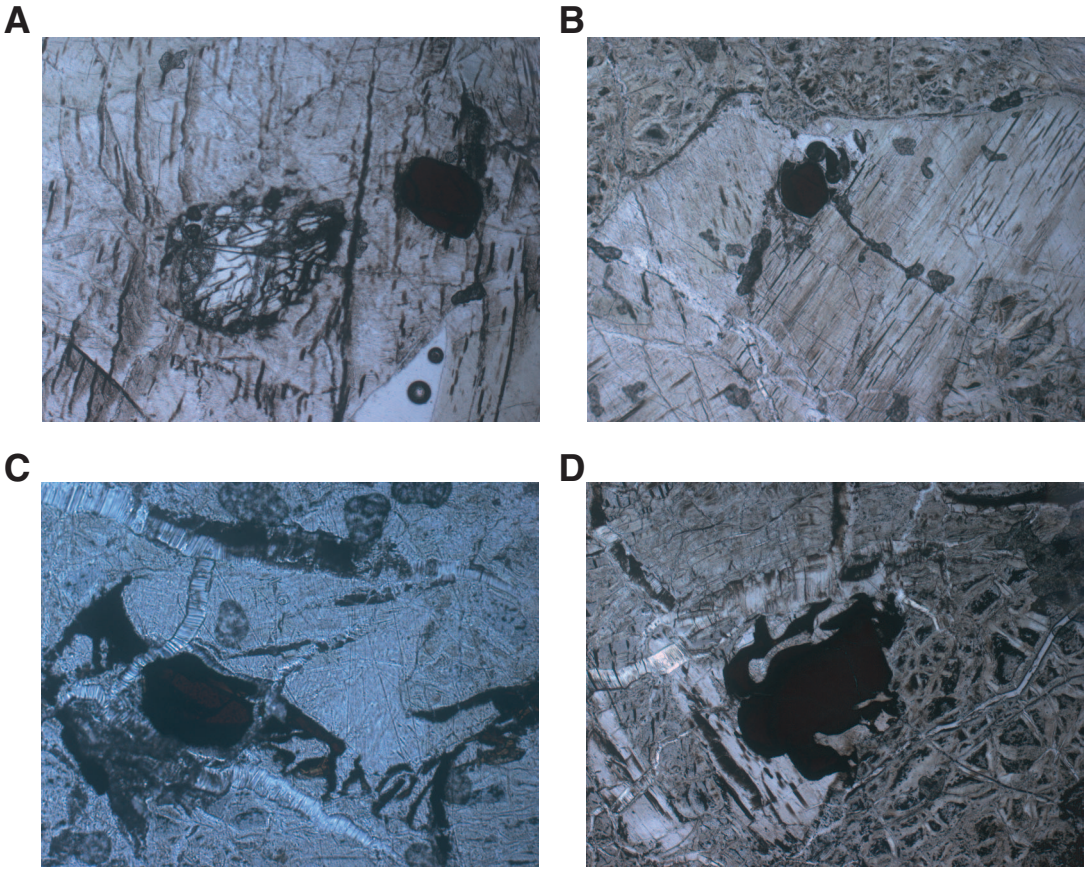

Figure F20. A. Close-up photograph of interval 209-1272A-23R-1, 62–70.5 cm. **B.** XRD spectrum of interval 209-1272A-23R-1, 67–69 cm (arrow indicates the approximate position of the analyzed powder). Note the positive identification of serpentine, magnetite, brucite, and iowaite. See text for discussion.

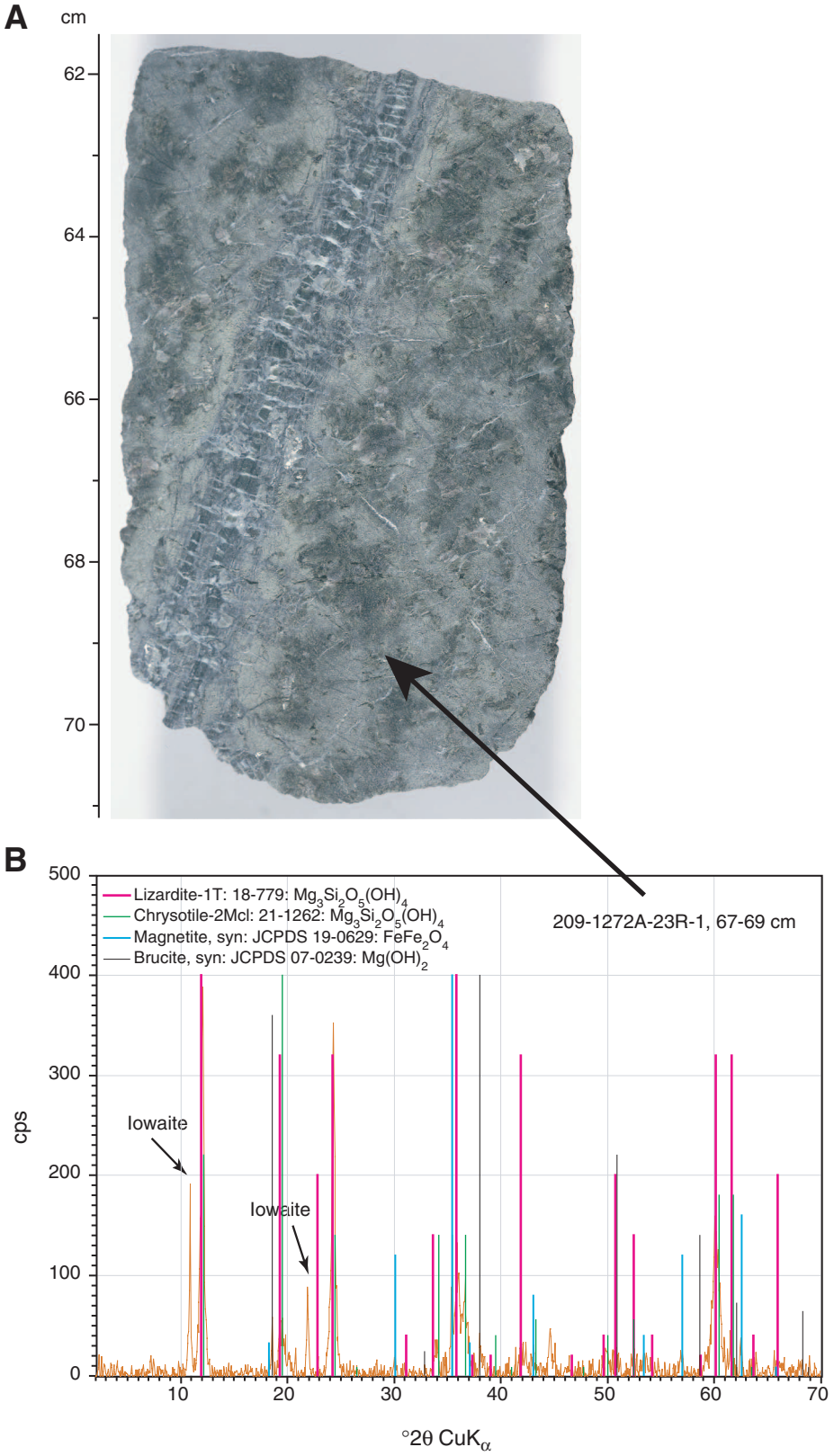

Figure F21. Photomicrograph showing ribbon-textured α-serpentine wrapped around bastite (Sample 209-1272A-21R-1, 50–53 cm) (cross-polarized light: blue + gray filters; field of view = 2.75 mm; image 1272A_013).

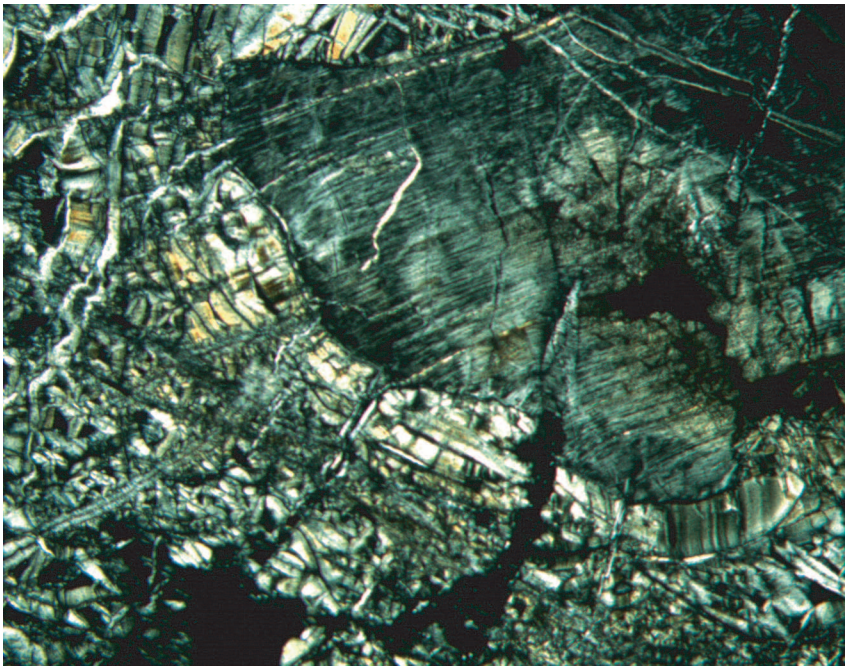

Figure F22. Plot of intensity of alteration vs. depth. Also shown are downhole variations in thermal conductivity, density, and porosity. Note that the decrease in background alteration intensity in the lowermost 20 m of Hole 1272A coincides with increases in thermal conductivity and density and a decrease in porosity. TD = total depth. Opx = orthopyroxene, ol = olivine. TS = thin section.

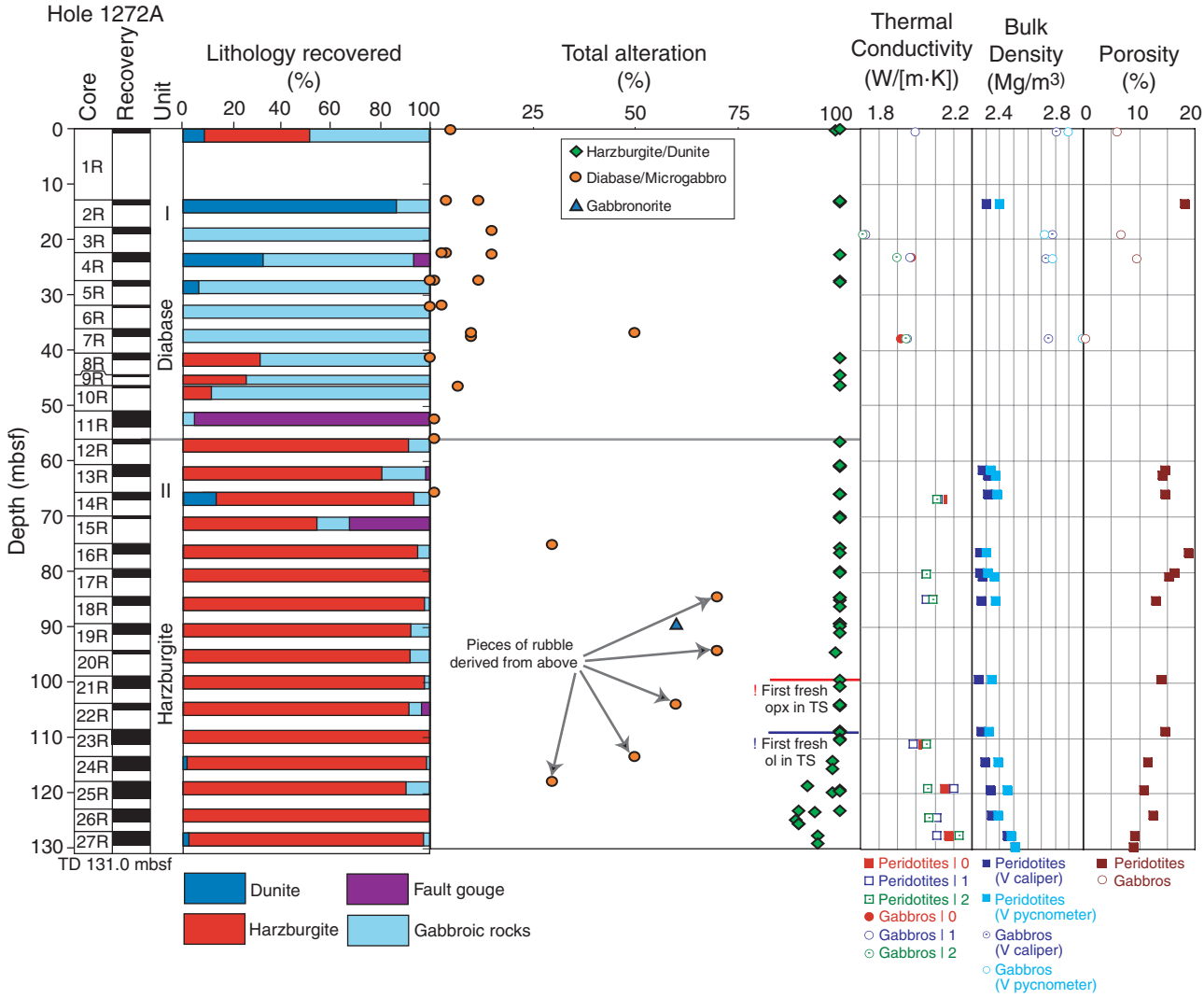

Figure F23. A. Close-up photograph of an oxidatively altered, aragonite-veined dunite (interval 209-1272A-2R-1, 60.5–72.5 cm). **B.** XRD spectrum of Sample 209-1272A-2R-1, 61–63 cm, showing significant proportions of aragonite along with serpentine and magnetite.

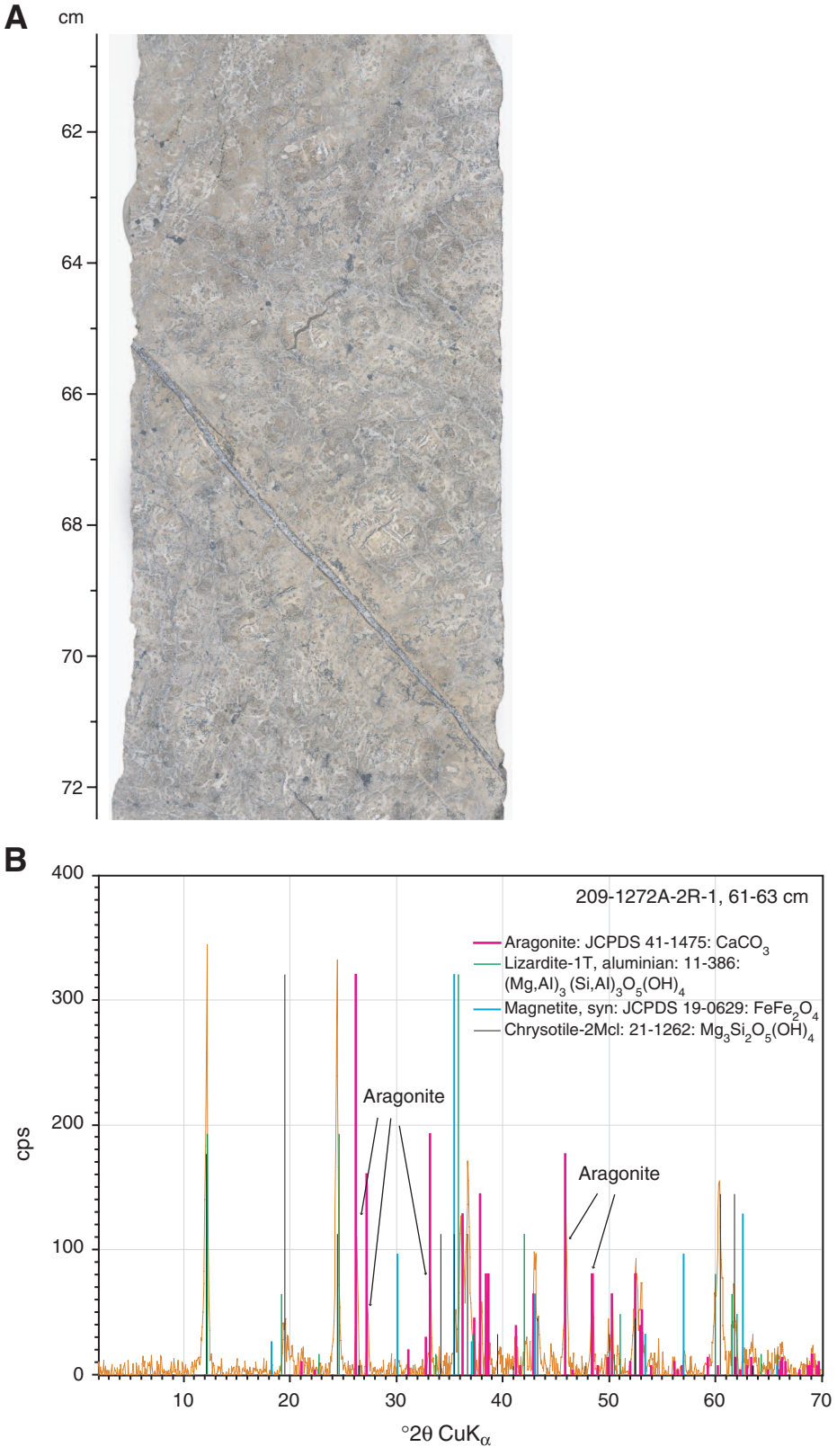

Figure F24. Photomicrograph showing coarse euhedral magnetite grains in the centers of a serpentine mesh-rim texture (Sample **209-1272A-21R-1, 50–53 cm**) (mixed reflected and transmitted light; cross-polarized light: blue + gray filters; field of view = 1.4 mm; image 1272A_014).

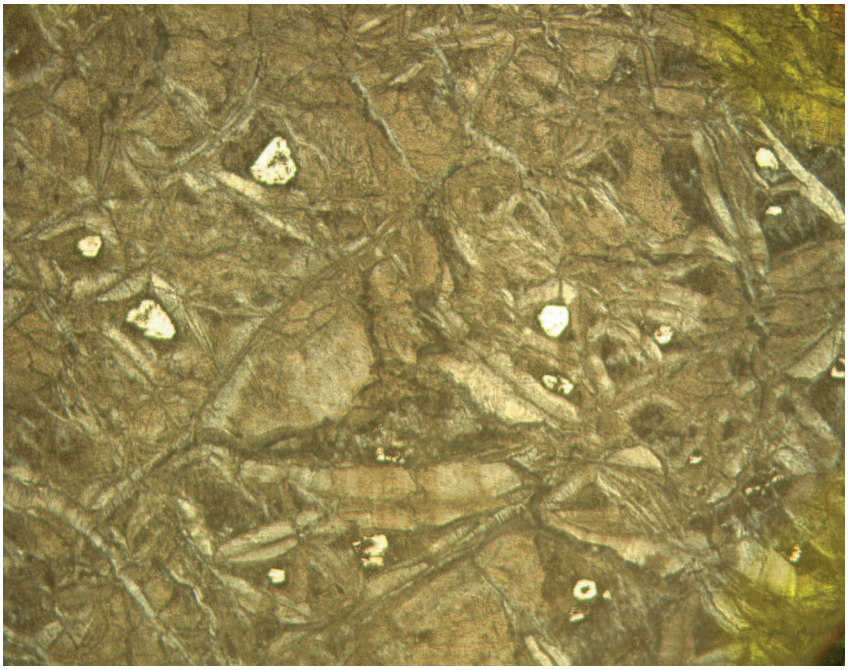

Figure F25. Series of XRD spectra for Sample 209-1272A-23R-1, 67–69 cm, after (**A**) freeze drying, (**B**) glycolization, and (**C**) heating to 370°C. Note that the iowaite peaks at 8.14 and 4.07 Å did not shift after glycolization and that these peaks disappear after heating the sample to 370°C.

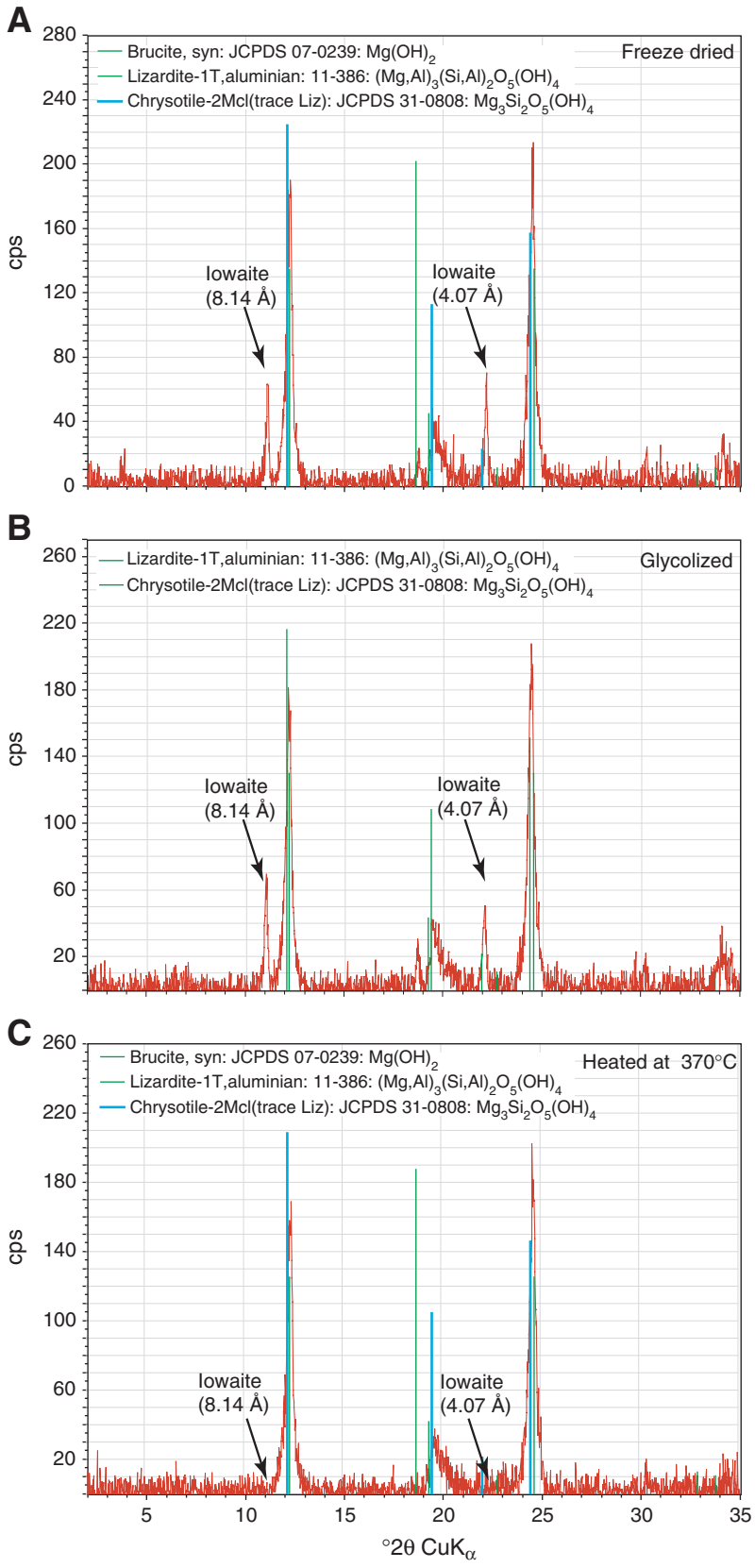

Figure F26. Photomicrograph showing a patch of talc, chlorite-smectite (in center), and magnetite in medium-grained gabbro. The formation of talc and magnetite after olivine is typical in low-grade metagabbros (Sample **209-1272A-1R-1, 41–43 cm**) (cross-polarized light: blue filter; field of view = 1.4 mm; image 1272A_008).

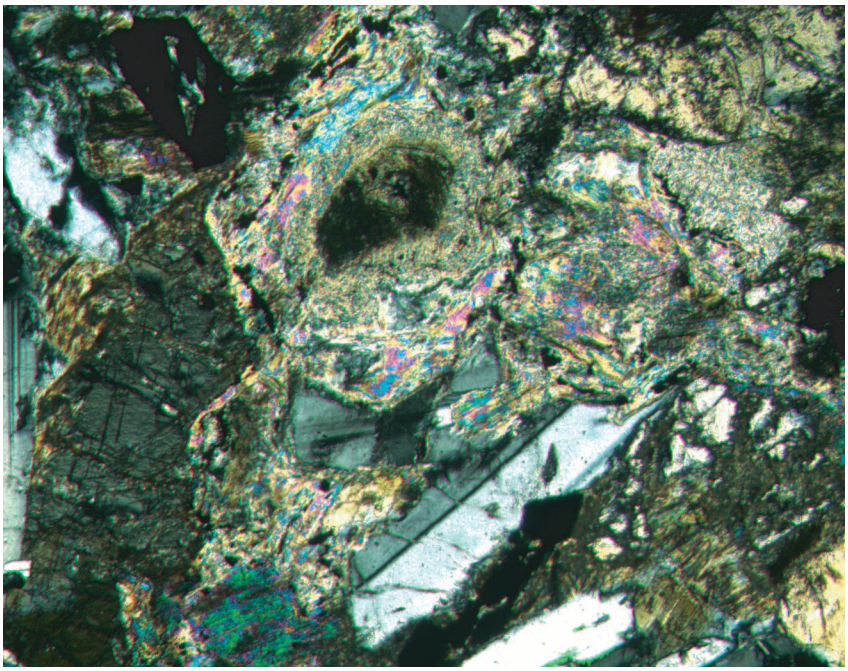

Figure F27. A. Close-up photograph of a medium-grained, myarolitic gabbro/diorite with a brown, near-vertical oxidation halo (interval 209-1272A-3R-1, 90–99 cm). **B.** Photomicrograph showing a highly differentiated melt pocket with oxide (o), biotite (bio), brown amphibole (ba), and secondary fibrous green amphibole (ga) (Sample 209-1272A-3R-1, 96–98 cm) (plane-polarized light: blue + gray + dark gray filters; field of view = 1.4 mm; image 1272A_011).

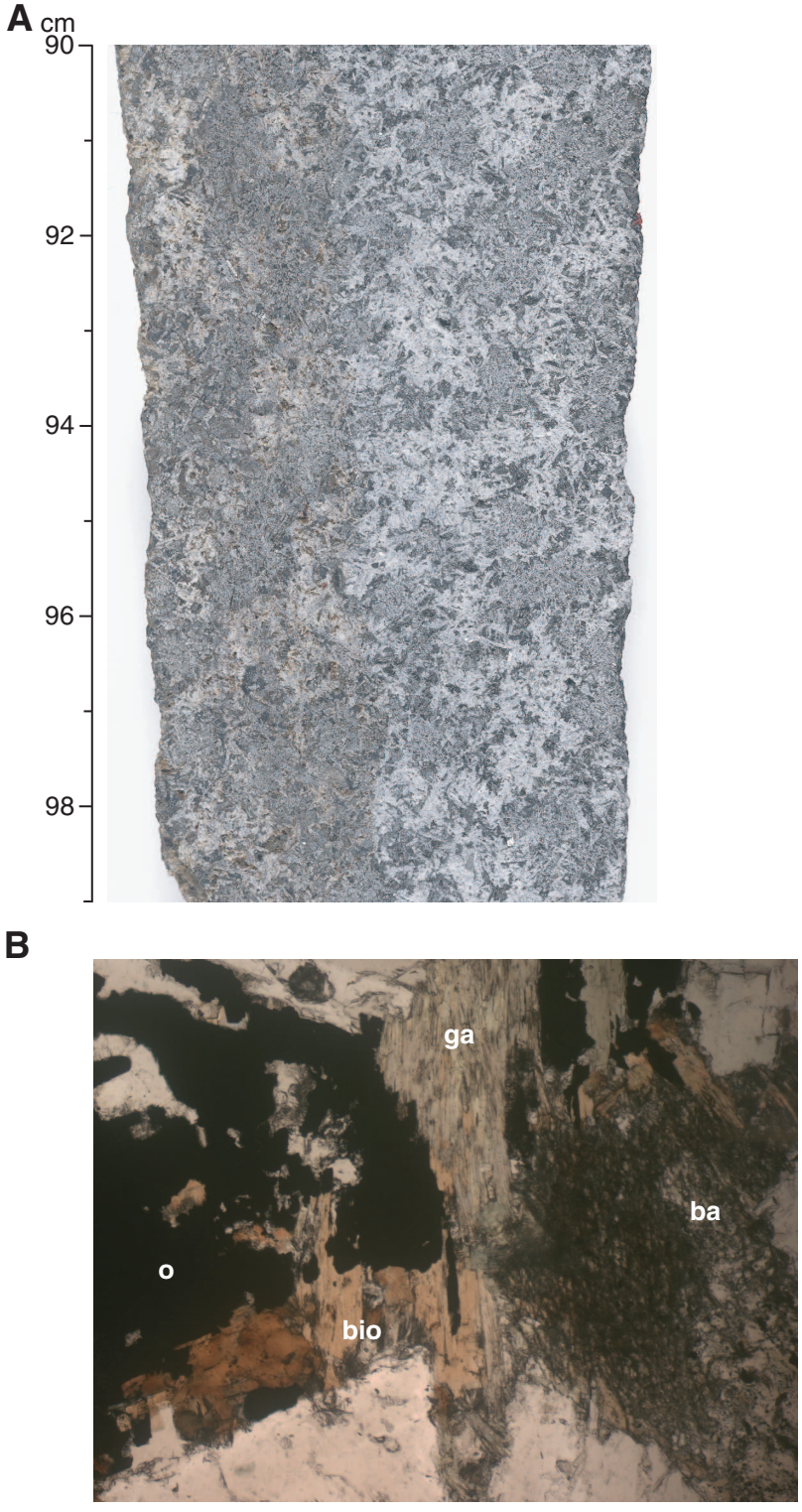

Figure F28. Photomicrograph showing patchy replacement of plagioclase by chlorite/smectite (Sample 209-1272A-1R-1, 41–43 cm) (cross-polarized light: blue filter; field of view = 1.4 mm; image 1272A_009).

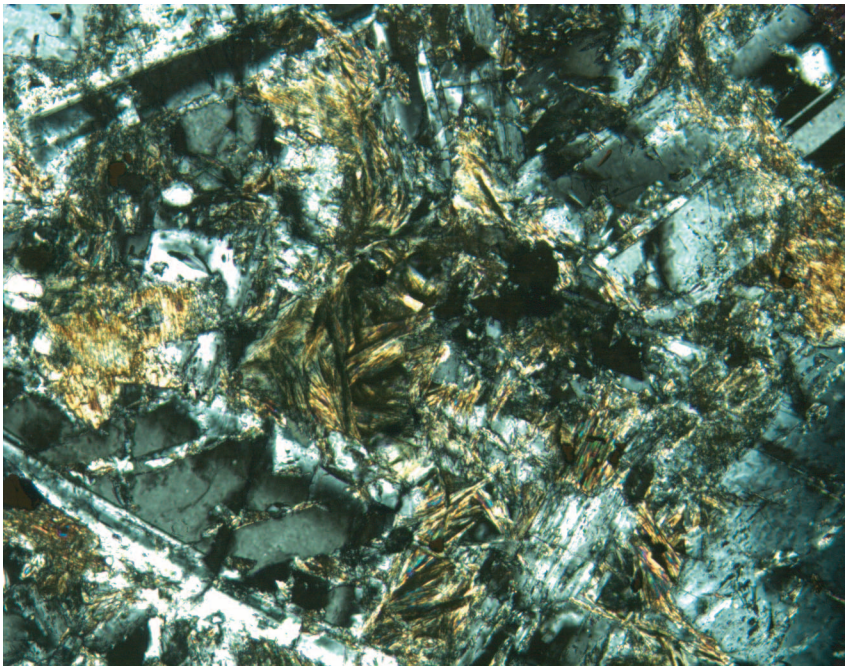

Figure F29. Photomicrograph showing a solid-liquid-vapor fluid inclusion (arrow) in quartz containing an isotropic (gray, upper right) and a birefringent daughter crystal (bright, lower left). The vapor bubble is in the upper left corner (Sample **209-1272A-3R-1, 96–98 cm**) (cross-polarized light: blue + dark gray filters; field of view = 0.35 mm; image 1272A_012).

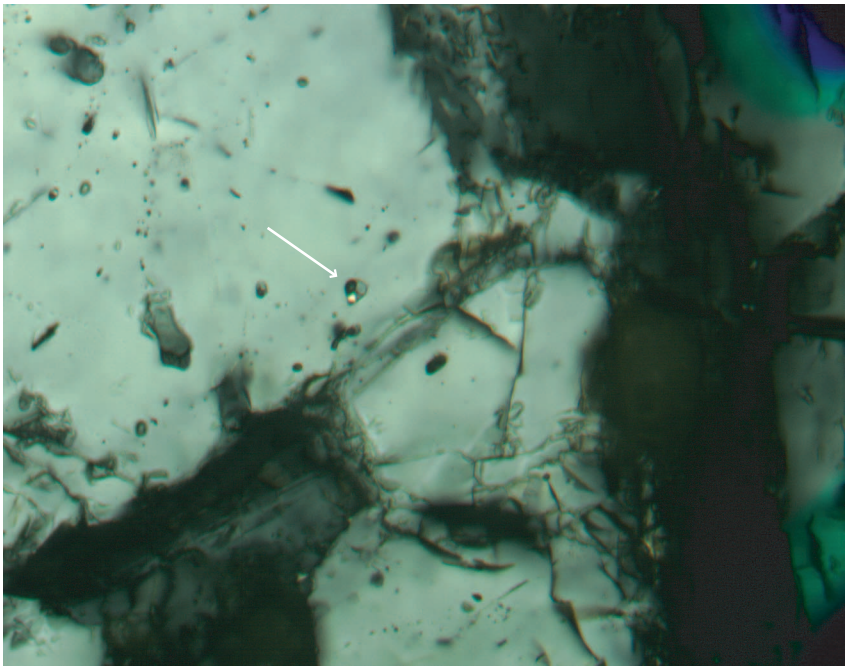

Figure F30. Downhole variation of vein mineral abundance in Hole 1272A.

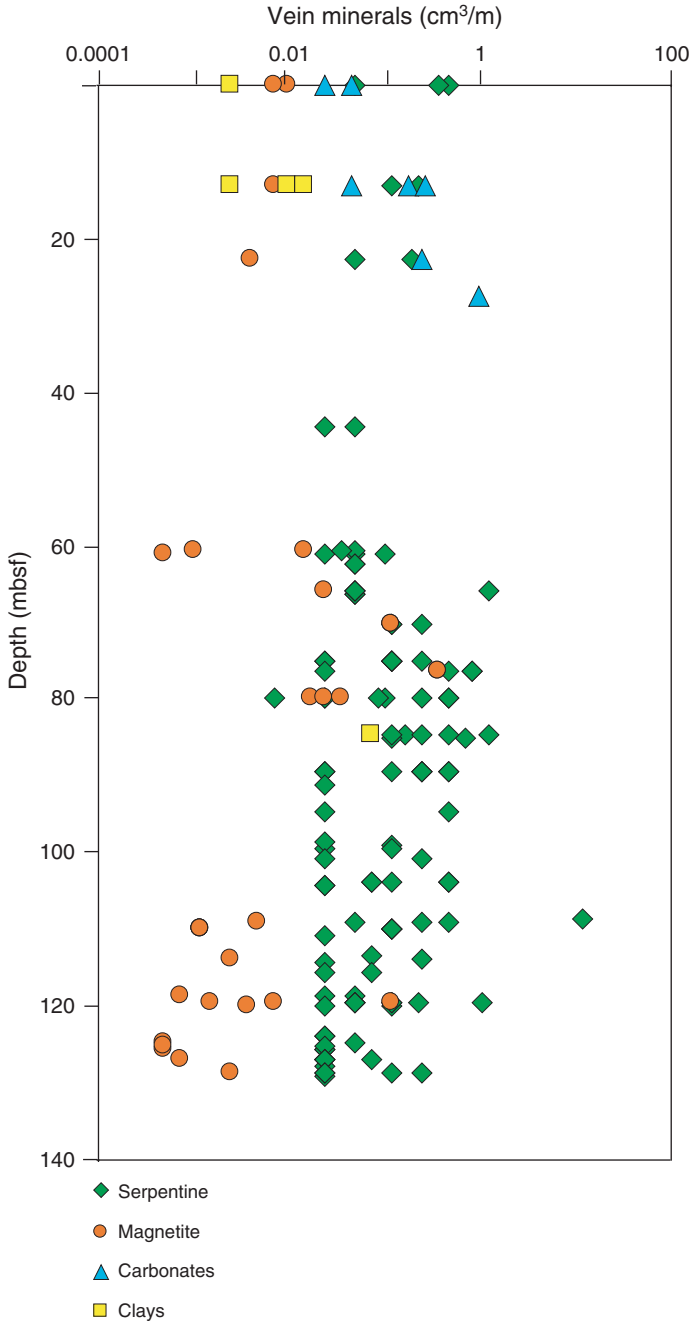

Figure F31. Relative proportions of vein minerals in Hole 1272A.

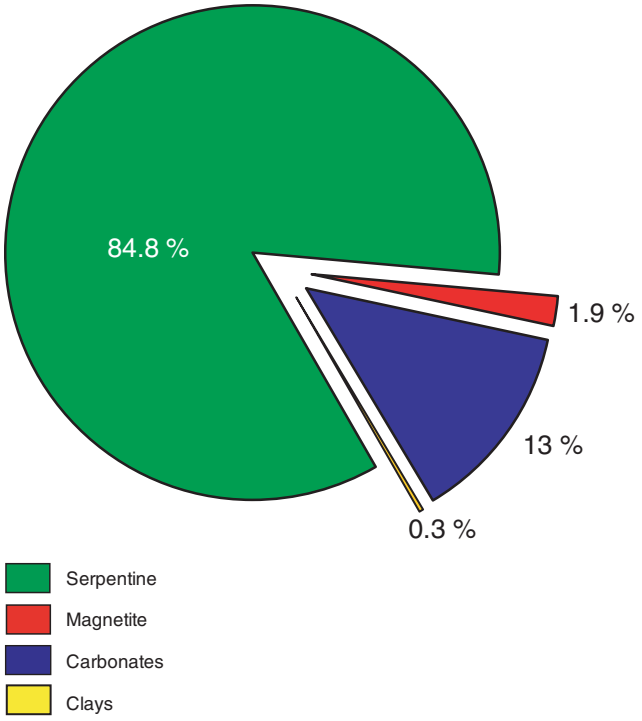

Figure F32. Close-up photographs of examples of weathered clasts from the rubble zone above 56 mbsf. Note rust-colored staining in both parts of the samples and throughout the samples. **A.** Sample 209-1272A-10R-1, 16–20 cm. **B.** Sample 209-1272A-3R-1, 88–110 cm. **C.** Sample 209-1272A-6R-1, 14–17.5 cm. **D.** Sample 209-1272A-7R-1, 130–138 cm. **E.** Sample 209-1272A-1R-1, 30–41 cm.

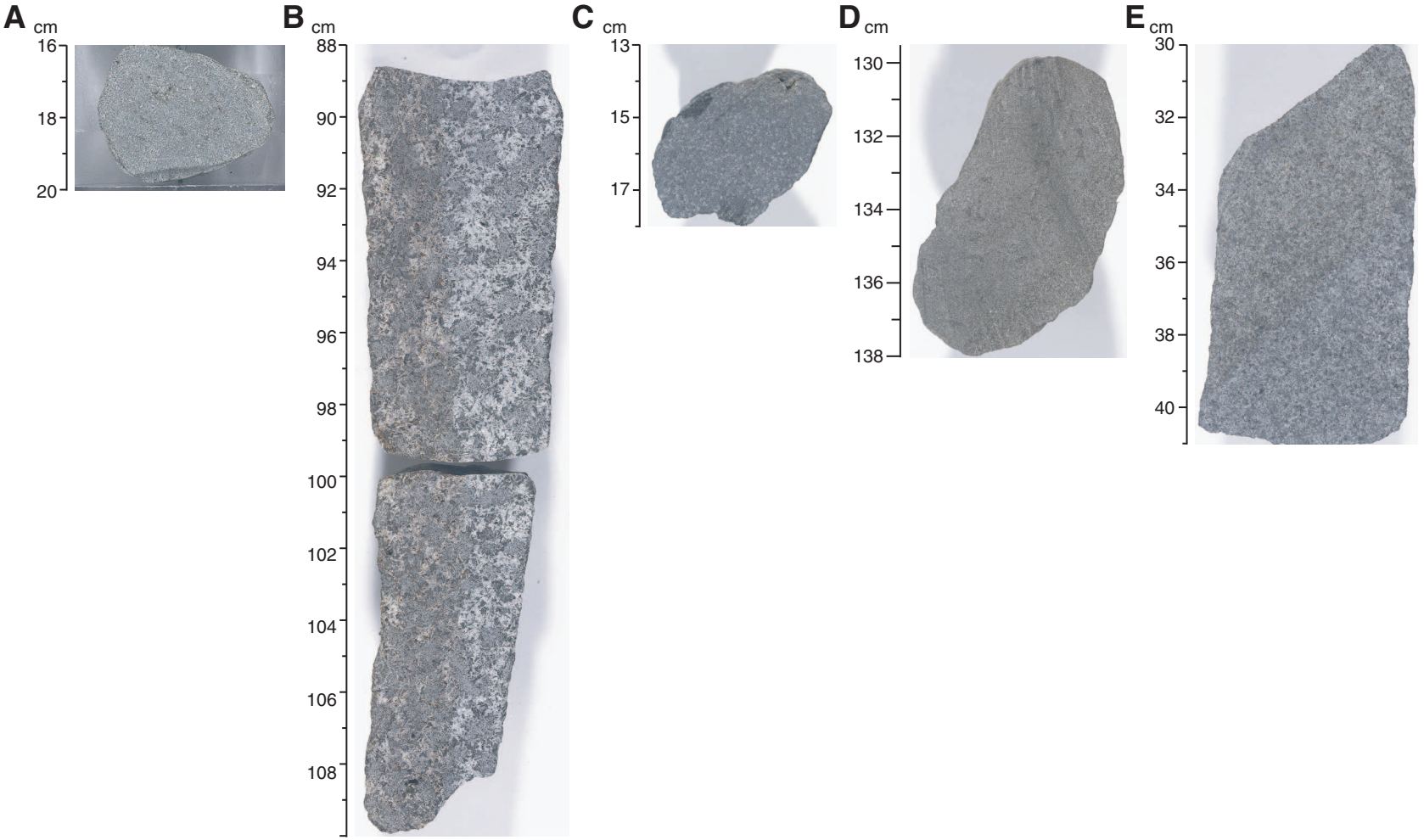

Figure F33. Close-up photographs of protocataclasite harzburgite clasts contained in a carbonate-cemented breccia (intervals 209-1272A-5R-1, 35–80 cm, 45–62 cm, and 47–55 cm).

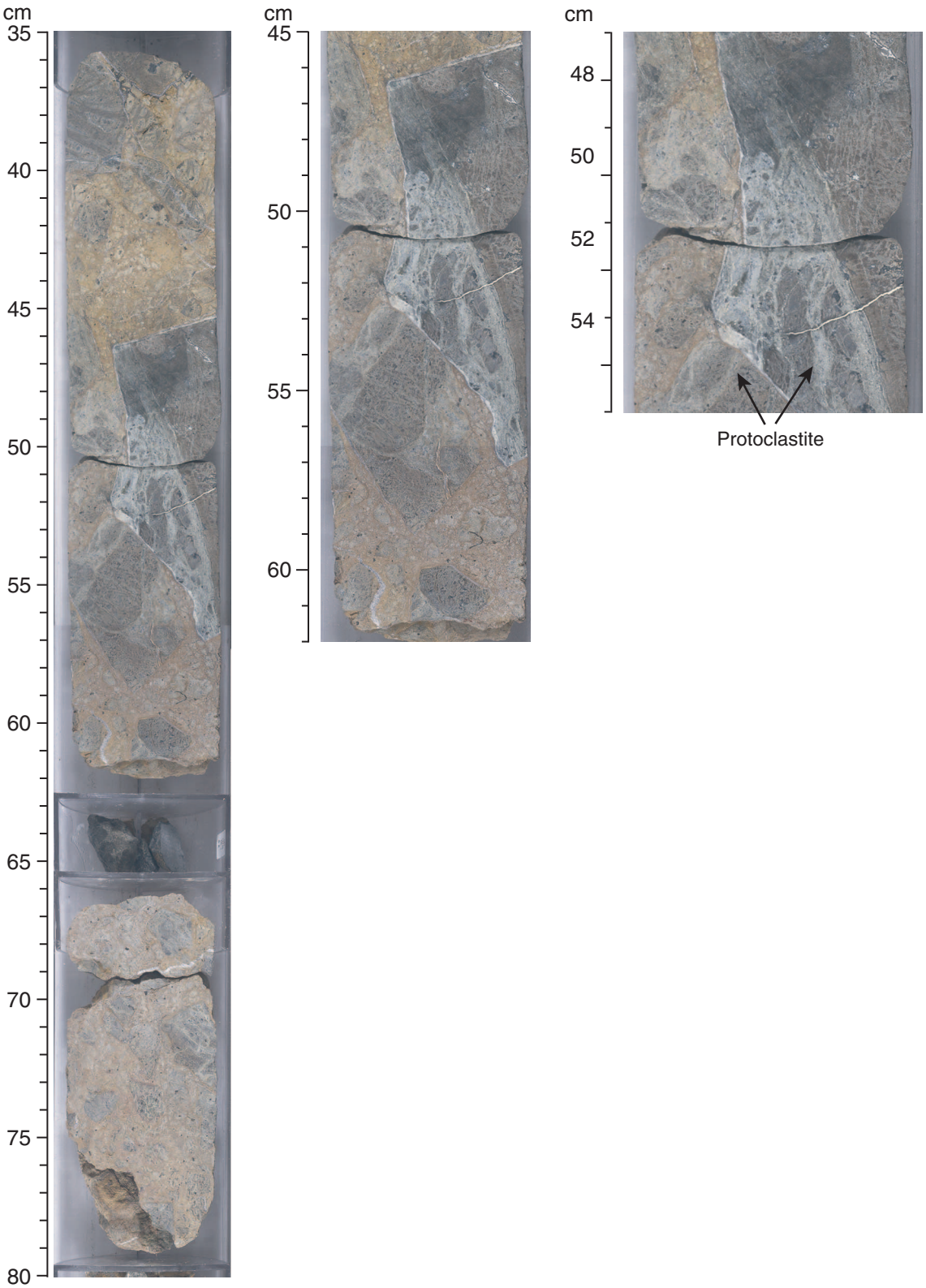

Figure F34. Archive-half magnetic measurements in Hole 1272A. Volume magnetic susceptibility, natural remanent magnetization (NRM) intensity (open diamonds), and characteristic remanent magnetization (ChRM) intensity (solid circles) calculated by principal component analysis, NRM and ChRM inclination, and percentage of the NRM intensity carried by the ChRM. Note variable inclinations above 56 mbsf and relatively constant inclinations below. TD = total depth.

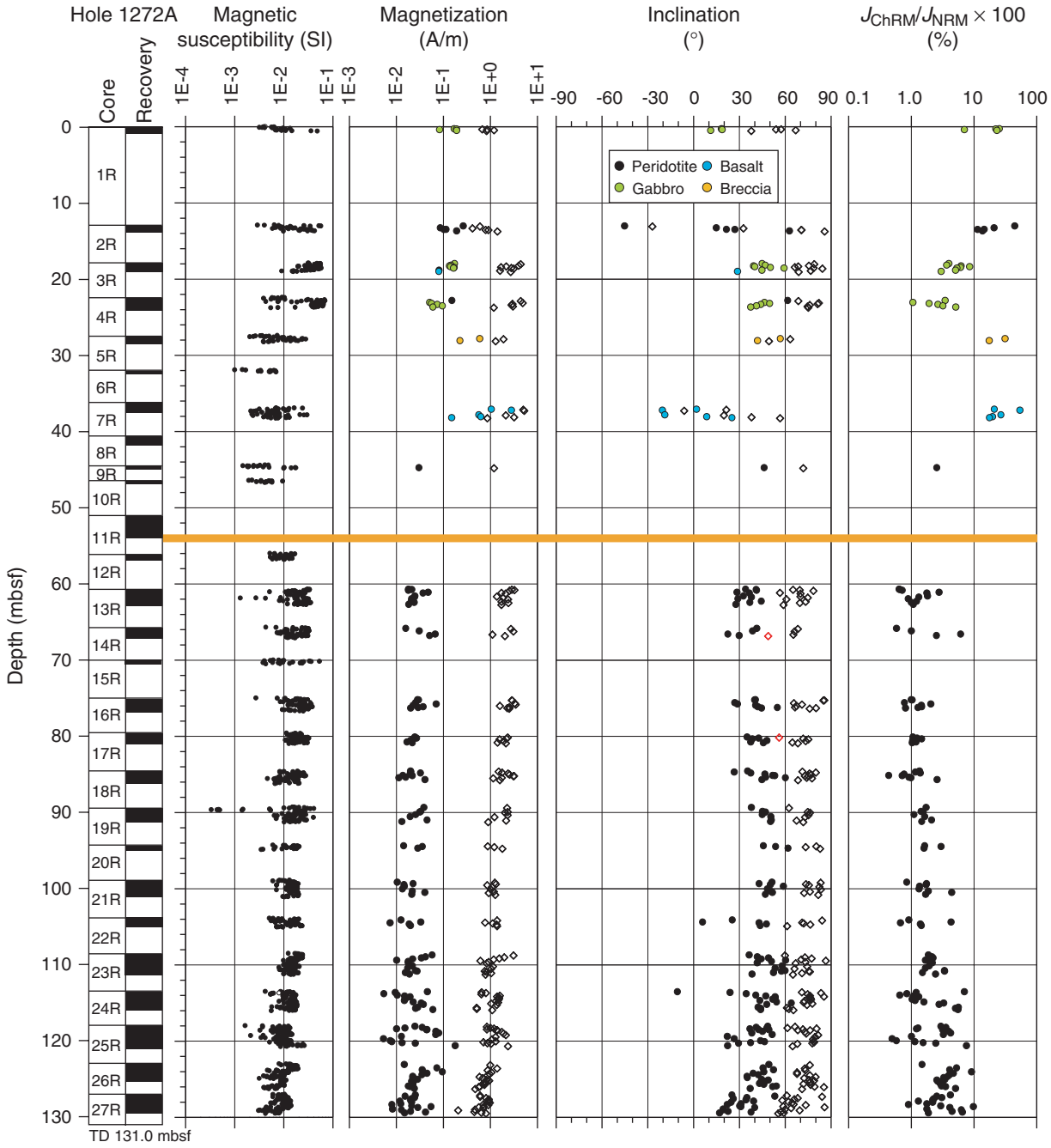

Figure F35. FMS image from 46 to 50 mbsf just above the harzburgitic basement. White to yellow parts of the image are most resistive, and dark brown is most conductive. The image is interpreted as indicating resistive clasts in a conductive matrix. The matrix is likely to be unconsolidated and fluid saturated. The core in this interval, 209-1272A-10R-1, 0–36 cm, is also shown. Note weathered and discolored clasts and the lack of cylindrical core.

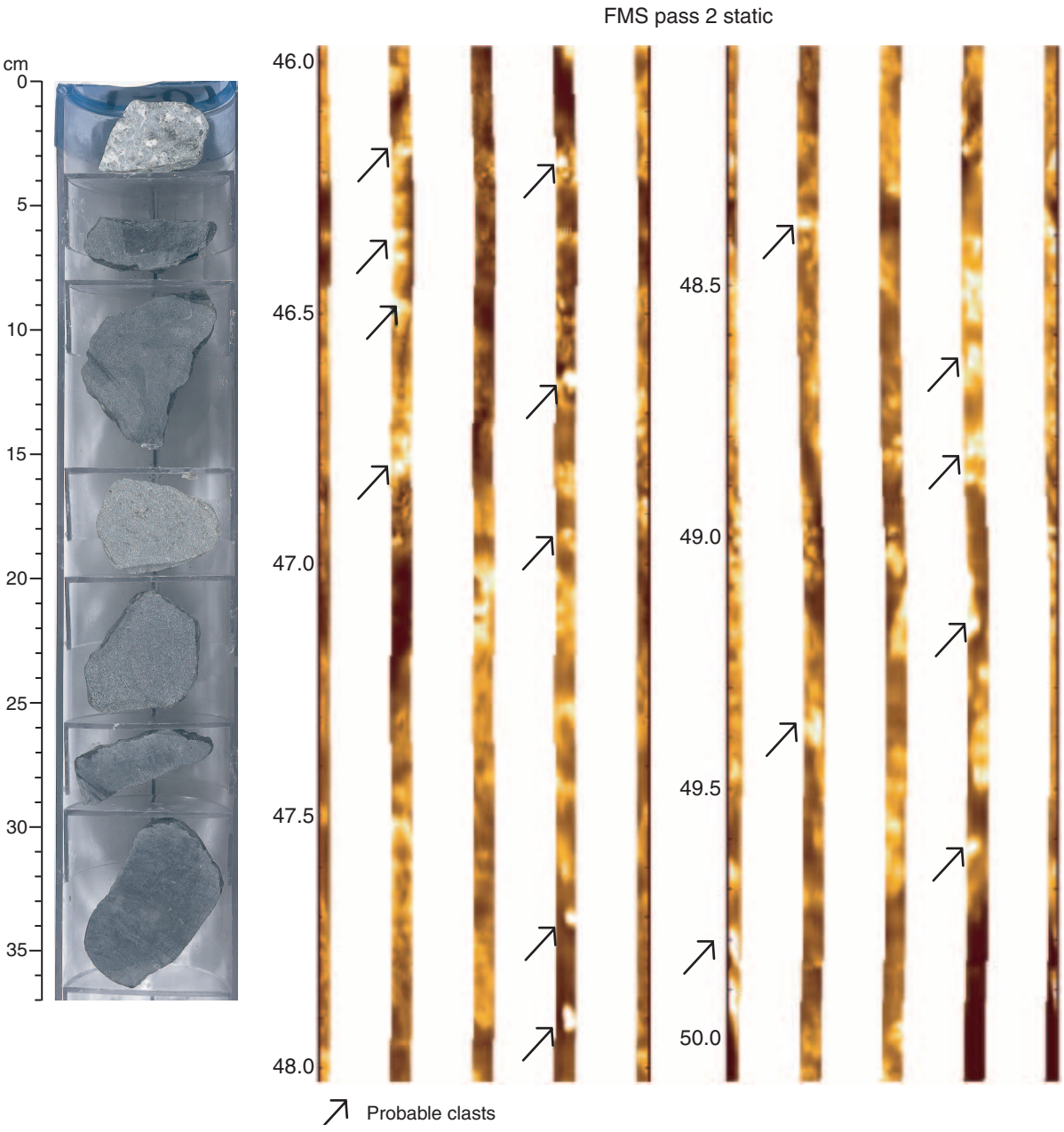

Figure F36. Close-up photographs of examples of pieces that are considered the uppermost part of the basement harzburgites in Hole 1272A. The harzburgite has been altered to mud that deforms plastically until dried (intervals 209-1272A-12R-1, 25–77 cm, and 67–77 cm).

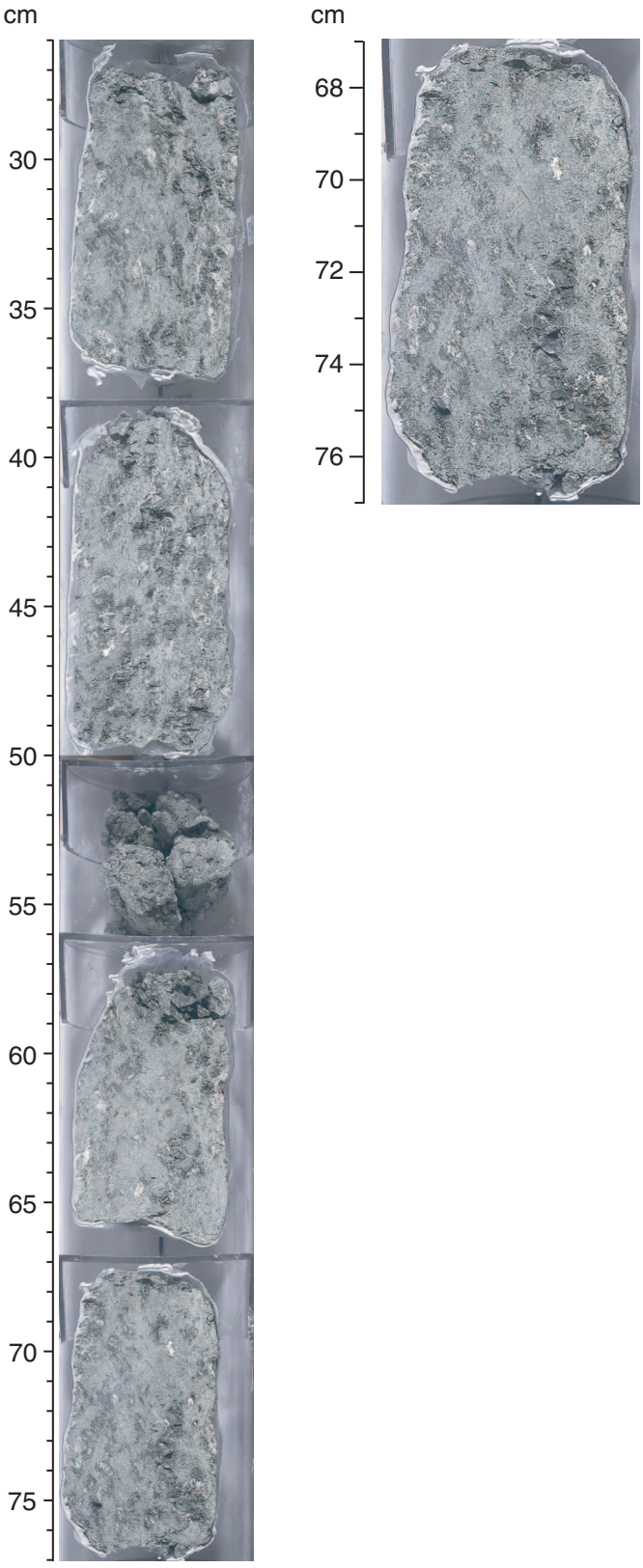

Figure F37. Core image of dunite band in harzburgite (interval 209-1272A-23R-1, 4–60 cm). Black lines show upper and lower contacts with harzburgite. Inset shows enlargement of upper contact, which is subparallel to the crystal plastic foliation in the adjacent harzburgite.

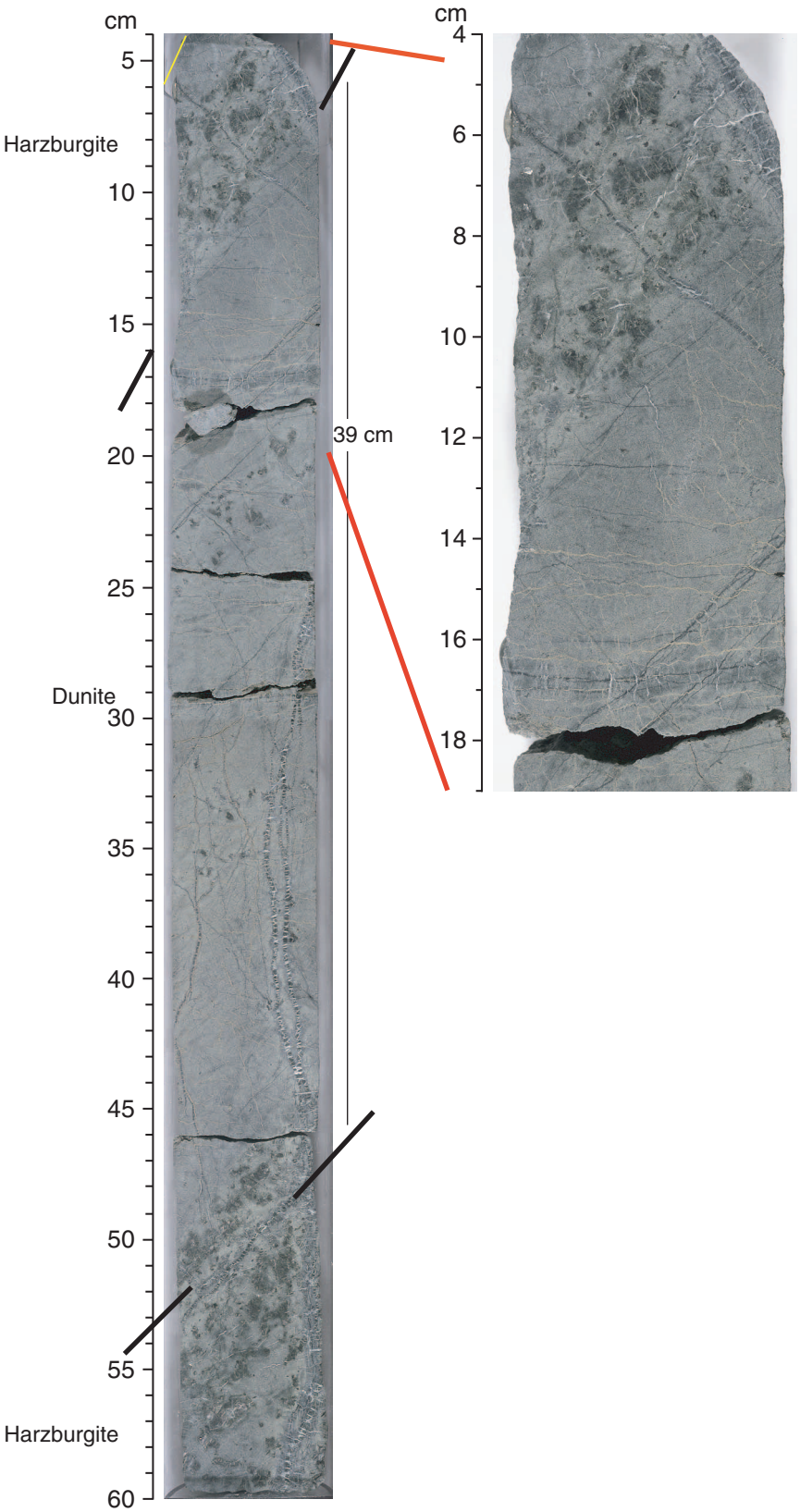

Figure F38. Lower hemisphere stereographic projection of poles to crystal-plastic foliation and compositional layering. Apparent dips rotated to a common orientation using the measured paleomagnetic declination. The crystal-plastic foliations are protogranular and porphyroclastic shape fabrics in harzburgite. Compositional layering (dunite contacts) was measured in Section 209-1272A-23R-1. A spinel foliation was measured in Section 209-1272A-2R-1 in the upper rubble zone and gives a result far from the main cluster of foliations.

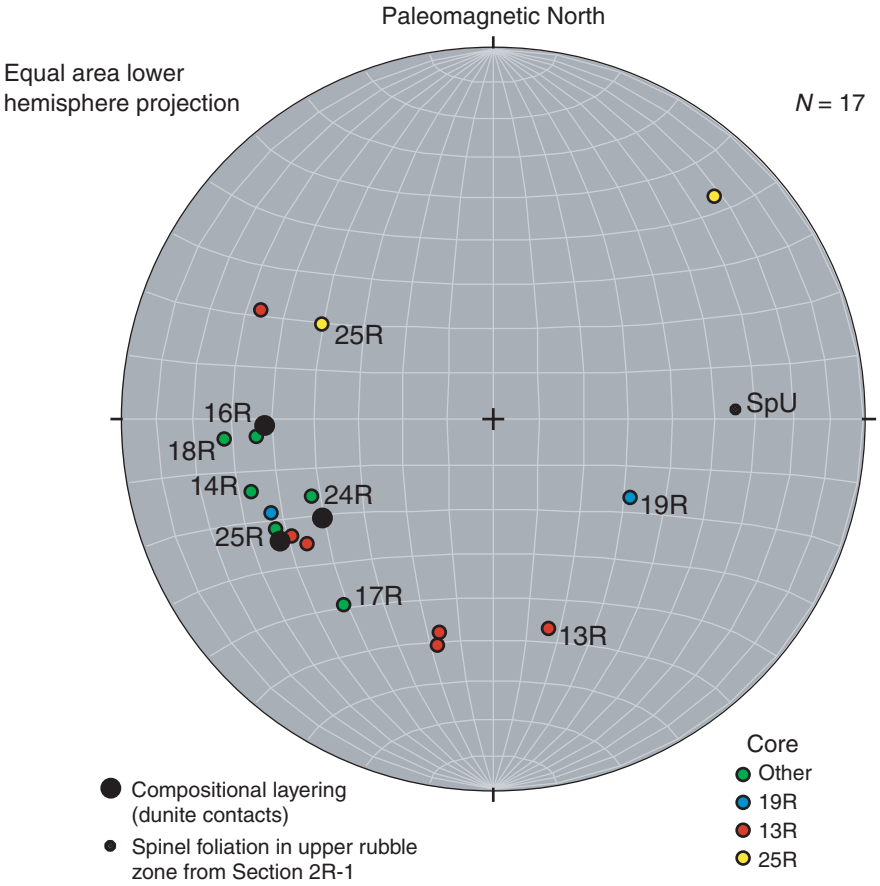

Figure F39. Downhole seven-piece running average, weighted by piece length, of crystal-plastic deformation intensity for Hole 1272A. TD = total depth.

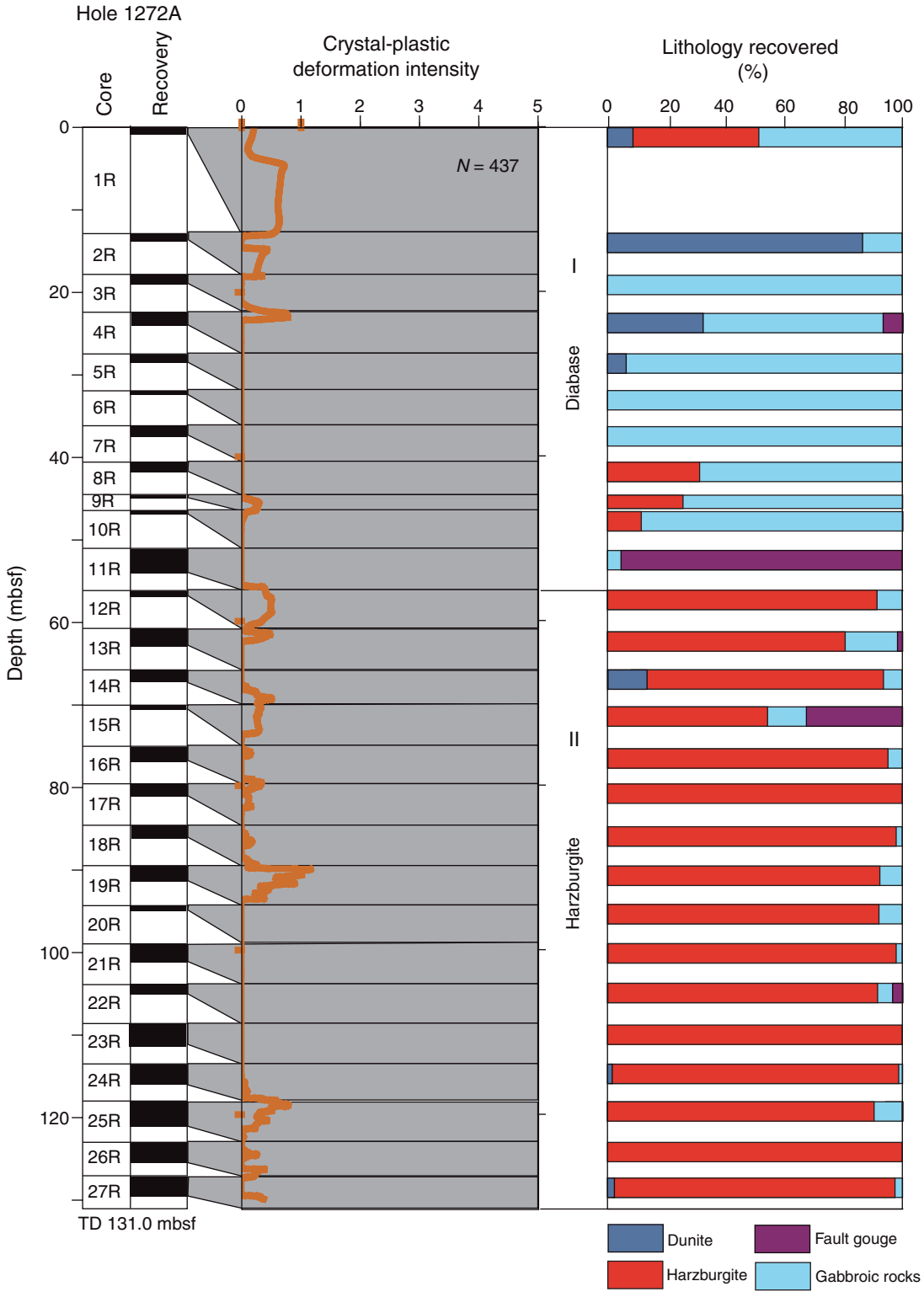

Figure F40. Close-up photographs of core showing the lack of mesoscopic crystal-plastic foliation in protogranular harzburgites. **A.** Interval 209-1272A-27R-2, 70–110 cm. **B.** Interval 209-1272A-23R-2, 100–121 cm. **C.** Interval 209-1272A-25R-2, 45–75 cm.

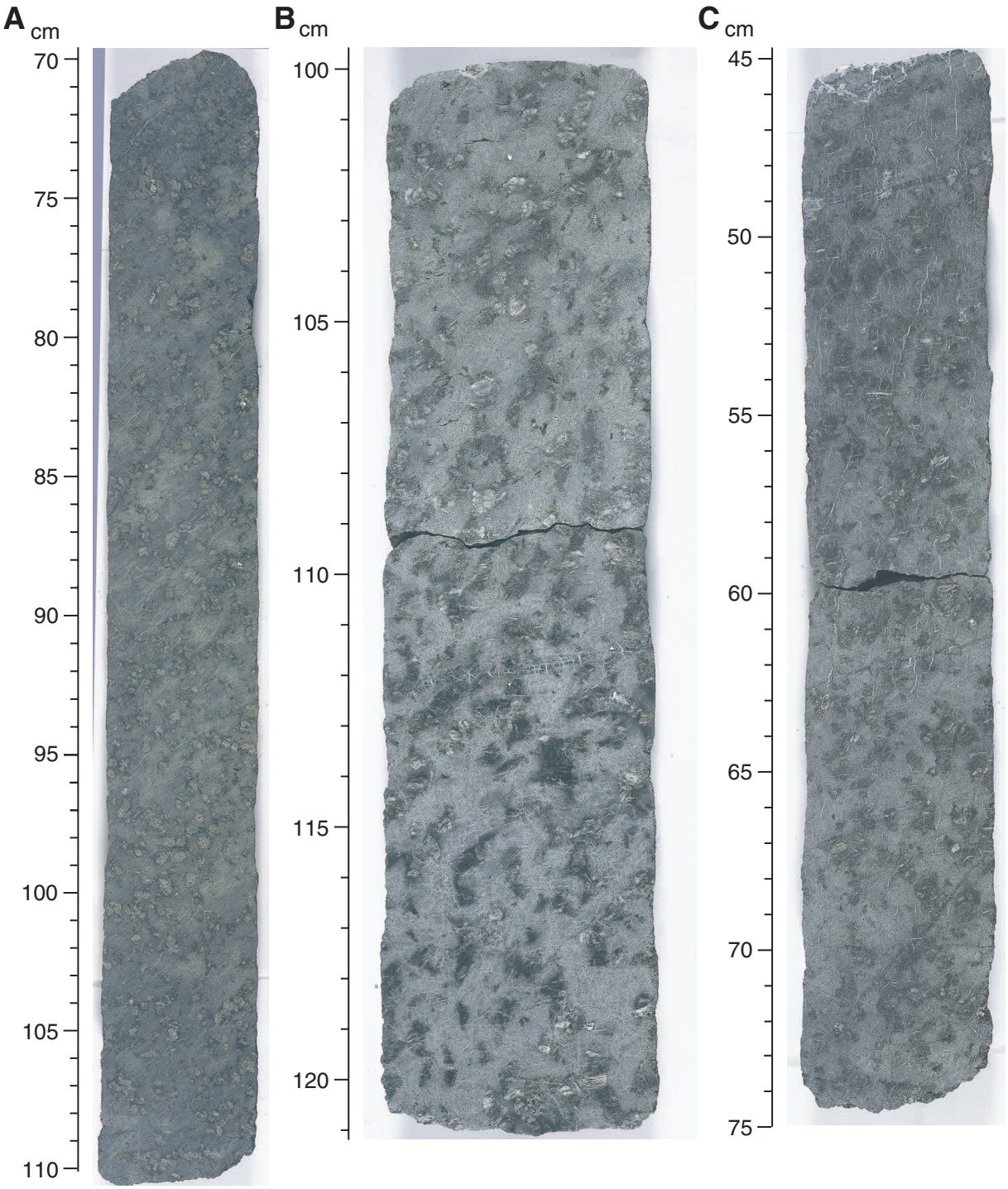

Figure F41. Crystal-plastic deformation (CPf) intensity for Hole 1272A using a scale from 0 (undeformed) to 5 (ultramylonite) as explained in **"Structural Geology,"** p. 9, in the "Explanatory Notes" chapter. A total of 3635 cm of core was logged in 437 pieces from the hole. Plot excludes sand, gravel, and fault gouge.

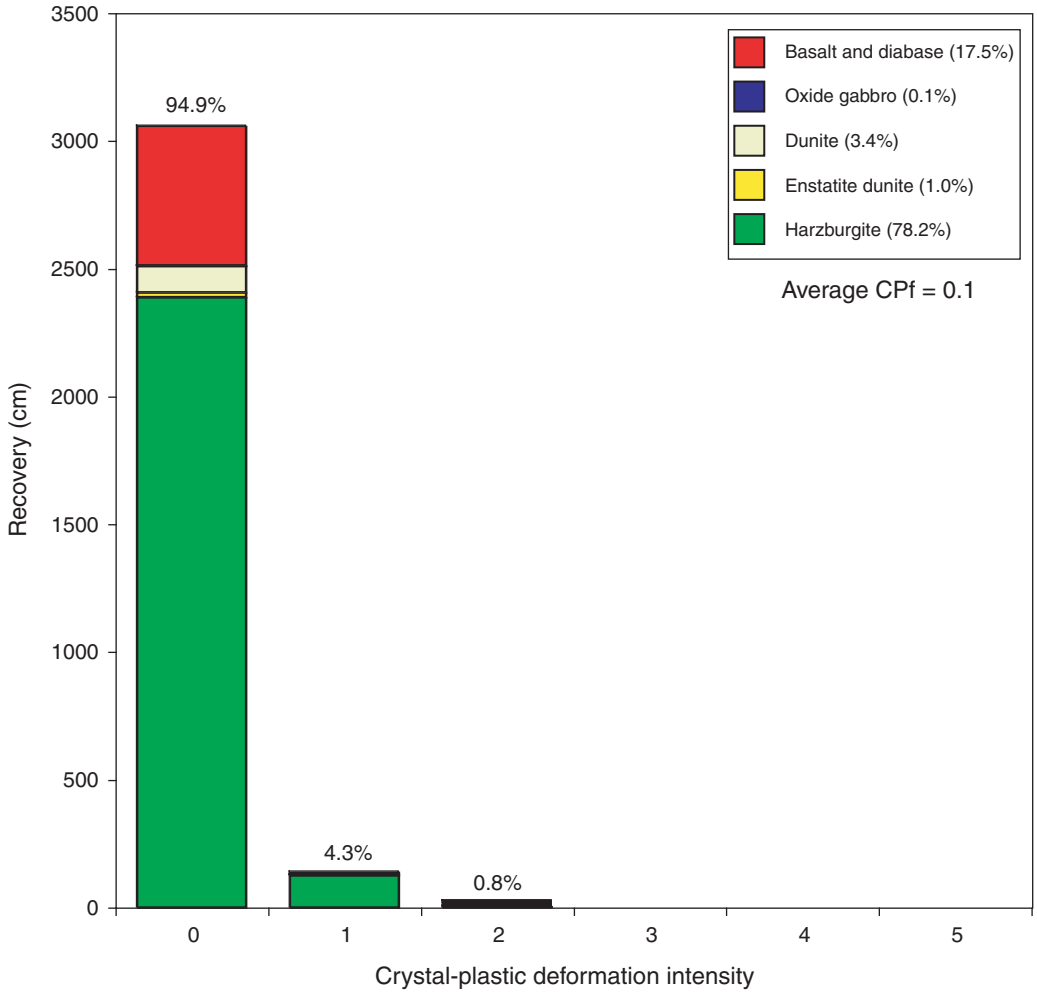

Figure F42. Photomicrographs showing high-temperature textures in Hole 1272A peridotites. Sp = spinel, Opx = orthopyroxene, Cpx = clinopyroxene, Cpx_1 = large primary clinopyroxene, Cpx_2 = clinopyroxene neoblasts. **A.** Bastite after protointergranular orthopyroxene in harzburgite (Sample 209-1272A-13R-2 [Piece 4, 33–36 cm]) (cross-polarized light [XPL]; field of view [FOV] = 2.75 mm; image 1272A_031). **B.** Bastite after protogranular orthopyroxene in harzburgite (Sample 209-1272A-25R-1 [Piece 15, 123–126 cm]) (XPL; FOV = 5.5 mm; image 1272A_035). **C.** Bastite after protogranular orthopyroxene in harzburgite (Sample 209-1272A-23R-1 [Piece 3, 62–64 cm]) (XPL; FOV = 5.5 cm; image 1272A_049). **D.** Bastite after protogranular orthopyroxene in harzburgite (Sample 209-1272A-19R-2 [Piece 3, 27–29 cm]) (XPL; FOV = 5.5 cm; image 1272A_047). **E.** Clinopyroxene neoblasts replacing large primary crystal in an oxide gabbro vein (Sample 209-1272A-19R-1 [Piece 6, 33–35 cm]) (XPL; FOV = 5.5 cm; image 1272A_44). **F.** Clinopyroxene neoblasts with interstitial oxides in the oxide gabbro (Sample 209-1272A-19R-1 [Piece 6, 33–35 cm]) (plane-polarized light; FOV = 1.4 mm; image 1272A_046).

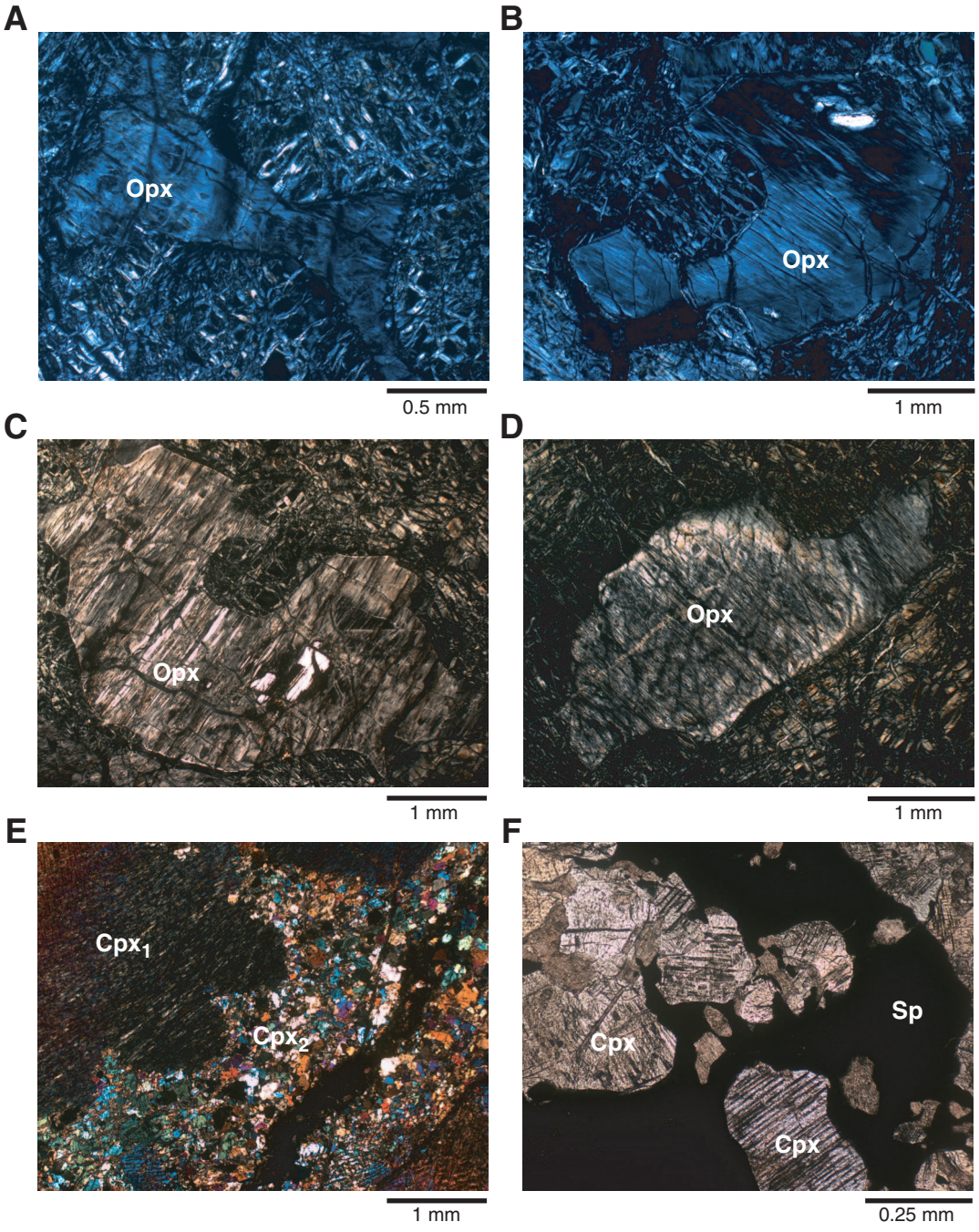

Figure F43. Close-up photographs of examples of alteration veins cutting harzburgites and dunites. **A.** Crosscutting black–dark green serpentine magnetite veins in a dunite (interval 209-1272A-23R-1, 10–26 cm). **B.** Early black–dark green serpentine veins cut by later white-green banded serpentine vein with orthogonal cracks filled with chrysotile in the same dunite (interval 209-1272A-23R-1, 25–41 cm). **C.** An example of the sigmoidal wispy white chrysotile veins defining a foliation dipping to the left (interval 209-1272A-23R-2, 126.5–139.5 cm). **D.** An example of a composite white-green banded serpentine vein with orthogonal, crosscutting chrysotile veins and a wallrock alteration halo (interval 209-1272A-24R-1, 86–100 cm).

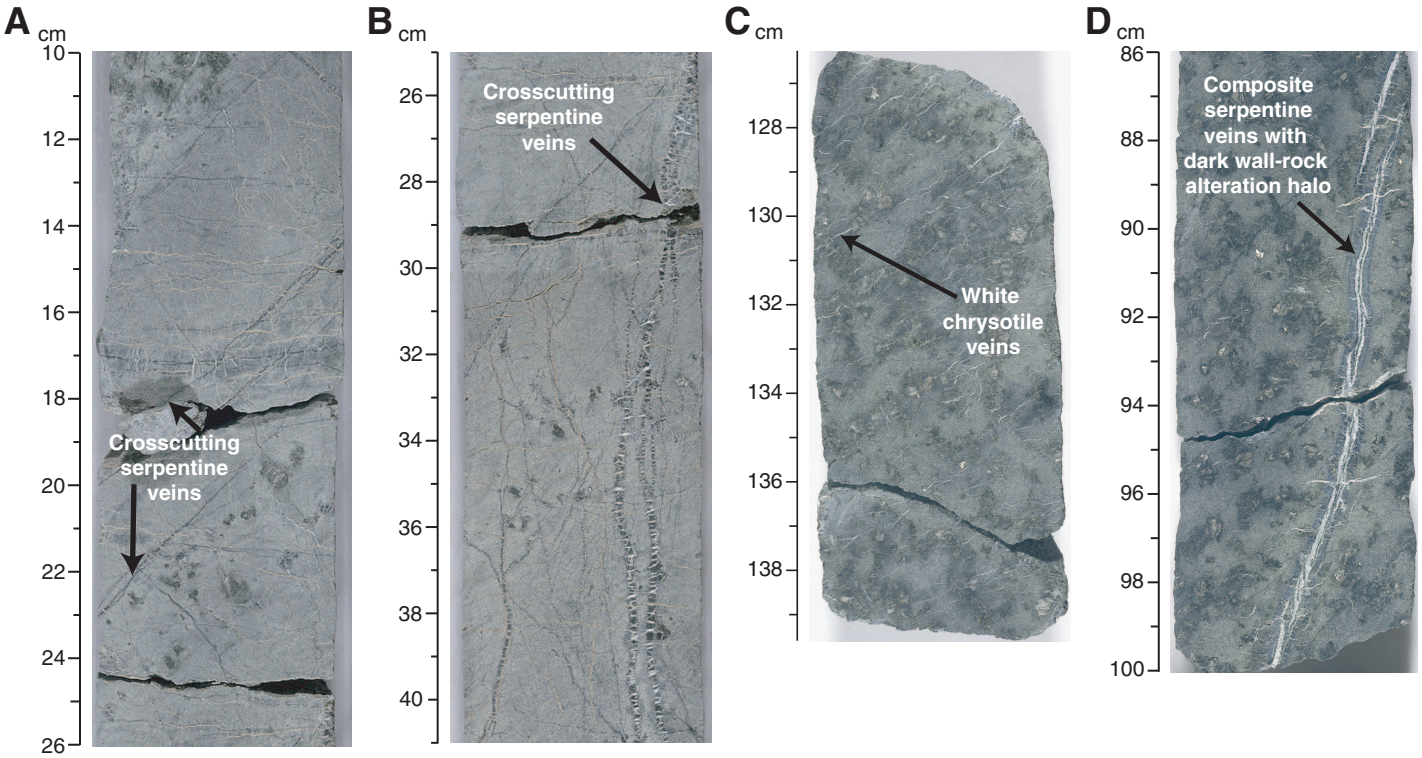

Figure F44. Downhole running average of alteration vein and cataclastic intensity. TD = total depth.

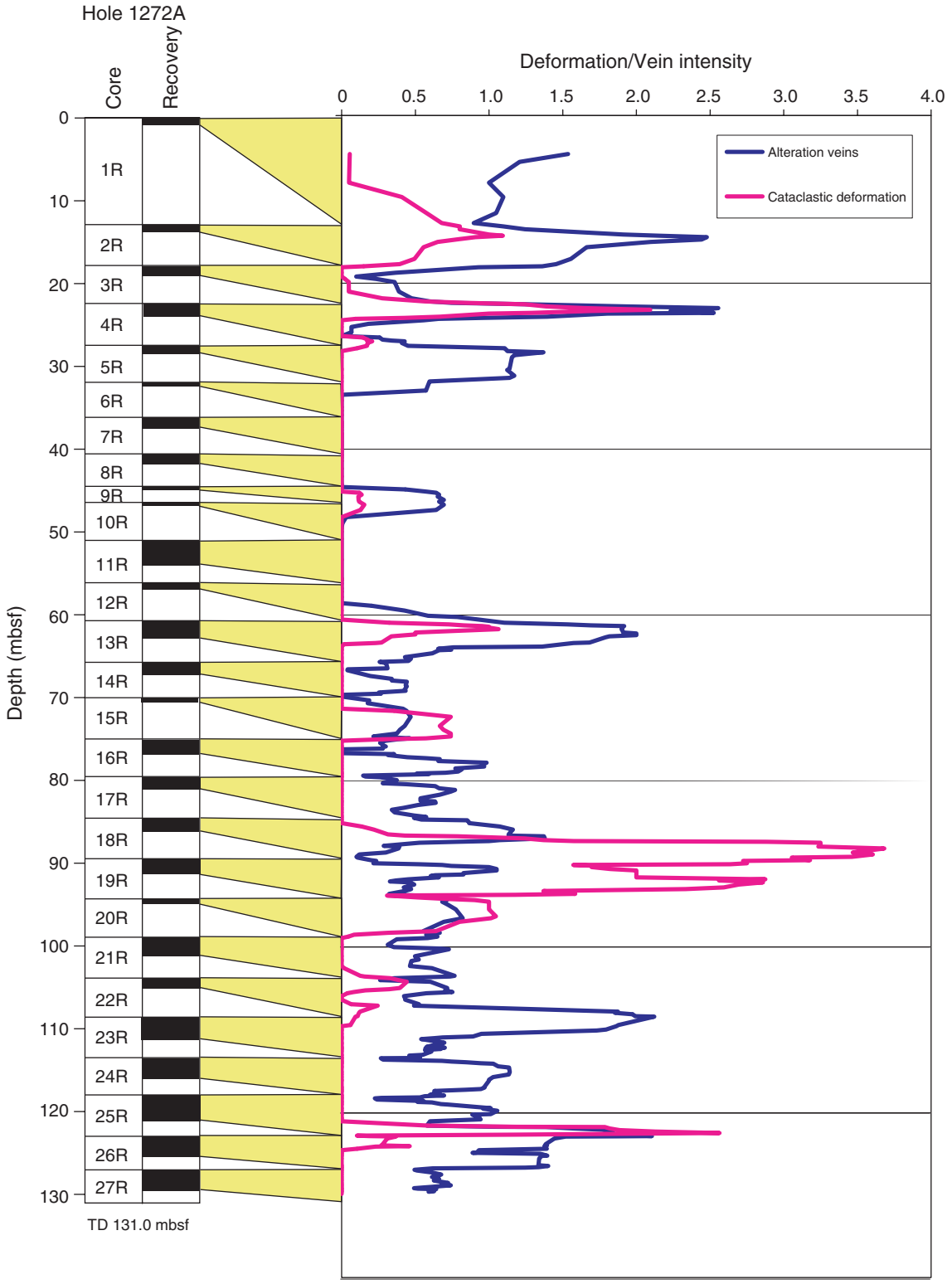

Figure F45. Dips of black–dark green serpentine, composite white/green serpentine, talc-serpentine, and chrysotile veins with expanded depth in the core reference frame for Hole 1272A.

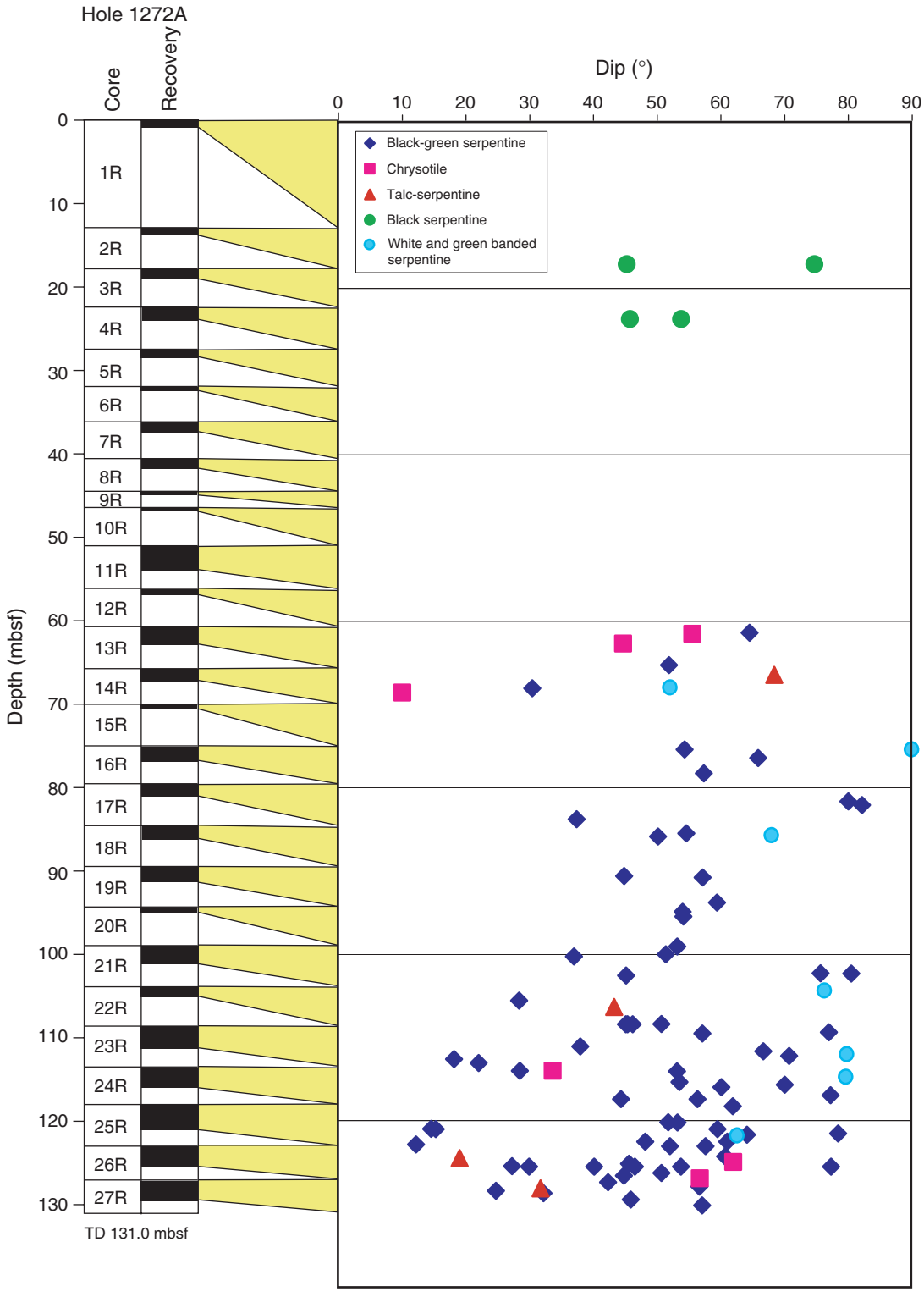

Figure F46. Lower hemisphere equal-area stereographic projection of poles to black–dark green serpentine and white- and green-banded serpentine veins in Hole 1272A, measured in the core reference frame and rotated using the measured paleomagnetic declination back to a common orientation as described in "Structures in Peridotite and Gabbroic Intrusions," p. 8, in "Mantle Upwelling, Melt Transport, and Igneous Crustal Accretion" in the "Leg 209 Summary" chapter.

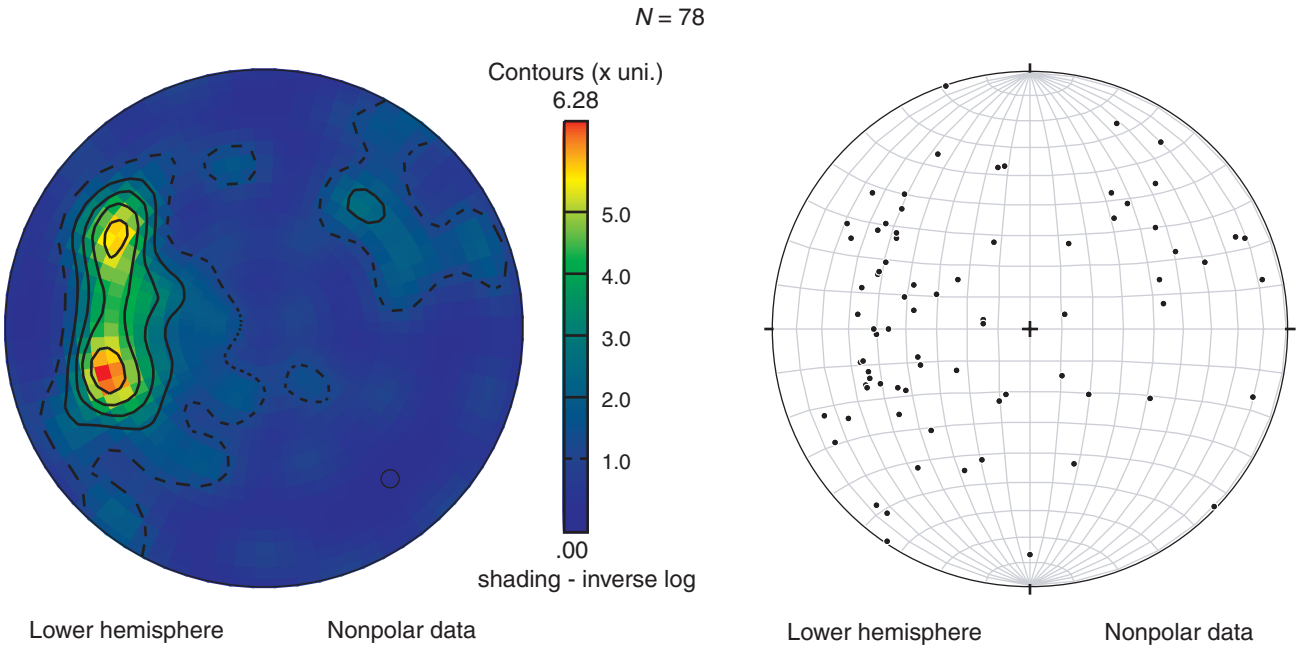

Figure F47. Examples of semiplastic fault gouges from Hole 1272A. The fault gouges were semicohesive fault breccias with matrix-supported clasts. **A.** Interval 209-1272A-18R-1, 134–149 cm. **B.** Interval 209-1272A-18R-2, 1–18 cm. **C.** Interval 209-1272A-19R-1, 138–150 cm. **D.** Interval 209-1272A-19R-2, 1–18 cm. **E.** Interval 209-1272A-25R-2, 108–126 cm.

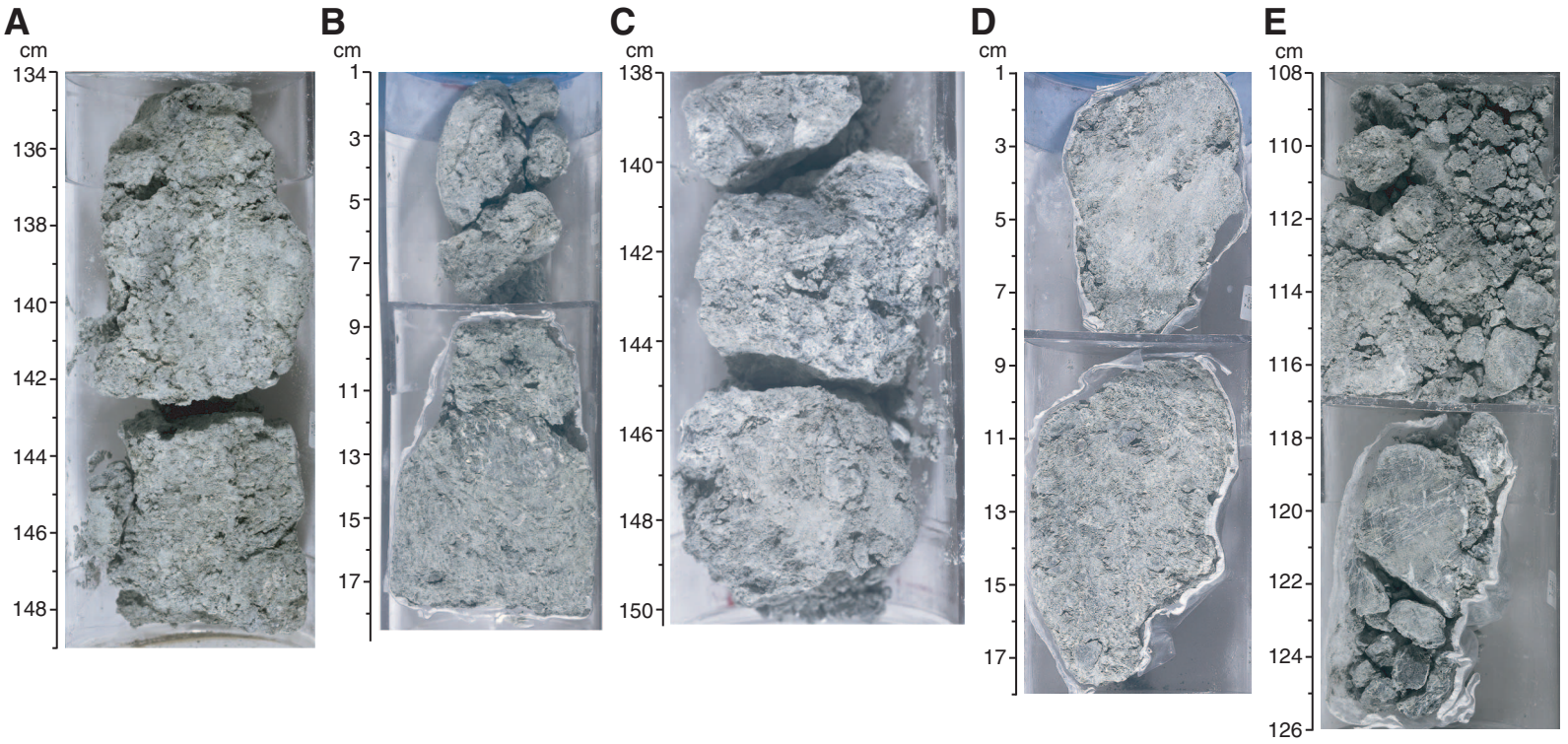

Figure F48. Formation MicroScanner (FMS) static image from logging pass 2 showing interval where two fault gouges and oxide gabbros were recovered along with harzburgites. Two conductive zones are present at the same depth as the first two fault gouges (outlined in yellow and correlated with yellow line in FMS image to denote gouge) in interval 209-1272A-19R-1, 0–56 cm. The banded conductive structure at greater depth may correspond to the presence of oxide gabbros. Gouges (again outlined in yellow) at the base of the same section and the top of the next section (209-1272A-19R-2) appear to be correlated with a conductive zone in the FMS image, interpreted as showing resistive clasts in a conductive matrix. Clasts in the FMS image are indicated with black arrows.

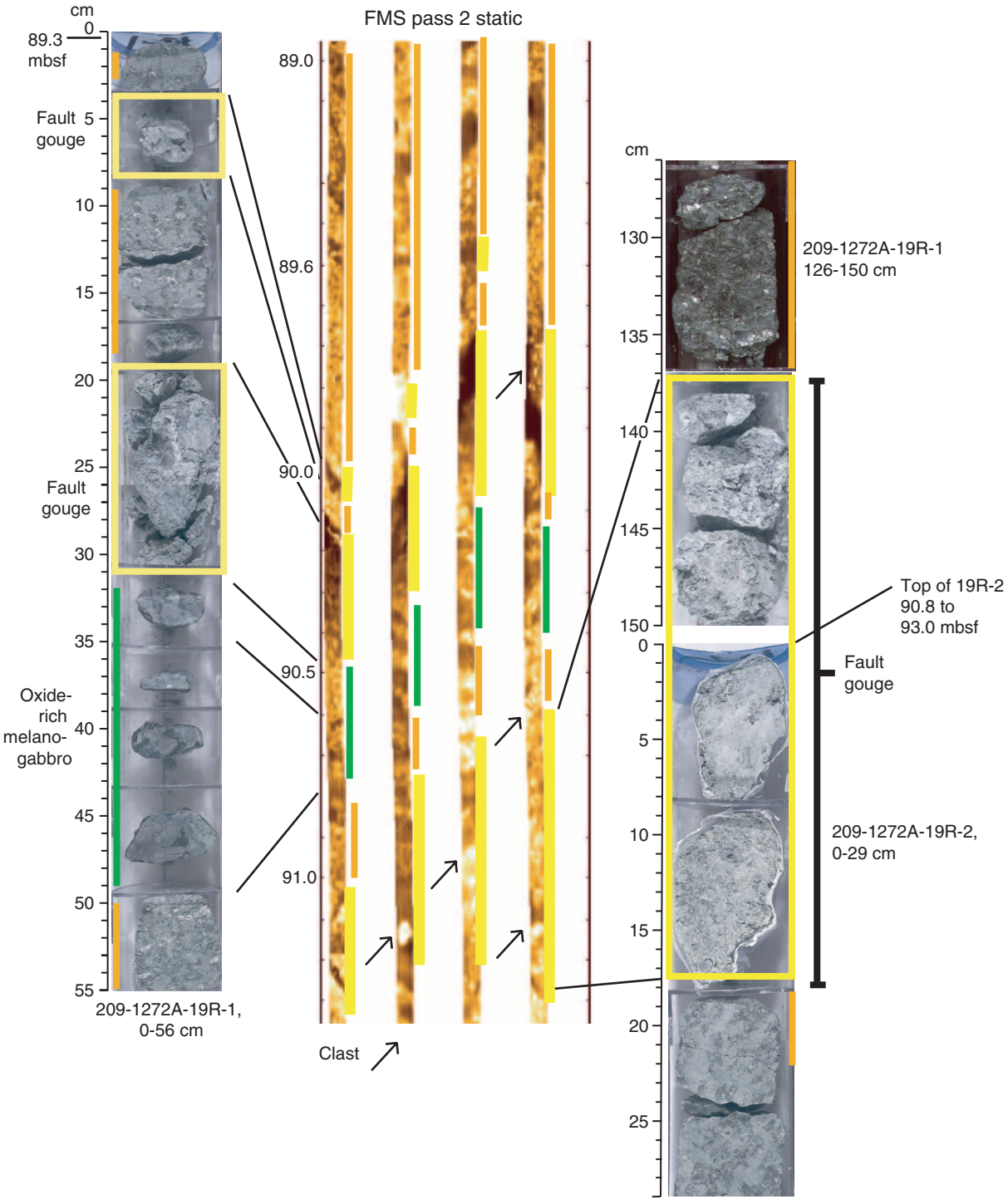

Figure F49. Formation MicroScanner (FMS) static image, from logging pass 1 of a 1.7-m conductive zone corresponding to the depth where a serpentine schist was recovered (Section 209-1272A-20R-1 [Piece 8]) at 94.89 mbsf (curated depth). The conductive zone associated with the schist may represent a gouge. Note resistive clasts in a conductive matrix (indicated by black arrows).

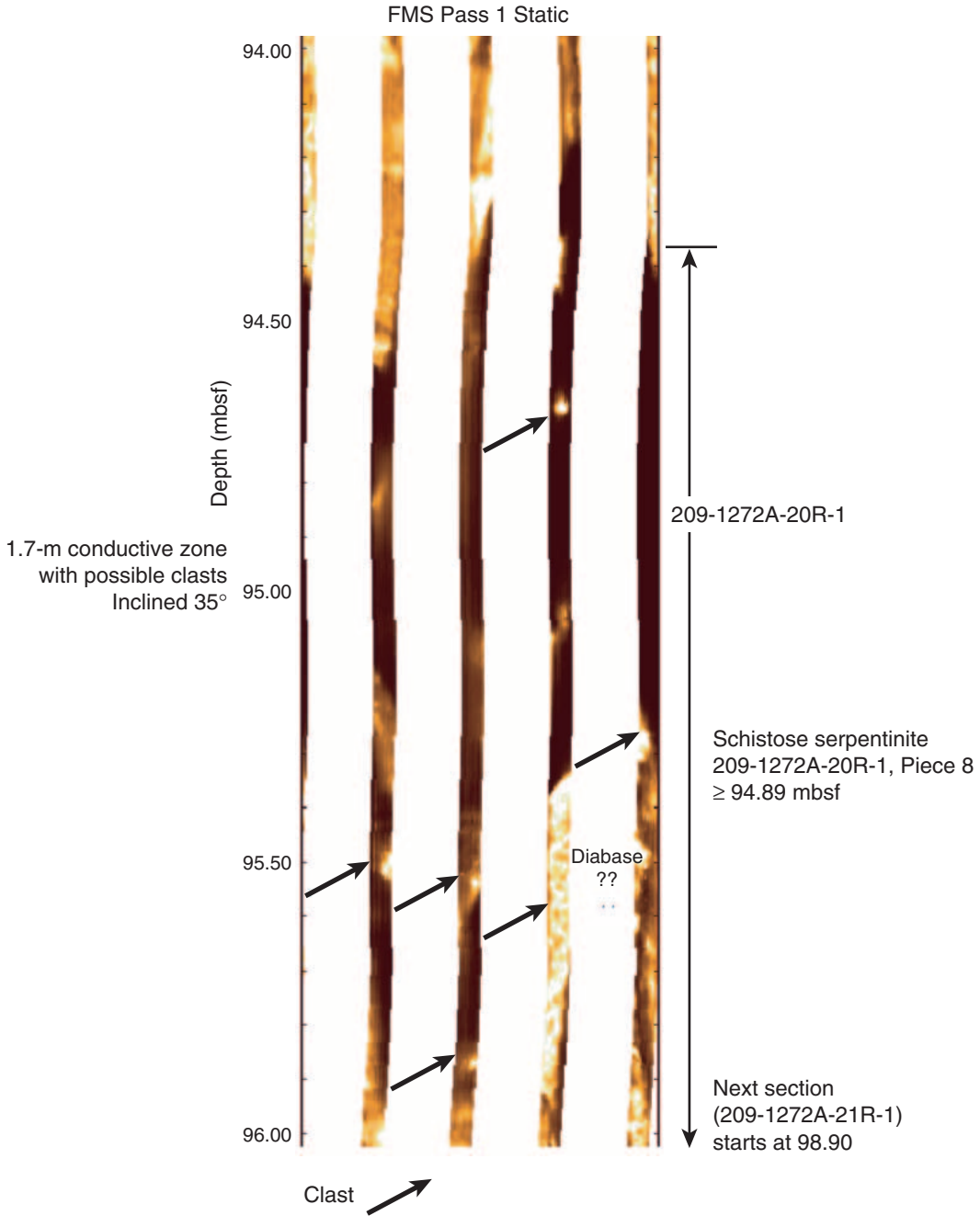

Figure F50. Formation MicroScanner (FMS) image interpreted as showing resistive clasts in a conductive matrix, probably a fault gouge. Black arrows point to resistive clasts.

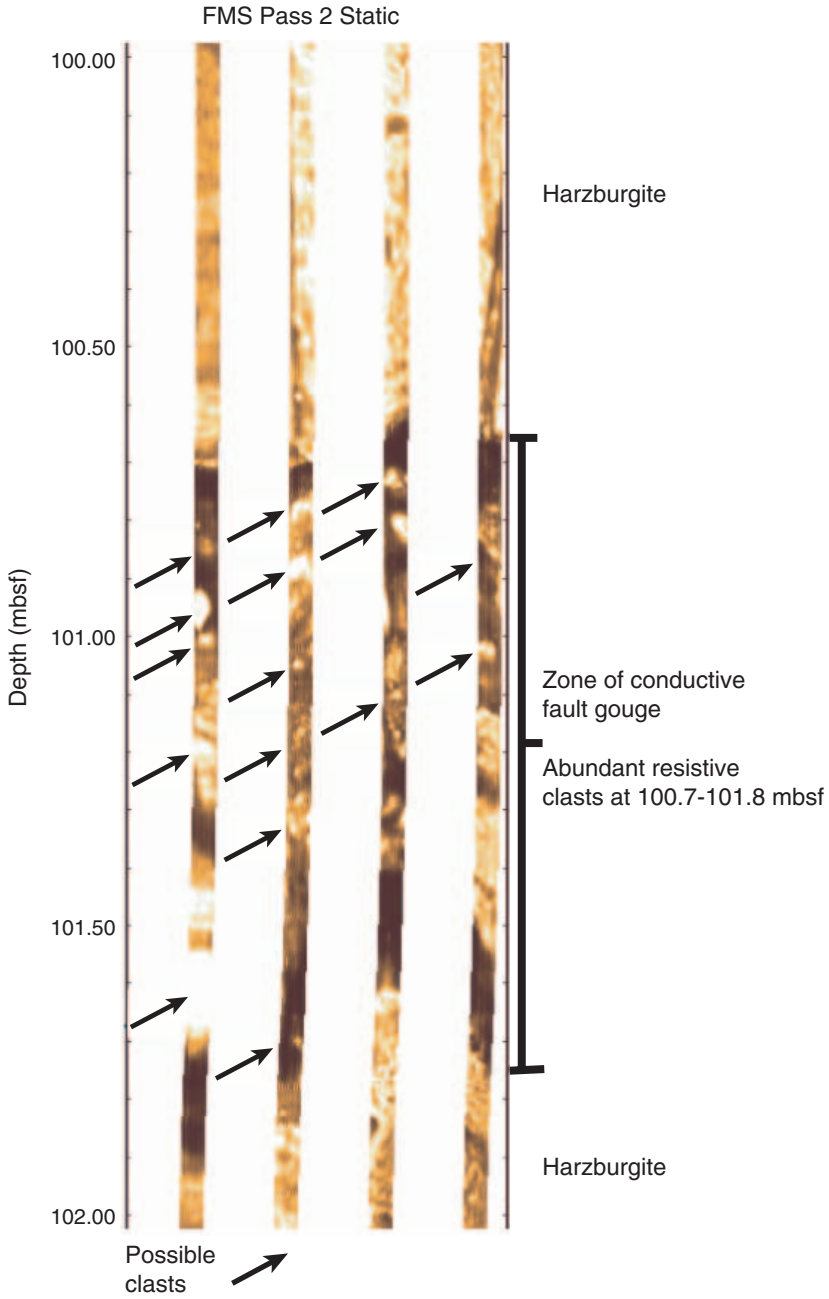

Figure F51. Lower hemisphere stereographic projection of poles to shear fractures and serpentine foliations. Apparent dips are rotated to a common orientation using the measured paleomagnetic declination. Fractures are generally shallowly dipping.

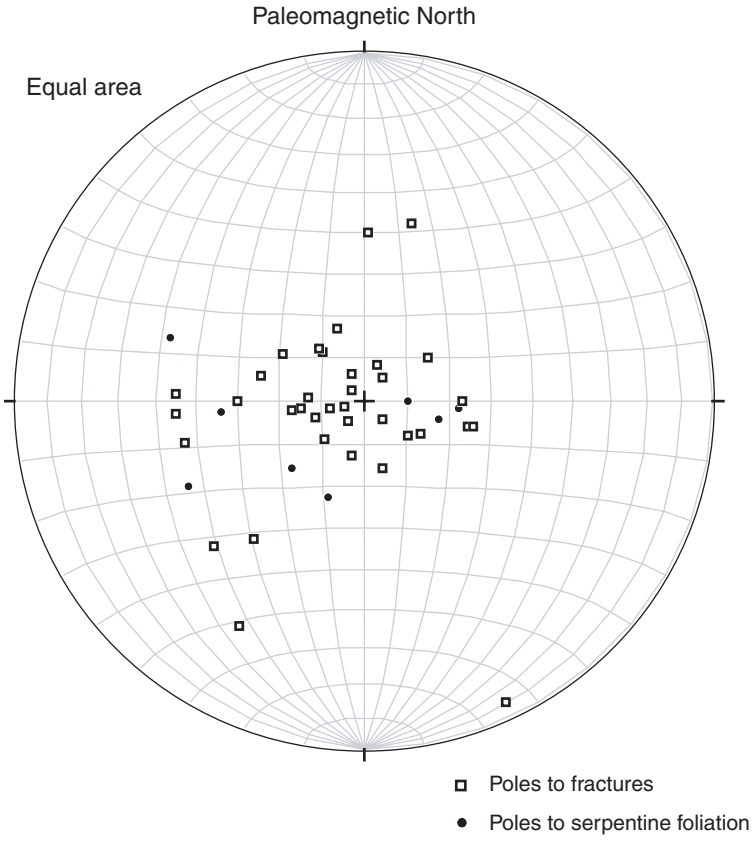

Figure F52. Downhole intensity of shear fractures and alteration vein intensity compared with the location of the fault gouges inferred from FMS images and plotted in Figure F79, p. 119. Note that most zones of high fracture intensity seem to be correlated with major fault gouge zones. There may also be a correlation between the location of the fault gouge and the intensity of veining. TD = total depth.

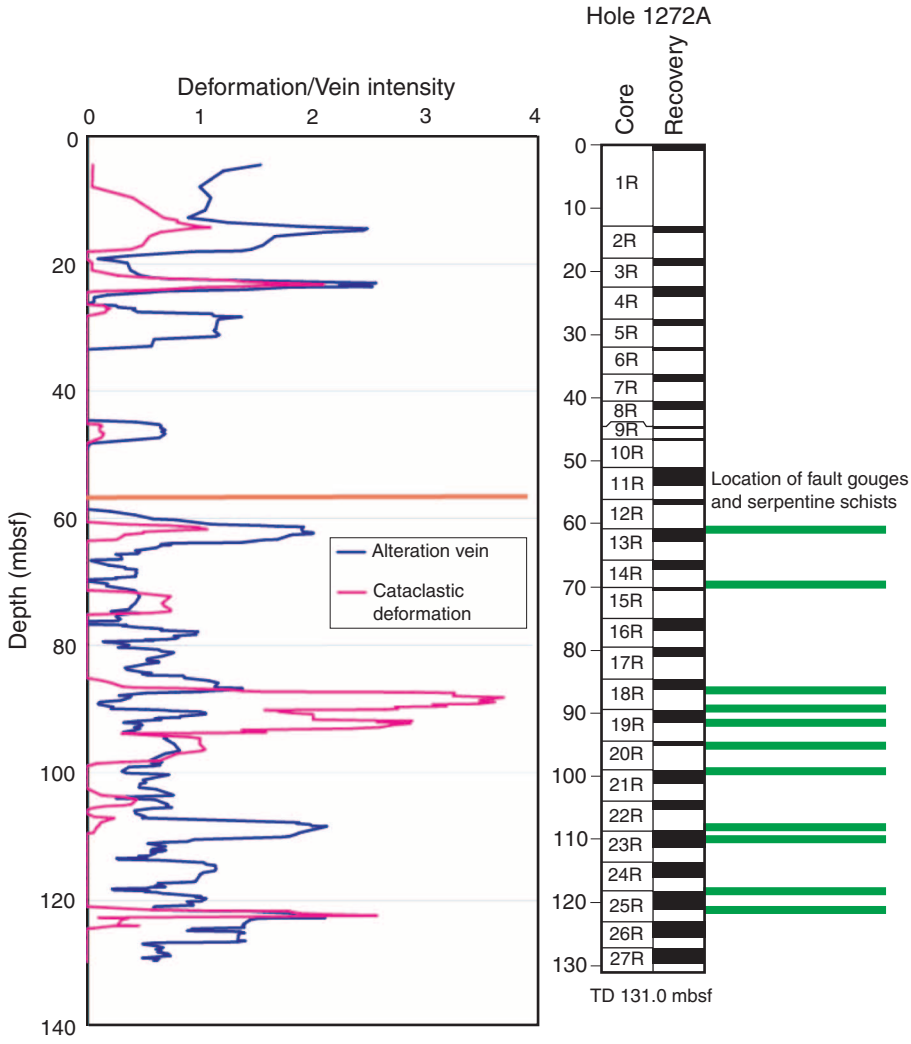

Figure F53. Loss on ignition (LOI), SiO_2, and Fe_2O_3 vs. MgO for peridotites from Site 1272. Bulk rock compositions of Site 1268, 1270, and 1271 peridotites as well as serpentinized peridotites from ODP Site 920 (Casey, 1997) are shown for comparison. Also shown for comparison are end-member compositions for lizardite and talc (Deer et al., 1992) and ODP Site 920 serpentinites (Dilek et al., 1997).

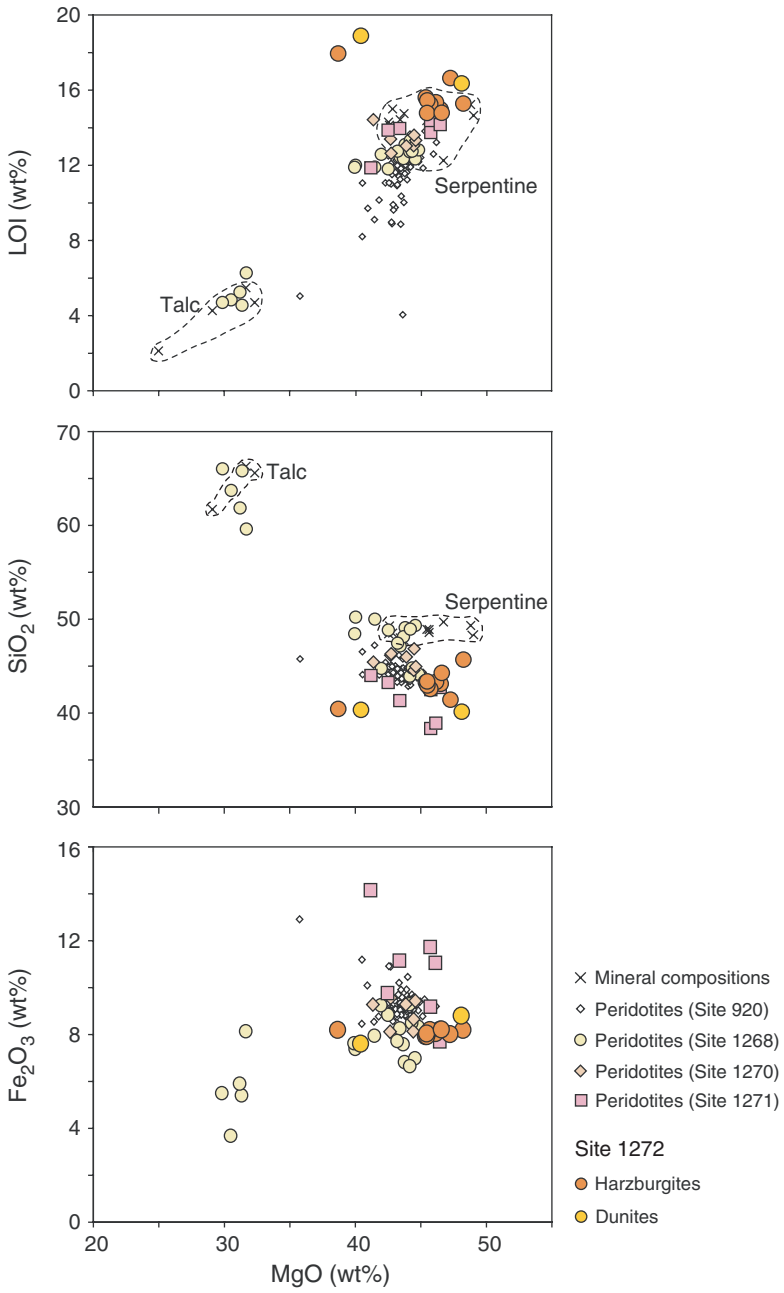

Figure F54. CaO vs. CO_2 for peridotites from Site 1272.

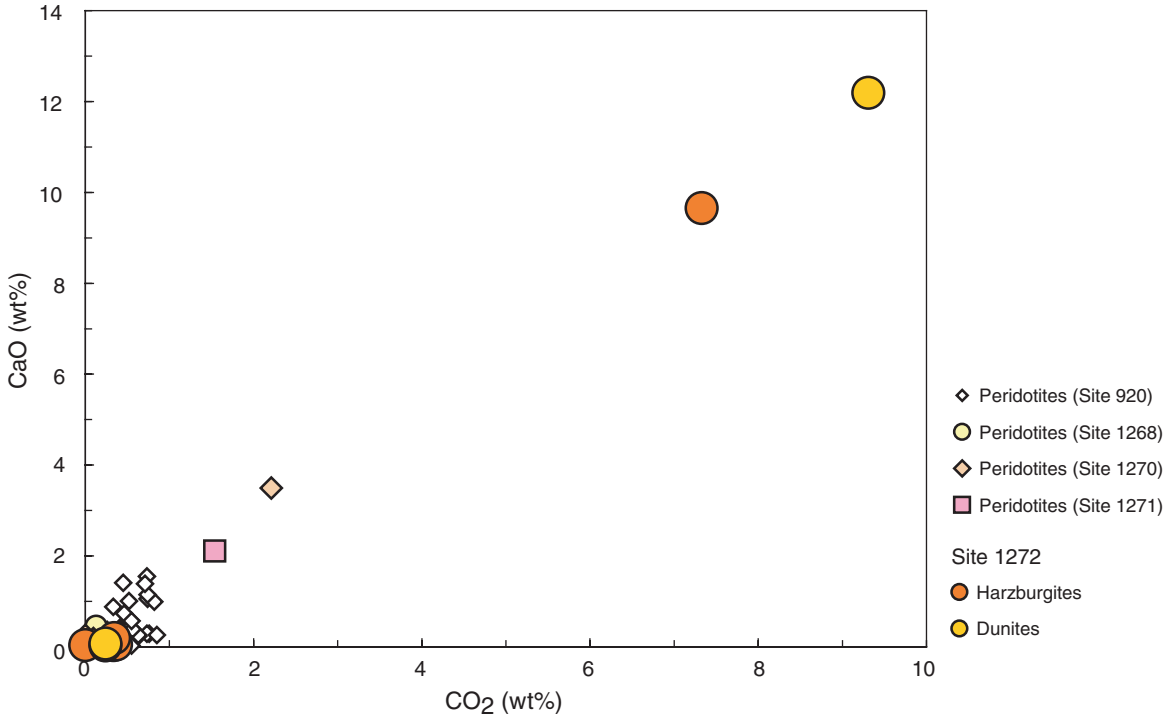

Figure F55. Ni vs. Mg# and Cr vs. Al_2O_3 in peridotites from Site 1272. Site 1268, 1270, and 1271 peridotite composition and published data on Leg 153 Site 920 peridotites (Casey, 1997) are shown for comparison.

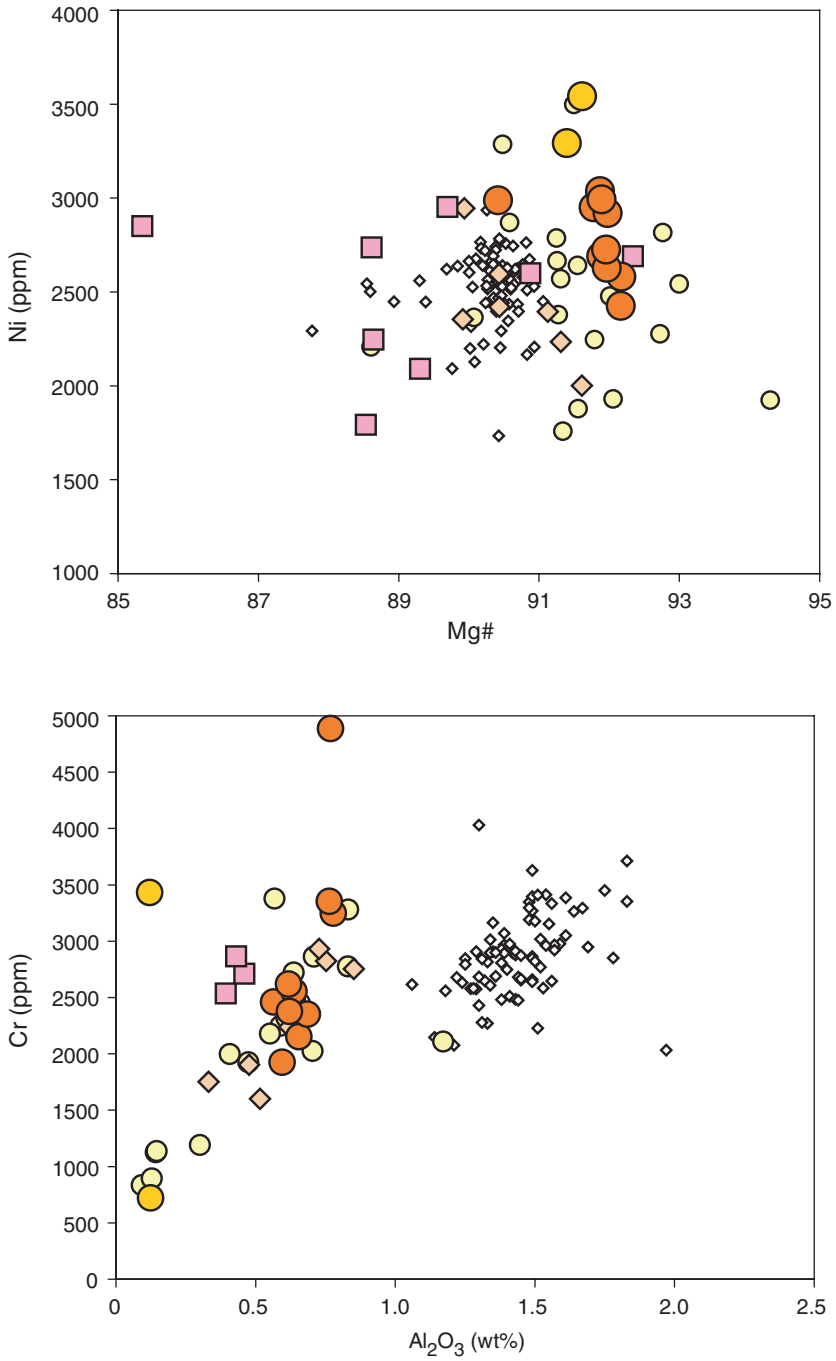

Figure F56. TiO_2, Zr, V, and Sc vs. Al_2O_3 in peridotites from Site 1272. Site 1268, 1270, and 1271 peridotite composition and published data on Leg 153 Site 920 peridotites (Casey, 1997) are shown for comparison. Dashed lines = detection limits (DL) for TiO_2, Sc, and Zr.

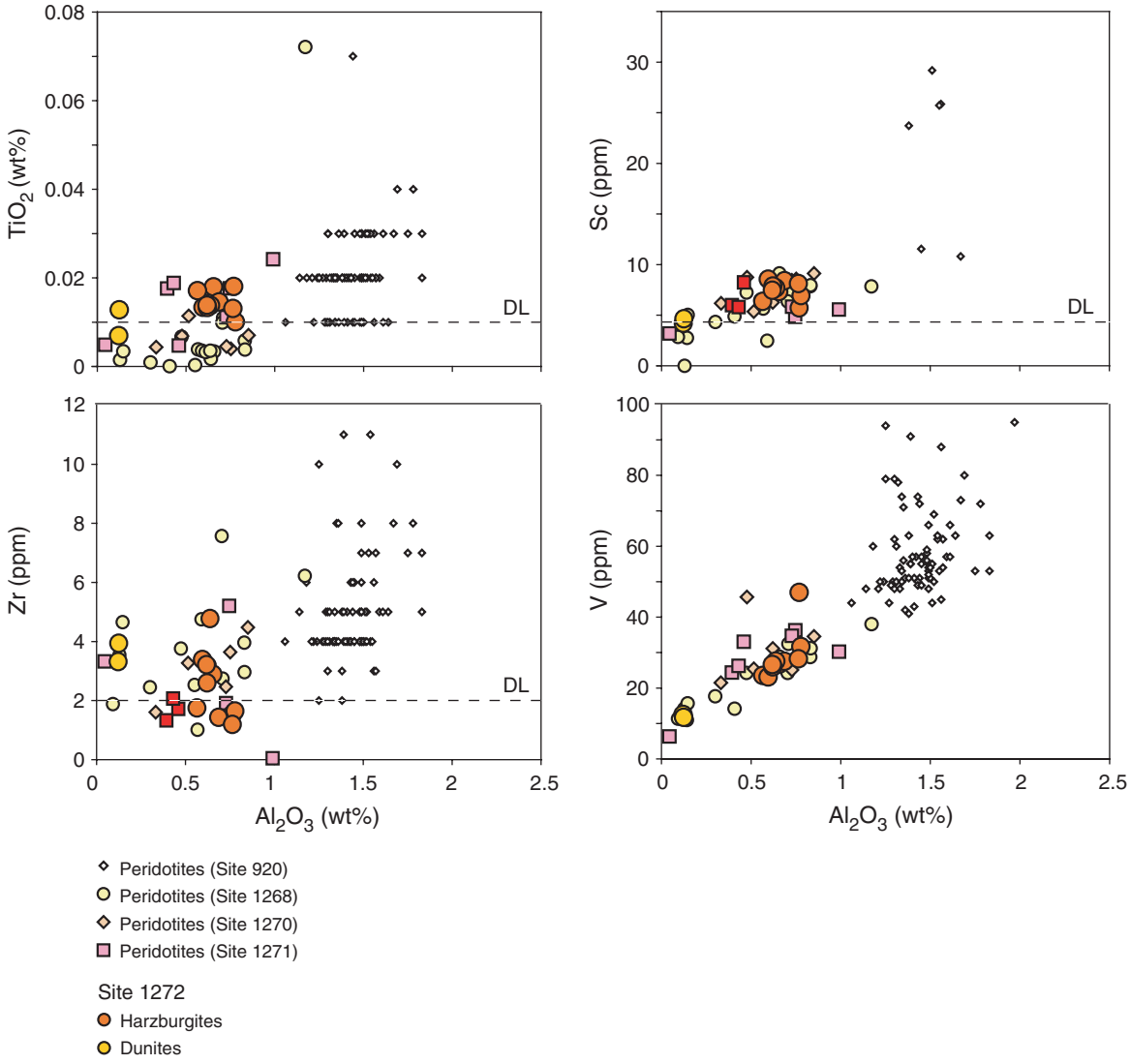

Figure F57. TiO_2, K_2O, Al_2O_3, CaO, Na_2O, and FeO vs. MgO for mafic rocks from Site 1272. FeO is total Fe calculated from Fe_2O_3. Basalts from the South Kane Fracture Zone (S MARK) area are shown for comparison (data from Meurer et al., 2001).

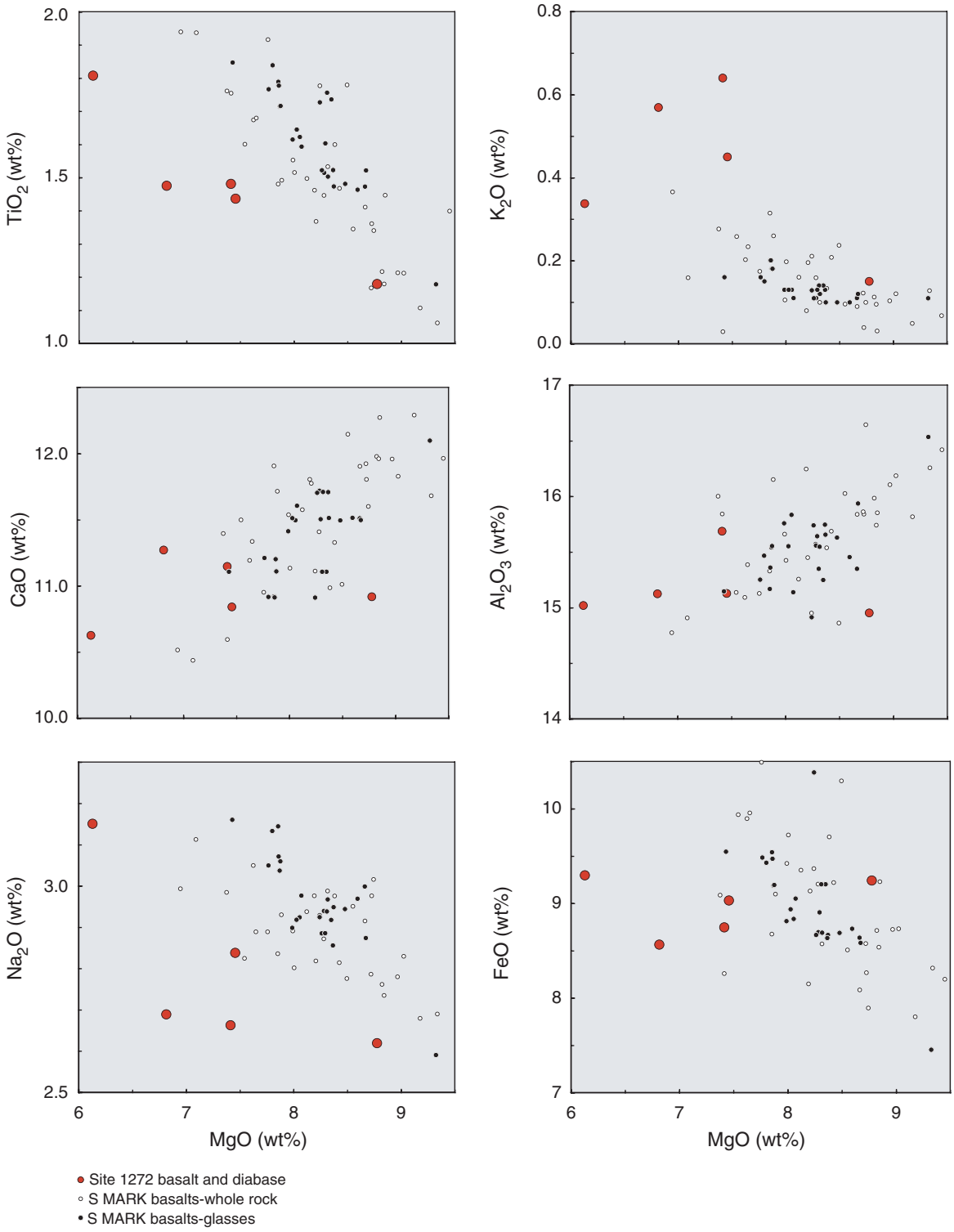

Figure F58. H_2O vs. K_2O for mafic rocks from Site 1272. Data from a global study of mid-ocean-ridge basalt (MORB) glasses (Michael, 1995) are shown for comparison.

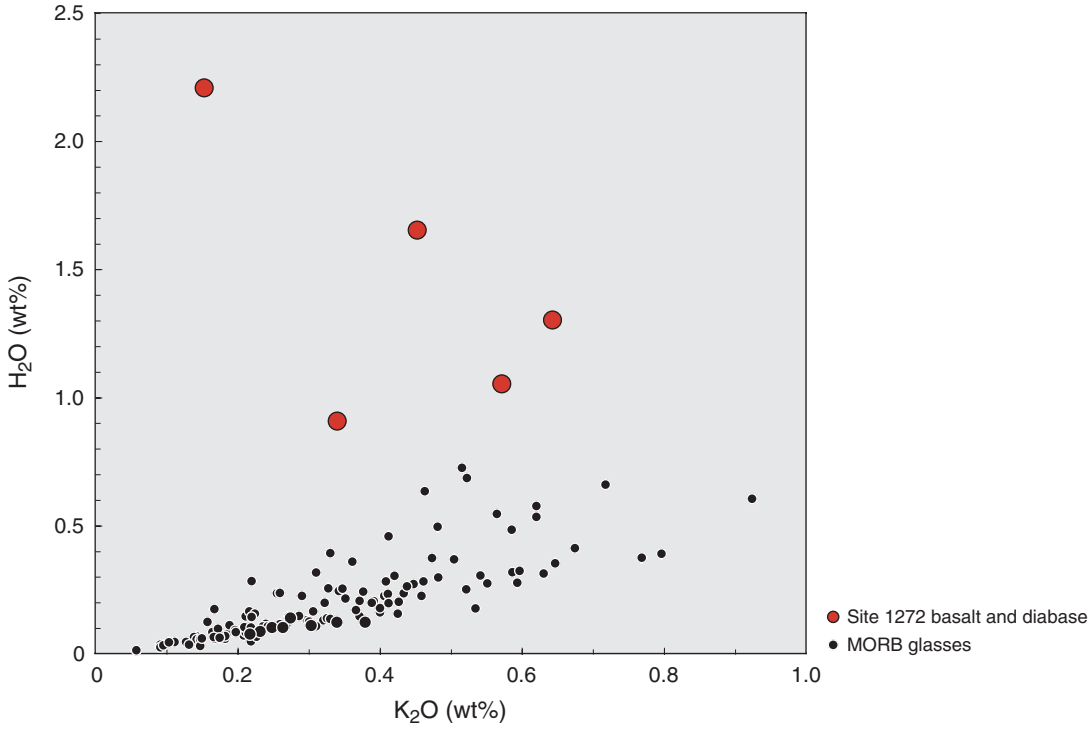

Figure F59. Cr vs. MgO for mafic rocks from Site 1272. Basalts from the South Kane Fracture Zone (S MARK) area are shown for comparison (data from Meurer et al., 2001). Dashed line = detection limit (DL) for Cr.

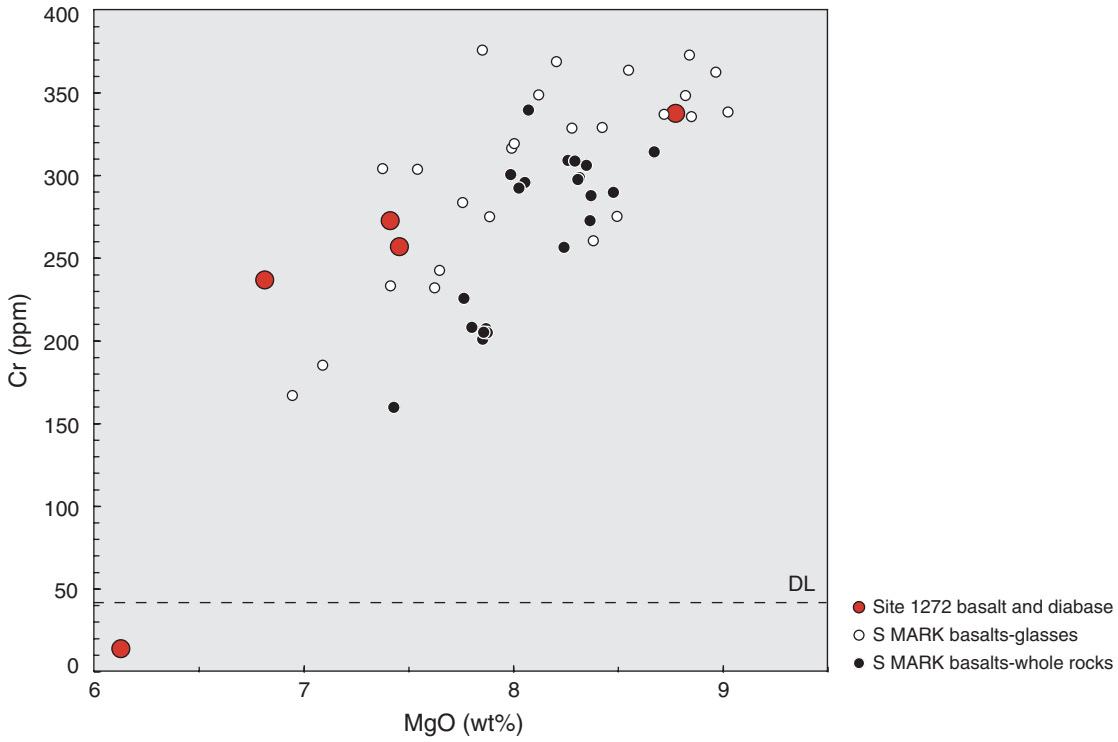

Figure F60. Zr vs. MgO and Sr vs. Zr for mafic rocks from Site 1272. Basalts from the South Kane Fracture Zone (S MARK) area are shown for comparison (data from Meurer et al., 2001).

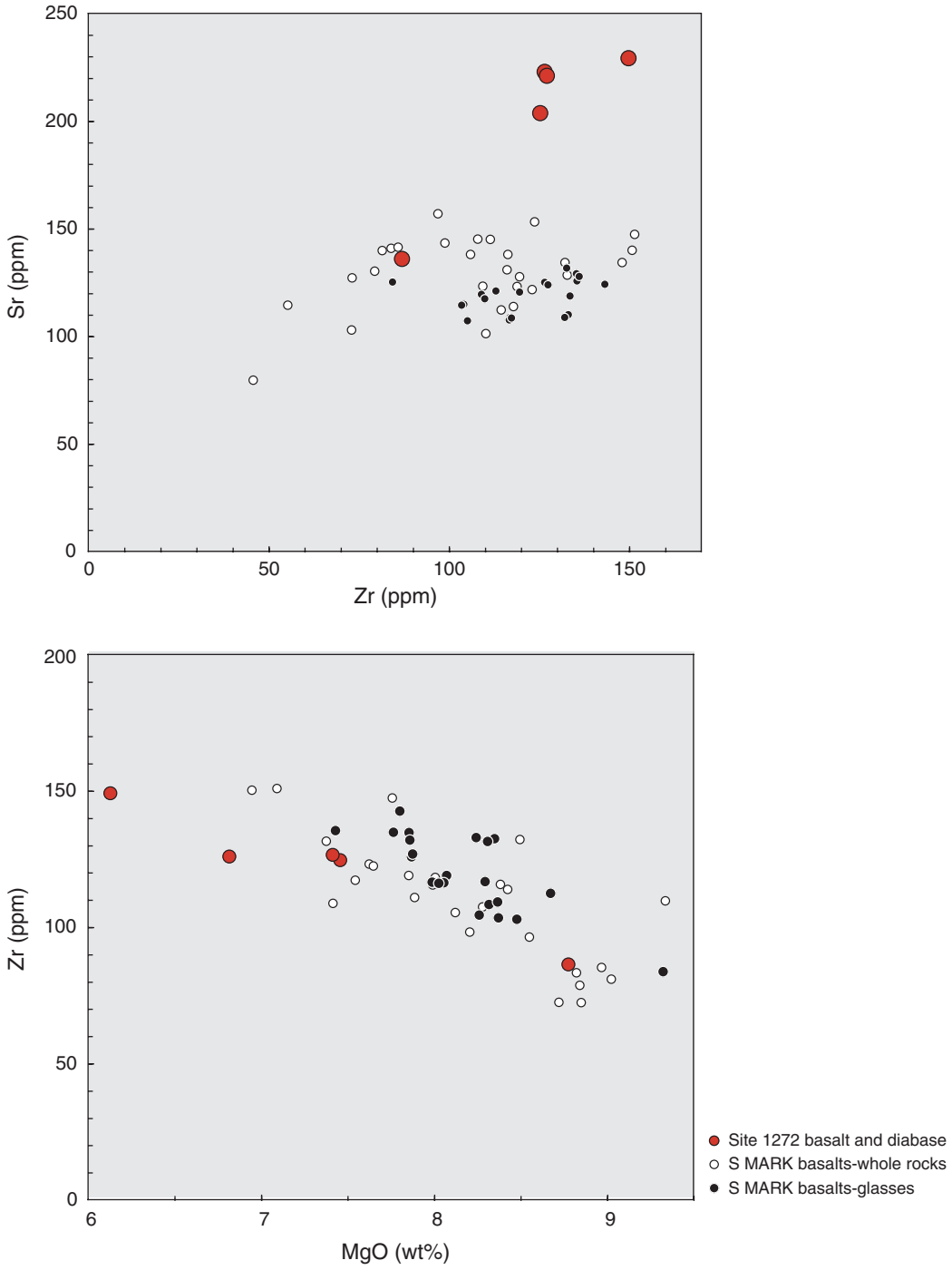

Figure F61. Thermal conductivity, *P*-wave velocity, apparent *P*-wave anisotropy, bulk density, and porosity in peridotites and gabbroic rocks (gabbros and diabases) recovered from Hole 1272A. The numbers 0, 1, and 2 in the legend of the thermal conductivity graph refer to the probe needle orientation with respect to the core axis (0 = parallel to the core axis, 1 and 2 = oblique to the core axis), as shown in Figure F11, p. 53, in the "Explanatory Notes" chapter. TD = total depth.

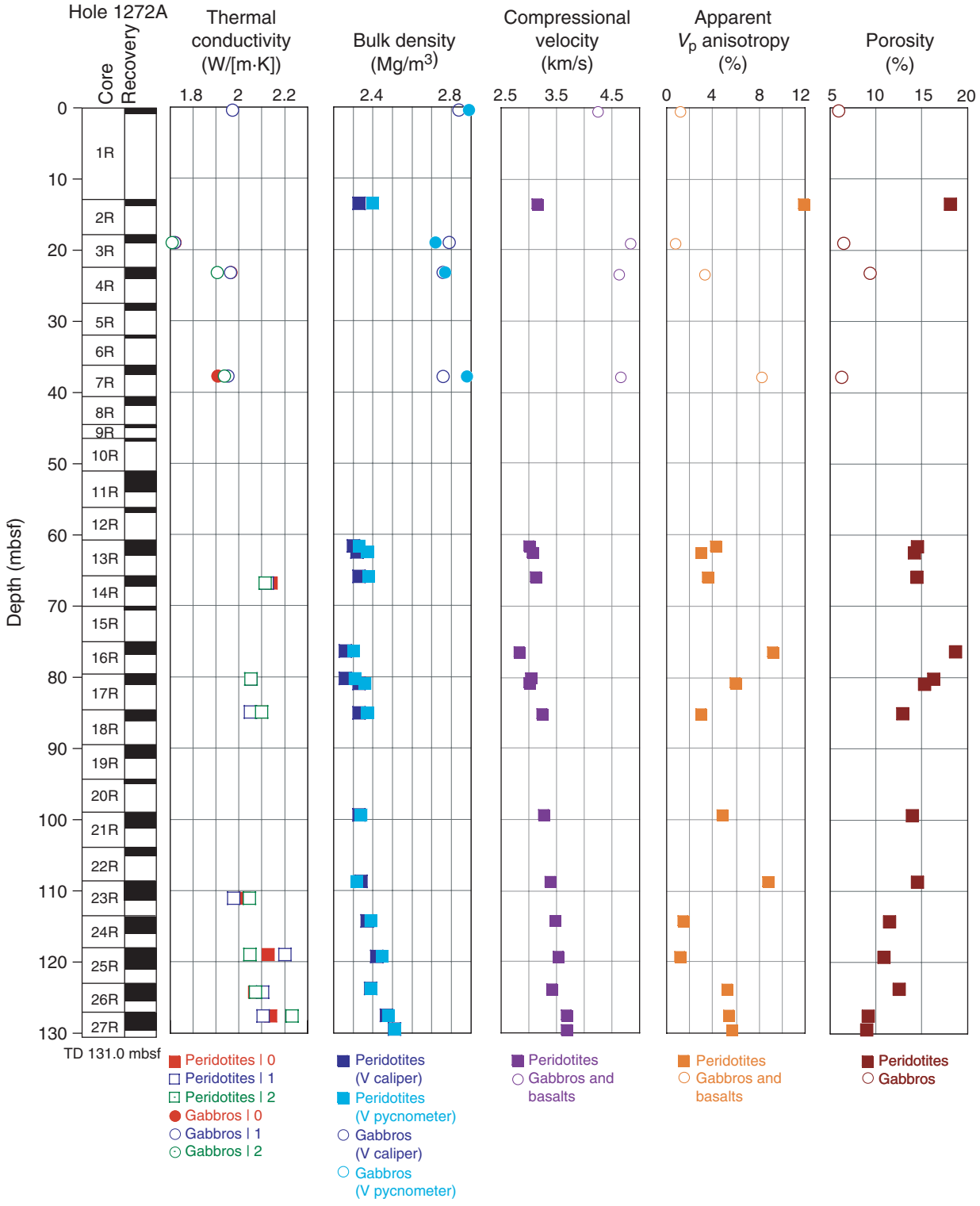

Figure F62. Magnetic susceptibility and natural gamma radiation (NGR) of cores from Hole 1272A, measured on the MST. TD = total depth.

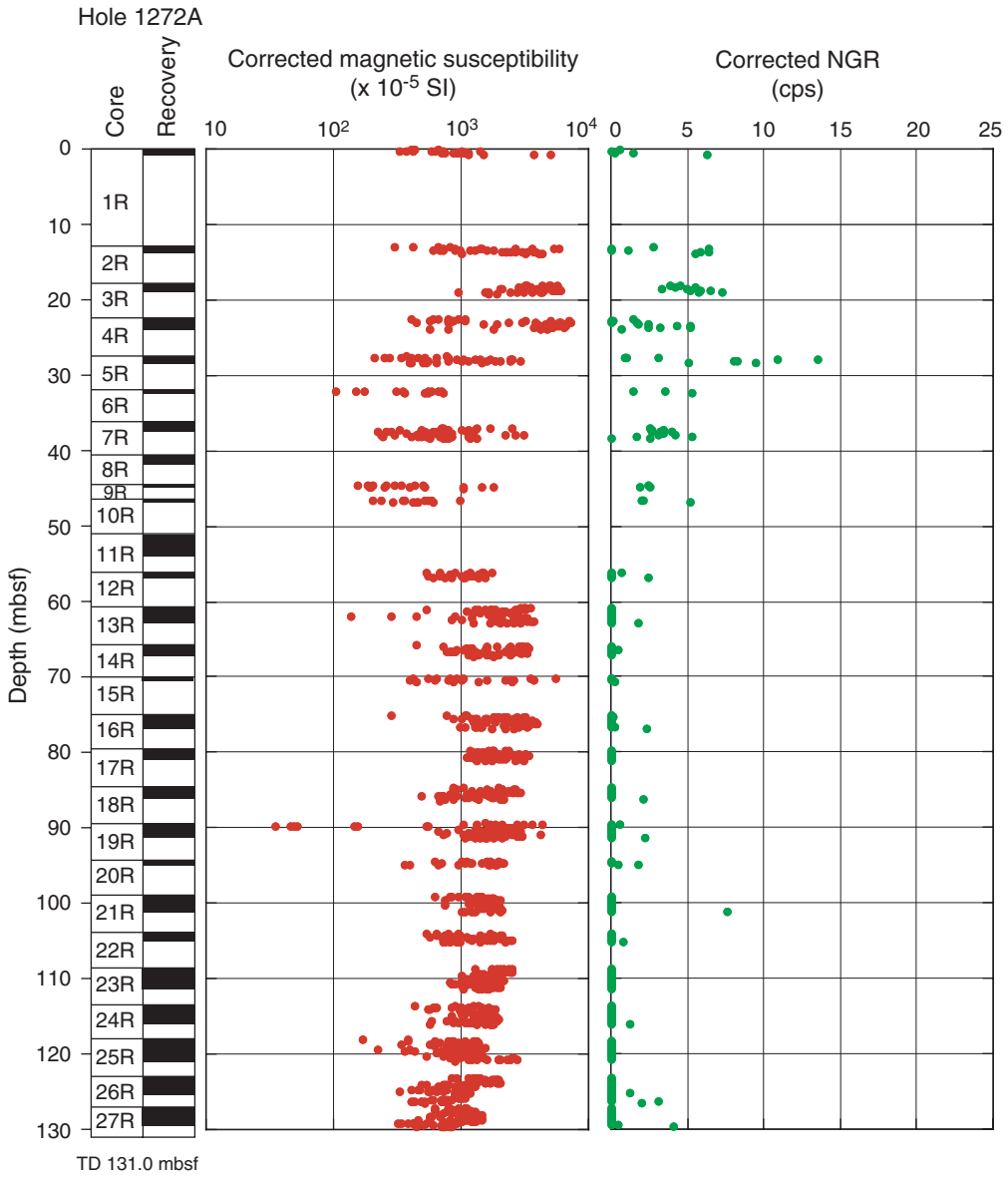

Figure F63. Thermal conductivity of peridotite, troctolite, gabbro, and diabase samples from Site 1272, compared with values from Sites 1268, 1270, and 1271, and from Legs 147 (Gillis, Mével, Allan, et al., 1993), 153 (Cannat, Karson, Miller, et al., 1995), and 176 (Robinson, Von Herzen, et al., 1989; Dick, Natland, Miller, et al., 1999).

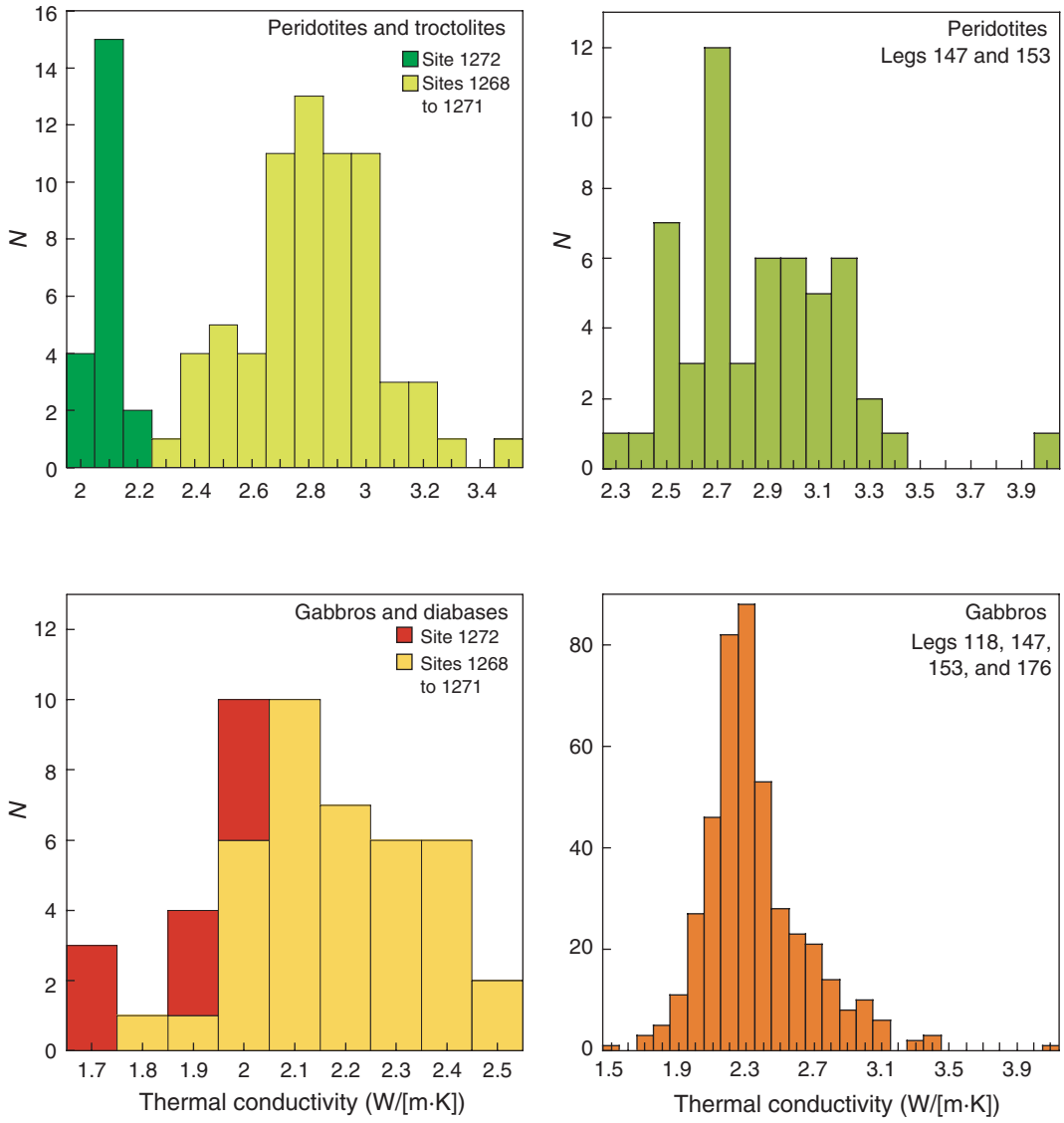

Figure F64. Apparent thermal conductivity anisotropy in peridotite and troctolite samples from Sites 1268, 1270, 1271, and 1272.

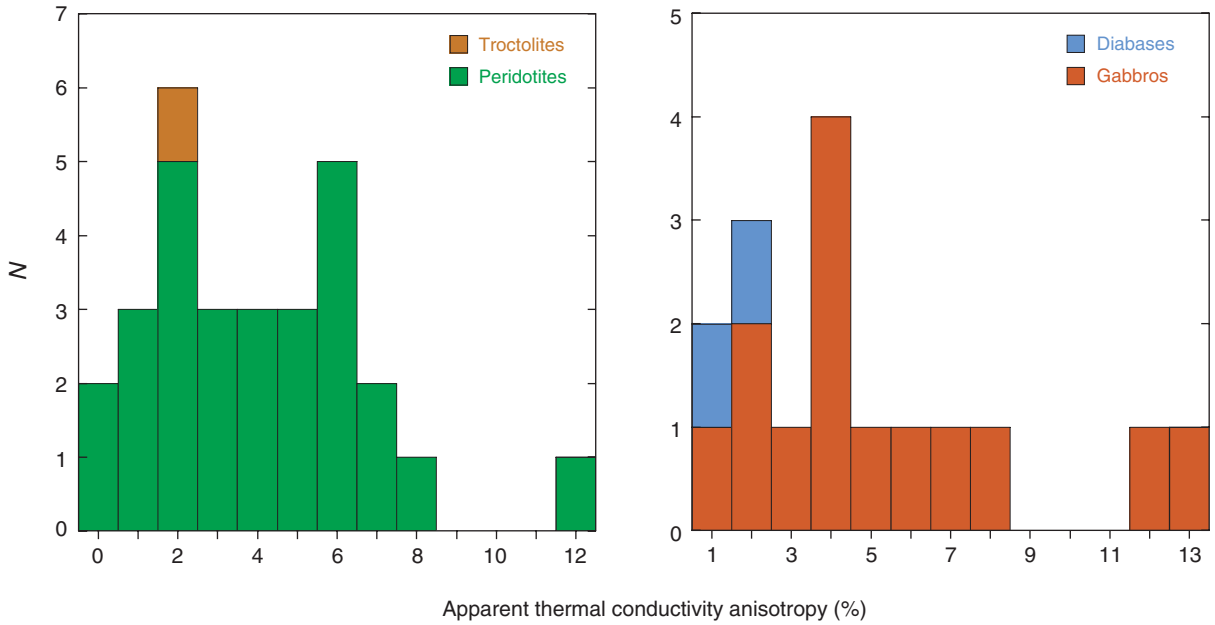

Figure F65. Thermal conductivity (mean of the three measured values for each sample) vs. bulk density in samples from Sites 1268, 1270, 1271, and 1272. The reference data are from Clark (1966) and Clauser and Huenges (1995).

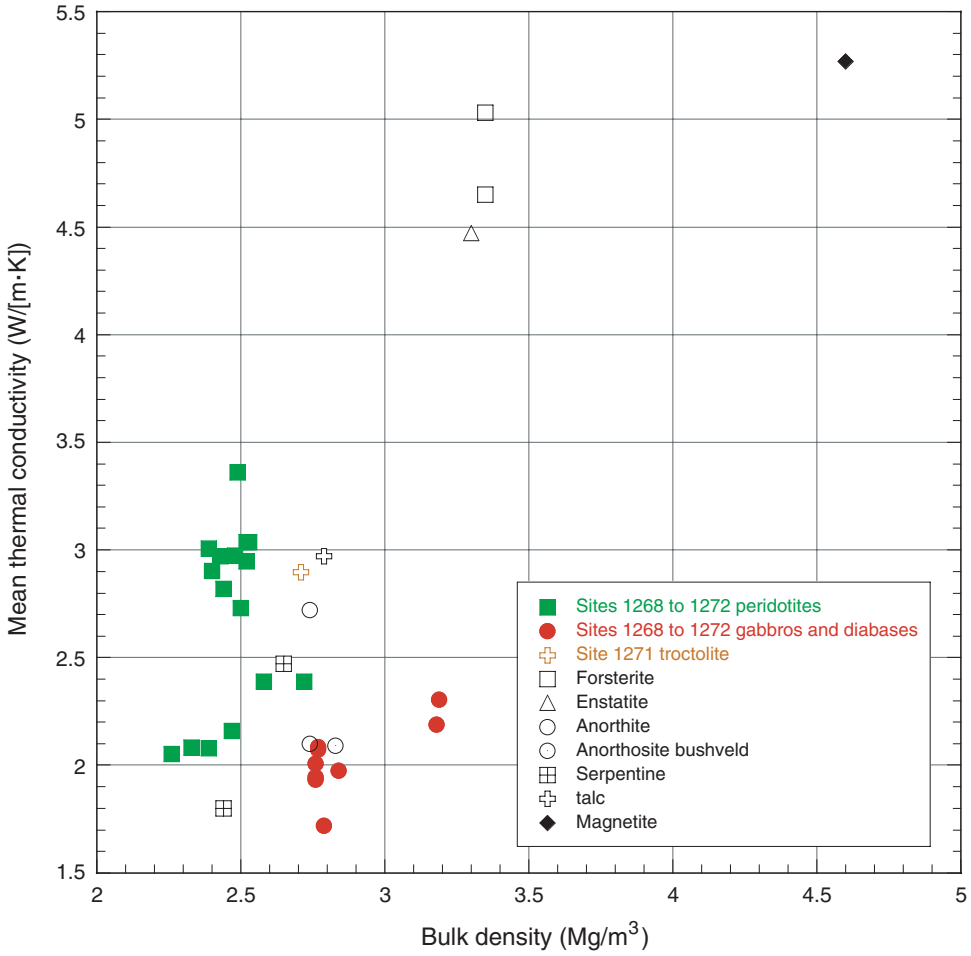

Figure F66. *P*-wave velocity vs. wet bulk density in samples from Site 1272, compared with data from Legs 147 (Gillis, Mével, Allan, et al., 1993; Iturrino et al., 1996) and 153 (Cannat, Karson, Miller, et al., 1995; Miller and Christensen, 1997), as well as Sites 1268, 1270, and 1271.

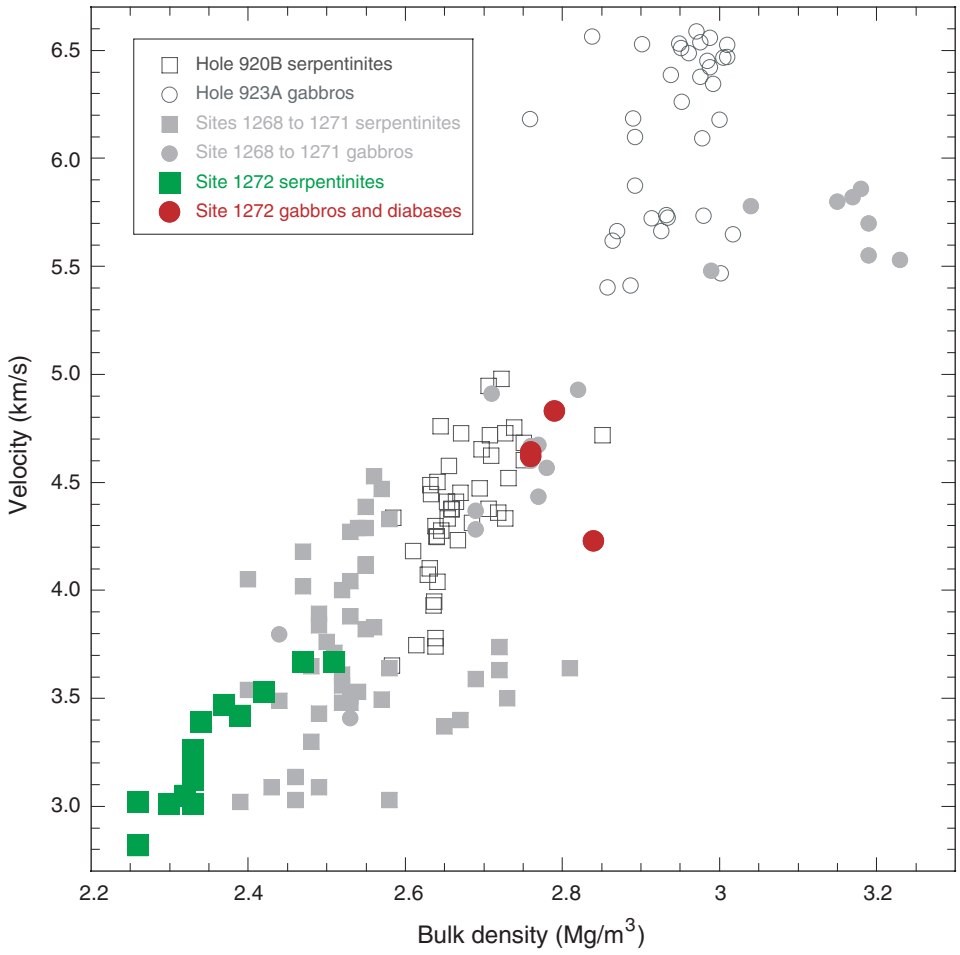

Figure F67. Archive-half magnetic measurements in Hole 1272A of volume magnetic susceptibility, natural remanent magnetization (NRM) intensity (open diamonds) and the characteristic remanent (ChRM) intensity (solid circles) calculated by principal component analysis, NRM and ChRM inclination, and percentage of the NRM intensity carried by the ChRM. TD = total depth.

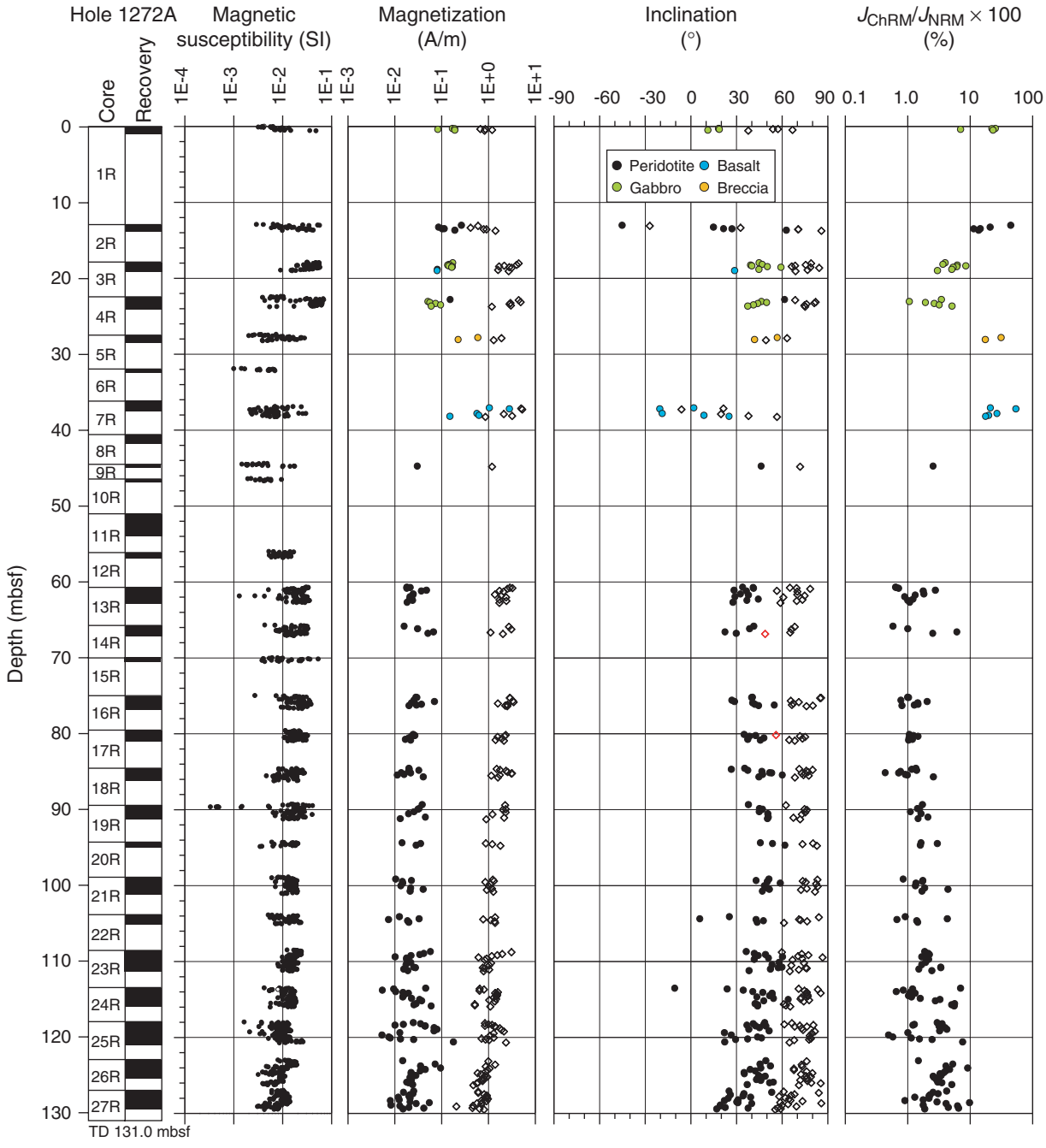

Figure F68. Representative vector endpoint demagnetization diagrams for discrete samples (A, C, E–G) and archive-half (B, D) measurements from Unit I. **A.** Microgabbro (Sample 209-1272A-1R-1, 44–46 cm). **B.** Altered dunite (Section 209-1272A-2R-1, 20 cm). **C.** Altered dunite (Sample 209-1272A-2R-1, 63–65 cm). **D.** Olivine gabbro (Section 209-1271A-3R-1, 54 cm). **E.** Diabase (Sample 209-1272A-3R-1, 114–116 cm). **F.** Olivine gabbro (Sample 209-1272A-4R-1, 85–87 cm). **G.** Diabase (Sample 209-1272A-7R-1, 96–98 cm). NRM = natural remanent magnetization. Open circles = projections of the remanence onto the vertical plane, solid circles = projections of the remanence onto the horizontal plane.

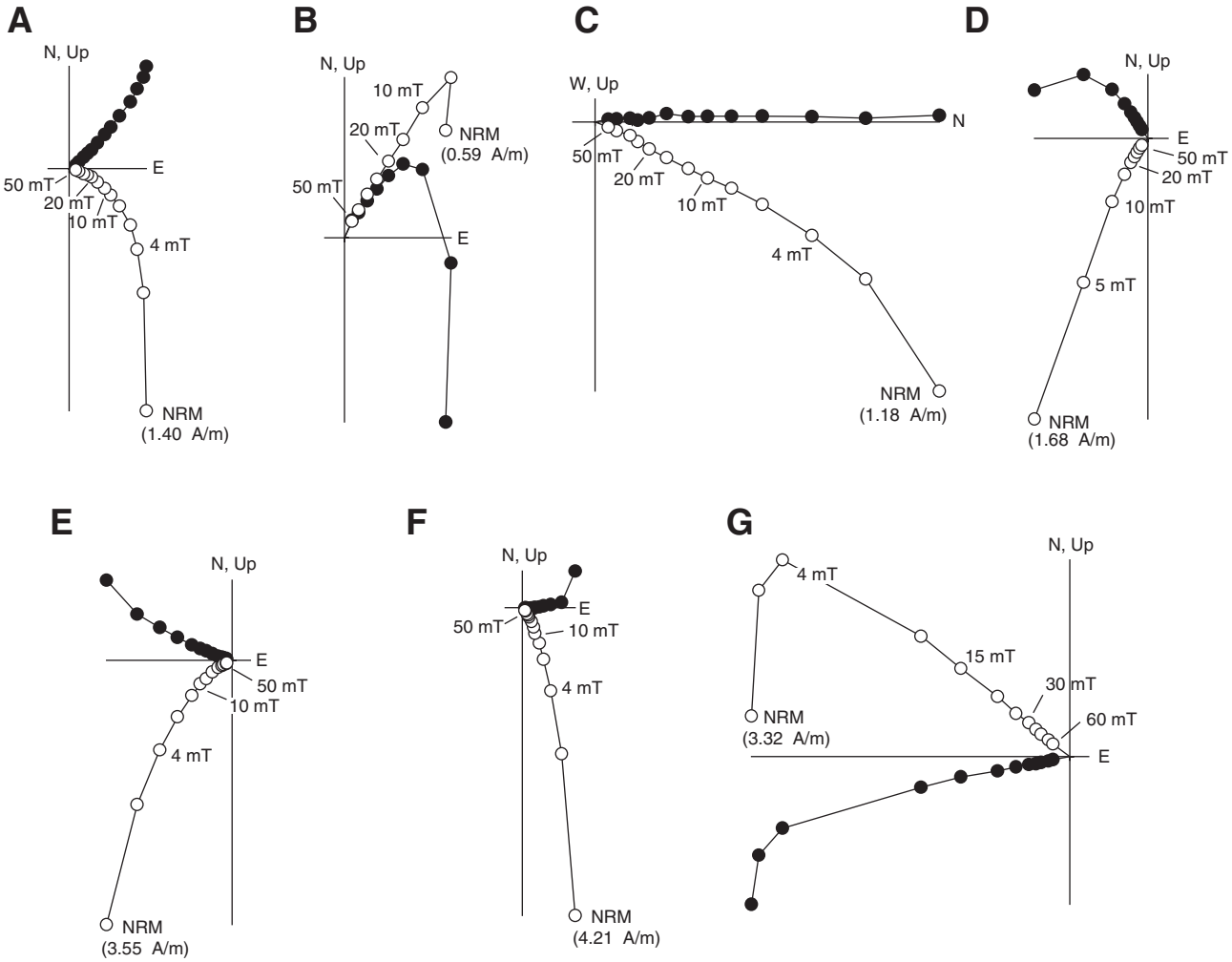

Figure F69. Representative vector endpoint demagnetization diagrams for discrete samples (A–C) and archive-half measurements (D–F) from Unit II. **A.** Sample 209-1272A-23R-1, 24–26 cm. **B.** Sample 209-1272A-27R-1, 52–54 cm. **C.** Sample 209-1272A-27R-2, 93–95 cm. **D.** Section 209-1272A-23R-1, 24 cm. **E.** Section 209-1272A-27R-1, 52 cm. **F.** Section 209-1272A-27R-2, 94 cm. NRM = natural remanent magnetization. Open circles = projections of the remanence onto the vertical plane, solid circles = projections of the remanence onto the horizontal plane.

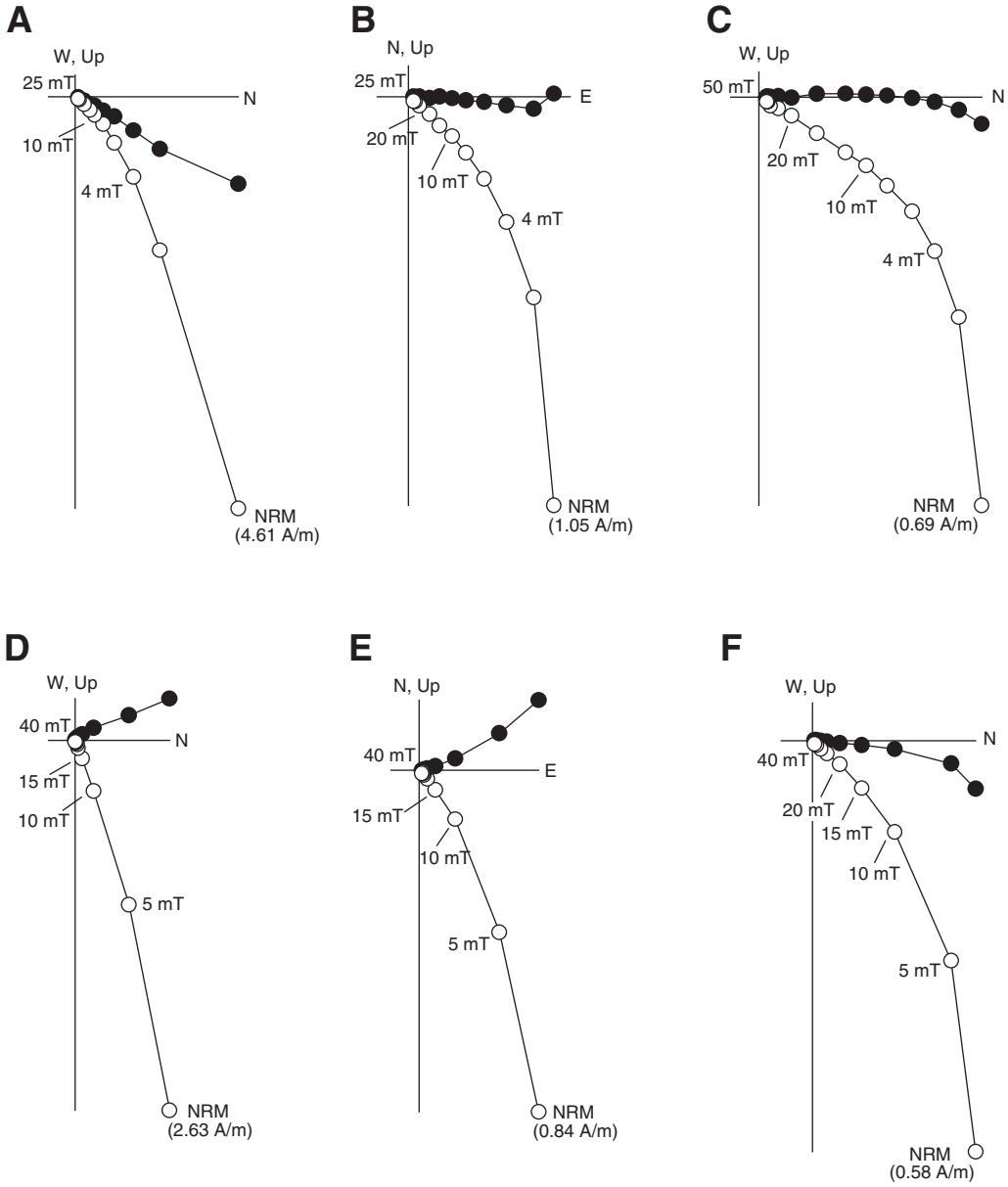

Figure F70. Histograms of (**A**) inclinations and (**B**) declinations for discrete samples (white bars) and archive halves (shaded bars) from Hole 1272A.

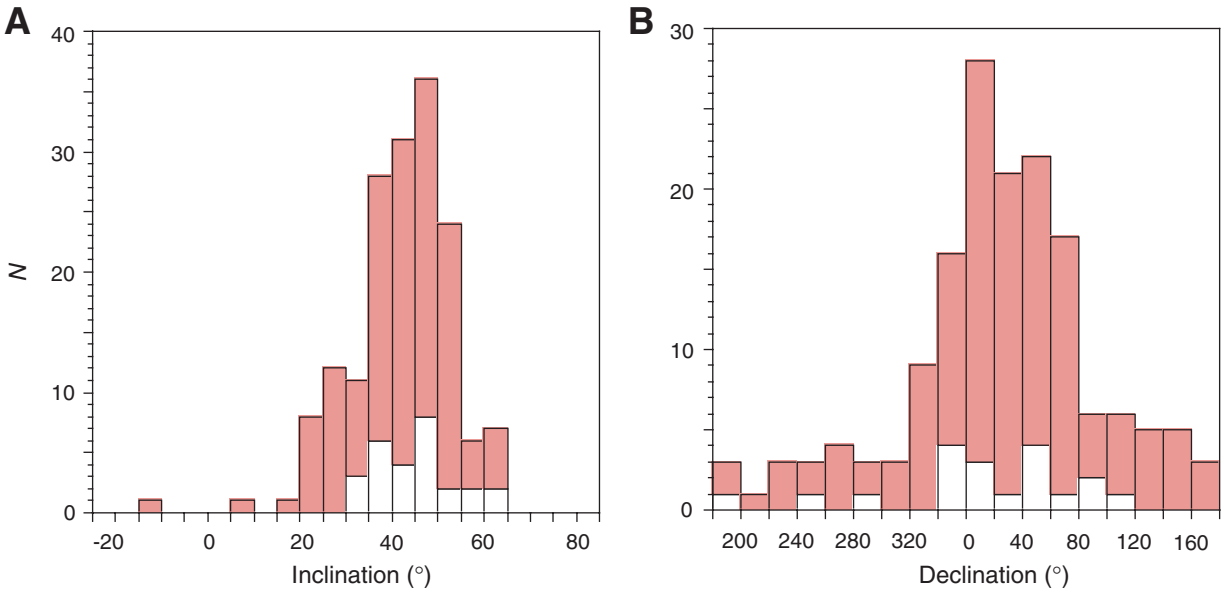

Figure F71. Lower hemisphere equal-area projections showing the eigenvectors associated with the (**A**) minimum and (**B**) maximum eigenvalues of the susceptibility tensor for peridotite samples from Unit II.

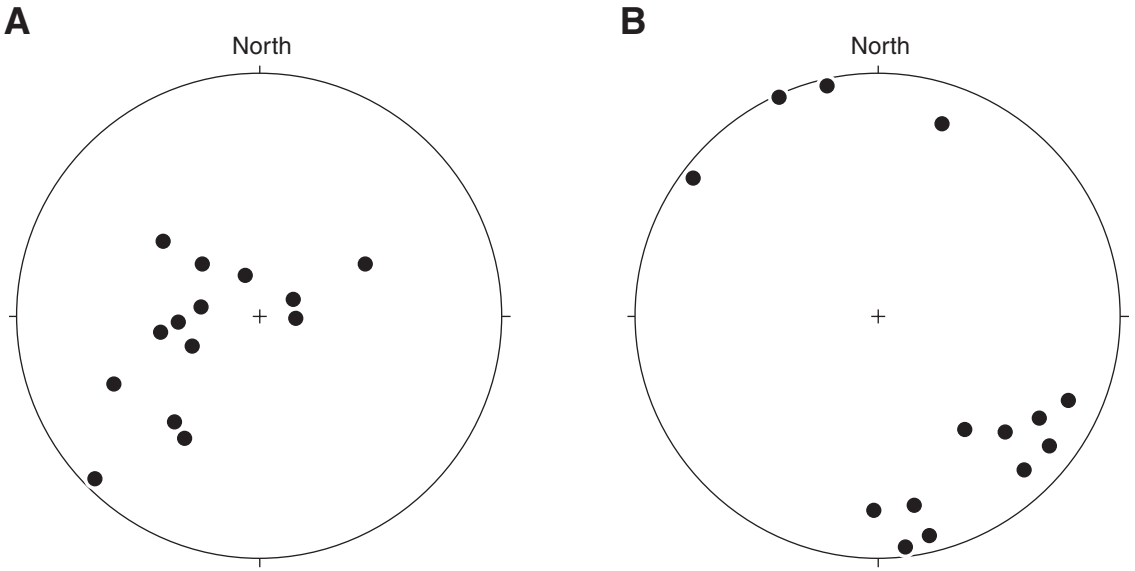

Figure F72. Correlation of geophysical logs and laboratory data (open and solid circles) from Hole 1272A. Also shown are core recovery and zones with high values (yellow bands) that are correlated throughout all the curves. TD = total depth. FMS = Formation MicroScanner. BHA = bottom-hole assembly.

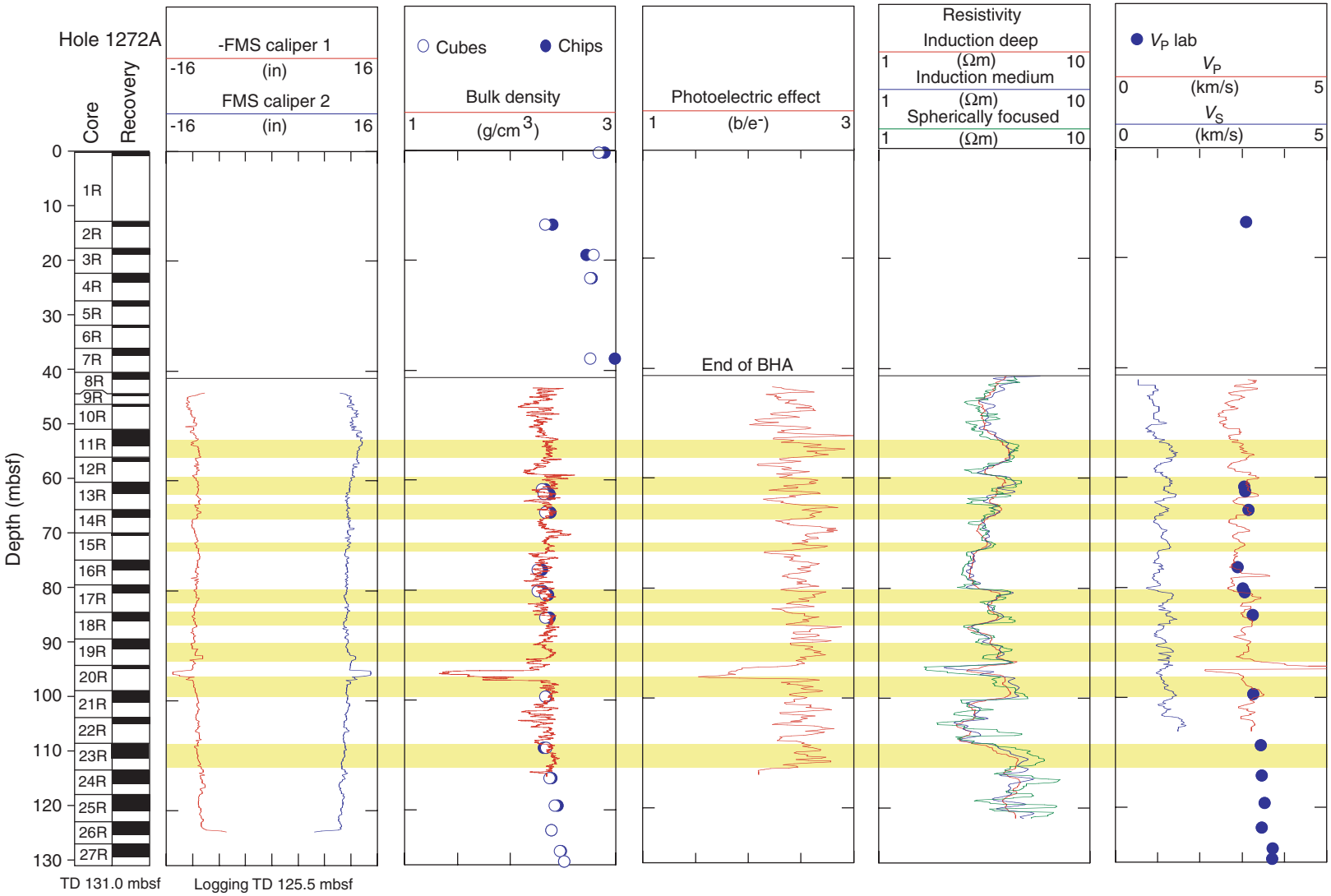

Figure F73. Downhole logs obtained with the GPIT showing borehole dimensions, hole azimuth, deviation, Formation MicroScanner (FMS) pad 1 azimuth, inclination, magnetic field components (F_x,F_y, and F_z), and total magnetic field values (FNOR). TD = total depth.

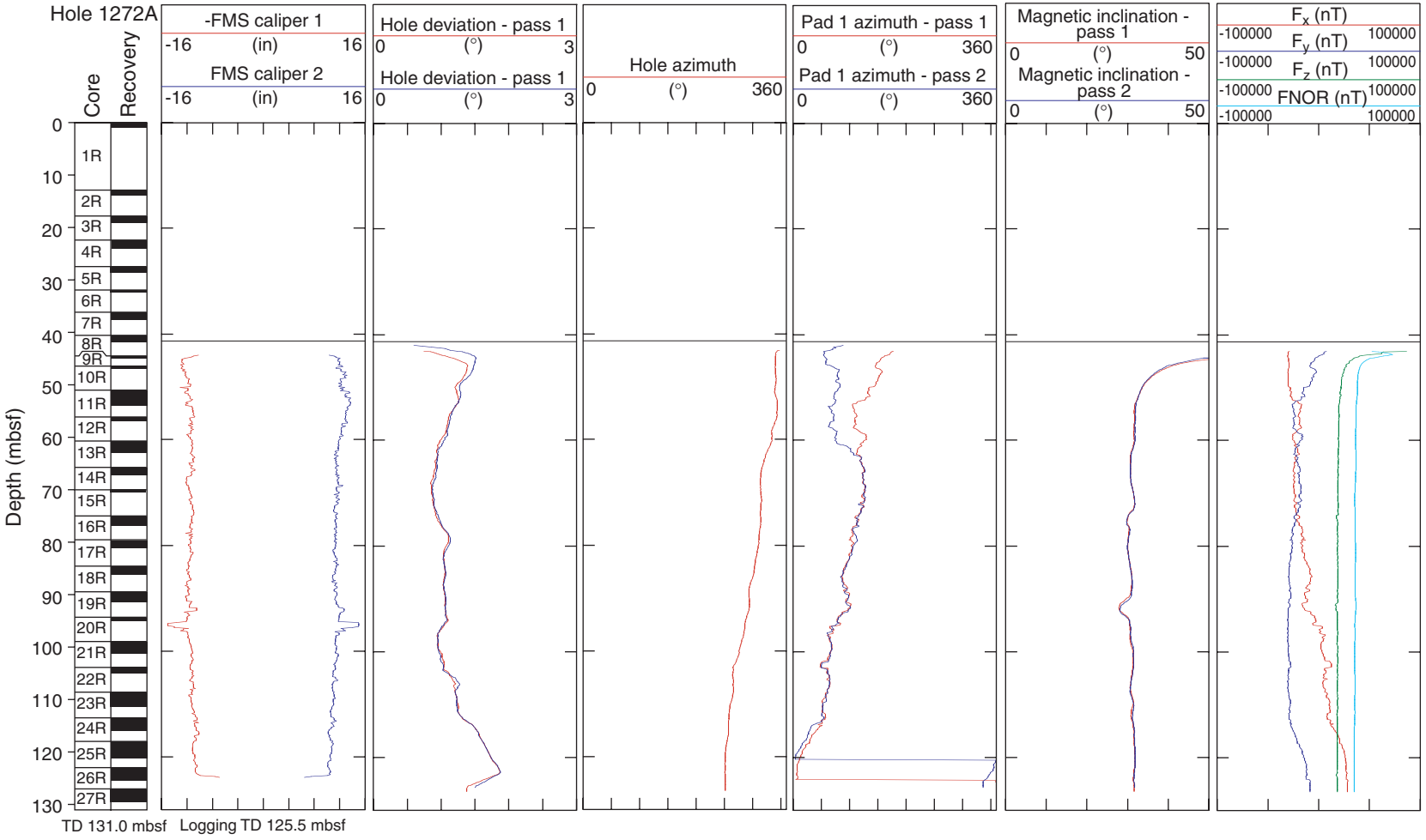

Figure F74. Estimation of magnetic anomalies using the GPIT magnetic measurements. **A.** Model used for estimating and removing the effect of the drill pipe on the vertical magnetic field component. **B.** Resulting magnetic anomalies after correcting for pipe effect and offset in vertical magnetic component.

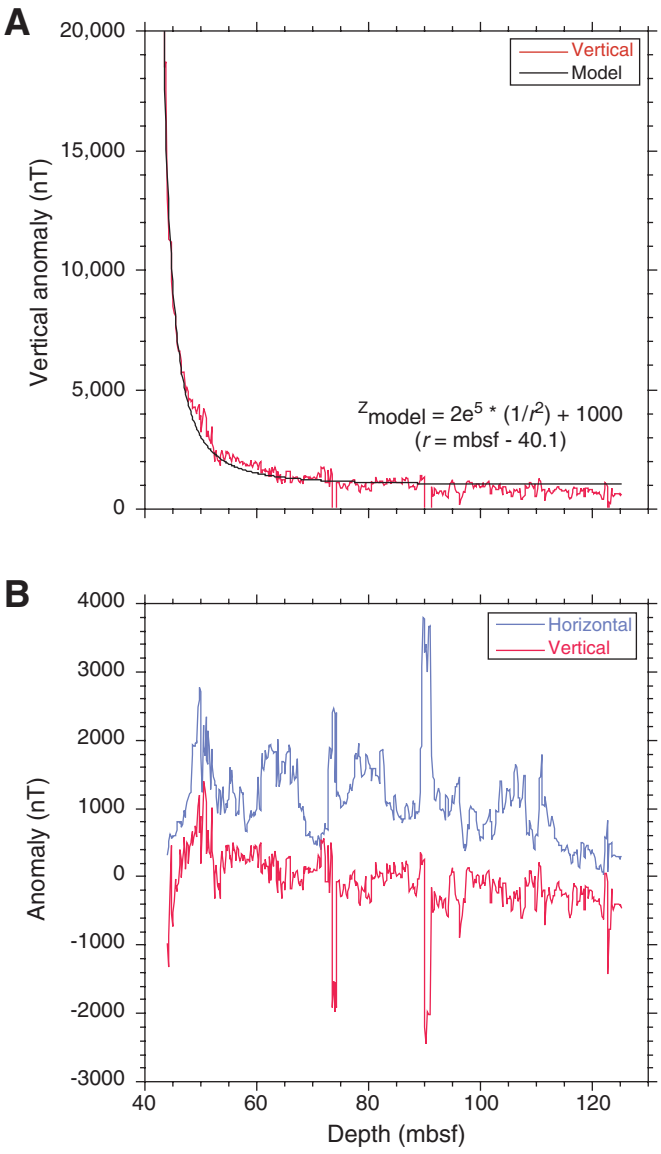

Figure F75. Static and dynamic FMS images for 89.5–93.5 mbsf showing a potential faulted zone. This zone correlates with fault gouge and oxide gabbro samples recovered from Section 209-1272A-19R-1.

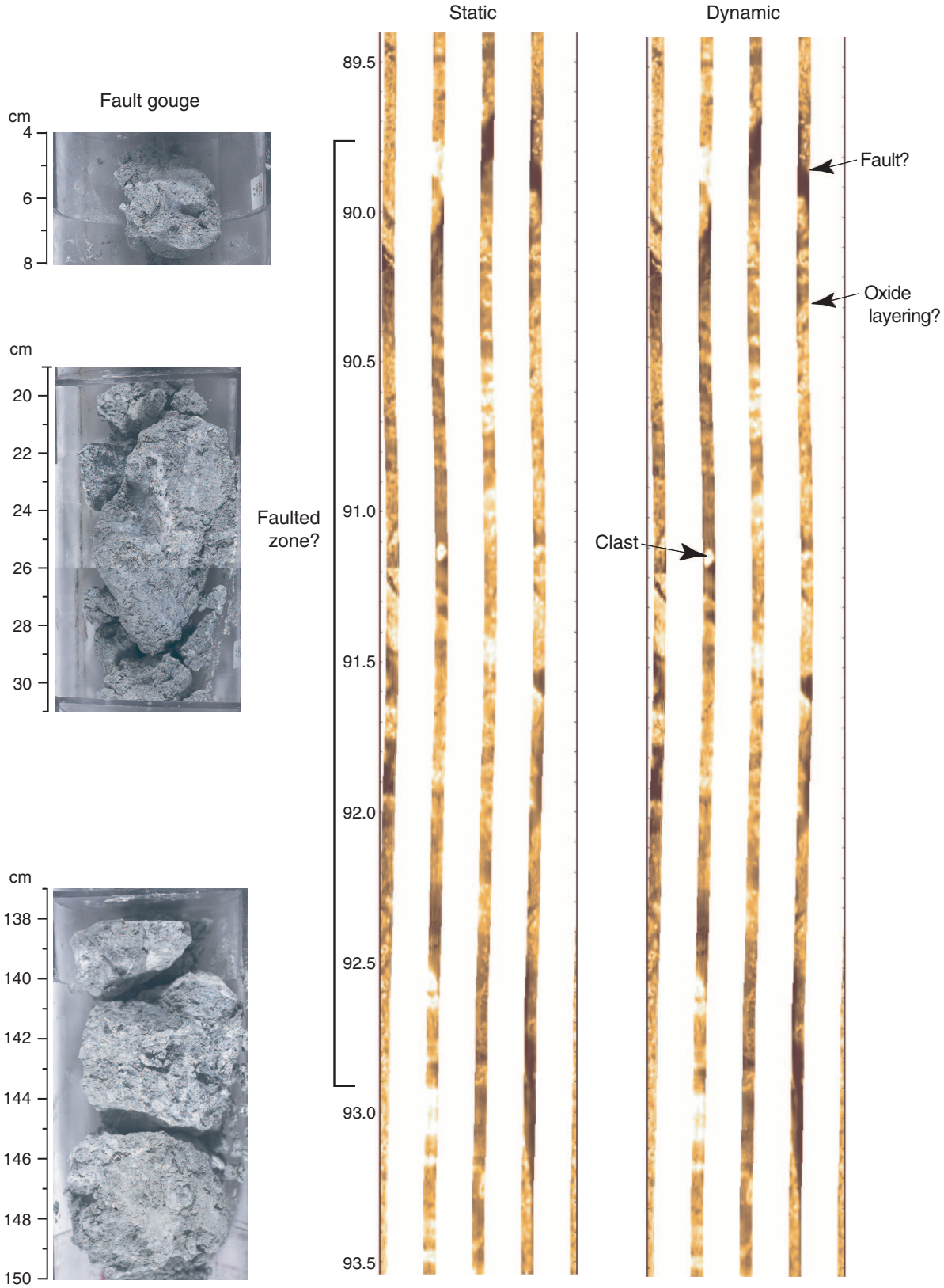

Figure F76. Apparent fault and steep fractures identified FMS images. Fault gouge samples were also recovered from this interval (209-1272A-19R-2, 0–18 cm).

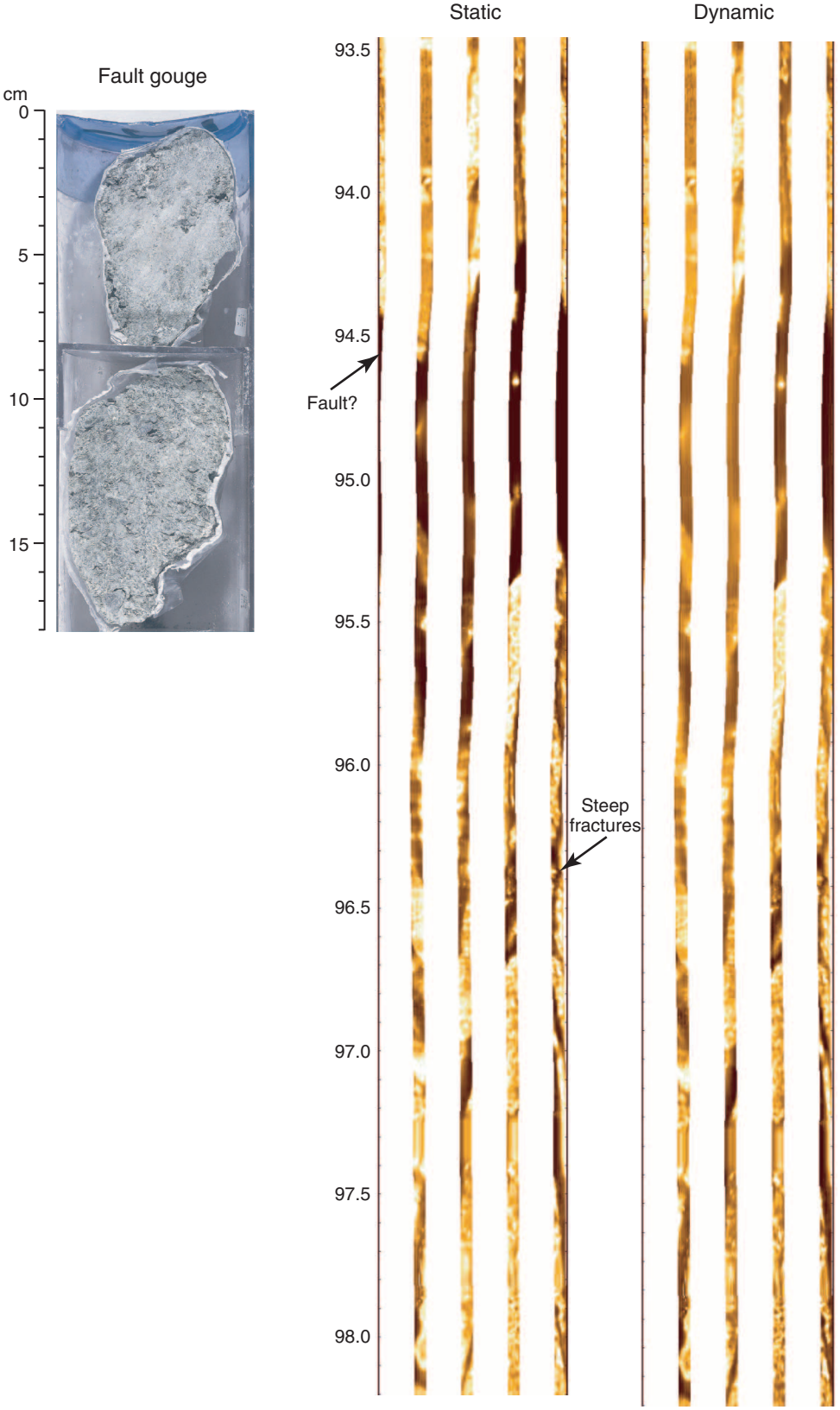

Figure F77. Strong resistivity contrast interpreted to be a fault zone in FMS images. This zone correlates with one soapstone sample recovered from Section 209-1272A-21R-1.

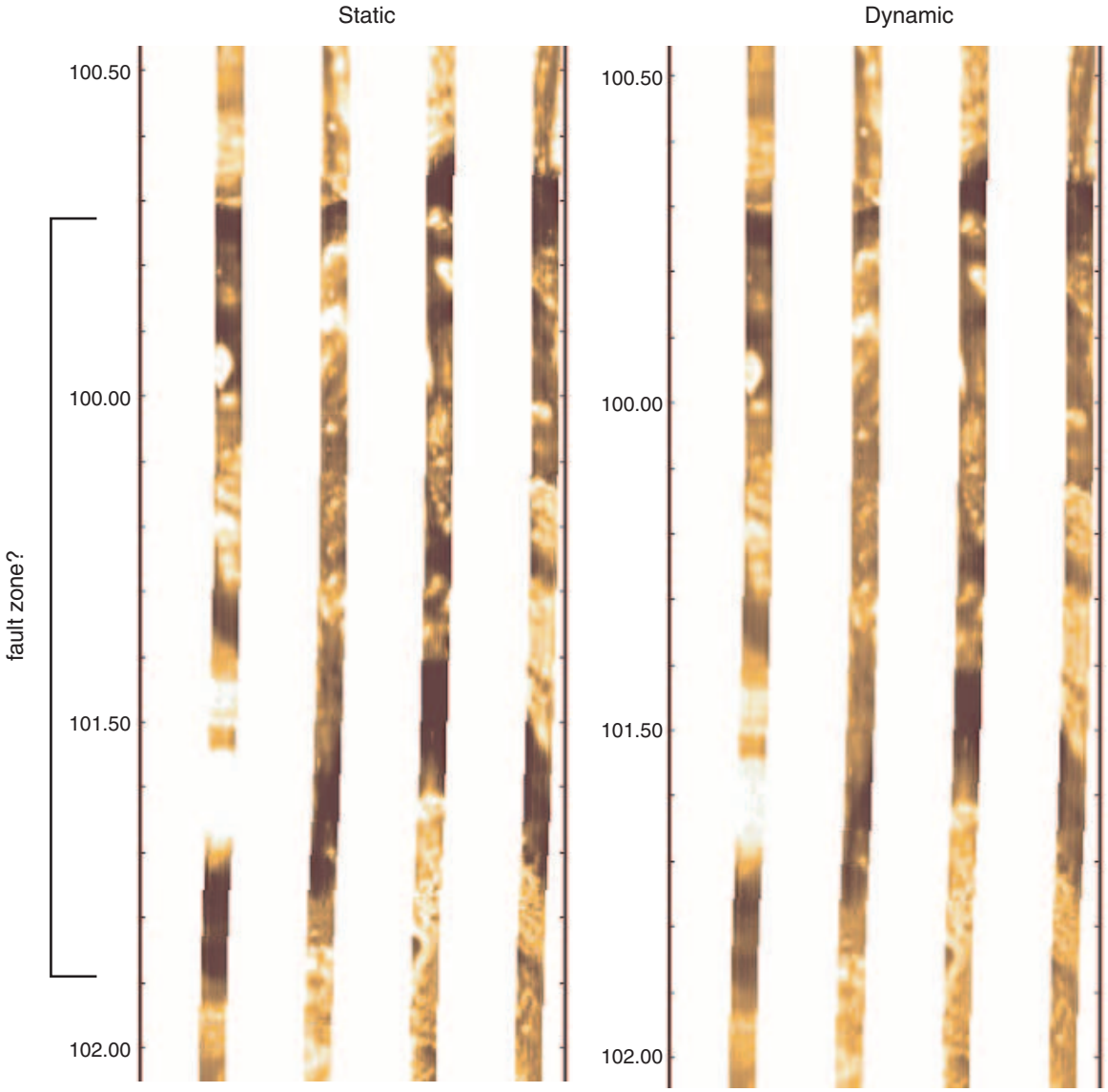

Figure F78. Strike, dip azimuth, and dip magnitude of features interpreted to be fractures in FMS images.

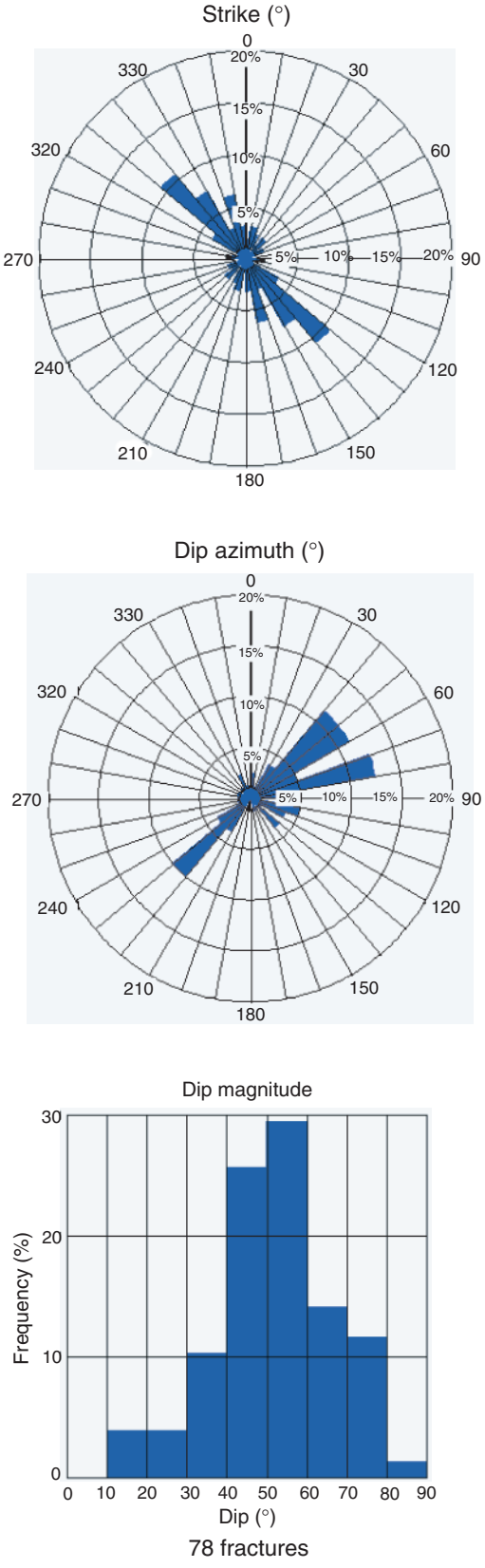

Figure F79. Equal-area lower hemisphere projection of fault dips and dip azimuths, from intervals where fault gouge occurs at the same depth as FMS data interpreted to represent fractures. Also included are two intervals picked solely from FMS data.

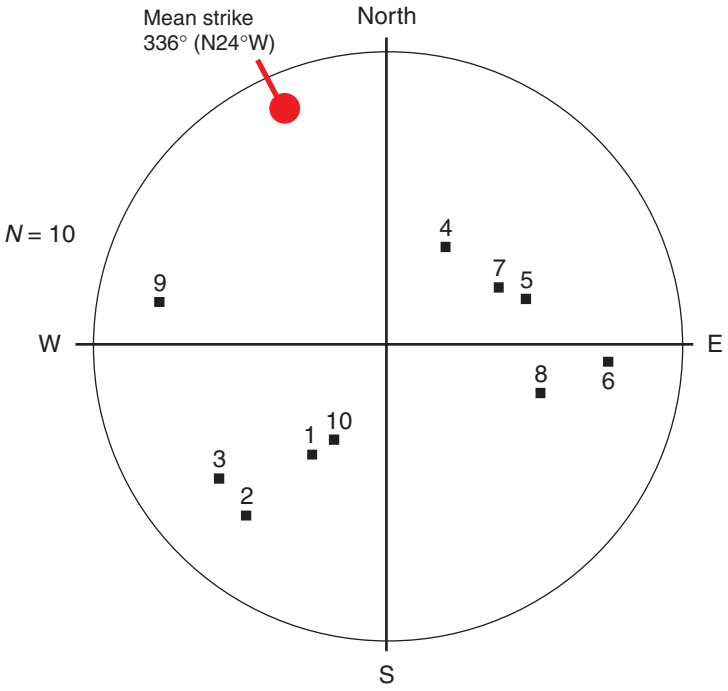

Fault #	Depth (mbsf)	Dip azimuth (°)	Dip (°)	Section correlated
1	61.0	215.0	53.8	13R-1
2	69.8	220.4	26.8	15R-1
3	85.93	232.6	28.2	18R-1 and 18R-2
4	89.4	30.3	58.0	19R-1
5	93.2	71.8	49.8	19R-2
6	100.0	93.9	26.8	21R-1
7	108.5	62.0	55.1	23R-1
8	111.8	107.8	45.2	FMS pick
9	119.0	281.0	22.0	FMS pick
10	122.4	210.1	60.5	25R-2

Figure F80. Correlation of resistivity and gamma ray measurements. TD = total depth.

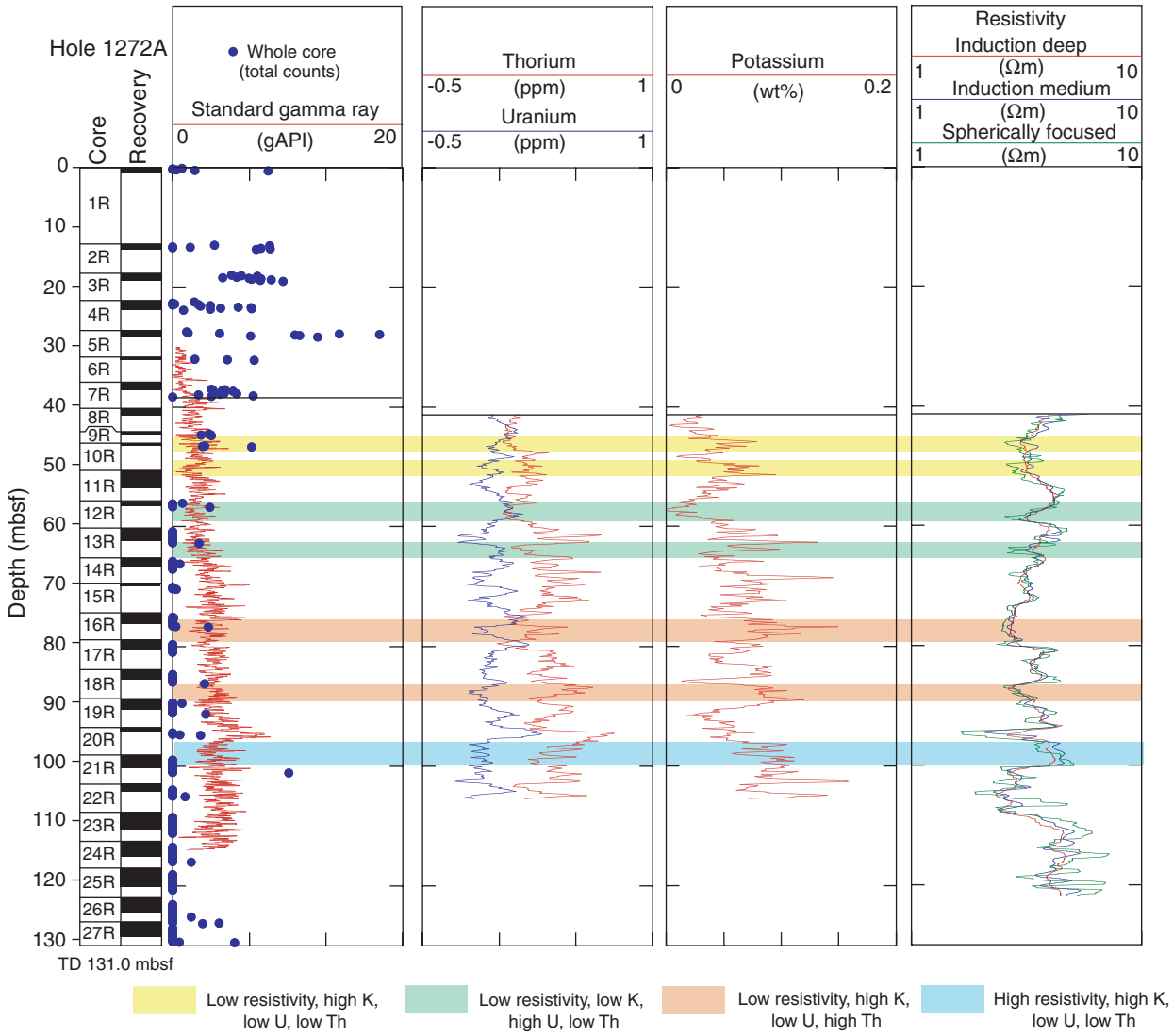

Table T1. Coring summary, Site 1272.

Hole 1272A
Latitude: 15°5.6665′N
Longitude: 44°58.3003′W
Time on hole: 119.75 (0745 hr, 7 June–0730 hr, 12 June 2003)
Seafloor (drill pipe measurement from rig floor, mbrf): 2571.0
Distance between rig floor and sea level (m): 11.2
Water depth (drill pipe measurement from sea level, m): 2559.8
Total depth (drill pipe measurement from rig floor, mbrf): 2702.0
Total penetration (meters below seafloor, mbsf): 131.0
Total length of cored section (m): 131.0
Total core recovered (m): 37.5
Core recovery (%): 28.6
Total number of cores: 27

Core	Date (Jun 2003)	Local time (hr)	Depth (mbsf) Top	Depth (mbsf) Bottom	Length (m) Cored	Length (m) Recovered	Recovery (%)
209-1272A-							
1R	7	2215	0.0	12.9	12.9	0.61	4.7
2R	8	0030	12.9	17.9	5.0	0.71	14.2
3R	8	0440	17.9	22.4	4.5	1.10	24.4
4R	8	0725	22.4	27.4	5.0	1.24	24.8
5R	8	0935	27.4	31.9	4.5	0.80	17.8
6R	8	1245	31.9	36.9	5.0	0.33	6.6
7R	8	1535	36.9	41.4	4.5	1.28	28.4
8R	8	1930	41.4	44.4	3.0	0.08	2.7
9R	8	2300	44.4	46.4	2.0	0.45	22.5
10R	9	0245	46.4	51.0	4.6	0.25	5.4
11R	9	0615	51.0	56.0	5.0	3.00	60.0
12R	9	0955	56.0	60.7	4.7	0.76	16.2
13R	9	1410	60.7	65.7	5.0	1.95	39.0
14R	9	1825	65.7	70.0	4.3	1.37	31.9
15R	9	2150	70.0	75.0	5.0	0.42	8.4
16R	10	0030	75.0	79.6	4.6	1.59	34.6
17R	10	0315	79.6	84.6	5.0	1.31	26.2
18R	10	0650	84.6	89.3	4.7	1.68	35.7
19R	10	0950	89.3	94.3	5.0	1.83	36.6
20R	10	1200	94.3	98.9	4.6	0.60	13.0
21R	10	1510	98.9	103.9	5.0	2.10	42.0
22R	10	1840	103.9	108.5	4.6	1.18	25.7
23R	10	2225	108.5	113.5	5.0	2.67	53.4
24R	11	0150	113.5	118.0	4.5	2.29	50.9
25R	11	0550	118.0	123.0	5.0	2.44	48.8
26R	11	0955	123.0	127.0	4.0	3.14	78.5
27R	11	1320	127.0	131.0	4.0	2.32	58.0
				Cored totals:	131.0	37.50	28.6

Table T2. XRD results, Hole 1272A.

Core, section, interval (cm)	Depth (mbsf)	Piece	Rock type	Mineralogy			ICP-EAS analyses	Thin section
				Major	Minor	Trace		
209-1272A-								
1R-1, 7–11	0.1	2	Harzburgite	Lizardite	Aragonite	Goethite, olivine	Yes	Yes
1R-1, 42–45	0.4	7	Gabbro	Plagioclase	Cpx		Yes	Yes
2R-1, 61–63	13.5	9	Dunite	Lizardite	Aragonite		Yes	Yes
3R-1, 110–114	19.0	9	Diabase	Plagioclase	Cpx		Yes	Yes
4R-1, 82–85	23.2	14	Gabbro	Plagioclase	Cpx	Amphibole	Yes	Yes
7R-1, 98–102	37.9	15	Spherulitic diabase	Plagioclase	Cpx, amphibole		Yes	Yes
7R-1, 109–113	38.0	17	Spherulitic diabase	Plagioclase	Cpx		Yes	Yes
12R-1, 73–76	56.7	8	Harzburgite	Lizardite		Magnetite, iowaite	Yes	—
13R-1, 93–98	61.6	15	Harzburgite	Lizardite	Brucite, iowaite	Magnetite	Yes	Yes
13R-2, 38–40	62.6	4	Harzburgite	Lizardite		Iowaite	—	Yes
16R-1, 135–137	76.4	22	Harzburgite	Lizardite	Iowaite	Magnetite	Yes	Yes
18R-1, 46–48	85.1	6	Harzburgite	Lizardite		Brucite, iowaite	Yes	Yes
19R-2, 24–27	91.0	3B	Harzburgite	Lizardite		Iowaite	Yes	Yes
21R-1, 50–52	99.4	4	Harzburgite	Lizardite	Iowaite		Yes	Yes
23R-1, 12–14	108.6	2	Harzburgite	Lizardite	Brucite, iowaite		Yes	Yes
23R-1, 67–69	109.2	3	Harzburgite	Lizardite	Iowaite	Brucite, magnetite	—	Yes
24R-1, 73–77	114.2	11	Harzburgite	Lizardite		Iowaite	Yes	Yes
25R-1, 124–126	119.2	15	Harzburgite	Lizardite		Brucite, iowaite, opx	Yes	Yes
26R-1, 80–83	123.8	4	Harzburgite	Lizardite	Iowaite	Brucite	Yes	Yes

Notes: Cpx = clinopyroxene, opx = orthopyroxene. Due to peak overlap, samples with identified lizardite may also contain chrysotile. Qualifiers "major, minor, and trace" indicate relative abundances based on peak heights and do not necessarily reflect true relative proportions. ICP-AES = inductively coupled plasma–atomic emission spectrometry. ICP-AES data are available in Table **T4,** p. 124. This table is also available in **ASCII.**

Table T3. Vein mineralogy, Hole 1272A.

Hole	1272A
Penetration depth (mbsf)	131.0
Recovery (%)	28.6
Length recovered (m)	37.5
Volume recovered (cm^3)	94,020
Veins in hole (cm^3/m)	17.5
Veins in hole (%)	0.7
Vein minerals in hole (cm^3/m):	
Serpentine	14.86
Magnetite	0.34
Carbonate	2.27
Clays	0.04
Vein minerals in hole (%):	
Serpentine	0.593
Magnetite	0.013
Carbonate	0.091
Clays	0.002
Vein minerals in veins (%):	
Serpentine	84.8
Magnetite	1.9
Carbonate	13.0
Clays	0.3

Notes: The volume of veins is based on macroscopic observations of vein mineralogy and estimates of vein percentages by pieces. We computed volume percentage of veins by using the volume weighted average of the macroscopic estimates using the relative curated length and assuming a constant core radius throughout the site. This table is also available in **ASCII.**

Table T4. Major and trace element compositions of rocks, Hole 1272A.

Core, section, interval (cm)	Depth (mbsf)	Piece	Unit	Lithology	Major element oxides (wt%)										LOI	Volatiles (wt%)	
					SiO_2	TiO_2	Al_2O_3	Fe_2O_3	MgO	MnO	CaO	Na_2O	K_2O	Total		CO_2	H_2O
209-1272A-																	
1R-1, 7–11	0.07	2	I	Harzburgite	40.43	0.02	0.77	8.21	38.70	0.14	9.65	0.12	0.01	98.04	17.95	7.33	14.87
1R-1, 42–45	0.42	7	I	Gabbronorite	52.08	1.18	14.96	10.28	8.77	0.16	10.92	2.62	0.15	101.11	1.27	0.08	2.21
2R-1, 61–63	13.51	9	I	Dunite	40.34	0.01	0.12	7.62	40.45	0.13	12.19	0.10	<0.01	100.94	18.89	9.31	14.02
3R-1, 110–114	19.00	9	I	Diabase	51.28	1.48	15.13	9.52	6.81	0.15	11.28	2.69	0.57	98.90	0.49	0.11	1.06
4R-1, 82–85	23.22	14	I	Gabbronorite	52.61	1.81	15.02	10.34	6.12	0.19	10.63	3.15	0.34	100.21	0.41	0.16	0.91
7R-1, 98–102	37.88	15	I	Basalt	50.32	1.44	15.13	10.04	7.45	0.15	10.85	2.84	0.45	98.67	1.18	0.58	1.66
7R-1, 109–113	37.99	17	I	Basalt	51.74	1.48	15.69	9.73	7.41	0.15	11.15	2.66	0.64	100.66	0.95	0.11	1.31
12R-1, 73–76	56.73	8	II	Harzburgite	45.70	0.02	0.65	8.21	48.26	0.10	<0.06	0.18	<0.01	103.16	15.28	NA	NA
13R-1, 93–98	61.63	15	II	Harzburgite	41.41	0.02	0.57	8.03	47.27	0.11	<0.06	0.06	<0.01	97.46	16.64	NA	NA
16R-1, 135–137	76.35	22	II	Harzburgite	43.12	0.01	0.78	8.21	46.53	0.11	<0.06	0.07	0.01	98.83	14.97	0.30	15.51
18R-1, 46–48	85.06	6	II	Harzburgite	43.31	0.01	0.69	8.07	46.18	0.12	0.15	0.04	<0.01	98.58	15.35	0.35	15.40
19R-2, 24–27	91.04	3B	II	Harzburgite	43.27	0.01	0.60	7.94	45.40	0.10	<0.06	0.06	<0.01	97.42	15.61	0.33	15.58
21R-1, 50–52	99.40	4	II	Harzburgite	42.56	0.01	0.64	8.19	45.73	0.10	<0.06	0.07	<0.01	97.31	15.25	0.27	15.54
23R-1, 12–14	108.62	2	II	Dunite	40.13	0.01	0.12	8.81	48.14	0.11	0.07	0.09	<0.01	97.49	16.35	0.24	15.58
24R-1, 73–77	114.23	11	II	Harzburgite	42.93	0.01	0.76	7.94	45.51	0.12	<0.06	0.06	<0.01	97.38	15.45	0.36	15.38
25R-1, 124–126	119.24	15	II	Harzburgite	43.36	0.01	0.62	8.05	45.49	0.12	0.19	0.06	0.01	97.91	14.78	0.34	15.03
26R-1, 80–83	123.80	4	II	Harzburgite	44.27	0.01	0.62	8.22	46.61	0.12	<0.06	0.07	0.01	99.96	14.79	0.24	15.23

Notes: Some low major element totals are due to the high concentrations of Cr and Ni that are probably not trace elements in these rocks. NA = not analyzed. This table is also available in **ASCII.**

Table T4 (continued).

Core, section, interval (cm)	Depth (mbsf)	Piece	Unit	Lithology	Trace elements (ppm)									
					S	Cr	Ni	Ba	Sr	V	Y	Zr	Sc	Co
209-1272A-														
1R-1, 7–11	0.07	2	I	Harzburgite	<350	4885	2987	<39	1786	47	<2	2	6	92
1R-1, 42–45	0.42	7	I	Gabbronorite	681	338	187	<39	136	260	24	87	38	41
2R-1, 61–63	13.51	9	I	Dunite	<350	3431	3293	39	2148	13	<2	3	4	113
3R-1, 110–114	19.00	9	I	Diabase	<350	237	144	109	223	257	27	126	37	55
4R-1, 82–85	23.22	14	I	Gabbronorite	856	14	35	107	230	310	29	150	40	44
7R-1, 98–102	37.88	15	I	Basalt	<350	257	124	74	204	247	27	125	37	46
7R-1, 109–113	37.99	17	I	Basalt	496	273	160	114	221	254	26	127	36	61
12R-1, 73–76	56.73	8	II	Harzburgite	NA	2153	2426	<39	<5	27	<2	3	7	127
13R-1, 93–98	61.63	15	II	Harzburgite	NA	2460	2581	<39	<5	24	<2	<2	6	105
16R-1, 135–137	76.35	22	II	Harzburgite	<350	3247	2690	<39	<5	32	<2	<2	7	94
18R-1, 46–48	85.06	6	II	Harzburgite	<350	2352	2627	<39	<5	28	<2	<2	8	97
19R-2, 24–27	91.04	3B	II	Harzburgite	<350	1926	2724	<39	<5	23	<2	3	9	90
21R-1, 50–52	99.40	4	II	Harzburgite	429	2553	2951	<39	<5	28	<2	5	8	79
23R-1, 12–14	108.62	2	II	Dunite	1137	720	3542	<39	<5	12	<2	4	5	141
24R-1, 73–77	114.23	11	II	Harzburgite	<350	3353	2919	<39	<5	28	<2	<2	8	89
25R-1, 124–126	119.24	15	II	Harzburgite	<350	2374	3036	<39	<5	26	<2	3	8	100
26R-1, 80–83	123.80	4	II	Harzburgite	<350	2619	2993	<39	<5	27	<2	3	8	101

Table T5. Thermal conductivity measurements, Hole 1272A.

Core, section, interval (cm)	Depth (mbsf)	Piece	Thermal conductivity* (W/[m·K])	Standard deviation	Standard error	Needle orientation	Apparent anisotropy (%)	Primary lithology
209-1272A-								
1R-1, 43–50	0.43	7	1.97	0.023	0.012	1		Microgabbro
3R-1, 110–120	19.00	9	1.72	0.005	0.002	0	0.8	Diabase
3R-1, 110–120	19.00	9	1.72	0.013	0.007	1		Diabase
3R-1, 110–120	19.00	9	1.71	0.006	0.003	2		Diabase
4R-1, 81–91	23.21	14	1.97	0.015	0.008	0	3.1	Olivine gabbro
4R-1, 81–91	23.21	14	1.96	0.011	0.006	1		Olivine gabbro
4R-1, 81–91	23.21	14	1.91	0.016	0.008	2		Olivine gabbro
7R-1, 93–102	37.83	15	1.91	0.011	0.005	0	2.2	Diabase
7R-1, 93–102	37.83	15	1.95	0.010	0.005	1		Diabase
7R-1, 93–102	37.83	15	1.94	0.007	0.003	2		Diabase
14R-1, 108–120	66.78	13	2.14	0.019	0.009	0	1.2	Harzburgite
14R-1, 108–120	66.78	13	2.12	0.007	0.004	1		Harzburgite
14R-1, 108–120	66.78	13	2.12	0.007	0.004	2		Harzburgite
17R-1, 66–77	80.26	11	2.05	0.015	0.007	0	0.1	Harzburgite
17R-1, 66–77	80.26	11	2.05	0.009	0.005	1		Harzburgite
17R-1, 66–77	80.26	11	2.05	0.011	0.005	2		Harzburgite
18R-1, 38–50	84.98	6	2.09	0.017	0.008	0	2.3	Harzburgite
18R-1, 38–50	84.98	6	2.05	0.010	0.005	1		Harzburgite
18R-1, 38–50	84.98	6	2.10	0.007	0.004	2		Harzburgite
23R-2, 109–120	111.05	11B	2.02	0.009	0.005	0	3.5	Harzburgite
23R-2, 109–120	111.05	11B	1.98	0.019	0.010	1		Harzburgite
23R-2, 109–120	111.05	11B	2.05	0.012	0.006	2		Harzburgite
25R-1, 95–108	118.95	15A	2.13	0.030	0.015	0	7.2	Harzburgite
25R-1, 95–108	118.95	15A	2.20	0.011	0.006	1		Harzburgite
25R-1, 95–108	118.95	15A	2.05	0.020	0.010	2		Harzburgite
26R-1, 126–139	124.26	7	2.07	0.006	0.003	0	1.7	Harzburgite
26R-1, 126–139	124.26	7	2.10	0.011	0.005	1		Harzburgite
26R-1, 126–139	124.26	7	2.07	0.015	0.008	2		Harzburgite
27R-1, 58–70	127.58	5	2.14	0.015	0.007	0	5.9	Harzburgite
27R-1, 58–70	127.58	5	2.11	0.019	0.010	1		Harzburgite
27R-1, 58–70	127.58	5	2.23	0.013	0.007	2		Harzburgite

Notes: * = average of four measurements. 0 = parallel to core axis, 1 = oblique to core axis (~35°), 2 = oblique to core axis (~35°) in opposite direction. This table is also available in **ASCII.**

Table T6. Porosity, density, and velocity on discrete samples, Hole 1272A.

Core, section, interval (cm)	Depth (mbsf)	Volume measured in pycnometer			Volume measured with caliper			V_P (km/s)				V_P apparent anisotropy (%)	Primary lithology
		Density (Mg/m³)		Porosity (%)	Density (Mg/m³)		Porosity (%)	x	y	z	Mean		
		Bulk	Grain		Bulk	Grain							
209-1272A-													
1R-1, 44–46	0.44	2.89	3.01	6.0	2.84	—	—	4.24	4.20	4.24	4.23	1.1	Microgabbro
2R-1, 63–65	13.53	2.40	2.70	18.1	2.33	—	—	2.92	3.27	3.29	3.16	11.8	Dunite
3R-1, 114–116	19.04	2.72	2.84	6.5	2.79	—	—	4.81	4.85	4.83	4.83	0.7	Diabase
4R-1, 85–87	23.25	2.77	2.95	9.4	2.76	—	—	4.64	4.69	4.54	4.62	3.2	Olivine gabbro
7R-1, 96–98	37.86	2.88	3.00	6.3	2.76	—	—	4.85	4.59	4.47	4.64	8.2	Diabase
13R-1, 96–98	61.66	2.33	2.55	14.5	2.30	—	—	3.05	3.05	2.92	3.01	4.3	Harzburgite
13R-2, 30–32	62.50	2.37	2.59	14.2	2.32	—	—	3.10	3.05	3.01	3.05	3.0	Harzburgite
14R-1, 22–24	65.92	2.38	2.61	14.5	2.33	—	—	3.15	3.16	3.05	3.12	3.6	Harzburgite
16R-1, 137–139	76.37	2.30	2.60	18.7	2.26	—	—	2.94	2.83	2.68	2.82	9.2	Harzburgite
17R-1, 59–61	80.19	2.31	2.56	16.3	2.26	—	—	3.06	2.97	—	3.02	—	Harzburgite
17R-1, 130–132	80.90	2.36	2.60	15.3	2.33	—	—	3.10	3.01	2.92	3.01	5.9	Harzburgite
18R-1, 44–46	85.04	2.37	2.57	12.9	2.33	—	—	3.28	3.23	3.18	3.23	3.0	Harzburgite
21R-1, 50–52	99.40	2.34	2.55	14.0	2.33	—	—	3.34	3.18	3.24	3.26	4.8	Harzburgite
23R-1, 24–26	108.74	2.32	2.54	14.6	2.34	—	—	3.58	3.30	3.28	3.39	8.8	Dunite/Harzburgite
24R-1, 77–79	114.27	2.39	2.57	11.5	2.37	—	—	3.49	3.44	3.47	3.47	1.4	Harzburgite
25R-1, 127–129	119.27	2.45	2.62	10.9	2.42	—	—	3.52	3.55	3.52	3.53	1.1	Harzburgite
26R-1, 75–77	123.75	2.39	2.59	12.5	2.39	—	—	3.44	3.50	3.32	3.42	5.2	Harzburgite
27R-1, 52–54	127.52	2.48	2.63	9.2	2.47	—	—	3.76	3.68	3.57	3.67	5.4	Harzburgite
27R-2, 93–95	129.43	2.51	2.65	9.0	2.51	—	—	3.80	3.61	3.59	3.67	5.7	Harzburgite

Note: This table is also available in **ASCII.**

Table T7. Summary of caliper test data.

	Standard dimension		Caliper 1		Caliper 2		Caliper 3			PWS3	
Standard	(in)	(mm)	(mm)	Error	(mm)	Error	(mm)	Error	(in)	(mm)	Error
Machinist's											
	0.500	12.70	12.75	0.050	12.7	0.000	12.7254	0.025	0.501	13.11	0.410
	0.400	10.16	10.15	–0.01	10.14	–0.02	10.1854	0.025	0.401	10.52	0.360
	0.300	7.62	7.59	–0.03	7.58	–0.04	7.6708	0.051	0.302	8.295	0.675
	0.200	5.08	5.1	0.02	5.03	–0.05	5.1054	0.025	0.201	5.74	0.660
	0.100	2.54	2.57	0.03	2.55	0.01	2.5654	0.025	0.101	3.19	0.650
		Average error:		0.012		–0.02		0.030			0.551
		Standard error:		0.014		0.011		0.005			0.068
Polycarbonate cylinders		20	20.03	0.03	19.93	–0.07	19.97	–0.03	0.7862	20.05	0.02
		30	30.02	0.02	30.02	0.02	30.05	0.05	1.1832	30.02	0
		40	39.92	–0.08	39.95	–0.05	39.98	–0.02	1.574	40.02	0.1
		50	49.92	–0.08	49.93	–0.07	49.99	–0.01	1.968	49.93	0.01
		Average error:		–0.027		–0.042		–0.003			0.032
		Standard error:		0.011		0.009		0.009			0.023

Note: This table is also available in **ASCII.**

Table T8. Bulk densities: caliper vs. PWS3 measurements, Sites 1268, 1270, 1271, and 1272.

Core, section, interval (cm)	Density (Mg/m³)			Error (%)
	Caliper	PWS3	Difference	
209-1268A-				
6R-1, 106–108	2.52	2.47	0.05	2.13
10R-2, 8–10	2.72	2.62	0.10	3.96
12R-1, 47–49	2.51	2.43	0.09	3.55
13R-1, 33–35	2.53	2.43	0.11	4.44
14R-2, 128–130	2.46	2.40	0.07	2.79
15R-2, 104–106	2.52	2.44	0.08	3.11
16R-1, 37–39	2.55	2.50	0.06	2.26
16R-2, 34–36	2.40	2.48	–0.07	–2.96
18R-2, 116–118	2.57	2.48	0.09	3.63
19R-1, 51–53	2.52	2.43	0.09	3.54
19R-4, 36–38	2.49	2.46	0.03	1.26
22R-1, 114–116	2.44	2.43	0.01	0.48
23R-1, 53–55	2.76	2.74	0.02	0.76
23R-3, 61–63	2.55	2.49	0.06	2.30
25R-2, 25–27	2.69	2.64	0.04	1.63
26R-2, 20–22	2.77	2.74	0.04	1.40
28R-2, 28–30	2.77	2.73	0.04	1.63
28R-2, 87–89	2.78	2.77	0.02	0.57
209-1270A-				
1R-1, 108–110*		2.48		
209-1270B-				
1R-1, 98–100	3.15	3.16	–0.01	–0.43
4M-2, 57–59	3.19	3.17	0.02	0.71
4M-2, 125–127	3.04	3.00	0.03	1.14
7R-1, 105–107	2.76	2.73	0.02	0.82
7R-2, 122–124	3.17	3.11	0.06	1.91
8R-1, 127–129	3.23	3.14	0.09	2.75
10M-1, 27–29	3.19	3.12	0.07	2.29
209-1270C-				
1R-1, 50–52	2.57	2.53	0.05	1.82
1R-1, 71–73	2.58	2.56	0.02	0.62
2R-1, 67–69	2.81	2.78	0.03	1.05
3R-1, 59–61	2.54	2.55	–0.01	–0.52
209-1270D-				
3R-2, 53–55*		2.53		
4R-1, 91–93*		2.55		
6R-1, 33–35	2.50	2.41	0.09	3.58
209-1271A-				
1R-1, 70–72	2.43	2.38	0.05	2.02
4R-1, 92–94	2.55	2.51	0.04	1.59
4R-2, 26–29	2.54	2.51	0.04	1.49
4R-2, 103–105	2.53	2.48	0.05	2.03
209-1271B-				
5R-1, 55–57	2.53	2.50	0.02	0.96
8R-1, 69–71	2.46	2.42	0.03	1.40
10R-1, 112–114	2.52	2.50	0.02	0.67
12R-1, 131–134	2.71	2.66	0.05	1.87
17R-1, 58–60	2.53	2.53	0.01	0.24
19R-1, 20–22	2.48	2.44	0.04	1.78
209-1272A-				
1R-1, 44–46	2.84	2.80	0.04	1.53
2R-1, 63–65	2.33	2.30	0.02	0.96
3R-1, 114–116	2.79	2.77	0.02	0.68
4R-1, 85–87	2.76	2.73	0.03	1.24
7R-1, 96–98	2.76	2.75	0.01	0.41
13R-1, 96–99	2.30	2.28	0.02	0.87
13R-2, 30–32	2.32	2.31	0.01	0.48
14R-1, 22–24	2.33	2.31	0.02	0.86
16R-1, 137–139	2.26	2.26	0.01	0.24
17R-1, 59–61	2.26	2.26	0.00	0.14
17R-1, 130–132	2.33	2.28	0.05	2.08
18R-1, 44–46	2.33	2.27	0.06	2.80
21R-1, 50–52	2.33	2.25	0.08	3.33
23R-1, 24–26	2.34	2.27	0.07	2.95
24R-1, 77–79	2.37	2.29	0.08	3.57
25R-1, 127–129	2.42	2.33	0.09	3.97
26R-1, 75–77	2.39	2.34	0.05	2.02
27R-1, 52–54	2.47	2.45	0.02	0.77
27R-2, 93–95	2.51	2.51	–0.01	–0.24
Mean:	2.59	2.55	0.04	1.61
Standard error:	0.032	0.032	0.004	0.175

Notes: * = these samples were polished after the first series of measurements for structural observations, leading to significant volume change. The densities of these samples are therefore not corrected. This table is also available in **ASCII.**

Table T9. Summary of discrete sample data, Hole 1272A.

Core, section, interval (cm)	Depth (mbsf)	Piece	Lithology	NRM (A/m)	MDF (mT)	*N*	Decay type	MAD (°)	Remanence direction (°)		Demagnetization (mT)		*J* (A/m)	PCA (%)
									Declination	Inclination	Low	High		
209-1272A-														
1R-1, 44	0.44	7	16	1.40	3.4	5	F	1.4	46.1	18.0	20	50	0.1178	8.41
2R-1, 63	13.53	9	1	1.18	4.7	11	A	1.5	357.7	26.7	4	50	0.6608	56.00
3R-1, 114	19.04	9	16	3.55	2.9	5	A	1.3	286.9	26.5	20	50	0.189	5.32
4R-1, 85	23.25	14	11	4.21	1.9	5	A	3.3	98.9	52.4	20	50	0.1578	3.75
7R-1, 96	37.86	15	16	3.32	8.3	6	A	0.7	258.7	–38.7	20	50	0.893	26.90
13R-1, 96	61.66	15	2	1.74	1.8	8	A	4.3	75.7	33.0	12	50	0.0943	5.42
13R-2, 30	62.50	4	2	2.97	1.5	7	A	17.1	345.9	41.9	15	50	0.0592	1.99
14R-1, 22	65.92	3C	2	4.58	1.4	8	F	9.9	17.2	49.0	12	50	0.0971	2.12
16R-1, 137	76.37	22	2	3.93	1.6	3	F	3.2	193.8	47.1	12	20	0.0658	1.67
17R-1, 59	80.19	10	2	4.81	1.7	8	F	5.0	51.5	50.9	12	50	0.1438	2.99
17R-1, 130	80.90	19	2	3.41	1.8	8	F	10.0	352.9	59.3	12	50	0.1081	3.17
18R-1, 44	85.04	6	2	3.56	1.6	8	F	5.8	41.4	46.2	12	50	0.1078	3.03
21R-1, 50	99.40	4	2	1.68	2.3	8	F	3.8	11.1	60.0	12	45	0.0868	5.17
23R-1, 24	108.74	2B	1	4.61	1.7	7	F	3.6	29.9	38.3	12	40	0.2028	4.40
24R-1, 77	114.27	11	2	2.43	1.7	5	A	10.4	3.0	36.1	20	40	0.0236	0.97
25R-1, 127	119.27	15	2	2.05	1.7	7	A	6.9	108.9	43.8	15	45	0.0405	1.98
26R-1, 75	123.75	3B	2	1.87	2.1	4	A	3.7	59.1	49.3	15	30	0.0672	3.59
27R-1, 52	127.52	4B	2	1.05	2.5	7	F	7.8	92.9	36.5	15	50	0.0584	5.56
27R-2, 93	129.43	10	2	0.69	3.7	9	F	1.7	358.0	32.7	10	50	0.1746	25.41

Notes: Lithology: 1 = dunite, 2 = harzburgite, 11 = olivine gabbro, 16 = microgabbro/diabase. NRM = natural remanent magnetization. MDF = median destructive field for vector difference sum. *N* = number of points. Decay type: A = anchored to origin, F = free of origin. MAD = maximum angular deviation. Principal component analysis (PCA) (%) = percentage of NRM intensity. This table is also available in **ASCII.**

Table T10. Piece orientations from archive half data, Site 1272. (See table notes. Continued on next two pages.)

Core, section, interval (cm)	Length (cm)	Piece	Lithology	PCA interval (cm)	Depth (mbsf)	*N*	Decay type	MAD (°)	Remanence direction (°)		Demagnetization (mT)		*J* (A/m)	PCA (%)
									Declination	Inclination	Low	High		
209-1272A-														
1R-1, 29–40	11	6	16	34	0.34	6	F	1.8	309.8	18.9	15	50	0.1744	26.1
1R-1, 29–40	11	6	16	36	0.36	6	F	3.3	302.7	18.6	15	50	0.1953	22.9
1R-1, 42–50	8	7	16	46	0.46	4	A	3.4	69.2	19.2	25	50	0.0859	7.2
1R-1, 51–61	10	8	16	56	0.56	5	A	1.4	132.7	11.6	20	50	0.1970	23.9
2R-1, 14–24	10	3	1	20	13.10	5	A	1.9	33.7	–44.8	20	50	0.2719	45.7
2R-1, 41–51	10	8	1	44	13.34	5	A	1.1	191.3	15.4	20	50	0.0886	21.5
2R-1, 52–76	24	9	1	64	13.54	5	A	2.3	3.2	22.0	20	50	0.1179	15.0
2R-1, 52–76	24	9	1	66	13.56	5	A	2.9	1.9	27.5	20	50	0.1059	11.7
2R-1, 77–88	11	10	1	84	13.74	4	A	2.4	326.2	63.2	25	50	0.1969	14.0
3R-1, 7–19	12	2	12	14	18.04	5	A	1.7	102.2	45.3	20	50	0.1789	4.1
3R-1, 28–40	12	4	12	34	18.24	5	F	2.3	97.2	47.4	20	50	0.1492	3.8
3R-1, 40–48	8	5	12	44	18.34	5	F	1.1	139.1	39.7	20	50	0.1385	6.4
3R-1, 48–57	9	6	12	54	18.44	5	F	1.5	327.6	40.6	20	50	0.1466	8.7
3R-1, 58–86	28	7	12	64	18.54	5	F	1.4	45.4	50.8	20	50	0.1737	6.3
3R-1, 58–86	28	7	12	72	18.62	5	F	2.9	59.3	59.7	20	50	0.1698	5.5
3R-1, 88–109	21	8	12	100	18.90	4	F	1.2	72.6	45.2	25	50	0.0835	5.2
3R-1, 110–119	9	9	9	116	19.06	4	F	1.7	282.5	29.3	25	50	0.0824	3.1
4R-1, 110–119	9	9	1	48	22.88	4	F	1.5	276.9	62.1	25	50	0.1564	3.5
4R-1, 68–80	12	13	12	74	23.14	2	A	1.2	73.2	46.9	40	50	0.0525	1.1
4R-1, 81–91	10	14	12	86	23.26	2	A	0.4	109.6	50.3	40	50	0.0580	2.0
4R-1, 92–110	18	15	12	100	23.40	2	A	2.1	152.2	44.5	40	50	0.0764	2.7
4R-1, 111–124	13	16	12	118	23.58	2	A	0.9	99.3	41.6	40	50	0.0983	3.3
4R-1, 130–138	8	18	12	134	23.74	2	A	0.7	162.2	37.9	40	50	0.0616	5.2
5R-1, 35–62	27	7	18	48	27.88	5	F	0.7	142.1	57.3	20	50	0.6081	32.2
5R-1, 66–80	14	9	18	74	28.14	3	F	0.9	180.8	42.3	30	50	0.2321	18.0
7R-1, 22–31	9	4	9	24	37.14	5	F	0.8	125.7	2.4	20	50	1.0762	21.6
7R-1, 32–43	11	5	9	38	37.28	5	F	0.6	300.5	–20	20	50	2.8912	55.2
7R-1, 93–103	10	15	9	98	37.88	5	F	0.8	270.8	–18.5	20	50	0.5843	27.6
7R-1, 116–125	9	18	9	122	38.12	5	F	0.8	34.2	9.1	20	50	0.6458	20.3
7R-1, 130–138	8	20	9	136	38.26	5	F	1.1	133.5	25.6	20	50	0.1555	18.2
9R-1, 37–45	8	8	2	42	44.82	5	F	6.2	4.2	46.7	15	40	0.0312	2.6
13R-1, 1–8	7	1	2	6	60.76	5	A	11.3	276.9	34.5	20	40	0.0187	0.7
13R-1, 1–8	7	1	2	10	60.80	5	A	7.3	284.9	41.4	20	40	0.0219	0.7
13R-1, 17–25	8	2	2	20	60.90	3	A	5.4	74.7	41.7	20	30	0.0186	0.7
13R-1, 42–49	7	7	2	46	61.16	3	A	2.9	66.3	28.8	20	30	0.0488	2.9
13R-1, 51–58	8	8	2	56	61.26	5	F	4.1	335.1	37.0	20	40	0.0381	1.8
13R-1, 92–116	24	15	2	96	61.66	5	F	8.7	69.9	33.1	20	40	0.0254	1.9
13R-1, 92–116	24	15	2	110	61.80	5	F	7.3	64.7	38.3	20	40	0.0251	1.4
13R-1, 127–138	12	18	2	132	62.02	5	A	10.8	14.8	29.5	20	40	0.0217	0.9
13R-2, 7–22	15	3	2	14	62.34	5	A	10.3	55.1	44.8	20	40	0.0214	1.2
13R-2, 23–40	17	4	2	30	62.50	5	A	9.8	6.3	37.3	20	40	0.0246	1.0
13R-2, 50–61	11	6	2	56	62.76	5	F	11.1	33.9	28.1	20	40	0.0189	1.1
14R-1, 9–31	22	3	2	20	65.90	3	A	4.6	44.7	41.8	25	35	0.0163	0.6
14R-1, 41–63	22	6	2	54	66.24	5	F	11.4	22.2	39.1	20	40	0.0315	1.0
14R-1, 88–102	14	11	1	96	66.66	5	F	6.4	235.5	22.9	20	40	0.0693	6.3
14R-1, 107–120	13	13	2	114	66.84	5	F	4.4	19.2	30.3	20	40	0.0525	2.6
16R-1, 23–35	12	5	2	28	75.28	4	F	5.7	269.1	41.0	20	40	0.0291	1.0
16R-1, 23–35	12	5	2	30	75.30	4	F	4.9	261.2	40.4	20	40	0.0306	1.1
16R-1, 62–69	7	12	2	66	75.66	4	A	12.9	82.2	27.4	20	40	0.0263	0.8
16R-1, 79–89	10	15	2	84	75.84	4	A	0.7	9.2	29.1	20	40	0.0721	2.1
16R-1, 98–106	8	18	2	102	76.02	4	A	4.7	355.3	41.1	20	40	0.0235	1.5
16R-1, 115–124	9	20	2	120	76.20	4	F	3.3	4.5	42.5	20	40	0.0382	1.5
16R-1, 125–132	7	21	2	130	76.30	4	A	4.6	304.6	55.3	20	40	0.0298	1.3
16R-1, 133–141	8	22	2	138	76.38	4	F	9.4	198.5	45.0	20	40	0.0208	0.8
17R-1, 54–64	10	10	2	58	80.18	4	F	8.5	37.0	35.5	20	40	0.0254	1.1
17R-1, 65–76	11	11	2	72	80.32	4	F	9.4	51.2	43.0	20	40	0.0277	1.3
17R-1, 78–85	7	12	2	82	80.42	4	F	7.4	133.3	38.9	20	40	0.0234	1.5
17R-1, 101–110	9	16	2	104	80.64	5	F	11	65.0	48.5	20	50	0.0205	1.1
17R-1, 118–125	7	18	2	122	80.82	5	F	11.9	26.2	37.9	20	50	0.0173	1.2
17R-1, 127–138	11	19	2	132	80.92	5	F	6.2	342.6	46.1	20	50	0.0225	1.1
18R-1, 1–7	6	1	2	4	84.64	5	F	10.8	346.1	35.8	20	50	0.0206	1.4
18R-1, 11–20	9	3	2	16	84.76	5	F	6.6	102.5	27.1	20	50	0.0210	1.2
18R-1, 24–37	13	5	2	30	84.90	4	A	4	349.2	37.9	20	40	0.0336	1.4
18R-1, 38–51	13	6	2	44	85.04	3	A	2.2	56.3	47.1	25	40	0.0201	0.8
18R-1, 52–76	24	7	2	62	85.22	3	F	1.7	356.9	52.2	25	40	0.0142	0.4
18R-1, 52–76	24	7	2	64	85.24	3	A	1.8	3.7	53.7	25	40	0.0226	0.7

Table T10 (continued).

Core, section, interval (cm)	Length (cm)	Piece	Lithology	PCA interval (cm)	Depth (mbsf)	N	Decay type	MAD (°)	Remanence direction (°)		Demagnetization (mT)		J (A/m)	PCA (%)
									Declination	Inclination	Low	High		
18R-1, 80–88	8	9	2	84	85.44	3	A	4.1	320.9	47.7	25	40	0.0163	0.9
18R-1, 90–96	6	10	2	92	85.52	3	A	7.5	24.7	60.6	25	40	0.0117	1.0
18R-1, 110–123	13	15	2	116	85.76	4	F	3.5	346.2	45.2	20	40	0.0418	2.6
19R-1, 9–16	7	3	2	12	89.42	4	F	6.1	67.9	38.3	20	40	0.0398	1.8
19R-1, 60–67	7	11	2	64	89.94	4	F	7.6	163.8	45.6	20	40	0.0342	1.5
19R-1, 68–74	6	12	2	72	90.02	4	F	7.8	235.9	47.6	20	40	0.0321	1.6
19R-1, 101–109	8	18	2	106	90.36	4	F	5.4	149.8	45.4	20	40	0.0264	1.1
19R-1, 126–136	10	22	2	132	90.62	4	F	8	311.0	51.1	20	40	0.0203	1.7
19R-2, 19–31	12	3	2	26	91.06	4	F	2.1	23.2	51.4	15	30	0.0465	2.2
19R-2, 41–49	8	6	2	46	91.26	4	A	10.2	93.6	50.9	20	40	0.0135	1.5
20R-1, 11–18	7	4	2	14	94.44	4	F	9.8	263.5	46.2	20	40	0.0147	1.7
20R-1, 19–30	11	5	2	24	94.54	4	F	1.1	106.5	54.2	15	30	0.0368	3.1
20R-1, 40–54	14	8	2	46	94.76	5	A	7.1	53.4	62.3	20	50	0.0294	1.6
21R-1, 16–44	28	3	2	32	99.22	4	F	9.4	86.8	51.8	25	50	0.0107	0.9
21R-1, 45–58	13	4	2	52	99.42	5	F	6.9	17.7	43.4	20	50	0.0234	1.8
21R-1, 59–67	8	5	2	64	99.54	5	F	6.4	171.3	50.7	20	50	0.0150	1.8
21R-1, 71–106	35	7	2	86	99.76	5	F	6.2	148.7	59.3	20	50	0.0151	1.4
21R-1, 108–126	18	8	2	120	100.10	4	+	5.4	152.6	48.8	25	40	0.0139	1.4
21R-2, 0–26	26	1	2	14	100.39	6	+	3.7	52.6	50.8	20	40	0.0226	1.9
21R-2, 27–38	11	2	2	32	100.57	6	A	3.3	5.8	52.1	15	40	0.0414	4.5
21R-2, 39–79	40	3	2	56	100.81	5	F	11.5	111.5	47.5	20	40	0.0219	1.7
22R-1, 13–32	19	3	2	28	104.18	4	F	10.9	77.4	25.8	25	40	0.0129	0.9
22R-1, 51–57	6	8	2	56	104.46	3	A	0.6	122.8	6.4	30	40	0.0340	4.4
22R-1, 60–67	7	9	2	66	104.56	4	F	10.9	54.1	43.3	25	40	0.0076	0.7
22R-1, 72–85	13	11	2	82	104.72	5	F	9.8	359.8	48.2	20	40	0.0193	1.4
22R-1, 92–110	18	13	2	102	104.92	5	F	4.4	19.2	44.1	20	40	0.0205	1.5
23R-1, 4–60	56	2	2	28	108.78	5	F	3.1	35.9	36.8	20	40	0.0594	1.9
23R-1, 4–60	56	2	2	52	109.02	5	F	7	18.8	42.2	20	40	0.0431	2.2
23R-1, 61–70	9	3	2	66	109.16	5	F	4.5	59.9	49.5	20	40	0.0350	2.3
23R-1, 70–92	22	4	2	80	109.30	5	F	7.7	16.0	44.7	20	40	0.0228	2.0
23R-1, 93–99	6	5	2	96	109.46	5	F	8.9	121.8	60.7	20	40	0.0105	1.7
23R-1, 100–120	20	6	2	112	109.62	5	F	6.6	67.4	51.5	20	40	0.0184	2.0
23R-1, 122–140	18	7	2	130	109.80	5	F	7.1	31.8	42.1	20	40	0.0184	2.2
23R-2, 12–37	25	3	2	24	110.20	5	F	6.7	314.1	58.4	20	40	0.0224	2.0
23R-2, 45–64	19	5	2	54	110.50	5	F	4.4	40.6	53.8	20	40	0.0179	1.7
23R-2, 81–89	8	9	2	86	110.82	6	F	3.8	44.1	60.3	15	40	0.0261	3.5
23R-2, 89–98	9	10	2	94	110.90	6	F	7.6	22.4	57.9	15	40	0.0286	3.5
23R-2, 99–120	21	11	2	112	111.08	5	F	9.1	63.8	52.8	20	40	0.0160	1.5
23R-2, 126–139	13	13	2	132	111.28	5	F	6.4	69.6	38.7	20	40	0.0196	2.5
24R-1, 5–13	8	3	2	10	113.60	3	A	0.5	125.4	–10.2	30	40	0.0468	7.2
24R-1, 14–22	8	4	2	20	113.70	3	A	4	173.7	24.3	30	40	0.0098	1.2
24R-1, 32–38	6	7	2	36	113.86	3	A	5.2	8.7	34.9	30	40	0.0056	0.9
24R-1, 43–60	17	9	2	54	114.04	3	A	6.6	44.7	41.2	30	40	0.0107	0.7
24R-1, 61–68	7	10	2	66	114.16	4	A	5.6	115.9	47.8	25	40	0.0154	1.1
24R-1, 69–100	31	11	2	76	114.26	5	A	4.5	0.8	53.8	20	40	0.0203	1.3
24R-1, 69–100	31	11	2	90	114.40	5	F	6.5	17.1	53.8	20	40	0.0167	1.1
24R-1, 101–116	15	12	2	108	114.58	5	F	3.1	44.0	52.2	20	40	0.0156	1.1
24R-1, 117–135	18	13	2	126	114.76	5	F	7.6	329.6	43.9	20	40	0.0153	1.2
24R-2, 0–17	17	1	2	8	114.94	5	F	9.3	23.5	54.8	20	40	0.0236	1.6
24R-2, 18–24	6	2	2	22	115.08	6	F	3.1	331.2	64.5	15	40	0.0349	3.4
24R-2, 25–69	44	3	2	40	115.26	6	A	9.7	66.1	48.4	15	40	0.0389	2.9
24R-2, 73–82	9	5	2	78	115.64	6	F	3.9	33.9	42.7	15	40	0.0295	5.8
24R-2, 88–95	7	7	2	92	115.78	6	F	7.3	54.6	44.4	15	40	0.0264	5.2
24R-2, 101–123	22	9	2	108	115.94	6	F	6.7	19.6	44.4	15	40	0.0619	5.7
25R-1, 9–16	7	3	2	14	118.14	6	F	6.9	245.4	49.1	15	40	0.0255	3.0
25R-1, 23–31	8	6	2	28	118.28	6	F	3.7	24.2	41.5	15	40	0.0366	3.7
25R-1, 32–40	8	7	2	36	118.36	5	F	10.6	22.8	48.5	20	40	0.0156	1.3
25R-1, 41–48	7	8	2	46	118.46	5	A	9.9	109.3	37.3	20	40	0.0104	1.2
25R-1, 52–62	10	10	2	56	118.56	6	F	4.2	15.7	43.1	15	40	0.0459	3.4
25R-1, 52–62	10	10	2	58	118.58	6	F	5	16.3	49.7	15	40	0.0453	3.2
25R-1, 66–90	24	12	2	80	118.80	6	F	3.7	357.5	45.6	15	40	0.0711	4.1
25R-1, 94–108	14	14	2	102	119.02	6	F	3.9	343.5	38.6	15	40	0.0817	4.3
25R-1, 109–131	22	15	2	122	119.22	6	F	4.8	97.8	51.9	15	40	0.0708	3.3
25R-2, 0–17	17	1	2	10	119.46	5	F	6.7	52.0	22.6	20	40	0.0132	1.0
25R-2, 33–43	10	5	2	40	119.76	5	F	12	3.6	27.1	20	40	0.0055	0.5
25R-2, 45–75	30	6	2	66	120.02	4	A	7.6	5.1	44.3	25	40	0.0077	0.6
25R-2, 76–82	6	7	2	80	120.16	4	A	7.4	28.4	47.0	25	40	0.0083	1.2
25R-2, 86–95	9	9	2	92	120.28	4	A	2.2	54.1	37.8	25	40	0.0136	1.6

Table T10 (continued).

Core, section, interval (cm)	Length (cm)	Piece	Lithology	PCA interval (cm)	Depth (mbsf)	*N*	Decay type	MAD (°)	Remanence direction (°)		Demagnetization (mT)		*J* (A/m)	PCA (%)
									Declination	Inclination	Low	High		
25R-2, 95–105	10	10	2	100	120.36	5	A	5.7	358.4	29.9	20	40	0.0259	2.5
25R-2, 126–136	10	13	2	132	120.68	5	A	8.1	249.1	22.8	20	40	0.1830	7.8
26R-1, 2–19	17	2	2	14	123.14	5	A	5.3	30.7	49.7	20	40	0.0151	1.5
26R-1, 20–78	58	3	2	60	123.60	6	A	2	53.5	45.9	15	40	0.0751	5.4
26R-1, 79–88	9	4	2	84	123.84	6	F	5	28.1	52.8	15	40	0.0365	4.2
26R-1, 99–123	24	6	2	112	124.12	7	F	2.1	3.5	46.4	10	40	0.0981	9.4
26R-1, 124–139	15	7	2	130	124.30	6	F	3.4	333.4	39.5	15	40	0.0458	4.8
26R-2, 1–23	22	1	2	10	124.49	6	F	2.9	69.9	42.8	15	40	0.0360	4.2
26R-2, 27–36	9	3	2	32	124.71	6	F	3.9	154.2	35.5	15	40	0.0229	3.9
26R-2, 41–55	14	5	2	48	124.87	6	F	5.4	37.1	35.7	15	40	0.0232	3.4
26R-2, 59–84	25	7	2	70	125.09	6	F	5.4	68.1	45.0	15	40	0.0289	3.5
26R-2, 59–84	25	7	2	80	125.19	6	F	4.7	65.3	49.3	15	40	0.0247	2.6
26R-3, 0–68	68	1	2	12	125.35	6	F	5.1	343.9	47.2	15	40	0.0217	2.7
26R-3, 0–68	68	1	2	20	125.43	6	F	4.6	339.6	44.5	15	40	0.0238	3.2
26R-3, 0–68	68	1	2	40	125.63	6	F	8.1	3.5	43.6	15	40	0.0223	3.0
26R-3, 0–68	68	1	2	52	125.75	6	F	4	3.9	46.4	15	40	0.0232	3.1
26R-3, 69–77	8	2	2	74	125.97	6	F	2.8	338.5	54.7	15	40	0.0185	3.1
26R-3, 77–86	9	3	2	82	126.05	6	F	5.6	45.6	52.2	15	40	0.0202	3.6
26R-3, 99–113	14	6	2	106	126.29	6	F	2.5	27.4	37.5	15	40	0.0248	5.2
27R-1, 7–19	12	2	2	14	127.14	3	A	1.3	193.4	25.6	30	40	0.0260	4.3
27R-1, 21–37*	16	3	2	30	127.30	3	A	5	133.2	20.3	30	40	0.0085	1.4
27R-1, 38–56	18	4	2	50	127.50	5	F	7.9	58.8	53.6	20	40	0.0158	2.0
27R-1, 57–71	14	5	2	64	127.64	5	F	5.7	73.4	35.3	20	40	0.0253	2.8
27R-1, 72–84	12	6	2	78	127.78	5	F	3.6	332.7	26.5	20	40	0.0217	2.4
27R-1, 86–102*	16	7	2	96	127.96	4	A	12.4	285.8	20.2	25	40	0.0132	1.4
27R-1, 104–117	13	8	2	110	128.10	5	F	6.9	359.7	34.8	20	40	0.0205	2.1
27R-1, 123–134*	11	10	2	130	128.30	5	A	10.1	76.6	21.6	20	40	0.0207	2.9
27R-1, 135–144	9	11	2	140	128.40	5	F	15.5	228.8	39.7	20	40	0.0123	1.4
27R-2, 3–10	7	2	2	8	128.58	5	F	5.5	28.7	25.1	20	40	0.0217	3.0
27R-2, 12–19*	7	3	2	18	128.68	6	A	9.5	200.6	36.1	15	40	0.0429	7.6
27R-2, 24–40	16	5	2	30	128.80	5	F	7.1	330.6	31.5	20	40	0.0128	1.8
27R-2, 46–53*	7	7	2	50	129.00	5	A	3.3	31.9	17.3	20	40	0.0154	3.3
27R-2, 56–64	8	8	2	60	129.10	5	F	7.2	148.8	22.6	20	40	0.0083	4.0
27R-2, 70–110	40	10	2	80	129.30	5	F	2.8	19.8	30.7	20	40	0.0218	4.8
27R-2, 70–110	40	10	2	90	129.40	5	F	2	9.6	31.4	20	40	0.0564	8.8
27R-2, 70–110	40	10	2	100	129.50	5	F	2.2	16.5	40.5	20	40	0.0296	3.7

Notes: Lithology: 1 = dunite, 2 = harzburgite, 9 = basalt, 12 = gabbronorite, 16 = microgabbro, 18 = breccia. Principal component analysis (PCA) interval = level at which PCA analysis was performed. *N* = number of samples. Decay type: A = anchored to origin, F = free of origin, + = includes origin as point. MAD = maximum angular deviation. PCA (%) = percentage of natural remanent magnetization intensity. * = pieces labeled upside down when measured; later fixed. This table is also available in **ASCII.**

Table T11. Anisotropy of magnetic susceptibility, Hole 1272A.

Core, section, interval (cm)	Depth (mbsf)	Piece	Susceptibility (SI)	1 σ	Maximum*			Intermediate*			Minimum*		
					Value	Dec (°)	Inc (°)	Value	Dec (°)	Inc (°)	Value	Dec (°)	Inc (°)
209-1272A-													
1R-1, 44	0.44	7	1.370E–02	0.00009	0.3355	61.9	17.2	0.3335	297.2	61.4	0.3311	159.1	22.0
2R-1, 63	13.53	9	3.638E–02	0.00026	0.3538	282.4	51.0	0.3387	102.7	39.0	0.3075	12.6	0.2
3R-1, 114	19.04	9	3.268E–02	0.00015	0.3367	251.1	72.9	0.3336	56.2	16.5	0.3297	147.4	4.2
4R-1, 85	23.25	14	6.663E–02	0.00007	0.3362	202.0	38.1	0.3325	8.7	51.2	0.3312	106.9	6.5
7R-1, 96	37.86	15	3.866E–02	0.00011	0.3352	44.3	9.4	0.3338	157.0	66.9	0.3310	310.7	21.0
13R-1, 96	61.66	15	2.648E–02	0.00035	0.3594	63.3	3.3	0.3361	332.6	11.7	0.3045	168.8	77.8
13R-2, 30	62.50	4	4.099E–02	0.00047	0.3757	152.7	7.4	0.3328	60.2	18.2	0.2915	264.0	70.2
14R-1, 22	65.92	3C	4.053E–02	0.00060	0.3815	352.9	1.6	0.3390	85.3	55.6	0.2795	261.8	34.3
16R-1, 137	76.37	22	3.554E–02	0.00029	0.3568	15.0	21.1	0.3425	119.1	32.3	0.3007	257.8	49.9
17R-1, 59	80.19	10	3.667E–02	0.00029	0.3565	358.2	6.0	0.3423	95.1	48.9	0.3012	263.0	40.5
17R-1, 130	80.90	19	3.598E–02	0.00010	0.3555	129.4	13.2	0.3351	220.7	5.6	0.3095	333.3	75.7
18R-1, 44	85.04	6	2.743E–02	0.00029	0.3638	155.5	15.0	0.3368	51.1	42.7	0.2994	260.2	43.4
21R-1, 50	99.40	4	1.918E–02	0.00022	0.3479	133.4	22.4	0.3394	37.1	14.9	0.3126	276.2	62.7
23R-1, 24	108.74	2B	2.464E–02	0.00062	0.3705	172.2	40.7	0.3348	75.9	7.3	0.2946	337.6	48.4
24R-1, 77	114.27	11	1.886E–02	0.00015	0.3507	172.0	21.4	0.3333	76.4	13.9	0.3160	315.7	64.1
25R-1, 127	119.27	15	1.250E–02	0.00007	0.3401	241.1	29.7	0.3323	73.5	59.7	0.3276	334.2	5.4
26R-1, 75	123.75	3B	1.707E–02	0.00018	0.3530	186.2	12.4	0.3323	91.3	21.3	0.3147	304.4	65.1
27R-1, 52	127.52	4B	1.203E–02	0.00014	0.3432	266.1	4.3	0.3340	357.0	12.1	0.3228	156.8	77.1
27R-2, 93	129.43	10	8.095E–03	0.00018	0.3428	16.7	17.5	0.3383	116.4	28.0	0.3188	258.7	56.1

Notes: σ = 1 standard deviation for normalized eigenvalues. Total anisotropy critical value = 3.4817. * = unrotated core coordinates (double line on working half = 360°, inclination positive down). Dec = declination, inc = inclination. F12 = max, min eigenvalues, F23 = int, min eigenvalues (critical value = 4.2565 for F12 and F23). *P* (degree of anisotropy) = max/min eigenvalues, *F* (magnetic foliation) = int/min eigenvalues, *L* (magnetic lineation) = max/int eigenvalues. AMS = anisotropy of magnetic susceptibility. † = anisotropy of magnetic susceptibility core coordinates rotated to 360°. This table is also available in **ASCII.**

Table T11 (continued).

Core, section, interval (cm)	Depth (mbsf)	Piece	Total anisotropy	F12	F23	*P*	*F*	*L*	Minimum†		Maximum†	
									Dec (°)	Inc (°)	Dec (°)	Inc (°)
209-1272A-												
1R-1, 44	0.44	7	508.2	257.7	381.6	1.013	1.007	1.006	113.0	22.0	15.8	17.2
2R-1, 63	13.53	9	6643.0	1696.5	7251.6	1.150	1.101	1.045	14.9	0.2	284.7	51.0
3R-1, 114	19.04	9	420.7	214.7	314.3	1.021	1.012	1.010	220.5	4.2	324.2	72.9
4R-1, 85	23.25	14	1099.0	1402.8	169.8	1.015	1.004	1.011	8.0	6.5	103.1	38.1
7R-1, 96	37.86	15	277.2	66.9	309.0	1.013	1.009	1.004	52.0	21.0	145.6	9.4
13R-1, 96	61.66	15	5038.0	2247.2	4146.5	1.180	1.104	1.069	93.1	77.8	347.6	3.3
13R-2, 30	62.50	4	6354.9	4119.8	3825.7	1.289	1.142	1.129	278.1	70.2	166.8	7.4
14R-1, 22	65.92	3C	5851.0	2515.5	4932.7	1.365	1.213	1.125	244.6	34.3	335.7	1.6
16R-1, 137	76.37	22	7900.5	1199.5	9999.9	1.187	1.139	1.042	64.0	49.9	181.2	21.1
17R-1, 59	80.19	10	7952.4	1202.8	9999.9	1.184	1.137	1.041	211.5	40.5	306.7	6.0
17R-1, 130	80.90	19	9999.9	9999.9	9999.9	1.149	1.083	1.061	340.4	75.7	136.5	13.2
18R-1, 44	85.04	6	9999.9	4448.0	8576.8	1.215	1.125	1.080	218.8	43.4	114.1	15.0
21R-1, 50	99.40	4	5591.8	738.9	7406.3	1.113	1.086	1.025	265.1	62.7	122.3	22.4
23R-1, 24	108.74	2B	3003.9	1659.0	2104.6	1.258	1.137	1.107	307.7	48.4	142.3	40.7
24R-1, 77	114.27	11	9999.9	6393.1	6355.3	1.110	1.055	1.052	312.7	64.1	169.0	21.4
25R-1, 127	119.27	15	5775.0	5453.8	2039.3	1.038	1.014	1.023	225.3	5.4	132.2	29.7
26R-1, 75	123.75	3B	9022.1	6603.4	4726.4	1.122	1.056	1.062	245.3	65.1	127.1	12.4
27R-1, 52	127.52	4B	4527.3	2328.9	3361.8	1.063	1.034	1.028	63.9	77.1	173.2	4.3
27R-2, 93	129.43	10	4010.8	307.4	5869.5	1.075	1.061	1.013	260.7	56.1	18.7	17.5

Table T12. Surface water and atmospheric microbiology results, 5–13 June 2003.

Sample	Date (June 2003)	Surface water (counts/mL)		Air growth* (CFU)		Atmospheric condition†
		Bacteria	Virus	Bacteria	Fungi	
a	5	5.75×10^5	5.72×10^6	0/0	0/2	No data
b	6	5.28×10^5	6.00×10^6	0/0	0/0	9.0: light dust
c	7	7.17×10^5	5.32×10^6	0/0	0/2	11.4: light/heavy dust
d	8	6.04×10^5	5.26×10^6	0/0	0/0	11.2: light dust
e	9	7.36×10^5	5.24×10^6	0/1	0/5	7.6: light cloud
f	10	4.34×10^5	5.66×10^6	0/0	0/1	No data
g	11	4.72×10^5	5.30×10^6	0/0	0/1	18.9: dust/heavy cloud cover
h	12	NCSR	NCSR	0/0	0/1	10.5: light dust
I	13	5.66×10^5	5.34×10^6	0/0	0/0	8.0: light cloud

Notes: * = colony-forming units (CFU) growth is measured at 48/96 hr. † = SeaWiFS image values. NCSR = not collected/ship relocation.